Development of Nonlinear Framework for Buffeting Analysis of Long-span Bridges in Time-domain by Volterra Series-based Wind Load Model

Volterra 級数空気力モデルによる長大橋の時刻歴ガスト応答解析のための非線形フレームワークの構築

KHAWAJA ALI

A dissertation submitted in partial fulfilment of the requirements for the degree of

Doctor of Philosophy in Civil Engineering

Department of Civil Engineering

YOKOHAMA NATIONAL UNIVERSITY, JAPAN

September, 2020

YOKOHAMA NATIONAL UNIVERSITY

Development of Nonlinear Framework for Buffeting Analysis of Long-span Bridges in Time-domain by Volterra Series-based Wind Load Model

A dissertation submitted in partial fulfilment of the requirements for the degree of

Doctor of Philosophy in Civil Engineering

By

KHAWAJA ALI

Academic Supervisor

Prof. Hiroshi KATSUCHI

Co-supervisor

Prof. Hitoshi YAMADA

Yokohama, Japan

September, 2020

DEDICATION

To my deceased father, who unfortunately didn't live long enough in this world to see his son become a doctor

Note:

This thesis is proudly dedicated to my beloved late father, Mr. Khawaja Javed Iqbal, who passed away on June 3, 2020 during the time of thesis write-up. I could not travel back to Pakistan from Japan to see my father for the last time because all flights were closed owing to the Coronavirus pandemic. I was totally broken, lost my motivation to move ahead and thought of quitting the PhD research for a moment. In the time of grief and depression, my mother and wife encouraged me and pushed me to do complete my PhD studies because it was a burning desire of my father to see me graduating with a doctor degree in civil engineering. He was desperately waiting for my graduation. I believe that no one else would have been much happier than my father. Therefore, I truly owe this feat to him and my beloved mother.

He was my support, inspiration and a role model to follow. To me, he is irreplaceable. Since childhood, he taught me to work hard and go beyond my limits to achieve what I yearn for. Whenever the things became burdensome for me, he was there to help me out to take my all burden and worries away from me. I honestly dedicate my all achievements to my parents who encouraged my ideas and developed me through thick and thin. They have always been so supportive to me in myriad of ways in which they have actively supported me in my determination to find my passion and realize my potential, and to make this contribution to our world.

ABSTRACT

With the quick development of construction material and computer technology, many super long-span bridges are currently being built all over the world. This trend of increasing the main span length of long-span bridges further increases their vibration periods, making them even more vulnerable to wind actions especially in typhoon prone regions owing to their high flexibility and low structural damping. After the failure of Tacoma Narrows bridge, the bridge engineers mainly focused on the wind-induced vibration of cable-supported bridges under strong winds. In this context, they developed several linear analytical frameworks to perform the buffeting analysis of line-like structures in frequency- and time-domain, primarily based on the assumption of two-dimensional stationary flow, in which the aerodynamic forces are linearized at the mean displaced position of the bridge deck. However, it has been widely recognized, based on the measurements, that the real typhoon winds are highly non-stationary by nature, which causes the time-varying mean response phenomenon of the bridges. Moreover, there is a hefty discrepancy between the buffeting responses obtained from the conventional linear buffeting analysis models and the real phenomenon of bridge vibration, which calls into question the efficacy and fidelity of the existing linear buffeting analysis frameworks. Therefore, the guarantee of bridge safety under such extreme wind events requires accurate modelling of wind-induced effects on the bridge structures such that the non-stationary wind fields can be incorporated accurately, in particular for the super long-span bridges.

The main goal of this dissertation is to develop a nonlinear buffeting analysis framework to better simulate the non-stationary wind-induced effects on long-span bridges by using the Volterra series-based wind load model. Three novel aerodynamic wind load models are developed in this study named *Volterra FD*, *Hybrid Volterra FD*, and *Volterra ANN* models. In the case of the Volterra FD model, the buffeting and self-excited forces on a bridge deck are first formulated in time-domain in terms of indicial functions (IFs) by using the Volterra series of second-order. Then, the first- and second-order Volterra kernels are identified through the experimental data of flutter derivatives and static force coefficients measured at zero angle of attack. Subsequently, the non-stationary turbulent wind fields are generated around the bridge based on the evolutionary power spectral density (EPSD) of measured data of typhoon-induced wind speed. At last, the wind loads based on the Volterra FD model are calculated numerically while considering the effect of non-stationary winds.

Since the wind forces on a bridge deck are very sensitive to the angle of attack showing a nonlinear function of the angle of attack, even a small change in turbulence may cause a significant change in the effective angle of attack due to bridge motions and wind fluctuations. Therefore, the aerodynamic nonlinearities arising from varying angles of attack, large flow

separations at large angle of attack, non-stationary wind, and nonlinear fluid memory effects may not be neglected. Following it, the Volterra FD model is extended to the Hybrid Volterra FD model to incorporate the effect of varying angles of attack on the flutter derivatives and static force coefficients at low- and high-frequency ranges. First, the effective angle of attack is divided into low- (large scale) and high-frequency (small scale) components corresponding to the frequencies lower and higher than a cut-off frequency (e.g., the fundamental frequency of the first mode). Accordingly, the wind forces are also separated into low- and high-frequency components. The low-frequency component of the nonlinear wind forces is modelled by using the QS model in which the low-frequency component of effective angle of attack, and static force coefficients measured at the statically deformed position of the bridge deck are used. The high-frequency component of nonlinear aerodynamic forces are further divided into the nonlinear buffeting and self-excited forces, which are modelled by employing the Volterra FD model while considering the effects of angle-varying static force coefficients, amplitude-dependency of flutter derivatives, non-stationary winds, and nonlinear fluid memory in the wind load modeling.

In the case of the Volterra ANN model, the first- and second-order Volterra kernels are identified by using the Artificial Neural Network (ANN) technique instead of using experimental data of FDs. For that, a Time-delayed Neural Network (TDNN) is designed for modeling the nonlinear aerodynamic forces on the bridge deck. The network is trained, tested, and validated based on the measured wind speed as input and measured bridge displacement as output to extract the synaptic weights of the neurons. These weights are then used to estimate the first- and second-order Volterra kernels.

Based on all three proposed aerodynamic models, the wind loads are calculated and applied to a real full-scale suspension bridge model to demonstrate the effectiveness of the proposed nonlinear framework. The dynamic analysis results show a good agreement in the simulation of typhoon-induced buffeting response of the bridge deck. Moreover, the simulation results of the proposed framework are also compared with the measurement response of the bridge as well as the buffeting responses obtained from the existing aerodynamic models to elucidate the efficiency of the proposed framework. The newly developed Volterra model can effectively investigate the change in bridge aerodynamics induced by time-varying transient and non-stationary winds. The work of this dissertation can by useful for the modification of current wind design guidelines for the flexible super long-span bridges subjected to typhoon-induced non-stationary winds.

ACKNOWLEDGEMENTS

The author wishes to record his great indebtedness to Professor Hiroshi Katsuchi under whose supervision this work was carried out, for his interest and encouragement. The author would also like to say thanks to the co-supervisor, Professor Hitoshi Yamada, for his kind guidance and valuable comments throughout this research work.

The author sincerely acknowledges the committee members, Professor Koichi Maekawa, Associate Prof. Dionysius M. Siringoringo, and Associate Prof. Hiroshi Tamura, for their constructive comments to make this work a valuable contribution to the field of bridge aerodynamics.

The author would also like to thank his wife, Aleena Saleem, whose unending support towards him was matchless and valuable. Without her kind cooperation, this would not have been possible. She experienced a hard time owing to the author's busy and tiring schedule from day to night while working in the structure laboratory, YNU. The author is very much thankful to her for sharing his worries, and for standing by him in his difficult time when the research work was not going in the right direction.

TABLE OF CONTENTS

LIST OF FIGURES

LIST OF TABLES

CHAPTER 1: INTRODUCTION

Wind-induced oscillations are one of the major threats to the safety, fatigue life, and comfort of the long-span bridges. Wind effects on such large and flexible civil infrastructures have received considerable attention after the failure of the Tacoma Narrows bridge in 1940. Preventing wind-induced vibrations on the slender structures with low damping such as suspension and cable-stayed bridges is a challenging task for bridge engineers. Many such structures suffer from unexpected behaviors caused by wind-related phenomena, such as buffeting, flutter, vortex shedding, and cable vibrations. The wind velocities in the atmospheric boundary layer (ABL) can be characterized as synoptic (e.g., Monsoon winds) and non-synoptic (e.g., typhoons, thunderstorm downbursts, and tornadoes). While significant efforts have been made on the synoptic wind-induced effects on long-span bridges over the last many decades, the main goal of this dissertation is to develop an efficient framework for performing the nonlinear buffeting analysis of long-span bridges under the typhoon-induced non-stationary winds. The work of this dissertation can be useful for revising the current wind design guidelines for the super long-span bridges in the typhoon prone areas.

1.1 Motivation of dissertation

It is widely recognized that the long-span bridges existing along the coastline areas are prone to suffering from the extreme winds spawned by typhoons/hurricanes. Owing to climate change and global warming, the intensity of such extreme wind events is increasing yearly all over the world, causing severe damages to the civil infrastructures and costing an immense portion of the budget on their maintenance. For example, the Akashi-Kaikyo bridge, located at central-west of Japan, was struck by a typhoon, numbered as 2018TY20, in 2018 and the bridge experienced a large lateral vibration of around 8 m which called for the costly bridge maintenance. Recently, one of the biggest typhoons *Hagibis*, numbered as 2019TY19, and an earthquake hit East Japan simultaneously in October 2019, damaging the infrastructures especially slender bridges very badly and calling into question their safety and serviceability. Currently, most of the long-span bridges having main span length over 1000 m in the world are located in the coastline area to cross the straits and rivers and in the mountainous area to overpass the deep valleys. Therefore, they can be frequently attacked by the non-stationary winds.

In the viewpoint of the plans for the construction of several super long-span bridges all over the world, it is important to investigate:

1. how well the existing buffeting analysis theory applies to long-span bridges already

constructed in the typhoon prone regions,

2. how to regenerate the real phenomenon of time-varying buffeting response of long-span bridges subjected to typhoon-induced non-stationary winds,
3. how to consider the aerodynamic and aeroelastic nonlinearities existing in the wind-bridge interaction arising from the varying angle of attack, nonlinear fluid memory and the non-proportional relationship between measured wind speed and bridge motion accurately and
4. to what extent the existing aerodynamic wind load models are capable of simulating the real typhoon-induced vibration of the bridge.

As a matter of fact, the design wind velocities with relatively large return periods are generally controlled by the extreme wind events of transient nature such as typhoons/tornados, which stresses the paramount importance of considering the non-stationary wind effects in the modeling of wind loads on bridges. However, the current design guidelines and existing analytical frameworks for long-span bridges are only limited to the constant-line/synoptic/stationary winds of the neutral ABL. Therefore, it is essential to develop an efficient framework for performing the nonlinear buffeting analysis to interrogate the non-stationary wind effects on long-span bridges, where the accurate modeling of the non-stationary winds (characteristics of wind inputs), the transient aerodynamics (from non-stationary wind inputs to load outputs), and aerodynamic nonlinearities (from wind-bridge interaction) are critically important.

1.2 Scope and objectives of dissertation

In this dissertation, an efficient nonlinear buffeting analysis framework to better understand the aerodynamic nonlinearity and non-stationary wind-induced effects on long-span bridges is developed, where the underlying mechanism of the change in bridge aerodynamics induced by time-varying winds is investigated during the development of a novel wind load model by using the concept of Volterra series. Based on the developed analysis framework, the typhoon-induced buffeting response of the long-span bridges can be simulated accurately including the effects of nonlinear fluid memory and aerodynamic nonlinearity. The main goal of this thesis is achieved through the accomplishment of a number of objectives which are herein listed:

1. Development of a nonlinear wind load model in terms of indicial functions (IFs) by using Volterra series for the prediction of buffeting response of long-span bridges under non-stationary winds because, generally, the conventional nonlinear wind load models cannot fully characterize the aerodynamic nonlinearity existing in the wind-bridge interaction system, thus a more advanced nonlinear aerodynamic wind load model is needed,
2. Development of a numerical procedure for the identification of IFs by developing the relationship between the experimentally determined amplitude-dependent flutter derivatives

and IFs, and by mapping the nonlinear relationship between wind speed as input and measured bridge displacement as output through the synaptic weights of neurons via Artificial Neural Network (ANN). An ANN-based unsteady aerodynamic model served as a novel reduced-order wind load model for the bridge deck,

3. Evaluation of the applicability of the existing aerodynamic load models when calculating the buffeting and self-excited forces generated under realistic bridge oscillations, and assessment of the aerodynamic response for each aerodynamic model,
4. Investigation of the presence of aerodynamic and aeroelastic nonlinearities existing in wind-bridge interaction by introducing higher-order Volterra kernels,
5. Investigation of how non-stationary winds and aerodynamic nonlinearities affect the buffeting response of long-span bridges,
6. Validation of quasi-steady assumption in the design of long-span bridges under the real typhoon-induced non-stationary winds,
7. Development of an efficient and reliable approach for simulating the artificial non-stationary wind fields around the bridge based on the measurement data of typhoon winds,
8. Comparison of the effects of non-synoptic and synoptic winds on the dynamic response of long-span bridges,

The summary of the scope and objectives of this dissertation are systematically shown in Figure (1-1).

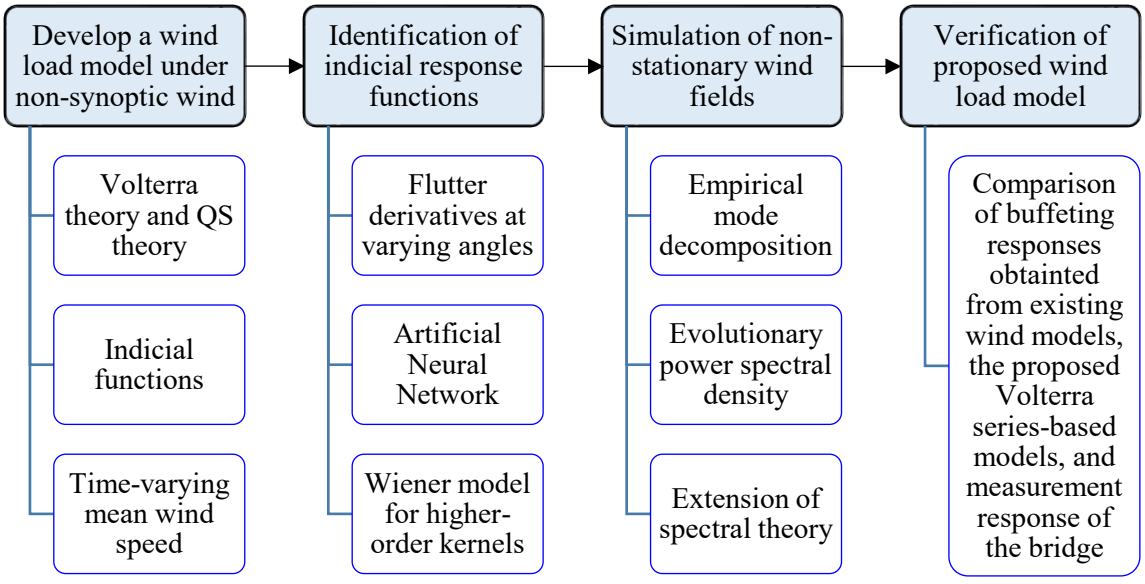

Figure 1-1 Outline of dissertation

1.3 Research methodology

In this dissertation, the time history data of typhoon wind speed is obtained from bridge monitoring authority. The wind speed raw data is decomposed in order to get time-varying mean wind speed based on the empirical mode decomposition (EMD) method. The remaining fluctuating wind speed is used to obtain the evolutionary power spectral density (EPSD) in the time-frequency-domain. Based on this EPSD, the non-stationary wind fields are generated around the bridge by extending the conventional spectral theory to accommodate the EPSD matrix at discrete nodes on the bridge deck with the help of the 2-dimensional uniform grid approach. After the detailed investigation of the existing aerodynamic load models, a novel and efficient nonlinear wind load model is developed in terms of IFs by using the Volterra series and QS theory. The static wind loads are computed by using time-varying mean wind speed instead of constant mean wind speed. In the case of buffeting and self-excited loads on the bridge deck, the aerodynamic and aeroelastic IFs are identified through the experimental and ANN techniques. First, static and buffeting loads are applied to the bridge deck in a three-dimensional (3D) manner. As a result, the bridge exhibits a 3D response which is utilized as a feedback system to evaluate the motion-dependent self-excited forces on the bridge deck. These motion-dependent forces are applied separately on the bridge deck in order to compute the buffeting response of the bridge accurately. The layout of the proposed framework is illustrated in Figure (1-2).

1.4 Contribution of the present work

The overall ambition of this thesis is to contribute to the advancement of the buffeting analysis by providing insights into the extension of the conventional analytical wind model to a Volterra series-based nonlinear wind load model which could capture the aerodynamic nonlinearity and nonlinear fluid memory effects, and could also simulate the real phenomenon of time-varying mean response of the bridge under typhoon-induced non-stationary winds. In other words, in this research work, a nonlinear framework for the buffeting analysis of flexible bridges under the non-stationary winds is developed, validated, and applied to a real full-scale bridge. The original scientific results and contributions of this dissertation are briefly summarized below:

1. Development of a novel nonlinear framework, consisting of 3D wind load models, for performing the buffeting analysis under typhoon-induced non-stationary winds,
2. Development of a generalized framework for the identification of IFs from the experimental data of flutter derivatives (FDs), which could simulate the aerodynamic loads accurately,
3. Development of a numerical procedure for the identification of IFs by using ANN approach,
4. Development of a computational framework for the analysis of long-span bridges under non-

stationary wind actions based on the finite element method,

5. The study on the following effects on the buffeting response of long-span bridges:
   - Effects of aerodynamic and aeroelastic nonlinearities,
   - Effects of stationary and non-stationary winds,
   - Effects of linear and nonlinear fluid memory,
6. Further development and validation of wind load models in time-domain for the computation of unsteady wind loads on the bridge deck,

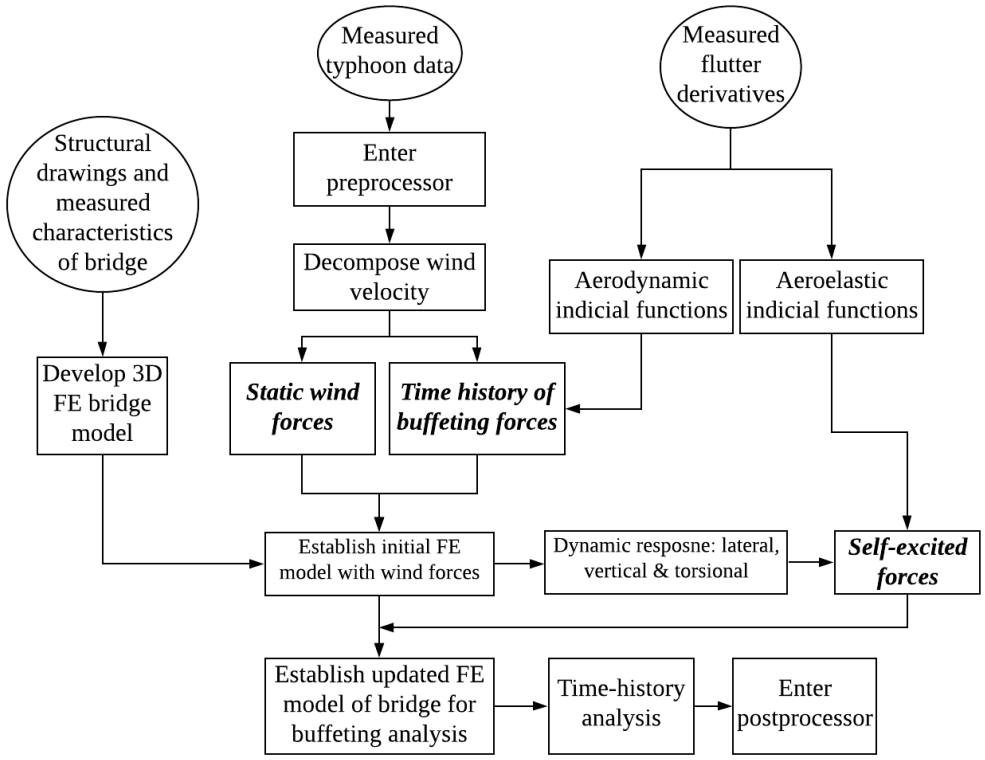

Figure 1-2 Layout of general calculation procedure for buffeting analysis

1.5 Organization of thesis

The amount of research work focusing on the regeneration of the real phenomenon of time-varying buffeting response of the bridge under non-stationary winds is lower than its counterpart of constant mean buffeting response under stationary winds. Hitherto, the wind turbulence statistics represent large uncertainties in the prediction of buffeting response of long-span cable-supported structures. To contribute to reduce the uncertainties, this thesis makes an effort to develop a nonlinear scheme to simulate the accurate buffeting response of the bridges closer to the real measurement data of bridge displacements induced by the typhoon winds. Apart from the

Chapter 1 which is the introduction, each chapter is devoted to one step towards the development of buffeting analysis framework while progressing ahead logically. A brief breakdown of the thesis is as follows:

Chapter 2 – Literature review

A review of the prominent literature in the study of buffeting is presented in this chapter. Also, the development of the understanding of the buffeting phenomenon is included and how this has allowed relevant theory to progress. In addition to that, a brief overview of the comparison of the existing aerodynamic load models is also given.

Chapter 3 – Volterra series-based wind load model

In this chapter, the buffeting and self-excited forces on the bridge deck are formulated in terms of indicial response functions by extending the conventional linear unsteady (LU) model to a Volterra-series based wind load model.

Chapter 4 – Identification of Volterra kernels

Volterra kernels are identified in this chapter by utilizing two approaches: the first approach is based on the experimentally determined flutter derivatives and the second approach is based on ANN. An understanding of these approaches will be beneficial for the advancement and discussion of the buffeting theory of bridges.

Chapter 5 – Simulation of non-stationary wind fields

This chapter concentrates on a simulation technique to generate the non-stationary wind fields around the bridge by incorporating the EPSD matrix into the conventional spectral theory based on the measured wind speed data of typhoon events, i.e., TY9807 and 2018TY20 in Japan.

Chapter 6 – Numerical example

This chapter presents a numerical example of a real full-scale bridge on which the proposed framework is tested. The efficacy of the proposed wind load model is checked by comparing its simulation results with the measurement response of the bridge. Special attention is paid on any similarities/dissimilarities existing between the conventional aerodynamic models and the proposed wind load model.

Chapter 7 – Conclusions and future directions

The concluding chapter comprises a summary of the dissertation and concluding remarks regarding the efficiency of proposed Volterra series-based wind load model. Furthermore, the key points of the future research work, an extension of the present research work, are also included in this chapter.

CHAPTER 2: LITERATURE REVIEW

This chapter entails the literature review of previous research works related to the buffeting analysis of long-span bridges subjected to turbulent winds. Various aerodynamic load models are reviewed and compared in order to address the questions on their assumption, complexity, suitability, and applicability. The design of a structure usually entails the use of mathematical models to duplicate the full-scale structural behavior and natural events that may possibly happen during the structure's lifetime. For long-span bridges, the wind-induced vibrations can be the governing criteria at the design stage. Thereby, the reliable mathematical models are indispensable to predict the vibrations of various structural components such as the deck, cables, and towers, in terms of their aerostatic, aeroelastic, and buffeting displacements. In this chapter, a brief literature review is first presented to throw the light on the ongoing advancements in the field of buffeting analysis from past to present. Then, the sources and forms of different aerodynamic load models are re-examined, which are usually used to analyse the response of long-span bridges subjected to the gusty winds. At last, the benefits of IFs and Volterra series in the modelling of aerodynamic wind loads on the bridge deck are discussed.

2.1 Introduction

Several civil engineering infrastructures such as long-span bridges, tall masts, and overhead power lines conform to a slender, elongated, and line-like form (Davenport 1962). Such structures are particularly vulnerable to wind loading. Thereby, the wind-induced oscillations commonly represent the leading criterion in the design of long-span bridges, which demands accurate modelling of the wind forces generated on the bridge deck due to the incoming wind flow. The interaction between wind flow and bridge deck can be interpreted as the trading of energy between them to provide the insight of damping effects on the structure. At low wind speed, the wind flow, and hence the wind force somehow acts as a damper to provide the positive aerodynamic damping for the structure. However, up to a certain high wind speed, which depends on the geometric shape of the deck and, the flow will feed energy significantly to the structure and quickly reduce the aerodynamic damping to zero or negative value to make the structure divergently oscillate. This is the critical condition of the flutter instability of the bridge deck, which would result in destructive failures of bridges as evidenced in the case of the Tacoma Narrows bridge in 1940.

Therefore, in flutter prediction, only the self-excited force is necessary for the analysis because the focal point is the critical point of instability or critical wind speed. On the other hand, the buffeting analysis needs considering both kinds of forces, self-excited and buffeting, to

analyse the random vibration of the bridge deck in a wide range of wind speed before the critical flutter wind speed. In Figure (2-1), it can be seen that there exists an interaction between these two forces when the feedback from self-excited force modifies the buffeting force (or vice versa). However, this interaction seems to be insignificant, and hence can be ignored. More discussions and formal formulations of this interaction can be found in (Scanlan 1993). Under the linearized assumption for the action of the aerodynamic force on the bridge deck, which has been widely accepted so far in bridge analysis, the external force (F_{ext}) is considered as the superposition of the wind forces, neglecting any possible interaction between them. The dashed line in Figure (2-1) depicts the linearized assumption of superposition law, indicating the self-excited force directly applying to structure i.e., $M\ddot{u} + Ku = F_{st} + F_b + F_{se}$, where F_{st} is the static force; F_b is buffeting force vector; F_{se} is self-excited force vector; M and K are the mass and stiffness matrices of the structural system, respectively, and $\ddot{u}$ and u are the acceleration and displacement vectors, respectively. The mean wind speed is responsible for the static forces acting on the structural components. The most important force out of static forces is the drag force acting on the bridge deck, towers, and main cables. The static forces produce large stresses in all structural components and are one of the most important factors considered during the design of super long-span bridges. For this reason, it is chiefly important to attain the low drag forces on the bridge decks: a requirement that has led the development of streamlined box girders.

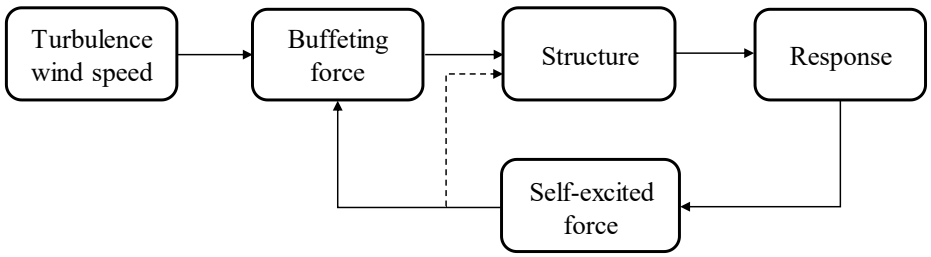

Figure 2-1 Aerodynamic and aeroelastic relationship between wind and structural vibration

2.2 Advances in buffeting analysis from past to present

The wind tunnel test-based models for the slender structures have been used in different forms since the late 1930s, and the progress continued in this field; however, the issues regarding the flutter and buffeting in long-span bridges under turbulent wind are complex and require recourse to wind tunnel models. The bridge flutter is generally a separated-flow phenomenon in which a single torsional mode becomes unstable and drives the system towards the excessive oscillations, whereas the buffeting problem occurs during exposure to natural wind, which

generally has both a mean velocity and random, turbulent velocity components, the rms value of the latter occasionally ranging as high as 20% of the mean (Scanlan 1978). Thus, the natural wind may pose both the stability and the buffeting problems simultaneously in the prototype bridge.

Since the 1960s, many methods for predicting buffeting response of long-span bridges have been proposed in both frequency- and time-domain. Several contributions, in the beginning, to the wind-bridge interaction problem are indicated by Davenport (1961; 1962a; 1962b; 1966). The developments in the analysis for the aerodynamic response of long-span bridges to turbulent winds also owe much to studies of the buffeting and flutter of aircraft (Scanlan 1951; Bisplinghoff et al. 1962). Forces acting on the bluff bodies like long-span bridge decks have been explicated by analytical and theoretical approaches, which are influenced by similar formulations as those of two-dimensional airfoil theory. The most conventional method is the admittance single mode method proposed by Davenport (1962), which is based on the quasi-steady assumption used for the formulation of aerodynamic forces on the line-like structures. Simiu and Scanlan (1996) further developed another single mode method while considering the effect of aeroelastic forces. In spite of their simplicity, these methods are unsuitable for the modern long-span bridges from the point of view of analysing the coupled buffeting responses.

With the advancement in computational capacity, numerous efforts have been made to solve the buffeting problem in time-domain by several methods. The bridge engineers mainly focused on the time-domain analysis of buffeting response, particularly of low-frequency structures such as suspension bridges. Relative velocity by Miyata et al. (1995) and Rational Functions by Boonyapinyo et al. (1997) are typical among others. Jain et al. (1996) also proposed a multi-mode method in frequency-domain. These methods consider the effects of aerodynamic and structural couplings simultaneously. Jakobsen et al. (2001) also developed a time-domain method for calculation of dynamic response of line-like structures subjected to the buffeting forces by combining the simulated wind speed time history to a quasi-steady load model and a finite element algorithm. The major reason for this is that the alternative approach of a mode-by-mode method (frequency-domain analysis approach) demands linearity in the loading assumption as well as in structural behavior, which is a limitation in the design guidelines under serviceability limit state but not under ultimate limit state.

In the time-domain computational procedure, nonlinear load effects can be included to provide a better understanding for the evaluation of the safety margin under extreme load events. Extensive comparisons between the frequency-domain and time-domain analyses based on the quasi-steady (QS) and linear unsteady (LU) models are conducted in (Petrini et al. 2007; Salvatori et al. 2007; Lazzari 2005). Diana et al. (2008) developed a novel concept of modelling the aerodynamic forces based on the hysteresis behavior of the aerodynamic force and moment coefficients with respect to the dynamic angle of attack for different reduced wind speeds. The

aim was to develop a rheological element that can easily capture the unsymmetrical nonlinear hysteresis. The model was based on many independent mechanical oscillators in a parallel configuration, whose coefficients are attained with the help of aerodynamic force transfer functions.

In Wu and Kareem (2011), a non-parametric model was developed based on the Artificial Neural Network (ANN), an input-output black box modelling technique, in order to describe the hysteretic behavior. Although promising results are elucidated for the coupled gust-induced and motion-induced forces, the model was still not applied for the computation of the buffeting response of a real full-scale bridge structure. Nevertheless, the same idea of ANN was used by Wu and Kareem (2013) for approximating the aerodynamic hysteresis with respect to the angle of attack in the modified hybrid model. To further examine the aerodynamic nonlinearities, Wu and Kareem (2015) used the Volterra series and associated Volterra kernels to simulate the nonlinear dynamical system with the fading memory concept. Using Volterra series, the nonlinear dynamical system is modelled as an infinite sum of multidimensional convolution integrals of increasing order, which correlates to the unsteady aerodynamic forces on the bridge deck. The accuracy of the Volterra series-based aerodynamic model is highly dependent on the accurate identification of the Volterra kernels. Further comparison of the modelling techniques and relevant discussions can be seen in (Scanlan 1993; Chen and Kareem 2002; Wu and Kareem 2013). The layout of advances in buffeting analysis from past to present is shown in Figure (2-2).

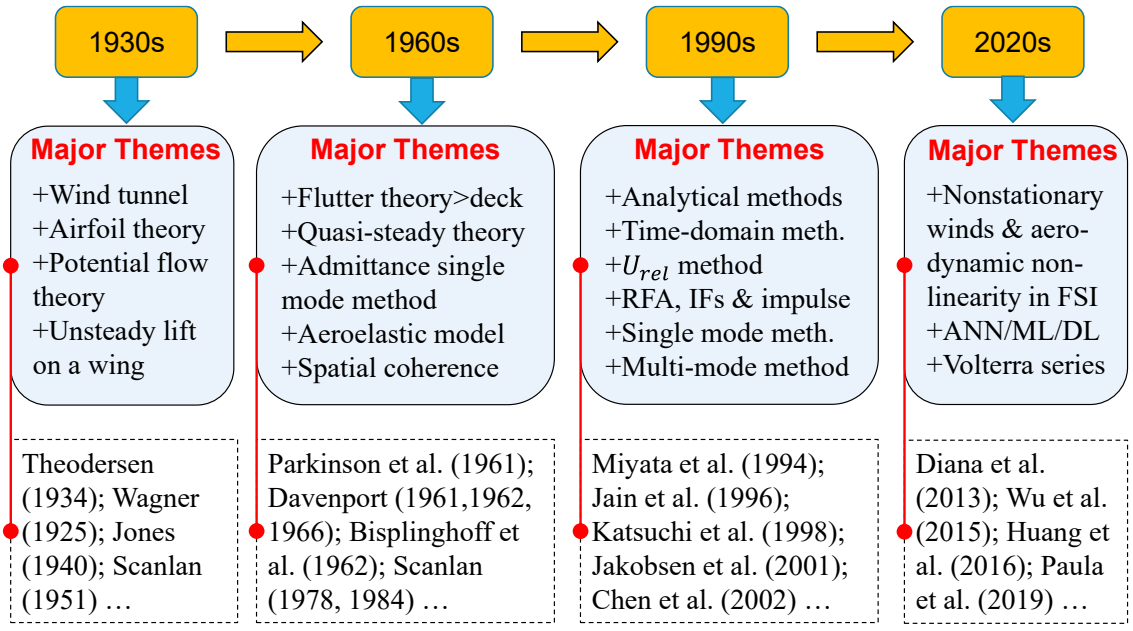

Figure 2-2 The advances in buffeting analysis from past to present

2.3 Existing aerodynamic wind load models

The wind-bridge interaction is a 3D complex phenomenon. Nevertheless, most of the aerodynamic wind load models are developed for 2D bridge section models, which are then applied to a 3D bridge to simulate the actual response of the bridge structure. In this context, there is a famous saying of Professor Scanlan (1987) that "It is true to state that no mathematical model, even a fully three-dimensional one, can duplicate real bridge behavior completely". Keeping it in mind, it is relevant to review some of the comparative analyses which have been performed in the field of semi-analytical aerodynamic modeling. The semi-analytical models formulate the aerodynamic forces using a set of mathematical equations, partially based on airfoil theory, and aerodynamic coefficient accounting for the wind-bridge interaction of a bridge deck. The significant discrepancies between the models instigate from the underlying physical assumptions used during the modelling phase. With these hypothetical assumptions, the semi-analytical models yield a simple formulation of the aerodynamic forces, which can neglect or account for certain factors such as aerodynamic nonlinearity, fading fluid memory, and aerodynamic coupling. A comprehensive review paper on various aerodynamic models can be found in (Kavrakov et al. 2017; Kavrakov et al. 2019), in which different categories of aerodynamic models are made based on their complexity and comparability. To shed some light on the impact of the underlying assumptions on the accuracy of aerodynamic modelling, some other studies regarding the comparison of different aerodynamic models have been done over the years (Scanlan 1978(I); 1978(II); Davenport 1962; Diana et al. 1993, Diana et al. 2010; Chen and Kareem 2001; Wu and Kareem 2013). Therein, it is shown that aerodynamic assumptions can significantly influence the structural response to wind actions.

In this section, a brief review of some contemporary aerodynamic models is presented. The eight different existing semi-analytical models in the time-domain are investigated including steady (S), linear steady (LS), quasi-steady (QS), linearized quasi-steady (LQS), corrected quasi-steady (CQS), mode-by-mode (MBM), linear unsteady (LU) and hybrid nonlinear (HNL) models. Conventionally, the wind-bridge interaction is treated as a 2D coupled problem of a bridge deck immersed in a fluid with a constant air density ρ and a width B as shown in Figure (2-3) in which U_{rel} denotes the relative wind velocity; ϕ is the dynamic angle of attack; L(t) is the lift force; $M(t)$ is the pitching moment; $u(t)$ is the longitudinal fluctuating wind, $w(t)$ is the vertical fluctuating wind, and $\overline{U}$ represents the mean wind speed which is assumed to be constant for the stationary process over a certain averaging time period. This assumption is common in most of the aerodynamic models for the design of structures (Davenport 1962; Simiu and Scanlan 1996). However, in the case of typhoons and other extreme wind events, such an assumption is no more valid. The deck with width B is assumed to be rigid and is supported by the vertical

spring with stiffness k_h and rotational spring with stiffness k_α, allowing the vertical and rotational displacements denoted by h and α, respectively. Congruently, the bridge deck has the inertial mass of m_h and moment of inertia of I_α, while the structural damping of the system is included by the vertical and rotational damping coefficients denoted by c_h and c_α, respectively. The equation of motion (EOM) of the wind-bridge interaction is defined in Eq. (2.1). The subsequent subsections focus on the existing aerodynamic wind load models for the bridge deck.

$$m_h\ddot{h} + c_h\dot{h} + k_h h = L(t) \tag{2.1a}$$

$$I_\alpha\ddot{\alpha} + c_\alpha\dot{\alpha} + k_\alpha\alpha = M(t) \tag{2.1b}$$

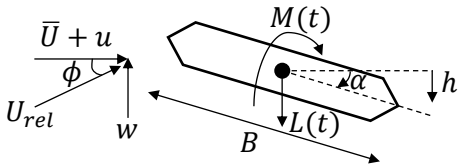

Figure 2-3 Coupled wind-structure interaction system for semi-analytical models

2.3.1 Steady model, *S*

This model computes the aerodynamic forces generated on a 2D bridge deck such as:

$$L(t) = F_L\cos(\phi) - F_D\sin(\phi) \tag{2.2a}$$

$$M(t) = \frac{1}{2}\rho U_{rel}^2 B^2 C_M(\alpha_{eff}) \tag{2.2b}$$

$$F_D = \frac{1}{2}\rho U_{rel}^2 B C_D(\alpha_{eff}) \tag{2.3a}$$

$$F_L = -\frac{1}{2}\rho U_{rel}^2 B C_L(\alpha_{eff}) \tag{2.3b}$$

$$U_{rel} = \sqrt{(\bar{U}+u)^2 + w^2} \tag{2.3c}$$

$$\alpha_{eff} = \alpha_s + \phi \tag{2.3d}$$

$$\phi = \arctan\left(\frac{w}{\bar{U}+u}\right) \tag{2.3e}$$

where α_{eff} is the effective angle of attack; ϕ is the dynamic angle of attack induced by the bridge deck motions and wind fluctuations (herein the term "effective angle of attack" means that only the deck motions are responsible for generation of the angle of attack), and α_s is the static angle of attack identified at an equilibrium position. C_D, C_L and C_M denote the static force coefficients for the drag, lift, and pitching moment, respectively. These coefficients are obtained from the wind tunnel tests under steady flow conditions or computational fluid dynamics (CFD) simulations under the laminar flow conditions, and depend on the angle of attack, generally in a nonlinear manner.

2.3.2 Linear steady model, *LS*

The linear steady (LS) model is also valid for 2D problems, which is obtained by the linearizing Eq. (2.2) at the equilibrium position of the angle of attack and neglecting the higher-order terms of the velocity such as:

$$L(t) = -\frac{1}{2}\rho\bar{U}^2 B\left[C_L + 2C_L\frac{u}{\bar{U}} + (C_L' + C_D)\frac{w}{\bar{U}}\right] \tag{2.4a}$$

$$M(t) = \frac{1}{2}\rho\bar{U}^2 B^2\left[C_M + 2C_M\frac{u}{\bar{U}} + C_M'\frac{w}{\bar{U}}\right] \tag{2.4b}$$

where $C_L = C_L(\alpha_s)$, $C_D = C_D(\alpha_s)$ and $C_M = C_M(\alpha_s)$ depend on α_s, and C_L', C_D' and C_M' are the first derivatives of C_L, C_D and C_M, respectively.

2.3.3 Quasi-steady model, *QS*

The quasi-steady theory has a preponderant role in the aeroelastic and aerodynamic analysis frameworks, which explicates the aerodynamic load through a static nonlinear relationship between the incoming wind flow and wind-induced forces on a structure. It was first used to model the onset mechanism of galloping, where the unsteady aerodynamic forces exerted on a vibrating structure were modelled by using the steady-state coefficients (Parkinson and Brooks 1961). This model is based on the assumption that in each time-step, the forces due to the wind-bridge interaction are the same as in an equivalent steady-state at infinite time. Hence, the rise time of the wind forces is assumed to be instantaneous and the fluid memory effects are not taken into account. The major advantage of this model is to consider the nonlinearity. However, no fluid memory effects are taken in account in the QS theory. Consequently, the QS theory is only appropriate if the time required by the incoming wind flow to pass around the structure and to be convected far enough downstream is less than the time taken by the structure to react to the disturbances occurred in the surrounding flow. Henceforth, the QS theory is usually used for the low-frequency structures (or equivalently for the high reduced velocity).

Based on the QS theory, the aerodynamic lift and torsional moment per unit span length of the bridge deck can be expressed in reference to (Kovacs et al. 1992; Miyata et al. 1995) such as:

$$L(t) = F_L\cos(\phi) - F_D\sin(\phi) \tag{2.5a}$$

$$M(t) = \frac{1}{2}\rho U_{rel}^2 B^2 C_M(\alpha_{eff}) \tag{2.5b}$$

where

$$F_D = \frac{1}{2}\rho U_{rel}^2 B C_D(\alpha_{eff}) \tag{2.6a}$$

$$F_L = -\frac{1}{2}\rho U_{rel}^2 B C_L(\alpha_{eff}) \tag{2.6b}$$

$$U_{rel} = \sqrt{(\bar{U} + u)^2 + (w + \dot{h} + m_1 B\dot{\alpha})^2} \tag{2.6c}$$

$$\alpha_{eff} = \alpha_s + \alpha + \phi \tag{2.6d}$$

$$\phi = \arctan\left(\frac{w + \dot{h} + m_1 B\dot{\alpha}}{\bar{U} + u}\right) \tag{2.6e}$$

where m_1 coefficient stipulates the position of the aerodynamic center which tells about a resultant point, where all components of the self-excited forces act, arising due to the rotational DOF. In other words, it stipulates an equivalent point at which there is an equivalent vertical velocity due to the angular displacement as the self-excited forces depend on the vertical velocity of the bridge deck. This point is valid for an equivalent quasi-steady state, which is generally identified based on the flutter derivatives.

2.3.4 Linear quasi-steady model, *LQS*

Among all, the simplest model is the LQS model which is linear and does not incorporate the unsteadiness of the aerodynamic forces. This model is developed by linearizing the QS model at the static equilibrium position to compute the wind-induced aerodynamic/aeroelastic forces. Based on the LQS model, the lift, drag, and torsional coefficients are expressed as:

$$C_L(\alpha_{eff}) \cong C_L(\alpha_s) + (\alpha + \phi)C_L'|_{\alpha_s} \tag{2.7a}$$

$$C_D(\alpha_{eff}) \cong C_D(\alpha_s) + (\alpha + \phi)C_D'|_{\alpha_s} \tag{2.7b}$$

$$C_M(\alpha_{eff}) \cong C_M(\alpha_s) + (\alpha + \phi)C_M'|_{\alpha_s} \tag{2.7c}$$

After the simplification, the lift force and pitching moment per unit span length of the bridge deck in the global bridge coordinates can be expressed as:

$$L(t) = -\frac{1}{2}\rho\bar{U}^2 B\left[C_L + 2C_L\frac{u}{\bar{U}} + (C_L' + C_D)\frac{w}{\bar{U}} + (C_L' + C_D)\frac{\dot{h} + m_1 B\dot{\alpha}}{\bar{U}} + C_L'\alpha\right] \tag{2.8a}$$

$$M(t) = \frac{1}{2}\rho\bar{U}^2 B^2\left[C_M + 2C_M\frac{u}{\bar{U}} + C_M'\frac{w}{\bar{U}} + C_M'\frac{\dot{h} + m_1 B\dot{\alpha}}{\bar{U}} + C_M'\alpha\right] \tag{2.8b}$$

2.3.5 Corrected quasi-steady model, *CQS*

A clear shortcoming of the QS model is that it cannot consider the unsteady fluid memory effects. In order to improve this model, a CQS model has been proposed where a modified coefficient is introduced by Diana et al. (1993) to account for the unsteady effects while retaining the effects of nonlinearity on the dynamic response. According to the CQS model, static wind force coefficients are modified as $C_j(\alpha_{eff}) = C_j(\alpha_s) + C_j^*(\alpha_{eff})$ for $j \in \{D, L, M\}$, where C_j^* denotes a corrected nonlinear static wind force coefficient evaluated as follows:

$$C_D^*(\alpha_{eff}) = \int_{\alpha_s}^{\alpha_e} K_D^*(\alpha)C_D'(\alpha)d\alpha \tag{2.9a}$$

$$C_L^*(\alpha_{eff}) = \int_{\alpha_s}^{\alpha_e} K_L^*(\alpha) C_L'(\alpha) d\alpha \tag{2.9b}$$

$$C_M^*(\alpha_{eff}) = \int_{\alpha_s}^{\alpha_e} K_M^*(\alpha) C_M'(\alpha) d\alpha \tag{2.9c}$$

where K_j^* denotes the frequency-dependent correction coefficient identified from dynamic tests. Alternatively, K_j^* can be identified from the FDs at different angles of attack as follows:

$$K_D^* = \frac{K^2 P_3^*}{C_D'}, \qquad K_L^* = \frac{K^2 H_3^*}{C_L'}, \qquad K_M^* = \frac{K^2 A_3^*}{C_M'} \tag{2.9d}$$

2.3.6 Linear unsteady model, *LU*

The linear unsteady (LU) model is based on the conventional convolution theory in which the output of a linear system is related to its output through an impulse response function. In the bridge aerodynamics, Davenport and Scanlan introduced an efficient way to treat unsteadiness by including the linear frequency-dependent coefficients (Davenport 1962; Scanlan 1978(I); Scanlan 1978(II)). The self-excited forces are then defined as a linear function of the vibration and its frequency content, including the aerodynamic coupling terms between the modes. The buffeting forces are also upgraded by introducing the linear frequency-dependent coefficients between the wind fluctuations and forces, which are known as aerodynamic admittance functions as:

$$D_b = \frac{1}{2}\rho \overline{U}^2 B \left[2C_D \chi_{Du} \frac{u}{\overline{U}} + (C_D' - C_L)\chi_{Dw} \frac{w}{\overline{U}}\right] \tag{2.10a}$$

$$L_b = -\frac{1}{2}\rho \overline{U}^2 B \left[2C_L \chi_{Lu} \frac{u}{\overline{U}} + (C_L' + C_D)\chi_{Lw} \frac{w}{\overline{U}}\right] \tag{2.10b}$$

$$M_b = \frac{1}{2}\rho \overline{U}^2 B^2 \left[2C_M \chi_{Mu} \frac{u}{\overline{U}} + C_M' \chi_{Mw} \frac{w}{\overline{U}}\right] \tag{2.10c}$$

where $\chi_{ju}(K)$ and $\chi_{jw}(K)$ for $j \in \{D,\ L,\ M\}$ are the aerodynamic admittance functions that are proposed to consider the unsteady effects of incoming wind fluctuations. This model neglects the aerodynamic nonlinearity; nevertheless, it takes the linear fluid memory effects into account. The buffeting and self-excited forces in frequency-domain are usually approximated using aerodynamic admittances and flutter derivatives, respectively, whereas the buffeting forces induced by the turbulent winds in time-domain are expressed as:

$$\begin{aligned} L_b(t) = -\frac{1}{2}\rho \overline{U}^2 B \Bigg[& C_L + 2C_L \int_0^t \dot{\psi}_{Lu}(\tau) \frac{u(t-\tau)}{\overline{U}} d\tau + (C_D + C_L') \Bigg\{ \int_0^t \dot{\psi}_{Lw}(\tau) \frac{w(t-\tau)}{\overline{U}} d\tau \\ & + \int_0^t \dot{\phi}_{L\dot{h}}(\tau) \frac{\dot{h}(t-\tau)}{\overline{U}} d\tau + \int_0^t \dot{\phi}_{L\dot{p}}(\tau) \frac{\dot{p}(t-\tau)}{\overline{U}} d\tau + \int_0^t \dot{\phi}_{L\alpha}(\tau)\, \alpha(t-\tau) d\tau \Bigg\} \Bigg] \end{aligned} \tag{2.11a}$$

$$M_b(t) = \frac{1}{2}\rho\bar{U}^2B^2\left[C_M + 2C_M\int_0^t \dot{\psi}_{Mu}(\tau)\frac{u(t-\tau)}{\bar{U}}d\tau + C'_M\left\{\int_0^t \dot{\psi}_{Mw}(\tau)\frac{w(t-\tau)}{\bar{U}}d\tau\right.\right.$$
$$\left.\left. + \int_0^t \dot{\phi}_{M\dot{h}}(\tau)\frac{\dot{h}(t-\tau)}{\bar{U}}d\tau + \int_0^t \dot{\phi}_{M\dot{p}}(\tau)\frac{\dot{p}(t-\tau)}{\bar{U}}d\tau + \int_0^t \dot{\phi}_{M\alpha}(\tau)\,\alpha(t-\tau)d\tau\right\}\right] \tag{2.11b}$$

$$D_b(t) = \frac{1}{2}\rho\bar{U}^2B\left[C_D + 2C_D\int_0^t \dot{\psi}_{Du}(\tau)\frac{u(t-\tau)}{\bar{U}}d\tau + (C'_D - C_L)\left\{\int_0^t \dot{\psi}_{Dw}(\tau)\frac{w(t-\tau)}{\bar{U}}d\tau\right.\right.$$
$$\left.\left. + \int_0^t \dot{\phi}_{D\dot{h}}(\tau)\frac{\dot{h}(t-\tau)}{\bar{U}}d\tau + \int_0^t \dot{\phi}_{D\dot{p}}(\tau)\frac{\dot{p}(t-\tau)}{\bar{U}}d\tau + \int_0^t \dot{\phi}_{D\alpha}(\tau)\,\alpha(t-\tau)d\tau\right\}\right] \tag{2.11c}$$

where $\psi(t)$ represents the aerodynamic unit-step response to buffeting forces (also known as aerodynamic indicial response function), and $\phi(t)$ represents the aeroelastic unit-step response to self-excited forces (also known as aeroelastic indicial response function), which are determined from the aerodynamic transfer functions and FDs, respectively. The formulation of the LU model will be discussed in detail in Chapter 3.

2.3.7 Mode-by-mode Model, *MBM*

The mode-by-mode model neglects the aerodynamic coupling between structural modes. It is conventionally used for the buffeting analysis in frequency-domain due to its simplicity. The simplification in the MBM model is to neglect the coupling between structural modes on the aerodynamic side. For a 3D system, the cross-terms between the vertical and torsional degrees of freedom (DOFs) in Eq. (2.11) are ignored; henceforth, the MBM model is developed as follows:

$$L_b(t) = -\frac{1}{2}\rho\bar{U}^2B\left[C_L + 2C_L\int_0^t \dot{\psi}_{Lu}(\tau)\frac{u(t-\tau)}{\bar{U}}d\tau\right.$$
$$\left. + (C_D + C'_L)\left\{\int_0^t \dot{\psi}_{Lw}(\tau)\frac{w(t-\tau)}{\bar{U}}d\tau + \int_0^t \dot{\phi}_{L\dot{h}}(\tau)\frac{\dot{h}(t-\tau)}{\bar{U}}d\tau\right\}\right] \tag{2.12a}$$

$$M_b(t) = \frac{1}{2}\rho\bar{U}^2B^2\left[C_M + 2C_M\int_0^t \dot{\psi}_{Mu}(\tau)\frac{u(t-\tau)}{\bar{U}}d\tau\right.$$
$$\left. + C'_M\left\{\int_0^t \dot{\psi}_{Mw}(\tau)\frac{w(t-\tau)}{\bar{U}}d\tau + \int_0^t \dot{\phi}_{M\alpha}(\tau)\,\alpha(t-\tau)d\tau\right\}\right] \tag{2.12b}$$

$$D_b(t) = \frac{1}{2}\rho\bar{U}^2 B \left[C_D + 2C_D \int_0^t \dot{\psi}_{Du}(\tau) \frac{u(t-\tau)}{\bar{U}} d\tau \right.$$
$$\left. + (C_D' - C_L) \left\{ \int_0^t \dot{\psi}_{Dw}(\tau) \frac{w(t-\tau)}{\bar{U}} d\tau + \int_0^t \dot{\phi}_{D\dot{p}}(\tau) \frac{\dot{p}(t-\tau)}{\bar{U}} d\tau \right\} \right] \quad (2.12c)$$

2.3.8 Hybrid nonlinear model, *HNL*

Recently, numerous aerodynamic models have been established including the fluid memory effects, which are based on the aerodynamic hysteretic behavior (Diana et al. 2008; Diana et al. 2010). The incentive of the hybrid nonlinear (HNL) model is to employ the benefits of LU and QS models for different range of reduced wind speeds. The bridge response and wind spectrum are separated into the low- and high-frequency components. The HNL model is introduced based on the idea that the effect of fluid memory is insignificant at low reduced frequency and the nonlinearity dominates the aerodynamic forces, while for high reduced frequencies, the effect of fluid memory is significant. The effective angle of attack is also split into a low- and high-frequency components, denoted as α_{eff}^l and α_{eff}^h, respectively. The low-frequency component of the force is modelled by using the QS model, resulting in a low-frequency effective angle of attack. On the other hand, a conventional convolution-based LU model is employed to compute the high-frequency component of the buffeting and self-excited forces on a bridge deck by linearizing the wind forces at low-frequency component of effective angle of attack (Chen and Kareem 2003). The total nonlinear aerodynamic force is then computed as follows:

$$\begin{aligned} \mathrm{F} = \mathrm{F}(\alpha_{eff}) &\cong \mathrm{F}(\alpha_{eff}^l) + \frac{d\mathrm{F}}{d\alpha}\Big|_{\alpha_{eff}^l} \times \alpha_{eff}^h \\ &= \mathrm{F}^l + \mathrm{F}_{\mathrm{se}}^h + \mathrm{F}_{\mathrm{b}}^h = \mathrm{F}^{QS} + \mathrm{F}^{LU} \end{aligned} \quad (2.13)$$

where F^{QS} is the nonlinear aerodynamic force due to the low-frequency components of wind speed fluctuations and bridge deck motions calculated by using Eq. (2.5) and F^{LU} is the force due to the high-frequency components of wind speed fluctuations and bridge motions computed by Eq. (2.11). The formulation of Diana et al. (2013) is employed in the following form:

$$\alpha_{eff}^l = \alpha_s + \alpha^l + \arctan\left(\frac{w^l + \dot{h}^l + m_1 B\dot{\alpha}^l + n_1\dot{w}^l}{\bar{U} + u^l - \dot{p}^l}\right) \quad (2.14)$$

where n_1 is introduced to account for the phase lag between the wind fluctuations and the quasi-steady aerodynamic force. The HNL model possesses the benefit of nonlinearity of QS model in the high reduced wind speed range, and since the unsteady characteristics are unique for the low reduced wind speed range, the LU model is used to capture the fluid memory effects. The cut-off frequency is selected based on the natural frequency of 1st mode of bridge (Wu and Kareem 2013).

2.4 Benefits of indicial response functions and Volterra series

The buffeting response of long-span bridges subjected to turbulent winds is a complex interaction of aerodynamic loading and coupled structural motion (Scanlan 1990), which can be simulated through a sophisticated aerodynamic model in time-domain. The most appropriate way to model for buffeting force in time-domain is through indicial functions (IFs), which has been pointed out by Scanlan (1984; 1993) because IFs can model the changing of bridge aerodynamics under turbulent winds. There are two types of IFs: (1) IFs represent the development of forces due to a step-change in the bridge deck motion also known as Wagner-type indicial functions and (2) IFs represent the development of forces due to a sharp-edged gust of wind turbulence also known as Kussner-type indicial functions. In other words, the Wagner function gives the response to a unit angle of attack change and the Kussner function, conversely, provides the aerodynamic response to a unit sharp gust.

Time-domain models also offer other advantages. For example, the combination of self-excited and buffeting forces is straightforward, and the along-span wind coherence can be easily considered. Once the time-domain analysis is followed, the advantages of using IFs are as follows:

- An accurate description of aerodynamic characteristics and the possibility of obtaining the unsteady wind loads on a structure undergoing arbitrary small motions,
- A unified formulation of the aerodynamics of long-span bridges,
- The expressions for IFs can be derived or approximated in various ways via analytical, computational fluid dynamics, or experimental methods,
- The effect of wake (which quasi-steady theory does not consider) is considered in IFs which can significantly affect and alter the flutter conditions,
- IFs have the nature of time-domain so that the formulation of aerodynamic forces will be straightforwardly expressed without any transformation technique,
- Using IFs will eliminate the limitations due to the quasi-static model so that the well-known lag of buffeting forces behind the incident wind turbulence can be included,
- The explicit expressions of aerodynamic forces by IFs in time-domain make it easy to directly solve the dynamic equation of motion of the three-dimensional model of a bridge,

Some other useful notes on indicial functions are as follows:

- For incompressible flows, the unsteady aeroelastic lift and twist moment are expressed in the frequency- and time-domain via the use of the Theodorsen's and Wagner functions respectively; these functions play the roles of aeroelastic IFs,
- For incompressible flows, the unsteady aerodynamic lift and twist moment are expressed in the frequency- and time-domain via the use of the Sears' and Kussner functions respectively; these functions play the roles of aerodynamic IFs,

- Wagner determined the indicial response for a thin airfoil in an incompressible flow as a function that tends asymptotically to unity and starts at a value of 0.5 for $s = 0$, explicating that half of the change in circulatory lift is obtained at the initial instant,
- Kussner determined the indicial response for a thin airfoil in incompressible flow as a function that tends asymptotically to unity and starts at 0 for $s = 0$,
- IFs of a bridge deck must originally be obtained from the flutter derivatives in any event as suggested by Scanlan (1993),
- Often a working hypothesis is suggested that IFs calculated from flutter derivatives for self-excited forces do not differ much from IFs calculated from admittance functions for buffeting forces. Some discussions are also available on the point that IFs for buffeting and self-excited forces are the same based on the assumption that vertical gust wind component and vertical bridge response component yield the same aerodynamic loads on a bridge deck (e.g., Tubino 2005). However, this assumption is not valid in the case of a real bridge deck. Hence, IFs for self-excited forces are particularly different from those for buffeting forces,
- Admittance functions, similar to flutter derivatives, are expressed as a function of the reduced frequency and can be measured in the wind tunnel. Otherwise, if wind tunnel test data is not available, a reference aerodynamic admittance function can be used, even if theoretically defined only for a thin-airfoil, i.e. the Sear's function $(\chi(K))$ for the identification of aerodynamic IFs,

To model the aerodynamic nonlinearities, the Volterra series serves as one of the best mathematical tools for the nonlinear dynamic systems. The following keynotes are interesting to state herein about the Volterra theory:

- A rigorous mathematical framework and provides a quantitative description of the dynamics,
- Provides the means of evaluation for the dynamic nonlinearity of a system,
- Scalable to arbitrary nonlinear orders,
- Non-Gaussian white noise input can be used,
- Serves as a non-parametric model because it does not need any prior knowledge about the system and no assumption is required,
- Robustness to noise and interference,
- Easily extensible to accommodate multiple-inputs and multiple-outputs,
- Volterra kernel size can be kept at tractable levels,
- Ubiquitous and significant nonlinearities of the dynamic systems can be modelled accurately while linear approaches fail to capture nonlinearities and do not reach the required accuracy,
- Contrary to the Taylor series which is only limited to the static nonlinear systems experiencing the steady flow problems, the Volterra series can model the dynamic nonlinear systems subjected to the unsteady flow such as:

$$y(t) = a_0 + a_1 x + a_2 x^2 + \cdots \tag{2.15}$$

If x is replaced by $\int h(\tau)x(t-\tau)\,d\tau$ in the Taylor series for a single-input single-output (SISO) system, Eq. (2.15) becomes,

$$y(t) = a_0 + a_1 \int h(\tau)x(t-\tau)\,d\tau + a_2 \int\int h(\tau_1)h(\tau_2)x(t-\tau_1)x(t-\tau_2)\,d\tau_1 d\tau_2 + \cdots \tag{2.16}$$

in which h denotes the impulse response function. Eq. (2.16) is a simplified form of the Volterra series of increasing order. An extensive discussion about the formulation of the Volterra series and its application to aerodynamic load modelling is presented in Chapter 3.

CHAPTER 3: VOLTERRA SERIES-BASED WIND LOAD MODEL

This chapter focuses on the development of wind load models in time-domain based on the Volterra series including the buffeting and self-excited forces on a bluff body. More specifically, the transient nature of the typhoon wind and its effects on the aerodynamic response of the bridge are modelled while considering the effects of nonlinear fluid memory arising from the past history of incoming wind flow and deck motion at two different time-scales, and aerodynamic nonlinearities arising from the dependency of aerodynamic forces on the effective angle of attack and large flow separation at a high angle of attack. For that, two schemes based on the Volterra series are herein proposed for modeling the buffeting forces on a bridge deck: (1) Volterra FD model (2) Hybrid Volterra FD model.

In the case of the scheme (1), a whole gamut of frequencies of wind speed fluctuation components (both longitudinal and vertical) and bridge deck motion components (lateral, vertical, and torsional) are used. With that, a conventional linear unsteady (LU) buffeting force model is extended to a nonlinear unsteady (NLU) buffeting force model by using the Volterra series to account for the nonlinear fluid memory effects as well as the aerodynamic nonlinearities existing in the non-proportional wind-bridge interaction. The aerodynamic nonlinearity in the scheme (1) is expressed in terms of higher-order IFs also called higher-order Volterra kernels interchangeably, which are identified at zero angle of attack of wind. The corresponding static force coefficients utilized in this scheme are measured at zero angle of attack. The effects of non-synoptic winds on the bridge aerodynamics are also incorporated in the Volterra FD model in terms of time-varying mean wind speed. Congruently, an LU-based self-excited force model in time-domain is extended to an NLU-based self-excited force model through the Volterra series by considering the higher-order aeroelastic Volterra kernels. Finally, both the Volterra FD-based buffeting and self-excited force models are combined to develop a unified formulation of the Volterra series-based wind load model which can simulate the effects of nonlinear fluid memory effects, non-synoptic wind effects as well as the aerodynamic and aeroelastic nonlinearity effects on the bridge deck response concurrently.

In the case of the scheme (2), the wind speed fluctuating components (both longitudinal and vertical), as well as the bridge motion components (lateral, vertical, and torsional), are separated into low- and high-frequency components based on a cut-off frequency. The low-frequency components of aerodynamic forces are modelled based on low-frequency components of wind speed fluctuations and bridge motions using QS model due to its high reduced velocity and ability to incorporate the nonlinearity arising from the angle-varying static force coefficients, whereas the high-frequency components of buffeting forces are modelled using the Volterra FD model in

which the Volterra kernels are identified from FDs determined at varying angles of attack of wind. The effects of non-synoptic winds on the bridge deck response are also incorporated in the low- and high-frequency components of buffeting forces in the scheme (2). The results highlighted the importance of extending the existing LU model to an NLU wind load model. Results also showed the modeling of effects of non-synoptic winds on the structural response as well as amplitude-dependency of IFs. The presented wind load modeling schemes can provide a straightforward physical explanation on the underlying mechanism of changing the bridge aerodynamics due to the transient effects of time-varying wind speed. This study may facilitate the bridge engineers to design super long-span bridges accurately by considering the non-synoptic wind loads and, aerodynamic and aeroelastic nonlinearities existing in the wind-bridge interaction.

3.1 Introduction

Non-stationary wind events, like typhoons, impact violently on the civil infrastructures in ABL, that may cause a large number of fatalities and big economic losses. Compared with the vertical structures like high-rise buildings, the long-span bridges have a large propensity to be attacked by the non-stationary winds. It is observed that the thin-section bridges in coastline areas are prone to typhoons which possess strong non-stationary characteristics. Actually, it is probable that the design wind speeds in those areas are controlled by typhoons of transient nature, which highlights the paramount importance of non-stationary consideration in the modeling of wind loads on long-span bridges. Generally, the stationary winds are characterized by the constant mean wind speed, whereas the non-stationary winds elucidate the time-varying mean wind speed behavior that generates the transient response (Xu and Chen 2004). Therefore, a comprehensive understanding of non-synoptic wind effects on changing the bridge aerodynamics is essential to predict the buffeting response accurately. For that, the time-domain simulations are performed these days because time-domain approaches not only provide the benefit of combining different types of loads and can consider the nonlinearities but also provide the only way to reproduce the bridge response to typhoon winds with time-varying mean characteristics.

Most of the current researches focusing on the non-stationary wind effects on the civil infrastructures fully depend on the conventionally determined aerodynamic coefficients from wind tunnel tests under the stationary wind conditions (Chen 2008; Chen 2015; Cao and Sarkar 2015). In other words, the current wind design guidelines mainly emphasize on the stationary winds, whereas the actual phenomenon of typhoon winds show the non-stationary behavior, and hence the associated aerodynamic parameters are often disregarded, which calls into question the applicability of the conventional existing aerodynamic load models (Kwon and Kareem 2009; Chen 2015). Moreover, the lack of experimental studies in the past also raised questions on the

accuracy of modeling the time-varying transient effects of non-stationary winds on the buffeting response of the bridges, and it is therefore difficult to judge the contribution from the gust-induced aerodynamic effects to the dynamic response (Chay and Letchford 2002; Letchford and Chay 2002; Cao et al. 2015). Moreover, the amalgamation of the motion-induced aeroelastic effects in the buffeting forces is very challenging owing to the limitations of the wind tunnel test facilities.

To circumvent this limitation, Kwon and Kareem (2009) offered a novel theoretical scheme for wind load effects on infrastructures based on the gust front factor which is capable to effectively investigate the transient aerodynamics. The results obtained in their study aimed to develop the analysis framework based on gust front factor for transient wind load effects on infrastructures. Specifically, the efforts were made to investigate the effects of transient behavior on the aeroelastic and aerodynamic characteristics based on a long-span bridge under artificial downburst winds. For that, the semi-empirical linear model in time-domain was used to analyse the aerodynamic and aeroelastic forces on the long-span bridge under downburst events and its equivalent stationary winds. The presented approach highlights the fundamental mechanism of the change in bridge aerodynamics brought about by the time-varying effects and offered new insights to explore the non-stationary wind effects on the bridges.

Besides the non-stationary wind effects on the bridge response, the wind-bridge interaction is a fade memory system and exhibits a nonlinear behavior aerodynamically. A main source of this nonlinearity existing in bridge aerodynamics is owing to the flow separation around the bridge deck because the wind flow around deck cannot accommodate the abrupt changes in the deck profile. Other reasons of the aerodynamic nonlinearities can be visualized in various point of views i.e., amplitude/frequency dependency of aeroelastic and aerodynamic forces, non-proportional and nonlinear relationship between wind speed and bridge dynamic response and hysteretic nature of aerodynamic forces against angles of attack (Wu et al. 2013).

Chen and Kareem (2001, 2003) presented a time-domain analysis framework for predicting the nonlinear response of long-span bridges under turbulent winds. The nonlinear unsteady forces are formulated on the basis of the static wind force coefficient, admittance functions, flutter derivatives, and their spatial correlations at different angles of attack. In their framework, the aerodynamic forces are separated into low- and high-frequency components at a suitable cut-off frequency based on the low- and high-frequency components of effective angle of attack. The low-frequency components of aerodynamic forces are modelled as a nonlinear function of the effective angle of attack using the QS model, whereas high-frequency component of aerodynamic forces is linearized at the low-frequency component of effective angle of attack and then modelled using conventional LU model. This combination of QS and LU models is famously known as hybrid nonlinear (HNL) wind load model. Further discussions regarding the aerodynamic modeling are presented in the subsequent sections.

3.2 Volterra series

The mathematician Vito Volterra (Volterra 1959) used a series of convolution-like expressions to define the input-output relationship of nonlinear time-invariant (NLTI) systems. The Volterra theory is of great importance because many real systems with a fading memory can be analysed using this approach. Fading memory is physically a meaningful concept. Instinctively, a dynamical system has fading memory if two input signals, which are close in the recent past, but not essentially close in the remote past, yield outputs which are close. For the dynamic systems, fading memory is related to the concept of a unique steady-state. This implies that a wide range of nonlinear systems can be approximated by the Volterra series representation with some reasonable assumptions. According to the Volterra series, the output of a continuous SISO, nonlinear time-invariant (NLTI), causal and fading memory system is related to the input signal through the multidimensional infinite convolution integrals of increasing order such as:

$$\begin{aligned} y(t) = h_0 + \int_{-\infty}^{\infty} h_1(\tau_1)u(t-\tau_1)d\tau_1 + \int_{-\infty}^{\infty}\int_{-\infty}^{\infty} h_2(\tau_1,\tau_2)u(t-\tau_1)u(t-\tau_2)d\tau_1 d\tau_2 + \cdots \\ + \int_{-\infty}^{\infty}\int_{-\infty}^{\infty}\dots\int_{-\infty}^{\infty} h_n(\tau_1,\tau_2,\dots,\tau_n)u(t-\tau_1)u(t-\tau_2)\dots u(t-\tau_n)d\tau_1 d\tau_2 \dots d\tau_n \end{aligned} \tag{3.1}$$

where $y(t)$ is the response of an nth-order system, which depends on multiple copies of the input and is the sum of the first-, second-, …, nth-order convolution-like expressions. The functions h_1, h_2, …, h_n are called the first-, second-, …, nth-order Volterra kernels; $u(t-\tau_i)$ is the lagged input to the system and h_0 is the zeroth-order Volterra kernel. The zeroth-order Volterra kernel shows the zero-input response of the dynamical system, whereas the first-order Volterra kernel signifies the linear response of the dynamical system to a single impulse input. The higher-order kernels are the system multidimensional impulse responses characterizing the temporal effects in the nonlinear dynamics, which measure the relative influence of a previous input on the current response. Figure (3-1) shows the Volterra series model of an NLTI-SISO system. Eq. (3.1) can also be written in a compact form such as:

$$y(t) = h_0 + \sum_{n=0}^{\infty}\int_{-\infty}^{\infty}\dots\int_{-\infty}^{\infty} h_n(\tau_1,\tau_2,\dots,\tau_n) \times \prod_{i=1}^{n} u(t-\tau_i)d\tau_i d\tau_2 \dots d\tau_n \tag{3.2}$$

Eq. (3.2) is similar to the finite impulse response (FIR) filter model except for the only difference of an additional constant term h_0. It has been verified that the stability of dynamical systems represented by the Volterra series can be guaranteed if the Volterra kernels satisfy the following condition:

$$\int_{-\infty}^{\infty}\dots\int_{-\infty}^{\infty} |h_n(\tau_1,\tau_2,\dots,\tau_n)| \prod_{i=1}^{n} d\tau_n < \infty, n = 1,2,\dots \tag{3.3}$$

Note that the *n*th-order Volterra kernels are symmetric by nature with respect to any

permutation of the arguments $(\tau_1, \ldots, \tau_n)$ (Paula et al. 2019). From the system causality, it results that the kernel $h_n(\tau_1, \ldots, \tau_n)$ is zero if any $\tau_i < 0$, thereby leading the lower limits of the integrals in Eq. (3.2) to be equal to zero. The causality theory also implies that the system response does not depend on future input values, making it possible to replace the upper limit of the integrals by *t*. Moreover, for any practical model, the maximum kernel order *P* of system nonlinearity according to Boyd and Chua (1985), and the memory length *T* must be finite.

$$y(t) = h_0 + \sum_{n=1}^{\mathrm{P}} \int_0^{\mathrm{t}} \ldots \int_0^{\mathrm{t}} h_n(\tau_1, \tau_2, \ldots, \tau_n) \times \prod_{i=1}^{n} u(t - \tau_i) d\tau_i d\tau_2 \ldots d\tau_n \tag{3.4}$$

It is possible to compute the continuous-time convolution integral numerically, but it is more efficient to represent the system in discrete-time and replace the integrals with summations. The is true for Volterra series, which can be represented in discrete time as:

$$y[t] = h_0 + \sum_{n=1}^{P} (\Delta t)^n \sum_{\tau_1=0}^{T} \cdots \sum_{\tau_n=0}^{T} h_n[\tau_1, \ldots, \tau_n] u[t - \tau_1] \cdots u[t - \tau_n] \tag{3.5}$$

where $y[k]$ and $u[k]$ are the inputs and outputs of the system. Notice that Eq. (3.5) can easily be derived by discretizing the convolution integral of Eq. (3.4), and hence called a convolution sum.

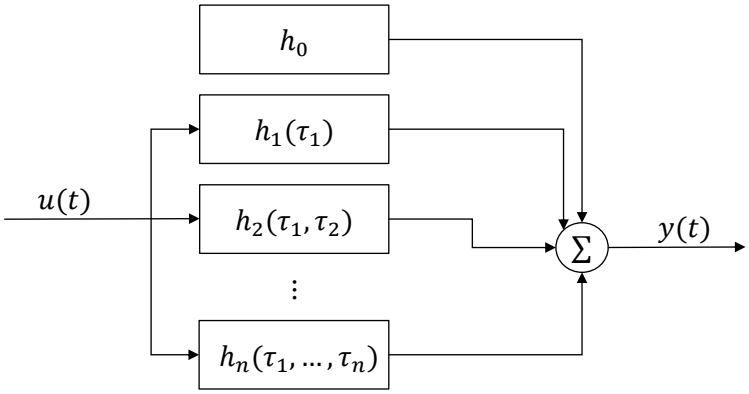

Figure 3-1 The Volterra series model of an NLTI-SISO system

As a matter of fact, the wind-bridge interaction system is a real example of an NLTI system involving the multi-input multi-output (MIMO) recording signals. Thus, it requires many input and output signals to make a complex Volterra series-based model involving the several direct and cross Volterra kernels. The procedures for determining these Volterra kernels will be discussed in Chapter 4 in detail. In general, a coupled problem of nonlinear wind-bridge interaction entails a 3D bridge model immersed in a non-stationary, unsteady and turbulent wind flow with a constant air density experiencing the wind loads of complex nature, which cause the three-dimensional motion of the bridge structure as shown in Figure (3-2). Since the wind-bridge interaction is a complex phenomenon, the overall quality of the bridge design significantly

depends on the accuracy of the wind load model. Because of the complex nature, the wind loads on the bridge deck in time-domain can be decomposed into three time-varying components i.e., static, buffeting, and self-excited components, which are presented in the subsequent sections.

3.3 Time-varying mean static wind load model

The time-varying mean static lift force $L_{st}(t)$, drag force $D_{st}(t)$ and pitching moment $M_{st}(t)$ acting on the bridge deck with unit span length and width B is expressed as:

$$L_{st}(t) = \frac{1}{2}\rho\overline{U_{tv}}(t)^2 B C_L\left(\bar{\alpha}(t)\right)$$

$$D_{st}(t) = \frac{1}{2}\rho\overline{U_{tv}}(t)^2 B C_D\left(\bar{\alpha}(t)\right) \tag{3.6}$$

$$M_{st}(t) = \frac{1}{2}\rho\overline{U_{tv}}(t)^2 B^2 C_M\left(\bar{\alpha}(t)\right)$$

where $\bar{\alpha}(t)$ and $\overline{U_{tv}}(t)$ are the time-varying mean angle of attack and wind speed, respectively.

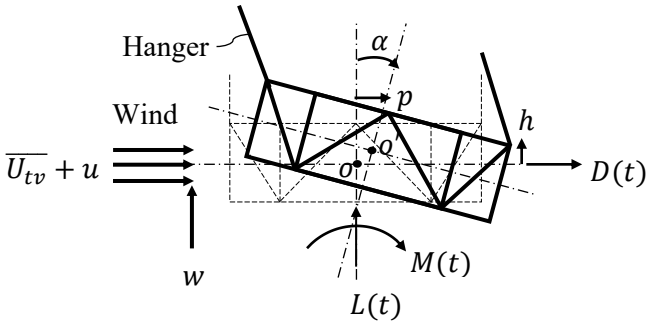

Figure 3-2 Motion of bridge deck and wind force components

3.4 Linear unsteady wind load model

The buffeting forces on the bridge deck in time-domain are conventionally formulated based on the linear convolution theory in which the output of a linear time-invariant (LTI) system is expressed through a linear convolution of the input signal and IF. Based on this model, if a unit-step gust or motion is introduced to the system, the resultant aerodynamic forces will have a rise time and attain their quasi-steady value asymptotically. That rise time is also called the fluid memory which accounts for the unsteadiness of the system. Moreover, this model also assumes that the variation of effective angle of attack is small enough that aerodynamic forces can be linearized at the statically deformed position and that the variation of FDs is negligible. The formulation of linear buffeting forces using the LU model is shown in the subsequent subsections.

3.4.1 Formulation of linear buffeting force

Suppose that lift force is induced by a suddenly applied constant gust given by Eq. (3.7).

$$L_t(t) = \frac{1}{2}\rho U(t)^2 B\psi(t) C_L(\alpha(t)) \tag{3.7}$$

where L_t is total lift force including static lift force (but excluding self-excited lift force); $U(t)$ is time-varying wind speed equal to the sum of the mean value of 10 min wind speed time-history ($\overline{U}$) and longitudinal fluctuating wind speed (u), and $\psi(t)$ is the aerodynamic IF which describes the unsteady aerodynamic forces on a bridge deck caused by a gust. Expansion of Eq. (3.7) yields Eq. (3.8), in which u_o and w_o are constant gusts; the first term indicates the static part of lift force and the second term is the buffeting part which is the point of interest here. If gust is of an arbitrary velocity distribution applied to the bridge deck then lift force becomes a convolution, involving the derivative of aerodynamic IF as described by Eq. (3.9), in which $L_b(t)$ is linear buffeting lift force, and $\dot{\psi}_{Lu}$ and $\dot{\psi}_{Lw}$ are the derivatives of first-order aerodynamic IFs representing the non-dimensional lift forces generated by the longitudinal and vertical fluctuating wind speeds i.e., u and w on the bridge deck, respectively. With the change of integral variables in Eq. (3.9) i.e., $\tau = t - \sigma$ and integrating it by parts, Eq. (3.10) can be obtained. Applying the differentiation property of convolution, the arguments of integral variables can be interchanged as shown in Eq. (3.11). Similarly, the buffeting pitching moment and buffeting drag force can also be formulated as shown in Eqs. (3.12) and (3.13), respectively. Thus, a general expression for the linear buffeting forces can be formulated as shown in Eq. (3.14), in which Q_b denotes the buffeting force on the bridge deck; the parameters ψ_{Qu}, and ψ_{Qw} are zero-order aerodynamic IFs elucidating the static response, and $\dot{\psi}_{Qu}$ and $\dot{\psi}_{Qw}$ are the derivatives of first-order aerodynamic IFs. These parameters are well-known Kussner functions in the airfoil theory, simulating the linear effects of the sudden action of u and w on the growth of buffeting force (Q_b) on the bridge deck. Note that Eq. (3.14) will be multiplied by the deck width B to find the moment.

$$L_t(t) = \frac{1}{2}\rho\overline{U}^2 B C_L + \frac{1}{2}\rho\overline{U}^2 B\left[2C_L\frac{u_o}{\overline{U}}\psi(t) + (C_D + C_L')\frac{w_o}{\overline{U}}\psi(t) + \frac{2u_o}{\overline{U}}\frac{w_o}{\overline{U}}(C_D + C_L')\psi(t)\right] \tag{3.8}$$

$$L_b(t) = \frac{1}{2}\rho\overline{U}^2 B\left[2C_L\left(\int_{-\infty}^{t}\dot{\psi}_{Lu}(\sigma)\frac{u(t-\sigma)}{\overline{U}}d\sigma\right) + (C_D + C_L')\left(\int_{-\infty}^{t}\dot{\psi}_{Lw}(\sigma)\frac{w(t-\sigma)}{\overline{U}}d\sigma\right)\right] \tag{3.9}$$

$$\begin{aligned} L_b(t) = \frac{1}{2}\rho\overline{U}^2 B\Bigg[2C_L\Bigg(&\psi_{Lu}(t)\frac{u(0)}{\overline{U}} + \int_0^t \psi_{Lu}(t-\tau)\frac{\dot{u}(\tau)}{\overline{U}}d\tau\Bigg) \\ &+ (C_D + C_L')\Bigg(\psi_{Lw}(t)\frac{w(0)}{\overline{U}} + \int_0^t \psi_{Lw}(t-\tau)\frac{\dot{w}(\tau)}{\overline{U}}d\tau\Bigg)\Bigg] \end{aligned} \tag{3.10}$$

$$L_b(t) = \frac{1}{2}\rho\bar{U}^2 B\left[2C_L\left\{\psi_{Lu}(0)\frac{u(t)}{\bar{U}} + \int_0^t \dot{\psi}_{Lu}(\tau)\frac{u(t-\tau)}{\bar{U}}d\tau\right\}\right.$$
$$\left. + (C_D + C_L')\left\{\psi_{Lw}(0)\frac{w(t)}{\bar{U}} + \int_0^t \dot{\psi}_{Lw}(\tau)\frac{w(t-\tau)}{\bar{U}}d\tau\right\}\right] \quad (3.11)$$

$$M_b(t) = \frac{1}{2}\rho\bar{U}^2 B^2\left[2C_M\left\{\psi_{Mu}(0)\frac{u(t)}{\bar{U}} + \int_0^t \dot{\psi}_{Mu}(\tau)\frac{u(t-\tau)}{\bar{U}}d\tau\right\}\right.$$
$$\left. + C_M'\left\{\psi_{Mw}(0)\frac{w(t)}{\bar{U}} + \int_0^t \dot{\psi}_{Mw}(\tau)\frac{w(t-\tau)}{\bar{U}}d\tau\right\}\right] \quad (3.12)$$

$$D_b(t) = \frac{1}{2}\rho\bar{U}^2 B\left[2C_D\left\{\psi_{Du}(0)\frac{u(t)}{\bar{U}} + \int_0^t \dot{\psi}_{Du}(\tau)\frac{u(t-\tau)}{\bar{U}}d\tau\right\}\right.$$
$$\left. + (C_D' - C_L)\left\{\psi_{Dw}(0)\frac{w(t)}{\bar{U}} + \int_0^t \dot{\psi}_{Dw}(\tau)\frac{w(t-\tau)}{\bar{U}}d\tau\right\}\right] \quad (3.13)$$

$$Q_b(t) = \frac{1}{2}\rho\bar{U}^2 B\left[2C_Q\left\{\psi_{Qu}(0)\frac{u(t)}{\bar{U}} + \int_0^t \dot{\psi}_{Qu}(\tau)\frac{u(t-\tau)}{\bar{U}}d\tau\right\}\right.$$
$$\left. + (C_Q')\left\{\psi_{Qw}(0)\frac{w(t)}{\bar{U}} + \int_0^t \dot{\psi}_{Qw}(\tau)\frac{w(t-\tau)}{\bar{U}}d\tau\right\}\right] \quad (3.14)$$

3.4.2 Formulation of linear self-excited force

Let us consider an abrupt step-change in the angle of attack (an incremental change in α_0), the lift force also undergoes an abrupt transient change expressed by:

$$L(s) = \frac{1}{2}\rho\bar{U}^2 B C_L'\alpha_0\phi(s) \quad (3.15)$$

where s is non-dimensional time equal to $\bar{U}t/B$, and $\phi(s)$ is aeroelastic IF. The Eq. (3.15) points out that the lift force, instead of self-generating immediately, undergoes a transient growth process, which makes it unsteady by nature. Under the small arbitrary motion of the bridge deck, the growth in lift force, due to the simultaneous occurrence of all three components of motion (p, h, α), can be expressed in terms of convolution integral assuming a linear superposition rule.

$$L_{se}(s) = \frac{1}{2}\rho\bar{U}^2 BC_L' \left[\int_{-\infty}^{s} \phi_{Lp''}(s-\sigma)\frac{p''(\sigma)}{B}d\sigma + \int_{-\infty}^{s} \phi_{Lh''}(s-\sigma)\frac{h''(\sigma)}{B}d\sigma + \int_{-\infty}^{s} \phi_{L\alpha'}(s-\sigma)\alpha'(\sigma)d\sigma \right] \tag{3.16}$$

where $p''(\sigma)$ and $h''(\sigma)$ are the second derivatives of lateral and vertical vibrations, respectively; $\alpha'(\sigma)$ is the first derivative of torsional vibration, and $\phi_{Q_{se}z}$ ($Q_{se} = L_{se}, M_{se}, D_{se};\ z = p'', h'', \alpha'$) is the aeroelastic IF representing the transient evolutionary feature of self-excited force (Q_{se}) due to the displacement (z). The negative sign of the lower limit of integral shows the history of bridge deck motion. With the change of integral variables in Eq. (3.16) i.e., $\tau = s - \sigma$ and $d\sigma = -d\tau$, Eq. (3.17) is obtained.

$$L_{se}(s) = \frac{1}{2}\rho\bar{U}^2 BC_L' \left[\int_{s}^{0} \phi_{Lp''}(\tau)\frac{p''(s-\tau)}{B}d\tau + \int_{s}^{0} \phi_{Lh''}(\tau)\frac{h''(s-\tau)}{B}d\tau + \int_{s}^{0} \phi_{L\alpha'}(\tau)\alpha'(s-\tau)d\tau \right] \tag{3.17}$$

Integrating Eq. (3.17) by parts and simplifying it gives,

$$L_{se}(s) = \frac{1}{2}\rho\bar{U}^2 BC_L' \left[\phi_{Lp'}(0)\frac{p'(s)}{B} + \int_{0}^{s} \phi'_{Lp'}(\tau)\frac{p'(s-\tau)}{B}d\tau + \phi_{Lh'}(0)\frac{h'(s)}{B} + \int_{0}^{s} \phi'_{Lh'}(\tau)\frac{h'(s-\tau)}{B}d\tau + \phi_{L\alpha}(0)\alpha(s) + \int_{0}^{s} \phi'_{L\alpha}(\tau)\alpha(s-\tau)d\tau \right] \tag{3.18}$$

Taking the first derivative of s yields $ds = \bar{U}dt/B$. As a result of converting the p', h' and α from s-domain into real time-domain, Eq. (3.18) yields Eq. (3.20).

$$\frac{p'}{B} = \frac{dp}{Bds} = \frac{dp}{\bar{U}dt} = \frac{\dot{p}}{\bar{U}} \quad \text{and} \quad \frac{h'}{B} = \frac{\dot{h}}{\bar{U}} \tag{3.19}$$

$$L_{se}(t) = \frac{1}{2}\rho\bar{U}^2 BC_L' \left[\phi_{L\dot{p}}(0)\frac{\dot{p}(t)}{\bar{U}} + \int_{0}^{t} \dot{\phi}_{L\dot{p}}(\tau)\frac{\dot{p}(t-\tau)}{\bar{U}}d\tau + \phi_{L\dot{h}}(0)\frac{\dot{h}(t)}{\bar{U}} + \int_{0}^{t} \dot{\phi}_{L\dot{h}}(\tau)\frac{\dot{h}(t-\tau)}{\bar{U}}d\tau + \phi_{L\alpha}(0)\alpha(t) + \int_{0}^{t} \dot{\phi}_{L\alpha}(\tau)\alpha(t-\tau)d\tau \right] \tag{3.20}$$

Similarly, the linear self-excited pitching moment and drag force on the bridge deck can be formulated as shown in Eqs. (3.21) and (3.22). A generalized form of the linear self-excited forces is shown in Eq. (3.23), in which Q_{se} represents D_{se}, L_{se} and M_{se} forces acting on the bridge deck, and $\dot{p}$, $\dot{h}$ and α are the derivative of lateral, derivative of vertical and torsional displacements with respect to t. The parameters $\phi_{Q\dot{p}}$, $\phi_{Q\dot{h}}$, and $\phi_{Q\alpha}$ are the zero-order

aeroelastic IFs, whereas $\dot{\phi}_{Q\dot{p}}, \dot{\phi}_{Q\dot{h}}$ and $\dot{\phi}_{Q\alpha}$ are the derivatives of first-order aeroelastic IFs. According to the airfoil theory, these parameters are known as Wagner functions, simulating the linear effects of deck motions on the growth of self-excited force (Q_{se}).

$$M_{se}(t) = \frac{1}{2}\rho\bar{U}^2B^2C'_M\left[\phi_{M\dot{p}}(0)\frac{\dot{p}(t)}{\bar{U}} + \int_0^t \dot{\phi}_{M\dot{p}}(\tau)\frac{\dot{p}(t-\tau)}{\bar{U}}d\tau + \phi_{M\dot{h}}(0)\frac{\dot{h}(t)}{\bar{U}}\right.$$
$$\left. + \int_0^t \dot{\phi}_{M\dot{h}}(\tau)\frac{\dot{h}(t-\tau)}{\bar{U}}d\tau + \phi_{M\alpha}(0)\alpha(t) + \int_0^t \dot{\phi}_{M\alpha}(\tau)\alpha(t-\tau)d\tau\right] \quad (3.21)$$

$$D_{se}(t) = \frac{1}{2}\rho\bar{U}^2BC'_D\left[\phi_{D\dot{p}}(0)\frac{\dot{p}(t)}{\bar{U}} + \int_0^t \dot{\phi}_{D\dot{p}}(\tau)\frac{\dot{p}(t-\tau)}{\bar{U}}(d\tau) + \phi_{D\dot{h}}(0)\frac{\dot{h}(t)}{\bar{U}}\right.$$
$$\left. + \int_0^t \dot{\phi}_{D\dot{h}}(\tau)\frac{\dot{h}(t-\tau)}{\bar{U}}(d\tau) + \phi_{D\alpha}(0)\alpha(t) + \int_0^t \dot{\phi}_{D\alpha}(\tau)\alpha(t-\tau)(d\tau)\right] \quad (3.22)$$

$$Q_{se}(t) = \frac{1}{2}\rho\bar{U}^2BC'_Q\left[\phi_{Q\dot{p}}(0)\frac{\dot{p}(t)}{\bar{U}} + \int_0^t \dot{\phi}_{Q\dot{p}}(\tau)\frac{\dot{p}(t-\tau)}{\bar{U}}d\tau + \phi_{Q\dot{h}}(0)\frac{\dot{h}(t)}{\bar{U}}\right.$$
$$\left. + \int_0^t \dot{\phi}_{Q\dot{h}}(\tau)\frac{\dot{h}(t-\tau)}{\bar{U}}d\tau + \phi_{Q\alpha}(0)\alpha(t) + \int_0^t \dot{\phi}_{Q\alpha}(\tau)\alpha(t-\tau)d\tau\right] \quad (3.23)$$

3.5 Nonlinear unsteady wind load model (Scheme 1)

In order to improve the capability of the LU model, a Volterra series-based nonlinear model, called Volterra FD model, has been proposed to consider the aerodynamic nonlinearity and nonlinear fluid memory effects. In this model, the output of an NLTI system is described through the input signal and multidimensional infinite convolution integrals of Volterra kernels. The consideration of nonlinearity arising from the flow separation and nonlinear fluid memory effects expressed in two time-scales is carried out by introducing the higher-order terms called Volterra kernels. With this strategy, the formulations of buffeting and self-excited forces (Eqs. (3.14), (3.23)) can be extended to new formulations by adding higher-order Volterra kernels. To avoid the high computational effort, the Volterra series is curtailed up to second-order kernel based on the idea that wind-bridge interaction system is weakly nonlinear without any issue of convergence (Wu et al. 2013). The second-order kernels are reminiscent of nonlinear IFs; therefore, these both will be called interchangeably in the subsequent subsections.

3.5.1 Formulation of nonlinear and non-stationary buffeting forces

The nonlinear aerodynamic buffeting forces exerting on a three-dimensional bridge immersed in the non-stationary turbulent winds can be simulated successfully using the NLU model based on the Volterra series written in Eq. (3.24).

$$\begin{aligned} Q_b(t) = \frac{1}{2}\rho\overline{U_{tv}}(t)^2 B\Bigg[2C_Q\Bigg\{\psi_{Qu}(0)\frac{u(t)}{\overline{U_{tv}}(t)} + \int_0^t \dot{\psi}_{Qu}(\tau)\frac{u(t-\tau)}{\overline{U_{tv}}(t)}d\tau + \int_0^t\int_0^t \dot{\psi}_{Quu}(\tau_1,\tau_2) \\ \times\frac{u(t-\tau_1)u(t-\tau_2)}{\overline{U_{tv}}^2(t)}d\tau_1 d\tau_2\Bigg\} + \left(C_Q'\right)\Bigg\{\psi_{Qw}(0)\frac{w(t)}{\overline{U_{tv}}(t)} + \int_0^t \dot{\psi}_{Qw}(\tau)\frac{w(t-\tau)}{\overline{U_{tv}}(t)}d\tau \\ + \int_0^t\int_0^t \dot{\psi}_{Qww}(\tau_1,\tau_2)\frac{w(t-\tau_1)w(t-\tau_2)}{\overline{U_{tv}}^2(t)}d\tau_1 d\tau_2 + 2\int_0^t\int_0^t \dot{\psi}_{Quw}(\tau_1,\tau_2) \\ \times\frac{u(t-\tau_1)w(t-\tau_2)}{\overline{U_{tv}}^2(t)}d\tau_1 d\tau_2\Bigg\}\Bigg] \end{aligned} \tag{3.24}$$

$$\begin{aligned} Q_b[n] = \frac{1}{2}\rho\overline{U_{tv}}[n]^2 B\Bigg[\Bigg\{\left(\frac{2C_Q\psi_{Qu}[0]}{\overline{U_{tv}}[n]}\right)u[n] + \left(\frac{C_Q'\psi_{Qw}[0]}{\overline{U_{tv}}[n]}\right)w[n]\Bigg\} + \Bigg\{\sum_{k=0}^{M}\left(\frac{2C_Q\dot{\psi}_{Qu}[k]}{\overline{U_{tv}}[n]}\right) \\ \times u[n-k] + \sum_{k=0}^{M}\left(\frac{C_Q'\dot{\psi}_{Qw}[k]}{\overline{U_{tv}}[n]}\right)w[n-k]\Bigg\} + \Bigg\{\sum_{k_1=0}^{M}\sum_{k_2=0}^{M}\left(\frac{2C_Q\dot{\psi}_{Quu}[k_1,k_2]}{\overline{U_{tv}}[n]^2}\right) \\ \times u[n-k_1]\,u[n-k_2] + \sum_{k_1=0}^{M}\sum_{k_2=0}^{M}\left(\frac{C_Q'\dot{\psi}_{Qww}[k_1,k_2]}{\overline{U_{tv}}[n]^2}\right)w[n-k_1]\,w[n-k_2] \\ +2\sum_{k_1=0}^{M}\sum_{k_2=0}^{M}\left(\frac{C_Q'\,\dot{\psi}_{Quw}[k_1,k_2]}{\overline{U_{tv}}[n]^2}\right)u[n-k_1]\,w[n-k_2]\Bigg\}\Bigg] \end{aligned} \tag{3.25}$$

where the parameters $\dot{\psi}_{Quu}$, $\dot{\psi}_{Qww}$, and $\dot{\psi}_{Quw}$ are the nonlinear aerodynamic IFs (second-order Volterra kernels) simulating the nonlinear behavior of buffeting forces (Q_b) due to the coupled effects of gust components on the bridge deck. Moreover, the parameters $\dot{\psi}_{Quu}$, $\dot{\psi}_{Qww}$ and $\dot{\psi}_{Quw}$ represent the direct and cross second-order kernels of Volterra series, respectively. The non-stationary wind effects are also considered in the formulation of nonlinear buffeting forces by introducing the time-varying mean wind speed. It is important to note here that first and second-order IFs used in the Volterra FD model (scheme 1) are assumed to be identified at zero angle of attack just the same as in the case of the LU model in order to compare the simulation results of LU and Volterra FD models. Similarly, the expressions for nonlinear buffeting drag force and pitching moment can be formulated by the Volterra series expansion. A general expression for the nonlinear typhoon-induced buffeting forces is shown in Eq. (3.25) in a discrete form. Particularly, Eq. (3.25) will be multiplied by *B* in order to find the pitching moment.

3.5.2 Formulation of nonlinear and non-stationary self-excited forces

The nonlinear self-excited forces, similar to nonlinear buffeting forces, can be simulated with the help of second-order Volterra series consisting of 21 terms of second-order aeroelastic IFs in an integrated form as shown in Eq. (3.26). All kinds of possibilities of coupled terms are considered and combined into one unified form. This unified form has taken into account the direct as well as cross second-order Volterra kernels which could capture the nonlinear features of wind-bridge aeroelasticity. In Eq. (3.26), the second-order kernels (say ϕ_{Qij}) will be the direct and cross kernels if $i = j$ and $i \neq j$, respectively, where i and j represent input signals. A general expression for the nonlinear self-excited forces is shown in Eq. (3.27) in a discrete form.

$$
\begin{aligned}
Q_{se}(t) = \frac{1}{2}\rho\overline{U_{tv}}(t)^2 BC_L' \Bigg[& \left\{ \phi_{Q\dot{p}}(0)\frac{\dot{p}(t)}{\overline{U_{tv}}(t)} + \phi_{Q\dot{h}}(0)\frac{\dot{h}(t)}{\overline{U_{tv}}(t)} + \phi_{Q\alpha}(0)\alpha(t) \right\} \\
& + \left\{ \int_0^t \dot{\phi}_{Q\dot{p}}(\tau)\frac{\dot{p}(t-\tau)}{\overline{U_{tv}}(t)}d\tau + \int_0^t \dot{\phi}_{Q\dot{h}}(\tau)\frac{\dot{h}(t-\tau)}{\overline{U_{tv}}(t)}d\tau + \int_0^t \dot{\phi}_{Q\alpha}(\tau)\alpha(t-\tau)d\tau \right\} \\
& + \left\{ \int_0^t\int_0^t \dot{\phi}_{Q\dot{p}\dot{p}}(\tau_1,\tau_2)\frac{\dot{p}(t-\tau_1)\dot{p}(t-\tau_2)}{\overline{U_{tv}}^2(t)}d\tau_1 d\tau_2 + \int_0^t\int_0^t \dot{\phi}_{Q\dot{h}\dot{h}}(\tau_1,\tau_2) \right. \\
& \times \frac{\dot{h}(t-\tau_1)\dot{h}(t-\tau_2)}{\overline{U_{tv}}^2(t)}d\tau_1 d\tau_2 + \int_0^t\int_0^t \dot{\phi}_{Q\alpha\alpha}(\tau_1,\tau_2)\alpha(t-\tau_1)\alpha(t-\tau_2)d\tau_1 d\tau_2 \\
& + 2\int_0^t\int_0^t \dot{\phi}_{Qu\alpha}(\tau_1,\tau_2)\frac{u(t-\tau_1)\alpha(t-\tau_2)}{\overline{U_{tv}}(t)}d\tau_1 d\tau_2 + 2\int_0^t\int_0^t \dot{\phi}_{Qu\dot{h}}(\tau_1,\tau_2) \\
& \times \frac{u(t-\tau_1)\dot{h}(t-\tau_2)}{\overline{U_{tv}}^2(t)}d\tau_1 d\tau_2 + 2\int_0^t\int_0^t \dot{\phi}_{Qu\dot{p}}(\tau_1,\tau_2)\frac{u(t-\tau_1)\dot{p}(t-\tau_2)}{\overline{U_{tv}}^2(t)}d\tau_1 d\tau_2 \\
& + 2\int_0^t\int_0^t \dot{\phi}_{Qw\alpha}(\tau_1,\tau_2)\frac{w(t-\tau_1)\alpha(t-\tau_2)}{\overline{U_{tv}}(t)}d\tau_1 d\tau_2 + 2\int_0^t\int_0^t \dot{\phi}_{Qw\dot{h}}(\tau_1,\tau_2) \\
& \times \frac{w(t-\tau_1)\dot{h}(t-\tau_2)}{\overline{U_{tv}}^2(t)}d\tau_1 d\tau_2 + 2\int_0^t\int_0^t \dot{\phi}_{Qw\dot{p}}(\tau_1,\tau_2)\frac{w(t-\tau_1)\dot{p}(t-\tau_2)}{\overline{U_{tv}}^2(t)}d\tau_1 d\tau_2 \\
& + 2\int_0^t\int_0^t \dot{\phi}_{Q\alpha\dot{h}}(\tau_1,\tau_2)\frac{\alpha(t-\tau_1)\dot{h}(t-\tau_2)}{\overline{U_{tv}}(t)}d\tau_1 d\tau_2 + 2\int_0^t\int_0^t \dot{\phi}_{Q\alpha\dot{p}}(\tau_1,\tau_2) \\
& \left. \times \frac{\alpha(t-\tau_1)\dot{p}(t-\tau_2)}{\overline{U_{tv}}(t)}d\tau_1 d\tau_2 + 2\int_0^t\int_0^t \dot{\phi}_{Q\dot{h}\dot{p}}(\tau_1,\tau_2)\frac{\dot{h}(t-\tau_1)\dot{p}(t-\tau_2)}{\overline{U_{tv}}^2(t)}d\tau_1 d\tau_2 \right\} \Bigg]
\end{aligned}
\tag{3.26}
$$

3.5.3 Unified formulation

Eq. (3.28) shows a general nonlinear formulation of non-stationary buffeting forces including the effects of self-excited forces on a bridge deck. This formulation consists of the linear

(first-order) and nonlinear (second-order) aerodynamic and aeroelastic kernels including the coupled effects between deck motions and turbulence on a bridge deck, in which all kinds of possibilities of coupled terms are considered and combined into one unified form. This unified form has also considered the second-order direct and cross kernels, which could capture the symmetric and asymmetric nonlinear features of bridge aerodynamics and aeroelasticity. For instance, $\dot{\phi}_{L\dot{p}}$, $\dot{\phi}_{L\dot{h}}$ and $\dot{\phi}_{L\alpha}$ denote the first-order aeroelastic kernels, and $\dot{\phi}_{L\dot{p}\dot{p}}$, $\dot{\phi}_{L\dot{h}\dot{h}}$ and $\dot{\phi}_{L\alpha\alpha}$ represent the second-order direct aeroelastic kernels. The remaining nine parameters in Eq. (3.28) denote the second-order cross aeroelastic kernels, which simulate the aeroelastic nonlinearity existing in wind-bridge interaction and encode the important information about intermodulation between input signals. The incorporation of cross kernels in the Volterra model is essential to represent the internal nonlinear couplings of the system when simultaneous inputs are applied. By counting all permutations and combinations, it can be observed that a second-order Volterra model consisting of five inputs has $(5! + 2!)/5!\,2! = 21$ Volterra kernels and the total number of flops scale with M^2 (where M is the memory length).

$$
\begin{aligned}
Q_{se}[n] = \frac{1}{2}\rho\overline{U_{tv}}[n]^2 B C_Q' \Bigg[& \left\{ \left(\frac{\phi_{Q\dot{p}}[0]}{\overline{U_{tv}}[n]} \right) \dot{p}[n] + \left(\frac{\phi_{Q\dot{h}}[0]}{\overline{U_{tv}}[n]} \right) \dot{h}[n] + \phi_{Q\alpha}[0]\alpha(t) \right\} \\
& + \left\{ \sum_{k=0}^{M} \left(\frac{\dot{\phi}_{Q\dot{p}}[k]}{\overline{U_{tv}}[n]} \right) \dot{p}[n-k] + \sum_{k=0}^{M} \left(\frac{\dot{\phi}_{Q\dot{h}}[k]}{\overline{U_{tv}}[n]} \right) \dot{h}[n-k] + \sum_{k=0}^{M} \left(\dot{\phi}_{Q\alpha}[k] \right) \alpha[n-k] \right\} \\
& + \left\{ \sum_{k_1=0}^{M} \sum_{k_2=0}^{M} \left(\frac{\dot{\phi}_{Q\dot{p}\dot{p}}[k_1,k_2]}{\overline{U_{tv}}[n]^2} \right) \dot{p}[n-k_1]\, \dot{p}[n-k_2] + \sum_{k_1=0}^{M} \sum_{k_2=0}^{M} \left(\frac{\dot{\phi}_{Q\dot{h}\dot{h}}[k_1,k_2]}{\overline{U_{tv}}[n]^2} \right) \right. \\
& \times \dot{h}[n-k_1]\, \dot{h}[n-k_2] + \sum_{k_1=0}^{M} \sum_{k_2=0}^{M} \left(\dot{\phi}_{Q\alpha\alpha}[k_1,k_2] \right) \alpha[n-k_1]\, \alpha[n-k_2] \\
& + 2 \sum_{k_1=0}^{M} \sum_{k_2=0}^{M} \left(\frac{\dot{\phi}_{Qu\alpha}[k_1,k_2]}{\overline{U_{tv}}[n]} \right) u[n-k_1]\, \alpha[n-k_2] + 2 \sum_{k_1=0}^{M} \sum_{k_2=0}^{M} \left(\frac{\dot{\phi}_{Qu\dot{p}}[k_1,k_2]}{\overline{U_{tv}}[n]^2} \right) \\
& \times u[n-k_1]\, \dot{p}[n-k_2] + 2 \sum_{k_1=0}^{M} \sum_{k_2=0}^{M} \left(\frac{\dot{\phi}_{Qu\dot{h}}[k_1,k_2]}{\overline{U_{tv}}[n]^2} \right) u[n-k_1]\, \dot{h}[n-k_2] \\
& + 2 \sum_{k_1=0}^{M} \sum_{k_2=0}^{M} \left(\frac{\dot{\phi}_{Qw\alpha}[k_1,k_2]}{\overline{U_{tv}}[n]} \right) w[n-k_1]\, \alpha[n-k_2] + 2 \sum_{k_1=0}^{M} \sum_{k_2=0}^{M} \left(\frac{\dot{\phi}_{Qw\dot{p}}[k_1,k_2]}{\overline{U_{tv}}[n]^2} \right) \\
& \times w[n-k_1]\, \dot{p}[n-k_2] + 2 \sum_{k_1=0}^{M} \sum_{k_2=0}^{M} \left(\frac{\dot{\phi}_{Qw\dot{h}}[k_1,k_2]}{\overline{U_{tv}}[n]^2} \right) w[n-k_1]\, \dot{h}[n-k_2] \\
& + 2 \sum_{k_1=0}^{M} \sum_{k_2=0}^{M} \left(\frac{\dot{\phi}_{Q\alpha\dot{p}}[k_1,k_2]}{\overline{U_{tv}}[n]} \right) \alpha[n-k_1]\, \dot{p}[n-k_2] + 2 \sum_{k_1=0}^{M} \sum_{k_2=0}^{M} \left(\frac{\dot{\phi}_{Q\alpha\dot{h}}[k_1,k_2]}{\overline{U_{tv}}[n]} \right) \\
& \left. \times \alpha[n-k_1]\, \dot{h}[n-k_2] + 2 \sum_{k_1=0}^{M} \sum_{k_2=0}^{M} \left(\frac{\dot{\phi}_{Q\dot{h}\dot{p}}[k_1,k_2]}{\overline{U_{tv}}[n]^2} \right) \dot{h}[n-k_1]\, \dot{p}[n-k_2] \right\} \Bigg]
\end{aligned}
\tag{3.27}
$$

$$
\begin{aligned}
Q_b[n] = \frac{1}{2}\rho\overline{U_{tv}}[n]^2 B \Bigg[& \Bigg\{ \left(\frac{2C_Q\psi_{Qu}[0]}{\overline{U_{tv}}[n]}\right)u[n] + \left(\frac{C'_Q\psi_{Qw}[0]}{\overline{U_{tv}}[n]}\right)w[n] + \left(C'_Q\phi_{Q\alpha}[0]\right)\alpha[n] \\
& + \left(\frac{C'_Q\phi_{Q\dot{h}}[0]}{\overline{U_{tv}}[n]}\right)\dot{h}[n] + \left(\frac{C'_Q\phi_{Q\dot{p}}[0]}{\overline{U_{tv}}[n]}\right)\dot{p}[n] \Bigg\} + \Bigg\{ \sum_{k=0}^{M} \Bigg(\left(\frac{2C_Q\dot{\psi}_{Qu}[k]}{\overline{U_{tv}}[n]}\right)u[n-k] \\
& + \left(\frac{C'_Q\dot{\psi}_{Qw}[k]}{\overline{U_{tv}}[n]}\right)w[n-k] + \left(C'_Q\dot{\phi}_{Q\alpha}[k]\right)\alpha[n-k] + \left(\frac{C'_Q\dot{\phi}_{Q\dot{h}}[k]}{\overline{U_{tv}}[n]}\right)\dot{h}[n-k] \\
& + \left(\frac{C'_Q\dot{\phi}_{Q\dot{p}}[k]}{\overline{U_{tv}}[n]}\right)\dot{p}[n-k] \Bigg) \Bigg\} + \Bigg\{ \sum_{k_1=0}^{M}\sum_{k_2=0}^{M} \Bigg(\left(\frac{2C_Q\dot{\psi}_{Quu}[k_1,k_2]}{\overline{U_{tv}}[n]^2}\right)u[n-k_1]u[n-k_2] \\
& + \left(\frac{C'_Q\dot{\psi}_{Qww}[k_1,k_2]}{\overline{U_{tv}}[n]^2}\right)w[n-k_1]w[n-k_2] + \left(C'_Q\dot{\phi}_{Q\alpha\alpha}[k_1,k_2]\right)\alpha[n-k_1]\alpha[n-k_2] \\
& + \left(\frac{C'_Q\dot{\phi}_{Q\dot{h}\dot{h}}[k_1,k_2]}{\overline{U_{tv}}[n]^2}\right)\dot{h}[n-k_1]\dot{h}[n-k_2] + \left(\frac{C'_Q\dot{\phi}_{Q\dot{p}\dot{p}}[k_1,k_2]}{\overline{U_{tv}}[n]^2}\right)\dot{p}[n-k_1]\dot{p}[n-k_2] \\
& + 2\left(\frac{C'_Q\dot{\psi}_{Quw}[k_1,k_2]}{\overline{U_{tv}}[n]^2}\right)u[n-k_1]w[n-k_2] + 2\left(\frac{C'_Q\dot{\phi}_{Qu\alpha}[k_1,k_2]}{\overline{U_{tv}}[n]}\right)u[n-k_1]\alpha[n-k_2] \\
& + 2\left(\frac{C'_Q\dot{\phi}_{Qu\dot{h}}[k_1,k_2]}{\overline{U_{tv}}[n]^2}\right)u[n-k_1]\dot{h}[n-k_2] + 2\left(\frac{C'_Q\dot{\phi}_{Qu\dot{p}}[k_1,k_2]}{\overline{U_{tv}}[n]^2}\right)u[n-k_1]\dot{p}[n-k_2] \\
& + 2\left(\frac{C'_Q\dot{\phi}_{Qw\alpha}[k_1,k_2]}{\overline{U_{tv}}[n]}\right)w[n-k_1]\alpha[n-k_2] + 2\left(\frac{C'_Q\dot{\phi}_{Qw\dot{h}}[k_1,k_2]}{\overline{U_{tv}}[n]^2}\right)w[n-k_1]\dot{h}[n-k_2] \\
& + 2\left(\frac{C'_Q\dot{\phi}_{Qw\dot{p}}[k_1,k_2]}{\overline{U_{tv}}[n]^2}\right)w[n-k_1]\dot{p}[n-k_2] + 2\left(\frac{C'_Q\dot{\phi}_{Q\alpha\dot{h}}[k_1,k_2]}{\overline{U_{tv}}[n]}\right)\alpha[n-k_1]\dot{h}[n-k_2] \\
& + 2\left(\frac{C'_Q\dot{\phi}_{Q\alpha\dot{p}}[k_1,k_2]}{\overline{U_{tv}}[n]}\right)\alpha[n-k_1]\dot{p}[n-k_2] + 2\left(\frac{C'_Q\dot{\phi}_{Q\dot{h}\dot{p}}[k_1,k_2]}{\overline{U_{tv}}[n]^2}\right)\dot{h}[n-k_1]\dot{p}[n-k_2] \Bigg) \Bigg\} \Bigg\} \Bigg]
\end{aligned}
\tag{3.28}
$$

The Eq. (3.28) can further be expressed in a condensed form for the sake of brevity such as shown in Eq. (3.29).

$$
Q_{BF} = Q_{Volterra\ FD}\left(t, C_Q(\alpha_s), C'_Q(\alpha_s = 0), u, w, \dot{p}, \dot{h}, \alpha, IF_1(t), IF_2(\tau_1, \tau_2)\right) \tag{3.29}
$$

where IF_1 and IF_2 indicate the first- and second-order Volterra kernels. The block diagram of the Volterra FD model is shown in Figure (3-3).

3.6 Nonlinear unsteady wind load model (Scheme 2)

For the bridge sections with aerodynamic forces that highly sensitive to the angle of attack, the aerodynamic nonlinearities not only arise due to nonlinear fluid memory effects that have already been incorporated in the Volterra FD model, but also partly due to the dependency of aerodynamic forces on the varying angles of attack. Following it, the nonlinear buffeting forces on the bridge

deck in scheme 2 can be modelled as a nonlinear function of the varying angles of attack with properly defined static force coefficients which also depend on the varying angles of attack. With that, the effective angle of attack is further divided into low-frequency (large-scale) and high-frequency (small-scale) components corresponding to the frequencies lower and higher than a cut-off frequency i.e., the lowest natural frequency of the bridge structure such as:

$$\alpha_{eff} = \alpha_{eff}^{low}(t) + \alpha_{eff}^{high}(t) \tag{3.30}$$

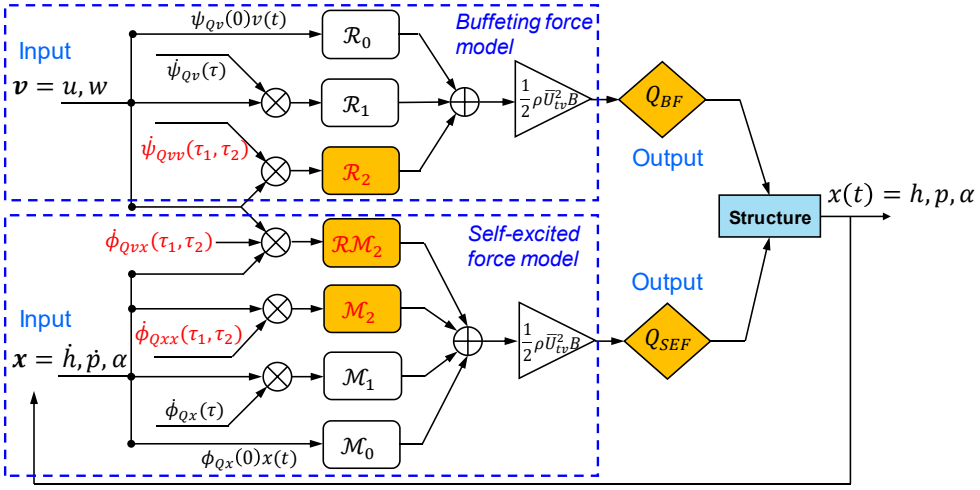

Figure 3-3 Block diagram of the Volterra FD model

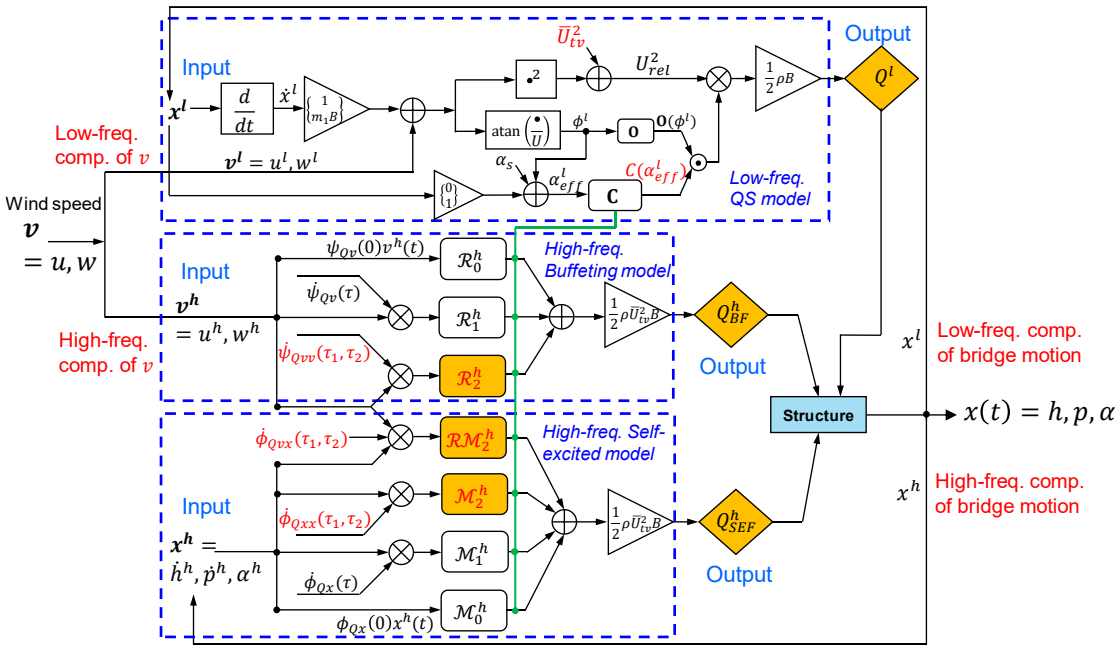

Figure 3-4 Block diagram of the Hybrid Volterra FD model

where $\alpha_{eff}^{low}(t)$ and $\alpha_{eff}^{high}(t)$ show the low-frequency (including static angle of attack, α_s) and high-frequency components of the effective angle of attack, respectively. Congruently, the nonlinear buffeting forces are also demarcated into corresponding low-frequency and high-frequency components. The low-frequency component of the nonlinear buffeting forces is modelled as a nonlinear function of the low-frequency component of the effective angle of attack by using the QS model presented in Chapter 2 as a 2D model. Here, the QS model is extended to a 3D model including drag force effects. Conversely, the high-frequency component of the nonlinear buffeting forces is modelled by using the Volterra FD model presented as a scheme 1 approach with the modification in the aerodynamic parameters. Instead of identifying IFs at zero angle of attack and identifying static force coefficients at the statically deformed position of the bridge deck (which have been assumed in the case of Volterra FD model), the Hybrid Volterra FD model considers the identification of IFs at varying angles of attack as well as the identification of static force coefficients at the low-frequency component of effective angle of attack. The concept of nonlinear IFs offers a general framework to simulate nonlinear aerodynamics. With that strategy, the nonlinear aerodynamic forces on a bridge deck can be generalized as:

$$\begin{aligned} Q_{BF} = Q_{BF}\left(t, \alpha_{eff}, u, w, \dot{p}, \dot{h}, \alpha, IF_1, IF_2\right) = Q_{QS}\left(t, \alpha_{eff}^{low}, u^{low}, w^{low}, \dot{h}^{low}, \dot{p}^{low}, \dot{\alpha}^{low}\right) \\ + Q_{Volterra\ FD}\left(t, \alpha_{eff}^{low}, C_Q\left(\alpha_{eff}^{low}\right), C_Q'(\alpha_s\right. \\ \left. = 0), IF_1\left(\theta_{varying}, t\right), IF_2\left(\theta_{varying}, \tau_1, \tau_2\right), u^{high}, w^{high}, \dot{h}^{high}, \dot{p}^{high}, \alpha^{high}\right) \end{aligned} \tag{3.31}$$

where superscripts low and high mean the low-frequency and high-frequency components. The low-frequency component of aerodynamic forces can be expressed using the QS model due to high value of the reduced velocity as the following nonlinear form (including static components):

$$\begin{aligned} L^{low}(t) &= F_L^{low}\cos(\phi^{low}) - F_D^{low}\sin(\phi^{low}) - L_{st}(t) \\ D^{low}(t) &= F_L^{low}\sin(\phi^{low}) + F_D^{low}\cos(\phi^{low}) - D_{st}(t) \\ M^{low}(t) &= F_M^{low} - M_{st}(t) \end{aligned} \tag{3.32}$$

where

$$\begin{aligned} F_L^{low} &= -\frac{1}{2}\rho U_{rel}^2 B C_L\left(\alpha_{eff}^{low}\right);\ F_D^{low} = \frac{1}{2}\rho U_{rel}^2 B C_D\left(\alpha_{eff}^{low}\right);\ F_M^{low} = \frac{1}{2}\rho U_{rel}^2 B^2 C_M\left(\alpha_{eff}^{low}\right) \\ U_{rel}^2 &= \left(\overline{U_{tv}} + u^{low} - \dot{p}^{low}\right)^2 + \left(w^{low} + \dot{h}^{low} + m_1 B\dot{\alpha}^{low}\right)^2 \\ \alpha_{eff}^{low} &= \alpha_s + \phi^{low};\ \phi^{low} = \arctan\left(\frac{w^{low} + \dot{h}^{low} + m_1 B\dot{\alpha}^{low}}{\overline{U_{tv}} + u^{low} - \dot{p}^{low}}\right) \end{aligned} \tag{3.33}$$

The high-frequency components of aerodynamic forces can be expressed by using Eq. (3.28) of Volterra FD model by replacing the parameters $C_Q(\alpha_s)$, $C_Q'(\alpha_s = 0)$, u, w, $\dot{p}$, $\dot{h}$, α, $IF_1(t)$, $IF_2(\tau_1, \tau_2)$ in Eq. (3.28) with $C_Q\left(\alpha_{eff}^{low}\right)$, $C_Q'(\alpha_s = 0)$, $IF_1\left(\theta_{varying}, t\right)$, $IF_2\left(\theta_{varying}, \tau_1, \tau_2\right)$, u^{high}, w^{high}, $\dot{h}^{high}$, $\dot{p}^{high}$, α^{high}, respectively. The block diagram of the Hybrid Volterra FD

model is shown in Figure (3-4). The practical application of Volterra FD and Hybrid Volterra FD models to a real full-scale bridge will be presented in Chapter 5.

CHAPTER 4: IDENTIFICATION OF VOLTERRA KERNELS

This chapter discusses the methods for the identification of Volterra kernels adopted in this dissertation. Two methods herein are employed based on the experimental and simulation approaches. The experimental approach entails the experimental data of flutter derivatives (FDs), obtained from the wind tunnel test at varying angles of attack, to build the relationships between IFs and FDs, whereas the simulation approach is adopted based on a nonparametric modeling technique called Artificial Neural Network (ANN) which uses the set of inputs and outputs to develop the nonlinear relationship with the help of associated synaptic weights. The IFs are expressed mathematically as an exponential function whose unknown parameters are determined by fitting the experimental data of FDs in a nonlinear least square manner. The FDs of a cross-section of the Akashi-Kaikyo bridge is taken from previous researchers at various angles of attack. The time-varying effects of non-synoptic winds are also considered in the exponential formulation of IFs. In the case of the experimental method, the first-order kernels are identified from the FDs for different angles of attack which, whereas the second-order kernels are identified by using the nonlinear system identification technique. For that, a Wiener model-based filter is designed by using the measurement data of wind speed and displacement of the bridge deck to envisage the type and level of nonlinearity existing in wind-bridge interaction. Conversely, in the case of the simulation method, a Time-delay Neural Network (TDNN) is adopted to develop a second-order aerodynamic model for wind loads, which is then compared with the Volterra series-based wind load model (presented in Chapter 3) and corresponding terms are equated to extract the first- and second-order Volterra kernels in terms of unknown parameters of the TDNN. For that, the measurement data of wind speed and bridge displacement are used to train the TDNN consisting of an input layer, hidden layer and output layer. The results highlighted the importance of using TDNN over the experimental method in terms of reduced-order modeling because the second-order kernels can be identified by TDNN with tremendously reduced computational effort. These methods may also help the designer to design long-span bridges accurately by considering the nonlinearity and non-stationary wind effects on the buffeting response of the bridge deck.

4.1 Introduction

Volterra series provides a suitable mathematical explanation of nonlinear dynamical systems through multidimensional convolution integrals, each related with a kernel function. These higher-order kernels can be idealized as extensions of the linear impulse response to multidimensions. Classical identification of Volterra kernels involves the exciting system with a

series of steps or impulses of various orders. Its application to weakly nonlinear aerodynamic and aeroelastic systems is well established (Silva 1997; Raveh 2000; Raveh 2001). The synthesis of Volterra kernels can be a computational resource-intensive procedure, especially when it comes to higher-order kernels and representation of stronger nonlinearities. Also, the proper identification of the cross-coupled terms, existing when multiple DOFs of a nonlinear dynamical system are excited simultaneously, represents another problem regarding the application of Volterra based reduced-order modeling (ROMs) (Silva 2005).

Generally, the Volterra kernels are identified by either experiment or numerical simulation. However, the accurate identification of IFs is critical and a tricky task when applying to a nonlinear system for the generation of an efficient, robust, and nonlinear model. As a matter of fact, IFs can be identified in both time- and frequency-domains. In the former, IFs are found by imposing an instantaneous change to a system state variable (angle of attack of wind flow), whereas, in the latter, IFs are derived from the FDs at varying angles of attack. According to the airfoil theory, the evolutionary growth of the aerodynamic forces in time-domain is described by the convolution integral of time-dependent functions representing the response of an airfoil section to the step-change of an aerodynamic input. The time-dependent function herein refers to a step-function excitation which means the excitation that grows abruptly from the initial state to a state with a certain stable value. Farsani et al. (2014) evaluated the aerodynamic response of a bridge deck due to a step-change and calculated the FDs from sinusoidal oscillations.

Some discussions are also available on the point that IFs for buffeting and self-excited forces are the same based on the assumption that vertical gust wind component and vertical bridge response component yield the same aerodynamic loads on a bridge deck (e.g., Tubino, 2005). However, this assumption is not valid in the case of a real bridge deck. Hence, IFs for self-excited forces are particularly different from those for buffeting forces. Several authors have also pointed out that only one IF is not enough to describe the self-excited forces on the bluff bodies (e.g., Øiseth et al. 2011). Costa et al. (2007) used different IFs to simulate the self-excited and buffeting forces in time-domain for a 2D sectional model of the bridge while ignoring the drag-like IFs for a three-dimensional (3D) bridge problem. A critical step in indicial modelling is the identification of IF coefficients. This is usually done via the minimization of an error function, in order to fit FDs. A nonlinear least-square method is proposed by Scanlan et al. (1974). A scheme, based on the Levenberg–Marquardt method, is also adopted by Caracoglia and Jones (2003a, 2003b), and applied to different bridge deck cross-sections, considering the Scanlan's formulation of self-excited forces. Costa and Borri (2006) also estimated sets of IF coefficients for rectangular cross-sections by time-domain simulations and compared with the experimental data.

In recent years, some researchers (Wu and Kareem 2013; Paula et al. 2019; Lin and Ng 2018) have presented some other useful techniques for the identification of higher-order kernels based

on the correlation analysis and scheme and neural network. Paula et. al. (2018) proposed a method for the assessment of Volterra kernels based on artificial neural networks. The relation between the Volterra kernels and the internal parameters of a TDNN is studied and explored for the application of reduced-order modeling of nonlinear aerodynamic loads. In this dissertation, both the experimental and simulation methods are adopted to extract the first- and second-order Volterra kernels which are presented in the subsequent sections.

4.2 Experimental technique

In this method, the aerodynamic and aeroelastic IFs are identified by using the experimental data of FDs of the bridge deck considering the amplitude-dependency of FDs on the angle of attack. The main idea is to transform the frequency-dependent FDs measured in frequency-domain into the equivalent frequency-independent IFs identified in time-domain. The following exponential function is used to express the aerodynamic and aeroelastic IFs mathematically:

$$IF(t, \overline{U_{tv}}(\tau)) = a_0 - \sum_{j=1}^{N} a_j \exp\left(-b_j \frac{\overline{U_{tv}}(\tau)}{B} t\right) \tag{4.1}$$

where a_0, a_j and b_j are the frequency-free IF coefficients to be evaluated such that $b_j \geq 0$; and N is the functional groups of exponential form that can be seen as a cascade filter, modelling the unsteady bridge aerodynamics. For a streamlined body immersed in two-dimensional flow, N equal to 2 is usually appropriate, whereas $N \geq 3$ is normally suitable for a bluff body like bridge deck (Caracoglia and Jones 2003b; Jones 1939). a_0 is taken as 1.0 to normalize IF as it represents the static state of the system. Moreover, IFs coefficients depend on the angle of attack of wind i.e., IF shows the significant overshooting behavior at a large angle of attack. The representation of IF shown in Eq. (4.1) was first used by Wagner (1925) for a thin airfoil, and Theodorsen (1935) utilized it for a flat plate. Later, Jones (1940) adopted it to present the excellent approximations to Wagner and Kussner functions for formulating the aeroelastic and aerodynamic IFs for a thin airfoil immersed in a two-dimensional flow as shown in Eqs. (4.2) and (4.3), respectively:

$$\phi_{Wagner}(s) = 1 - 0.165\exp(-0.0455s) - 0.355\exp(-0.3s) \tag{4.2}$$

$$\psi_{Kussner}(s) = 1 - 0.236\exp(-0.058s) - 0.513\exp(-0.364s) - 0.171\exp(-2.42s) \tag{4.3}$$

where s denotes the non-dimensional time equal to $\overline{U}t/B$. However, Jones proposed the same functions for each component of gust-induced and motion-induced vibrations, which is not true in the case of a bluff body. Therefore, IF should be different for each component of the gust, motion, and their coupling for a real bridge deck. Using the experimental approach, the aerodynamic and aeroelastic IFs are identified directly by fitting the FDs in a nonlinear least-square manner as described in (Caracoglia and Jones 2003b; Costa and Borri 2006). For that, the

wind static force coefficients and experimental data of FDs are taken from (Katsuchi et al. 1998; Xu, 2014) for the Akashi-Kaikyo bridge deck section shown in Figure (4-1). The static force coefficients at the varying angles of incidence for this section are also shown in Figure (4-2). A full set of 18 FDs (H_i^*, P_i^*, A_i^*, where $i = 1, \ldots, 6$) at varying angles of attack from -4° to +3° is used for three-dimensional modelling of wind loads based on aerodynamic and aeroelastic IFs, which not only depends on time but also the bridge motion as suggested by Wu and Kareem (2013). Figure (4-3) shows the experimental results of 18 FDs at zero angle of attack. For the sake of illustration, only variations of A_2^*, A_4^* and H_4^* are considered in the nonlinear buffeting analysis framework as shown in Figures (4-4)−(4-6). Experimental data indicates that A_2^*, A_4^* and H_4^* are highly sensitive to the angle of attack for this section.

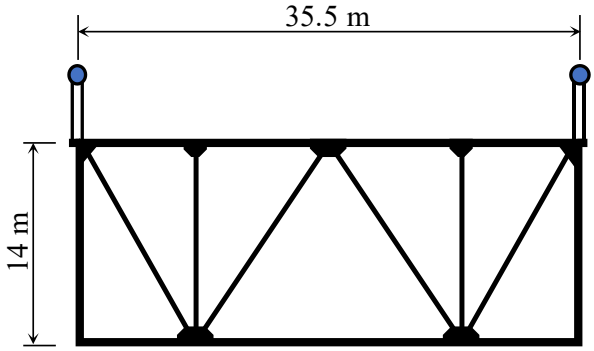

Figure 4-1 Cross-section of the Akashi-Kaikyo bridge deck

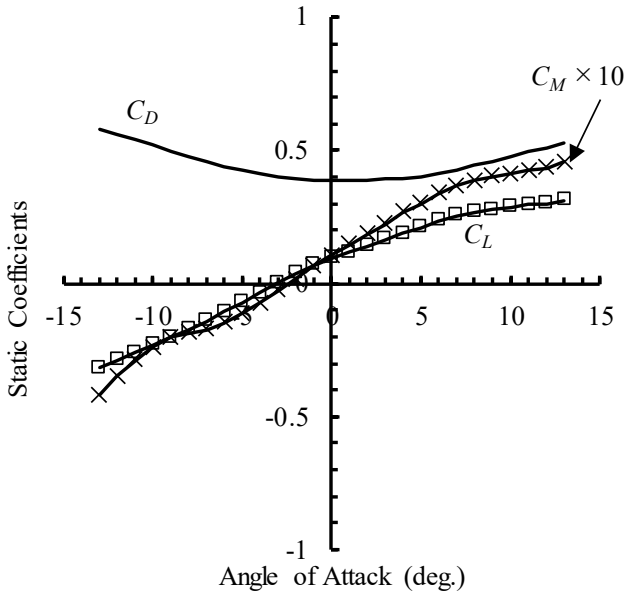

Figure 4-2 Static force coefficients for the Akashi-Kaikyo bridge

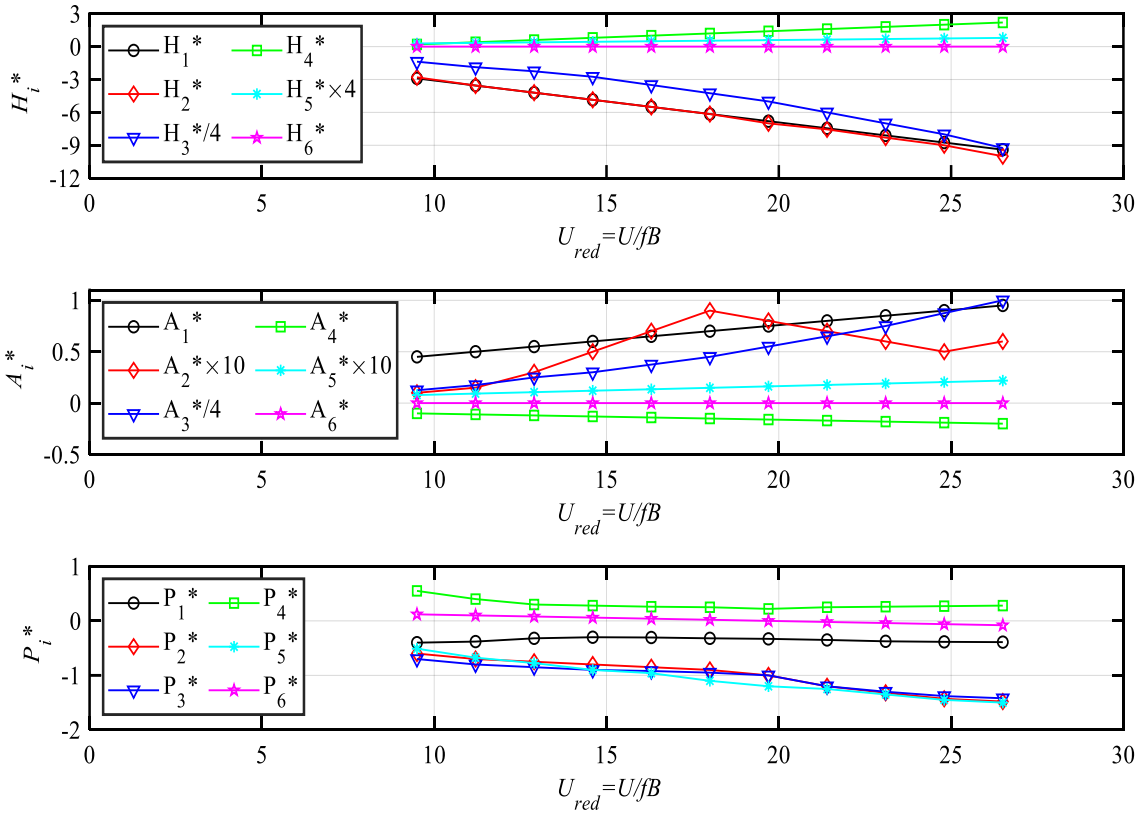

Figure 4-3 Flutter derivatives of the Akashi-Kaikyo bridge deck

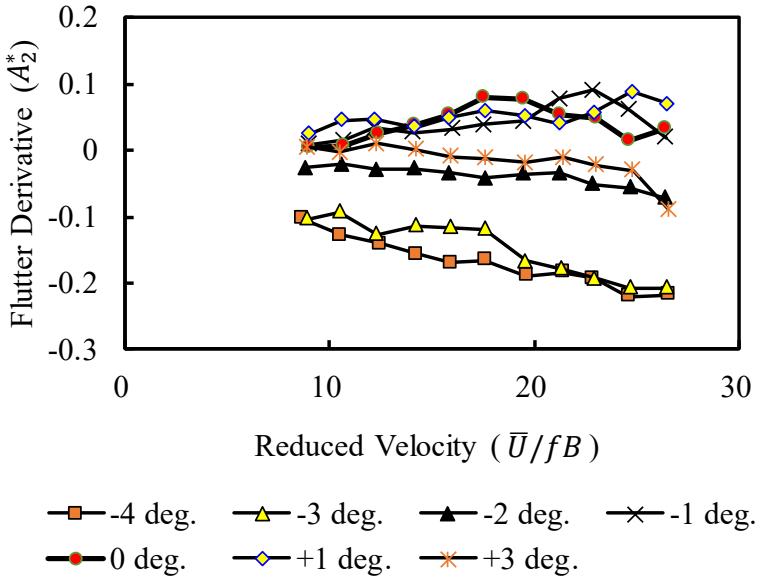

Figure 4-4 Flutter derivative A_2^* at varying angles of attack for the Akashi-Kaikyo bridge deck

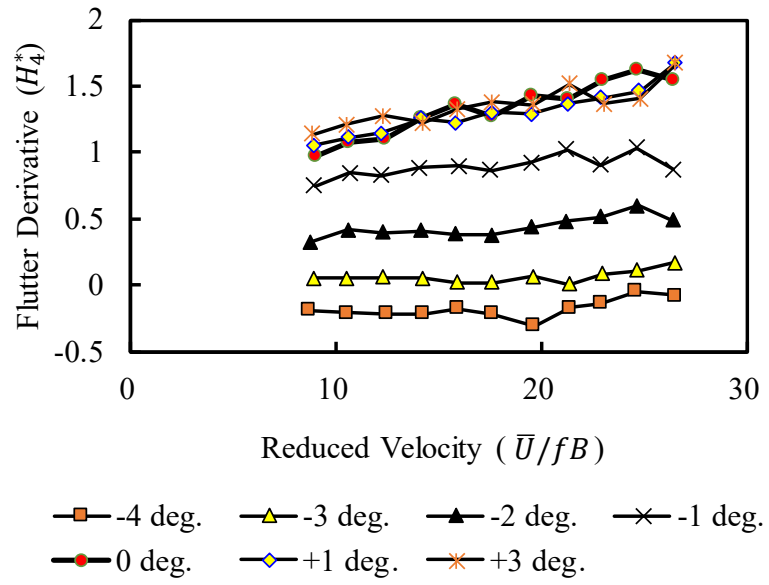

Figure 4-5 Flutter derivative H_4^* at varying angles of attack for the Akashi-Kaikyo bridge deck

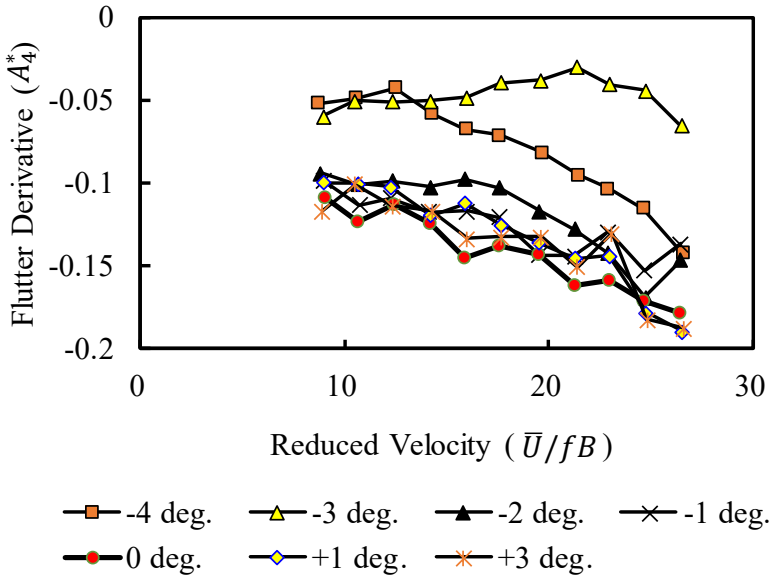

Figure 4-6 Flutter derivative A_4^* at varying angles of attack for the Akashi-Kaikyo bridge deck

To identify the IFs of the deck section at a certain angle of attack, the relationships are first established between IFs and frequency-dependent functions by using FDs. The following pairs of FDs are used to establish these relationships for each component of gust-induced and motion-induced vibrations: $\psi_{Du}(P_1^*,\ P_4^*)$, $\psi_{Dw}(P_5^*,\ P_6^*)$, $\psi_{Lu}(H_5^*,\ H_6^*)$, $\psi_{Lw}(H_1^*,\ H_4^*)$, $\psi_{Mu}(A_5^*,\ A_6^*)$,

$\psi_{Mw}(A_1^*,\ A_4^*)$, $\phi_{L\dot{h}}(H_1^*,\ H_4^*)$, $\phi_{M\dot{h}}(A_1^*,\ A_4^*)$, $\phi_{D\dot{h}}(P_5^*,\ P_6^*)$, $\phi_{L\alpha}(H_2^*,\ H_3^*)$, $\phi_{M\alpha}(A_2^*,\ A_3^*)$, $\phi_{D\alpha}(P_2^*,\ P_3^*)$, $\phi_{L\dot{p}}(H_5^*,\ H_6^*)$, $\phi_{M\dot{p}}(A_5^*,\ A_6^*)$, $\phi_{D\dot{p}}(P_1^*,\ P_4^*)$. The subsequent subsections will discuss the formulation of these relationships for the identification of aerodynamic and aeroelastic IFs through the experiment.

4.2.1 Relationship between IFs and FDs for identification of aerodynamic IFs

For the identification of aerodynamic IFs, the relationship between IFs and FDs of the bridge deck are formulated with the help of (1) buffeting force model in frequency-domain (2) self-excited force model proposed by Scanlan (1990; 1993) and (3) Fourier transformation of linear unsteady buffeting load model derived in chapter 3.

(1) Frequency-dependent buffeting force model

For turbulence intensities of wind in ABL, and for turbulence components with frequencies that are of interest in practice, it may be assumed that the squares and products of velocity fluctuations u and w are negligible with respect to the square of mean velocity $\overline{U}$. Following it, the expression for lift force in frequency-domain can be written as:

$$L_b = \frac{1}{2}\rho\overline{U}^2 B\left[2C_L\frac{u}{\overline{U}} + (C_D + C_L')\frac{w}{\overline{U}}\right] \tag{4.4}$$

Owing to the frequency-dependence of buffeting forces at high-reduced frequency, Eq. (4.4) is only valid up to the first approximation of forces. The insufficiency can be observed through the frequency-domain approach by estimating the attendant response due to a sinusoidally acting vertical or horizontal component of the fluctuating wind speed. By putting the transfer function separately to both components, the Fourier transform of the buffeting force is expressed as:

$$L_b = \frac{1}{2}\rho\overline{U}^2 B\left(2C_L\chi_{Lu}\frac{u}{\overline{U}} + (C_D + C_L')\chi_{Lw}\frac{w}{\overline{U}}\right) \tag{4.5}$$

Similarly, buffeting drag force and pitching moment can be formulated such as:

$$D_b = \frac{1}{2}\rho\overline{U}^2 B\left(2C_D\chi_{Du}\frac{u}{\overline{U}} + (C_D' - C_L)\chi_{Dw}\frac{w}{\overline{U}}\right) \tag{4.6}$$

$$M_b = \frac{1}{2}\rho\overline{U}^2 B^2\left(2C_M\chi_{Mu}\frac{u}{\overline{U}} + (C_M')\chi_{Mw}\frac{w}{\overline{U}}\right) \tag{4.7}$$

where χ_{Lu}, χ_{Lw}, χ_{Du}, χ_{Dw}, χ_{Mu} and X_{Mw} are the aerodynamic force transfer functions between fluctuating wind speeds and buffeting forces. These are functions of frequency, which depend on the deck configuration. The absolute magnitudes of these functions are also known as the aerodynamic admittance functions which express the transfer functions between the turbulent wind components and aerodynamic forces. In the quasi-steady formulation, the admittance functions take the value of unity. Writing Eqs. (4.5), (4.6) and (4.7) into a matrix form:

$$\begin{Bmatrix} L_b \\ D_b \\ M_b \end{Bmatrix} = \frac{1}{2}\rho\overline{U}^2 B \begin{bmatrix} 2C_L\chi_{Lu} & (C_D + C_L')\chi_{Lw} \\ 2C_D\chi_{Du} & (C_D' - C_L)\chi_{Dw} \\ 2C_M\chi_{Mu}B & C_M'\chi_{Mw}B \end{bmatrix} \begin{Bmatrix} \frac{u}{\overline{U}} \\ \frac{w}{\overline{U}} \end{Bmatrix} \tag{4.8}$$

(2) Scanlan's self-excited force model

The self-excited forces result from the oscillation between fluid and deck oscillation. Scanlan (1990; 1993) proposed a model for self-excited forces such as:

$$L_{se}(K) = \frac{1}{2}\rho\overline{U}^2 B\left[KH_1^*\frac{\dot{h}}{\overline{U}} + KH_2^*\frac{B\dot{\alpha}}{\overline{U}} + K^2H_3^*\alpha + K^2H_4^*\frac{h}{B} + KH_5^*\frac{\dot{p}}{\overline{U}} + K^2H_6^*\frac{p}{B}\right] \tag{4.9}$$

$$D_{se}(K) = \frac{1}{2}\rho\overline{U}^2 B\left[KP_1^*\frac{\dot{p}}{\overline{U}} + KP_2^*\frac{B\dot{\alpha}}{\overline{U}} + K^2P_3^*\alpha + K^2P_4^*\frac{p}{B} + KP_5^*\frac{\dot{h}}{\overline{U}} + K^2P_6^*\frac{h}{B}\right] \tag{4.10}$$

$$M_{se}(K) = \frac{1}{2}\rho\overline{U}^2 B^2\left[KA_1^*\frac{\dot{h}}{\overline{U}} + KA_2^*\frac{B\dot{\alpha}}{\overline{U}} + K^2A_3^*\alpha + K^2A_4^*\frac{h}{B} + KA_5^*\frac{\dot{p}}{\overline{U}} + K^2A_6^*\frac{p}{B}\right] \tag{4.11}$$

where K is defined as the reduced frequency of oscillations equal to $\omega B/\overline{U}$ (which is further equal to $2\pi/U_{red}$). Ignoring terms related to α and $\dot{\alpha}$ in Eqs. (4.9), (4.10) and (4.11) because there are only two components of the velocity of wind in Eq. (4.8) i.e., horizontal, and vertical, and there is not a rotational wind velocity component. Therefore, the terms related to α and $\dot{\alpha}$ in Eqs. (4.9), (4.10) and (4.11) can be ignored. For instance, the self-excited lift force without terms related to α and $\dot{\alpha}$ is shown in Eq. (4.12). For the sake of Fourier transformation, putting $h = \dot{h}/i\omega$ and $p = \dot{p}/i\omega$ in Eq. (4.12) yields Eq. (4.13), which after further simplification becomes Eq. (4.14) such as:

$$L_{se}(K) = \frac{1}{2}\rho\overline{U}^2 B\left[KH_1^*\frac{\dot{h}}{\overline{U}} + K^2H_4^*\frac{h}{B} + KH_5^*\frac{\dot{p}}{\overline{U}} + K^2H_6^*\frac{p}{B}\right] \tag{4.12}$$

$$L_{se}(K) = \frac{1}{2}\rho\overline{U}^2 B\left[KH_1^*\frac{\dot{h}}{\overline{U}} - iKH_4^*\frac{\dot{h}}{\overline{U}} + KH_5^*\frac{\dot{p}}{\overline{U}} - iKH_6^*\frac{\dot{p}}{\overline{U}}\right] \tag{4.13}$$

$$L_{se}(K) = \frac{1}{2}\rho\overline{U}^2 B\left[K(H_5^* - iH_6^*)\frac{\dot{p}}{\overline{U}} + K(H_1^* - iH_4^*)\frac{\dot{h}}{\overline{U}}\right] \tag{4.14}$$

Similarly, self-excited drag force and pitching moment in frequency-domain can also be formulated such as:

$$D_{se}(K) = \frac{1}{2}\rho\overline{U}^2 B\left[K(P_1^* - iP_4^*)\frac{\dot{p}}{\overline{U}} + K(P_5^* - iP_6^*)\frac{\dot{h}}{\overline{U}}\right] \tag{4.15}$$

$$M_{se}(K) = \frac{1}{2}\rho\overline{U}^2 B^2\left[K(A_5^* - iA_6^*)\frac{\dot{p}}{\overline{U}} + K(A_1^* - iA_4^*)\frac{\dot{h}}{\overline{U}}\right] \tag{4.16}$$

Writing Eqs. (4.14), (4.15) and (4.16) into a matrix form:

$$\begin{Bmatrix} L_b(K) \\ D_b(K) \\ M_b(K) \end{Bmatrix} = \frac{1}{2}\rho\overline{U}^2 B \begin{bmatrix} K(H_5^* - iH_6^*) & K(H_1^* - iH_4^*) \\ K(P_1^* - iP_4^*) & K(P_5^* - iP_6^*) \\ K(A_5^* - iA_6^*)B & K(A_1^* - iA_4^*)B \end{bmatrix} \begin{Bmatrix} \frac{\dot{p}}{\overline{U}} \\ \frac{\dot{h}}{\overline{U}} \end{Bmatrix} \tag{4.17}$$

(3) Fourier transformation of the linear unsteady buffeting load model

Referring to Chapter 3 and taking the Fourier transform of Eqs. (3.11), (3.12) and (3.13) yields:

$$L_b(K) = \frac{1}{2}\rho\bar{U}^2 B\left[2C_L\left\{\psi_{Lu}(0) + \bar{\psi}_{Lu}\right\}\frac{u(K)}{\bar{U}} + (C_D + C_L')\left\{\psi_{Lw}(0) + \bar{\psi}_{Lw}\right\}\frac{w(K)}{\bar{U}}\right] \tag{4.18}$$

$$D_b(K) = \frac{1}{2}\rho\bar{U}^2 B\left[2C_D\left\{\psi_{Du}(0) + \bar{\psi}_{Du}\right\}\frac{u(K)}{\bar{U}} + (C_D' - C_L)\left\{\psi_{Dw}(0) + \bar{\psi}_{Dw}\right\}\frac{w(K)}{\bar{U}}\right] \tag{4.19}$$

$$M_b(K) = \frac{1}{2}\rho\bar{U}^2 B^2\left[2C_M\left\{\psi_{Mu}(0) + \bar{\psi}_{Mu}\right\}\frac{u(K)}{\bar{U}} + C_M'\left\{\psi_{Mw}(0) + \bar{\psi}_{Mw}\right\}\frac{w(K)}{\bar{U}}\right] \tag{4.20}$$

Writing Eqs. (4.18), (4.19) and (4.20) into a matrix form such as:

$$\begin{Bmatrix} L_b(K) \\ D_b(K) \\ M_b(K) \end{Bmatrix} = \frac{1}{2}\rho\bar{U}^2 B\begin{bmatrix} 2C_L\left\{\psi_{Lu}(0) + \bar{\psi}_{Lu}\right\} & (C_D + C_L')\left\{\psi_{Lw}(0) + \bar{\psi}_{Lw}\right\} \\ 2C_D\left\{\psi_{Du}(0) + \bar{\psi}_{Du}\right\} & (C_D' - C_L)\left\{\psi_{Dw}(0) + \bar{\psi}_{Dw}\right\} \\ 2C_M\left\{\psi_{Mu}(0) + \bar{\psi}_{Mu}\right\}B & C_M'\left\{\psi_{Mw}(0) + \bar{\psi}_{Mw}\right\}B \end{bmatrix}\begin{Bmatrix} \frac{u(K)}{\bar{U}} \\ \frac{w(K)}{\bar{U}} \end{Bmatrix} \tag{4.21}$$

By comparing the corresponding elements of Eqs. (4.8), (4.17) and (4.21), the relationship functions can be obtained such as:

Element (1,1)

$$2C_L\chi_{Lu} = K(H_5^* - iH_6^*) = 2C_L\left\{\psi_{Lu}(0) + \bar{\psi}_{Lu}\right\} \tag{4.22a}$$

$$\therefore \chi_{Lu} = \psi_{Lu}(0) + \bar{\psi}_{Lu} = \frac{K}{2C_L}(H_5^* - iH_6^*) \tag{4.22b}$$

Element (1,2)

$$(C_D + C_L')\chi_{Lw} = K(H_1^* - iH_4^*) = (C_D + C_L')\left\{\psi_{Lw}(0) + \bar{\psi}_{Lw}\right\} \tag{4.23a}$$

$$\therefore \chi_{Lw} = \psi_{Lw}(0) + \bar{\psi}_{Lw} = \frac{K}{(C_D + C_L')}(H_1^* - iH_4^*) \tag{4.23b}$$

Element (2,1)

$$2C_D\chi_{Du} = K(P_1^* - iP_4^*) = 2C_D\left\{\psi_{Du}(0) + \bar{\psi}_{Du}\right\} \tag{4.24a}$$

$$\therefore \chi_{Du} = \psi_{Du}(0) + \bar{\psi}_{Du} = \frac{K}{2C_D}(P_1^* - iP_4^*) \tag{4.24b}$$

Element (2,2)

$$(C_D' - C_L)\chi_{Dw} = K(P_5^* - iP_6^*) = (C_D' - C_L)\left\{\psi_{Dw}(0) + \bar{\psi}_{Dw}\right\} \tag{4.25a}$$

$$\therefore \chi_{Dw} = \psi_{Dw}(0) + \bar{\psi}_{Dw} = \frac{K}{(C_D' - C_L)}(P_5^* - iP_6^*) \tag{4.25b}$$

Element (3,1)

$$2C_M\chi_{Mu}B = BK(A_5^* - iA_6^*) = 2C_M\left\{\psi_{Mu}(0) + \bar{\psi}_{Mu}\right\}B \tag{4.26a}$$

$$\therefore \chi_{Mu} = \psi_{Mu}(0) + \bar{\psi}_{Mu} = \frac{K}{2C_M}(A_5^* - iA_6^*) \tag{4.26b}$$

Element (3,2)

$$C'_M \chi_{Mw} B = BK(A_1^* - iA_4^*) = C'_M \left\{ \psi_{Mw}(0) + \bar{\dot{\psi}}_{Mw} \right\} B \tag{4.27a}$$

$$\therefore \chi_{Mw} = \psi_{Mw}(0) + \bar{\dot{\psi}}_{Mw} = \frac{K}{C'_M}(A_1^* - iA_4^*) \tag{4.27b}$$

in which $\bar{\dot{\psi}}$ denotes the Fourier transformation of the first derivative of aerodynamic IF. This can be calculated by taking the first derivative of Eq. (4.1), followed by the Fourier transformation, which upon further simplification yields the generalized form of $\bar{\dot{\psi}}$ such as:

$$\dot{\psi}(s) = \sum_{j=1}^{N} a_j b_j \exp(-b_j s) \tag{4.28a}$$

$$FT\left(\dot{\psi}(s)\right) = \int_{-\infty}^{\infty} a_1 b_1 e^{-b_1 s} e^{-iKs} ds \tag{4.28b}$$

$$\bar{\dot{\psi}} = \sum_{j=1}^{N} \left(\frac{a_j b_j^2}{b_j^2 + K^2} - iK \frac{a_j b_j}{b_j^2 + K^2} \right) \tag{4.28c}$$

Thus, the expression for $\psi(0) + \bar{\dot{\psi}}$ can be shown explicitly as follows:

$$\psi(0) + \bar{\dot{\psi}} = 1 - \sum_{j=1}^{N} a_j + \sum_{j=1}^{N} \left(\frac{a_j b_j^2}{b_j^2 + K^2} - iK \frac{a_j b_j}{b_j^2 + K^2} \right) \tag{4.29}$$

in which $\psi(0) + \dot{\psi}(s)$ is a complex number and its real part is equivalent to the real part of Sears' functions, denoted by $S(K)$, as shown in Eq. (4.30). In the theory of airfoil, Sears' function is the lift admittance function i.e., the frequency-based transfer function which relates the vertical fluctuations owing to turbulent winds to the lift force and pitching moment experienced by the bridge. Usually, Sears' function is determined by combining the Bessel functions of first kind and Theodorsen's complex circulation function. Following it, the relationships are established between aerodynamic IFs and Sears' functions using FDs by means of Fourier-integral superposition of the linear results for simple harmonic motion as pointed out by Garrick (Garrick, 1938) such as:

$$S(K) \equiv \chi(K) = C(K)[J_0(K) - iJ_1(K)] + iJ_1(K) \tag{4.30a}$$

$$= F_S(K) + iG_S(K) = iK \int_0^{\infty} \psi(s) e^{-iKs} ds \tag{4.30b}$$

where $J_0(K)$ and $J_1(K)$ represent the Bessel functions of first kind with ν equal to 0 and 1; $F_S(K)$ and $G_S(K)$ indicate the real and imaginary parts of $S(K)$, respectively, and $C(K)$ is the Theodorsen's circulatory complex function consisting of a real part denoted by $F_{Th}(K)$ and a complex part denoted by $G_{Th}(K)$. In the case of a thin airfoil, $C(K)$ is usually determined from the Hankel functions of second kind ($H_\nu^{(2)}$ where ν=0,1) such as:

$$C(K) = F_{Th}(K) + iG_{Th}(K) = \frac{H_1^{(2)}(K)}{H_1^{(2)}(K) + iH_0^{(2)}(K)} \tag{4.30c}$$

Since the mechanism of generation of the aeroelastic forces due to bridge motion is different

from the generation of the buffeting forces due to wind turbulence, these forces can be characterized in terms of different functions, i.e., the Wagner function and Kussner function in the time-domain, and the Theodorsen's function and Sears' function in the frequency-domain. As a matter of fact, Wagner and Kussner functions in the time-domain are the counterparts of the Theodorsen's and Sears' functions in the frequency-domain, respectively and the Fourier synthesis is helpful to show the strong duality between frequency- and time-domain functions. Figure (4-7) shows the comparison of Theodorsen's and Sears' functions in frequency-domain, and the comparison of the Wagner and Kussner functions in time-domain, respectively. As a function of 1/K, as shown in Figure (4-7a), the imaginary part of Theodorsen's function dies out for 1/K tending to infinity (low-frequency regime), while the real part of Theodorsen's function starts at 0.5 and approaches unity, i.e., the quasi-stationary behavior. On the other hand, the imaginary part of Sears' function shows sinusoidal behavior and disappears for infinity value of 1/K, whereas the real part of Sears' function starts at 0 and approaches unity asymptotically as a function of 1/K. In Figure (4-7b), the Wagner and Kussner functions start at 0.5 and 1.0, respectively, both of which asymptotically approach unity as a function of s. The subsequent subsections will present the development of the relationships between IFs and FDs for the identification of aerodynamic and aeroelastic IFs.

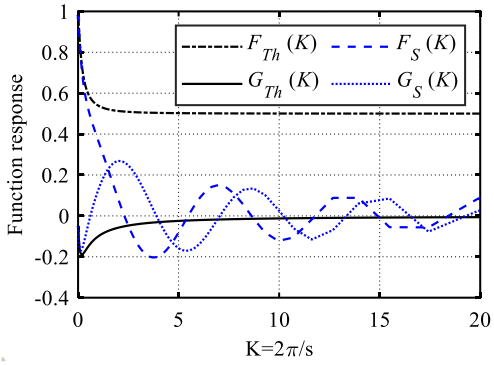

(a) Real and imaginary parts of Theodorsen's and Sears' functions in frequency-domain

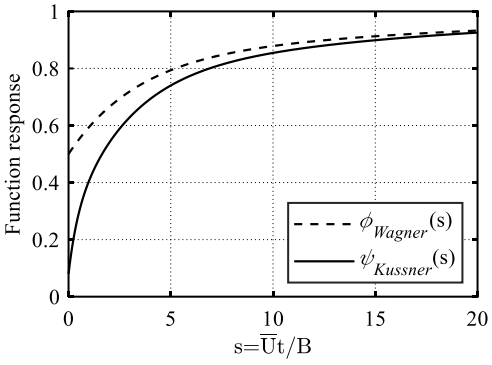

(b) Wagner and Kussner functions in time-domain

Figure 4-7 Comparison of unsteady aerodynamic force functions for airfoil section

By separating the real and imaginary parts from Eq. (4.29):

$$F_S(K) = 1 - \sum_{j=1}^{N} a_j + \sum_{j=1}^{N} \left(\frac{a_j b_j^2}{b_j^2 + K^2} \right) \tag{4.31a}$$

$$G_S(K) = -\sum_{j=1}^{N} \left(\frac{a_j b_j K}{b_j^2 + K^2} \right) \tag{4.31b}$$

The problem of finding the indicial function coefficients (a_j and b_j) requires the

simultaneous solutions of Eqs. (4.31a) and (4.31b) such that the extrema of relationships between IFs and FDs yield a minimum squared-error function. Eq. (4.32) shows the extremum of the relationship derived from the Eq. (4.22b) by using the principle of the sum of squares of residuals. A Levenberg-Marquart optimization algorithm is used to optimize these extrema in a nonlinear least square manner to find the aerodynamic IF coefficients. This algorithm computes the least absolute residuals such that the IF coefficients fit the $F_S(K)$ and $G_S(K)$ simultaneously. Figure (4-8) presents the verification results from the application of the optimization technique described, for each of six aerodynamic IFs to be sought. They are visualized, after optimization, by means of the corresponding real and imaginary parts of Sears' functions as shown in Figure (4-8). Similarly, the extrema of relationships between IFs and FDs for other terms shown in Eq. (4.23) to Eq. (4.27) can also be written as:

$$\min \sum_{l=1}^{m} E_{Lu}^2(a_j, b_j) = \min \sum_{l=1}^{m} \left[\left(\frac{F_{S_{Lu}}}{K_l} - \frac{H_5^*}{2C_L} \right)^2 + \left(\frac{-G_{S_{Lu}}}{K_l} - \frac{H_6^*}{2C_L} \right)^2 \right] \tag{4.32}$$

$$\min \sum_{l=1}^{m} E_{Lw}^2(a_j, b_j) = \min \sum_{l=1}^{m} \left[\left(\frac{F_{S_{Lw}}}{K_l} - \frac{H_1^*}{(C_D + C_L')} \right)^2 + \left(\frac{-G_{S_{Lw}}}{K_l} - \frac{H_4^*}{(C_D + C_L')} \right)^2 \right] \tag{4.33}$$

$$\min \sum_{l=1}^{m} E_{Du}^2(a_j, b_j) = \min \sum_{l=1}^{m} \left[\left(\frac{F_{S_{Du}}}{K_l} - \frac{P_1^*}{2C_D} \right)^2 + \left(\frac{-G_{S_{Du}}}{K_l} - \frac{P_4^*}{2C_D} \right)^2 \right] \tag{4.34}$$

$$\min \sum_{l=1}^{m} E_{Dw}^2(a_j, b_j) = \min \sum_{l=1}^{m} \left[\left(\frac{F_{S_{Dw}}}{K_l} - \frac{P_5^*}{(C_D' - C_L)} \right)^2 + \left(\frac{-G_{S_{Dw}}}{K_l} - \frac{P_6^*}{(C_D' - C_L)} \right)^2 \right] \tag{4.35}$$

$$\min \sum_{l=1}^{m} E_{Mu}^2(a_j, b_j) = \min \sum_{l=1}^{m} \left[\left(\frac{F_{S_{Mu}}}{K_l} - \frac{A_5^*}{2C_M} \right)^2 + \left(\frac{-G_{S_{Mu}}}{K_l} - \frac{A_6^*}{2C_M} \right)^2 \right] \tag{4.36}$$

$$\min \sum_{l=1}^{m} E_{Mw}^2(a_j, b_j) = \min \sum_{l=1}^{m} \left[\left(\frac{F_{S_{Mw}}}{K_l} - \frac{A_1^*}{C_M'} \right)^2 + \left(\frac{-G_{S_{Mw}}}{K_l} - \frac{A_4^*}{C_M'} \right)^2 \right] \tag{4.37}$$

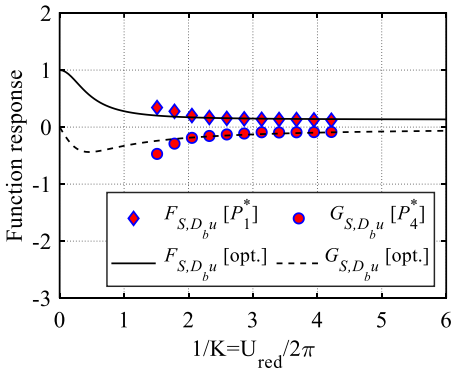

(a) Transfer function between D and u

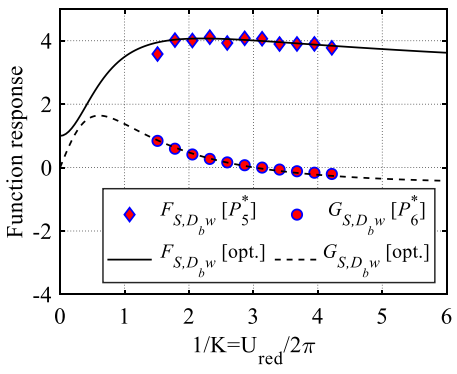

(b) Transfer function between D and w

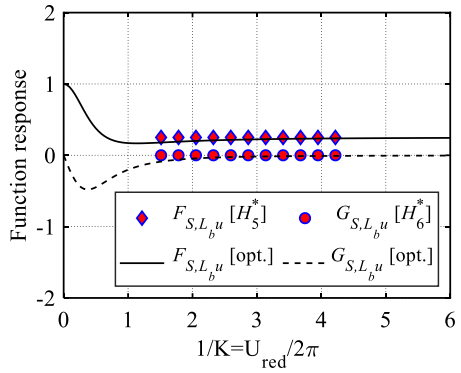

(c) Transfer function between L and u

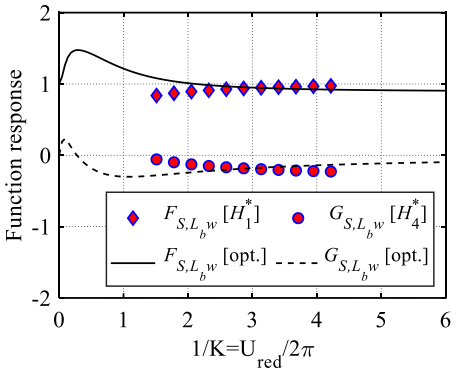

(d) Transfer function between L and w

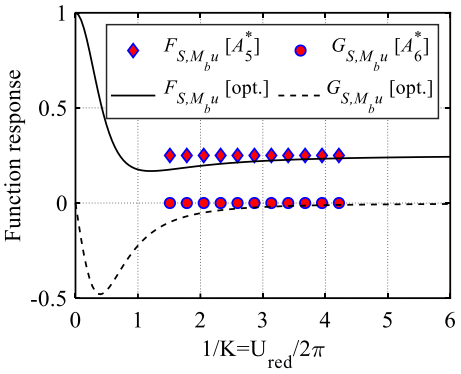

(e) Transfer function between M and u

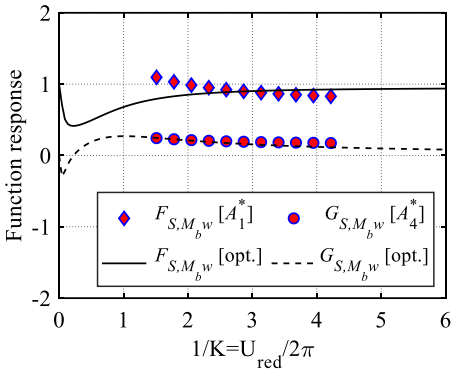

(f) Transfer function between M and w

Figure 4-8 The real and imaginary parts of Sears' functions between aerodynamic wind loads (D: drag, L: lift and M: moment) and fluctuating wind speeds (u: longitudinal and w: vertical) and their optimization for aerodynamic IFs at zero angle of attack of Akashi-Kaikyo bridge deck

4.2.2 Relationship between IFs and FDs for identification of aeroelastic IFs

For the identification of aeroelastic IFs, the relationship between aeroelastic IFs and FDs of the bridge deck are formulated by comparing (1) Fourier transformation of linear self-excited load model derived in Chapter 3 and (2) self-excited force model proposed by Scanlan (1990; 1993).

(1) Fourier transformation of the linear unsteady self-excited load model

Referring to Chapter 3 and taking the Fourier transform of Eq. (3.18) yields the self-excited lift force in frequency-domain such as:

$$L_{se}(K) = \frac{1}{2}\rho\bar{U}^2 B C_L' \left[\left(\phi_{Lp'}(0) + FT\left(\phi'_{Lp'}\right)\right)\frac{p'(K)}{B} + \left(\phi_{Lh'}(0) + FT\left(\phi'_{Lh'}\right)\right)\frac{h'(K)}{B} + \left(\phi_{L\alpha}(0) + FT\left(\phi'_{L\alpha}\right)\right)\alpha(K) \right] \tag{4.38}$$

where FT denotes the Fourier transformation. By replacing $p'(K)$ and $h'(K)$ by $iKp(K)$ and $iKh(K)$, respectively yields the following expressions:

$$L_{se}(K) = \frac{1}{2}\rho\bar{U}^2 B\left[C_L'\left(\phi_{Lp'}(0) + FT\left(\phi'_{Lp'}\right)\right)\frac{iKp(K)}{B} + C_L'\left(\phi_{Lh'}(0) + FT\left(\phi'_{Lh'}\right)\right) \times \frac{iKh(K))}{B} + C_L'\left(\phi_{L\alpha}(0) + FT\left(\phi'_{L\alpha}\right)\right)\alpha(K)\right] \tag{4.39}$$

Similarly, self-excited drag force and pitching moment can also be determined as follows:

$$D_{se}(K) = \frac{1}{2}\rho\bar{U}^2 B\left[C_D'\left(\phi_{Dp'}(0) + FT\left(\phi'_{Dp'}\right)\right)\frac{iKp(K)}{B} + C_D'\left(\phi_{Dh'}(0) + FT\left(\phi'_{Dh'}\right)\right) \times \frac{iKh(K))}{B} + C_D'\left(\phi_{D\alpha}(0) + FT\left(\phi'_{D\alpha}\right)\right)\alpha(K)\right] \tag{4.40}$$

$$M_{se}(K) = \frac{1}{2}\rho\bar{U}^2 B^2\left[C_M'\left(\phi_{Mp'}(0) + FT\left(\phi'_{Mp'}\right)\right)\frac{iKp(K)}{B} + C_M'\left(\phi_{Mh'}(0) + FT\left(\phi'_{Mh'}\right)\right)\frac{iKh(K)}{B} + C_M'\left(\phi_{M\alpha}(0) + FT\left(\phi'_{M\alpha}\right)\right)\alpha(K)\right] \tag{4.41}$$

Writing Eqs. (4.39), (4.40) and (4.41) into a matrix form:

$$\begin{Bmatrix} L_{se}(K) \\ D_{se}(K) \\ M_{se}(K) \end{Bmatrix} = \frac{1}{2}\rho\bar{U}^2 B \times \begin{bmatrix} C_L'\left(\phi_{Lp'}(0) + FT\left(\phi'_{Lp'}\right)\right)iK & C_L'\left(\phi_{Lh'}(0) + FT\left(\phi'_{Lh'}\right)\right)iK & C_L'\left(\phi_{L\alpha}(0) + FT\left(\phi'_{L\alpha}\right)\right) \\ C_D'\left(\phi_{Dp'}(0) + FT\left(\phi'_{Dp'}\right)\right)iK & C_D'\left(\phi_{Dh'}(0) + FT\left(\phi'_{Dh'}\right)\right)iK & C_D'\left(\phi_{D\alpha}(0) + FT\left(\phi'_{D\alpha}\right)\right) \\ BC_M'\left(\phi_{Mp'}(0) + FT\left(\phi'_{Mp'}\right)\right)iK & BC_M'\left(\phi_{Mh'}(0) + FT\left(\phi'_{Mh'}\right)\right)iK & BC_M'\left(\phi_{M\alpha}(0) + FT\left(\phi'_{M\alpha}\right)\right) \end{bmatrix} \begin{Bmatrix} \frac{p}{B} \\ \frac{h}{B} \\ \alpha \end{Bmatrix} \tag{4.42}$$

(2) Scanlan's self-excited force model

By replacing $\dot{h}$, $\dot{p}$ and $\dot{\alpha}$ by $i\omega h$, $i\omega p$ and $i\omega\alpha$, respectively in Eqs. (4.9), (4.10) and (4.11) yields the following expressions:

$$L_{se}(K) = \frac{1}{2}\rho\bar{U}^2 B\left[K^2(iH_1^* + H_4^*)\frac{h}{B} + K^2(iH_2^* + H_3^*)\alpha + K^2(iH_5^* + H_6^*)\frac{p}{B}\right] \tag{4.43}$$

$$D_{se}(K) = \frac{1}{2}\rho\bar{U}^2 B\left[K^2(iP_1^* + P_4^*)\frac{p}{B} + K^2(iP_2^* + P_3^*)\alpha + K^2(iP_5^* + P_6^*)\frac{h}{B}\right] \tag{4.44}$$

$$M_{se}(K) = \frac{1}{2}\rho\bar{U}^2 B^2\left[K^2(iA_1^* + A_4^*)\frac{h}{B} + K^2(iA_2^* + A_3^*)\alpha + K^2(iA_5^* + A_6^*)\frac{p}{B}\right] \tag{4.45}$$

Writing Eqs. (4.43), (4.44) and (4.45) into a matrix form:

$$\begin{Bmatrix} L_{se}(K) \\ D_{se}(K) \\ M_{se}(K) \end{Bmatrix} = \frac{1}{2}\rho\bar{U}^2 B\begin{bmatrix} K^2(iH_5^* + H_6^*) & K^2(iH_1^* + H_4^*) & K^2(iH_2^* + H_3^*) \\ K^2(iP_1^* + P_4^*) & K^2(iP_5^* + P_6^*) & K^2(iP_2^* + P_3^*) \\ BK^2(iA_5^* + A_6^*) & BK^2(iA_1^* + A_4^*) & BK^2(iA_2^* + A_3^*) \end{bmatrix} \begin{Bmatrix} \frac{p}{B} \\ \frac{h}{B} \\ \alpha \end{Bmatrix} \tag{4.46}$$

By comparing the corresponding terms of Eqs. (4.42) and (4.46), the relationships between

FDs and aeroelastic IFs can be obtained such as:

Element (1,1)

$$K(H_5^* - iH_6^*) = C_L' \left(\phi_{Lp'}(0) + FT\left(\phi'_{Lp'} \right) \right) \tag{4.47}$$

Element (1,2)

$$K(H_1^* - iH_4^*) = C_L' \left(\phi_{Lh'}(0) + FT\left(\phi'_{Lh'} \right) \right) \tag{4.48}$$

Element (1,3)

$$K(H_2^* - iH_3^*) = C_L' \left(\phi_{L\alpha}(0) + FT\left(\phi'_{L\alpha} \right) \right) \tag{4.49}$$

Element (2,1)

$$K(iP_1^* - P_4^*) = C_D' \left(\phi_{Dp'}(0) + FT\left(\phi'_{Dp'} \right) \right) \tag{4.50}$$

Element (2,2)

$$K(P_5^* - iP_6^*) = C_D' \left(\phi_{Dh'}(0) + FT\left(\phi'_{Dh'} \right) \right) \tag{4.51}$$

Element (2,3)

$$K(P_2^* - iP_3^*) = C_D' \left(\phi_{D\alpha}(0) + FT\left(\phi'_{D\alpha} \right) \right) \tag{4.52}$$

Element (3,1)

$$K(A_5^* - iA_6^*) = C_M' \left(\phi_{Mp'}(0) + FT\left(\phi'_{Mp'} \right) \right) \tag{4.53}$$

Element (3,2)

$$K(A_1^* - iA_4^*) = C_M' \left(\phi_{Mh'}(0) + FT\left(\phi'_{Mh'} \right) \right) \tag{4.54}$$

Element (3,2)

$$K(A_2^* - iA_3^*) = C_M' \left(\phi_{M\alpha}(0) + FT\left(\phi'_{M\alpha} \right) \right) \tag{4.55}$$

in which $FT(\phi')$ denotes the Fourier transformation of the first derivative of aeroelastic IF. This can be calculated by taking the first derivative of Eq. (4.1), followed by the Fourier transformation, which upon further simplification yields the generalized form of $FT(\phi')$. Similar to the case of aerodynamic IF, the expression for $\phi(0) + FT(\phi')$ can be shown explicitly in terms of indicial response function coefficients such as:

$$\phi(0) + FT(\phi') = 1 - \sum_{j=1}^{N} a_j + \sum_{j=1}^{N} \left(\frac{a_j b_j^2}{b_j^2 + K^2} - iK \frac{a_j b_j}{b_j^2 + K^2} \right) \tag{4.56a}$$

$$F_{Th}(K) = 1 - \sum_{j=1}^{N} a_j + \sum_{j=1}^{N} \left(\frac{a_j b_j^2}{b_j^2 + K^2} \right) \tag{4.56b}$$

$$G_{Th}(K) = -\sum_{j=1}^{N} \left(\frac{a_j b_j K}{b_j^2 + K^2} \right) \tag{4.56c}$$

Eq. (4.57) shows the extremum of the relationships between IFs and FDs derived from the Eq. (4.48) by using the principle of the sum of squares of residuals. Similarly, the expressions for the extremums of other sets of aeroelastic IFs are developed as shown in Eqs. (4.57)−(4.65). In

order to find the aeroelastic IF coefficients, the extremums of relationship functions are optimized by Levenberg-Marquart optimization algorithm such that they yield a minimum squared-error function and aeroelastic IF coefficients fit the $F_{Th}(K)$ and $G_{Th}(K)$ simultaneously. Figure (4-9) presents the verification results from the application of the optimization technique described, for each of the nine aeroelastic IFs to be sought. They are visualized, after optimization, by means of the corresponding real and imaginary parts of the Theodorsen's functions.

$$\min \sum_{l=1}^{m} E_{Lh'}^2(a_j, b_j) = \min \sum_{l=1}^{m} \left[\left(\frac{F_{Th_{Lh'}}}{K_l} - \frac{H_1^*}{C_L'} \right)^2 + \left(\frac{-G_{Th_{Lh'}}}{K_l} - \frac{H_4^*}{C_L'} \right)^2 \right] \tag{4.57}$$

$$\min \sum_{l=1}^{m} E_{Mh'}^2(a_j, b_j) = \min \sum_{l=1}^{m} \left[\left(\frac{F_{Th_{Mh'}}}{K_l} - \frac{A_1^*}{C_M'} \right)^2 + \left(\frac{-G_{Th_{Mh'}}}{K_l} - \frac{A_4^*}{C_M'} \right)^2 \right] \tag{4.58}$$

$$\min \sum_{l=1}^{m} E_{Dh'}^2(a_j, b_j) = \min \sum_{l=1}^{m} \left[\left(\frac{F_{Th_{Dh'}}}{K_l} - \frac{P_5^*}{C_D'} \right)^2 + \left(\frac{-G_{Th_{Dh'}}}{K_l} - \frac{P_6^*}{C_D'} \right)^2 \right] \tag{4.59}$$

$$\min \sum_{l=1}^{m} E_{L\alpha}^2(a_j, b_j) = \min \sum_{l=1}^{m} \left[\left(\frac{F_{Th_{L\alpha}}}{K_l} - \frac{H_2^*}{C_L'} \right)^2 + \left(\frac{-G_{Th_{L\alpha}}}{K_l} - \frac{H_3^*}{C_L'} \right)^2 \right] \tag{4.60}$$

$$\min \sum_{l=1}^{m} E_{M\alpha}^2(a_j, b_j) = \min \sum_{l=1}^{m} \left[\left(\frac{F_{Th_{M\alpha}}}{K_l} - \frac{A_2^*}{C_M'} \right)^2 + \left(\frac{-G_{Th_{M\alpha}}}{K_l} - \frac{A_3^*}{C_M'} \right)^2 \right] \tag{4.61}$$

$$\min \sum_{l=1}^{m} E_{D\alpha}^2(a_j, b_j) = \min \sum_{l=1}^{m} \left[\left(\frac{F_{Th_{D\alpha}}}{K_l} - \frac{P_2^*}{C_D'} \right)^2 + \left(\frac{-G_{Th_{D\alpha}}}{K_l} - \frac{P_3^*}{C_D'} \right)^2 \right] \tag{4.62}$$

$$\min \sum_{l=1}^{m} E_{Lp'}^2(a_j, b_j) = \min \sum_{l=1}^{m} \left[\left(\frac{F_{Th_{Lp'}}}{K_l} - \frac{H_5^*}{C_L'} \right)^2 + \left(\frac{-G_{Th_{Lp'}}}{K_l} - \frac{H_6^*}{C_L'} \right)^2 \right] \tag{4.63}$$

$$\min \sum_{l=1}^{m} E_{Mp'}^2(a_j, b_j) = \min \sum_{l=1}^{m} \left[\left(\frac{F_{Th_{Mp'}}}{K_l} - \frac{A_5^*}{C_M'} \right)^2 + \left(\frac{-G_{Th_{Mp'}}}{K_l} - \frac{A_6^*}{C_M'} \right)^2 \right] \tag{4.64}$$

$$\min \sum_{l=1}^{m} E_{Dp'}^2(a_j, b_j) = \min \sum_{l=1}^{m} \left[\left(\frac{F_{Th_{Dp'}}}{K_l} - \frac{P_1^*}{C_D'} \right)^2 + \left(\frac{-G_{Th_{Dp'}}}{K_l} - \frac{P_4^*}{C_D'} \right)^2 \right] \tag{4.65}$$

4.2.3 Optimization results of aerodynamic and aeroelastic IF coefficients

The optimization results of unknown coefficients (a_j and b_j) of aerodynamic and aeroelastic IFs are listed in Table 4-1. The coefficients of determination denoted by R^2, in addition to the root-mean square error (RMSE) normalized by the maximum value, are also computed for each component of motion-induced vibration as given in Table 4-1. The curve representing P_5^* and P_6^* in Figure (4-9a) show the experimental data with apparently good accuracy of rational function approximation i.e., R^2 of 0.745 and 0.992 for P_5^* and P_6^* derivatives, respectively. These derivatives are responsible for generating $\phi_{Dh'}$ which shows the transient nature (short rise time) as compared to the one proposed by Jones approximation to Wagner function as shown in Figure (4-10a). On the other hand, the fitting curves of P_2^* and P_3^* derivatives shown in Figure (4-9b) exhibit relatively better results for P_2^* than P_3^*, which

indicates that it is difficult to approximate P_2^* than P_3^* derivatives simultaneously in the frequency range covered by the experimental data. Moreover, the IFs coefficients extracted from P_2^* than P_3^* derivatives, which are responsible for $\phi_{D\alpha}$, indicates that low value of b_j and high value a_j result in an IF with a long rise time, such that a very long time series of IF is required before attaining the steady-state solution.

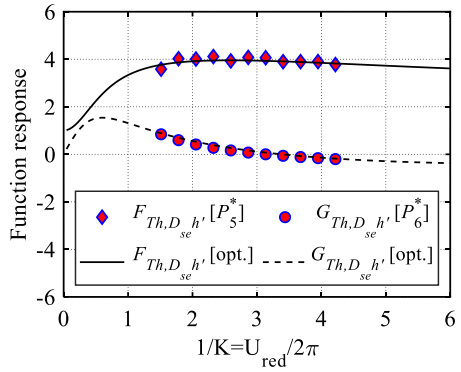

(a) Transfer function between D and h'

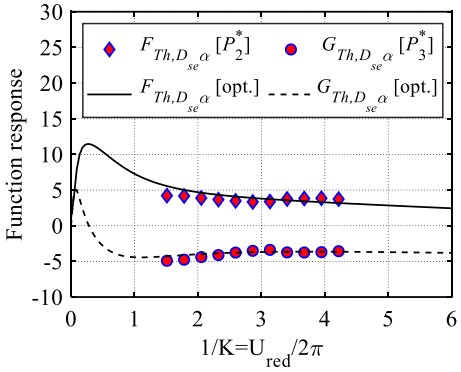

(b) Transfer function between D and α

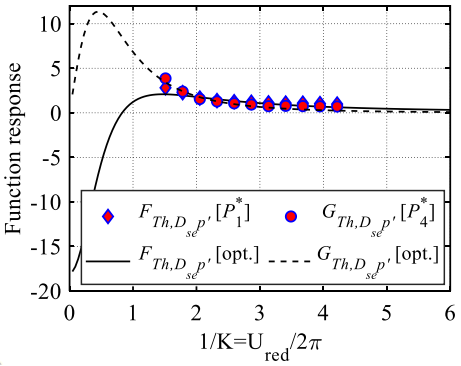

(c) Transfer function between D and p'

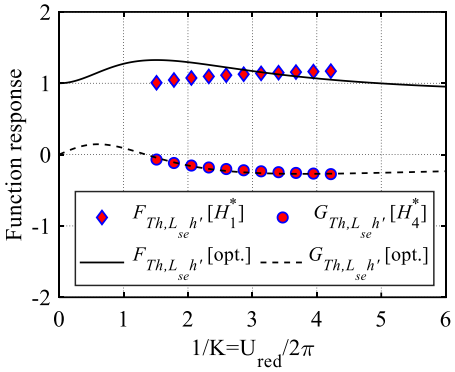

(d) Transfer function between L and h'

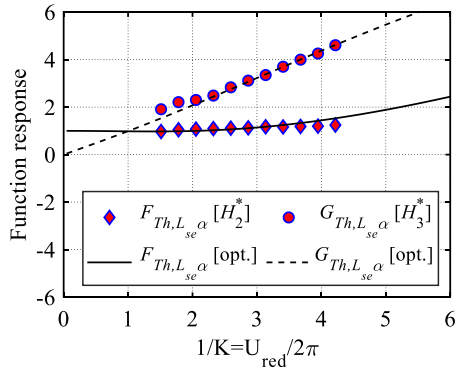

(e) Transfer function between L and α

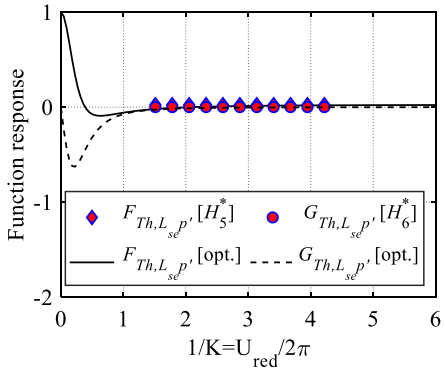

(f) Transfer function between L and p'

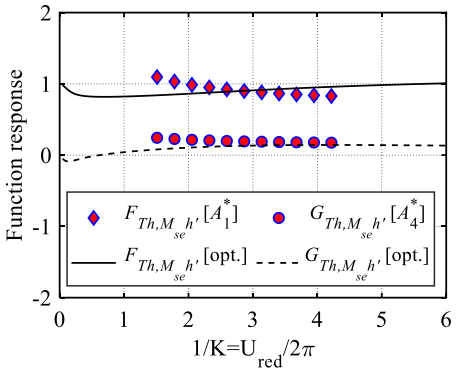

(g) Transfer function between M and h'

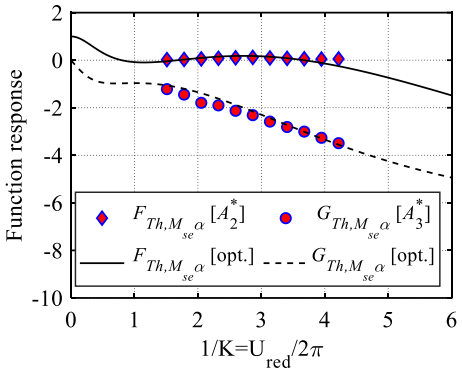

(h) Transfer function between M and α

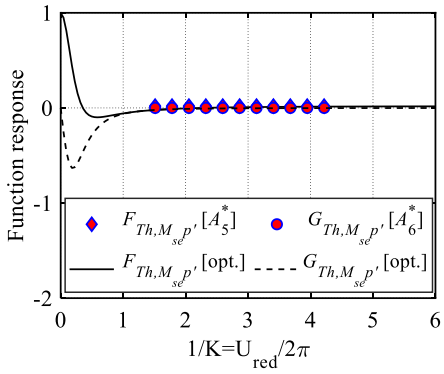

(e) Transfer function between M and p'

Figure 4-9 The real and imaginary parts of Theodorsen's functions between aeroelastic wind loads (D: drag, L: lift and M: moment) and deck motions (h: vertical, p: lateral and α: torsional) and their optimizations for aeroelastic IFs at zero angle of attack of Akashi-Kaikyo bridge deck

Similarly, the identification analysis of aerodynamic IFs shows that N=3 is necessary to characterize the behavior of the Akashi-Kaikyo bridge aerodynamically since no convergence to a stable solution is obtained with $N < 3$. The fitting curves of F_S and G_S for almost all aerodynamic IFs tend to approach quasi-stationary behavior (the feature of a streamlined body) when 1/K increases. These results seem to be adequate and reliable as the optimized F_S and G_S are in good correspondence with the experimental data of FDs. The results of aerodynamic IF coefficients are also tabulated in Table 4-1 along with the coefficient of determination (R^2) and RMSE normalized by the maximum value. Figure (4-11) shows the comparison of aerodynamic IFs of the Akashi-Kaikyo bridge and Kussner function of an airfoil. For the drag-related function, the analysis shows that ψ_{Dw}, ψ_{Lw} and ψ_{Mw} illustrate the overshooting features in a short time period as compared to Kussner function. This discrepancy is owing to the fact that the Akashi-

Table 4-1 Coefficient of determination, R^2, and normalized RMSE for aerodynamic and aeroelastic IF coefficients fitted to FDs at 0 angle of attack for the Akashi-Kaikyo bridge deck

IF	FD	R^2	$RMSE$	a_1	b_1	a_2	b_2	a_3	b_3
ψ_{Du}	P_1^*	0.968	0.057	0.12	0.55	-2.00	0.53	2.75	0.505
	P_4^*	0.855	0.300						
ψ_{Dw}	P_5^*	0.390	1.000	1.158	2.863	-3.92	0.70	0.883	8.32
	P_6^*	0.998	0.252						
ψ_{Lu}	H_5^*	-	0.295	-7.282	0.642	-8.767	0.663	16.79	0.625
	H_6^*	-	0.391						
ψ_{Lw}	H_1^*	0.995	0.060	0.860	1.00	-0.60	0.10	-0.15	1.40
	H_4^*	0.979	0.116						
ψ_{Mu}	A_5^*	-	0.306	-7.315	0.698	-8.793	0.688	16.856	0.663
	A_6^*	-	0.444						
ψ_{Mw}	A_1^*	0.994	0.052	-0.85	1.00	0.25	1.25	0.65	0.05
	A_4^*	0.983	0.093						
$\phi_{Dh'}$	P_5^*	0.745	0.049	-3.386	0.6528	1.473	6.026	0.00	0.00
	P_6^*	0.992	0.050						
$\phi_{D\alpha}$	P_2^*	0.340	1.000	7.00	13.00	10.00	0.80	-12.50	0.08
	P_3^*	0.909	0.115						
$\phi_{Dp'}$	P_1^*	0.805	0.366	16.20	1.25	-35.00	0.57	20.00	0.04
	P_4^*	0.952	0.359						
$\phi_{Lh'}$	H_1^*	0.904	0.050	-0.70	1.20	-0.82	1.40	1.70	2.20
	H_4^*	0.963	0.024						
$\phi_{L\alpha}$	H_2^*	0.809	0.143	-24.0	19.13	0.90	3.10	0.00	0.00
	H_3^*	0.992	0.157						
$\phi_{Lp'}$	H_5^*	-	0.190	-5.749	0.373	-5.758	0.379	12.481	0.347
	H_6^*	-	0.012						
$\phi_{Mh'}$	A_1^*	0.933	0.017	-0.30	4.00	0.20	0.15	0.00	0.00
	A_4^*	0.992	0.003						
$\phi_{M\alpha}$	A_2^*	0.464	0.160	-5.00	3.00	14.50	8.80	1.90	0.60
	A_3^*	0.990	0.139						
$\phi_{Mp'}$	A_5^*	-	0.017	-5.734	0.349	-5.792	0.351	12.506	0.323
	A_6^*	-	0.009						

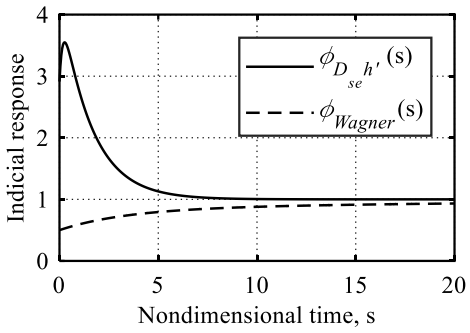
Indicial response
Nondimensional time, s
$\phi_{D_{se}h'}(s)$
$\phi_{Wagner}(s)$

(a)

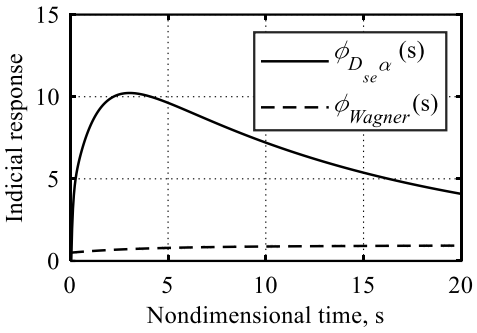
Indicial response
Nondimensional time, s
$\phi_{D_{se}\alpha}(s)$
$\phi_{Wagner}(s)$

(b)

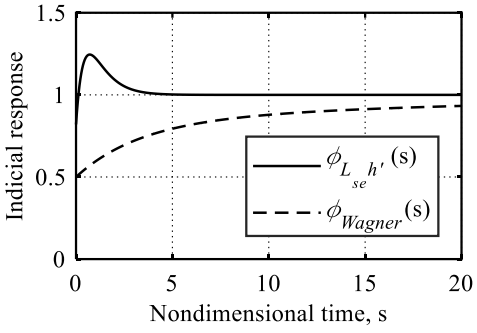
Indicial response
Nondimensional time, s
$\phi_{L_{se}h'}(s)$
$\phi_{Wagner}(s)$

(c)

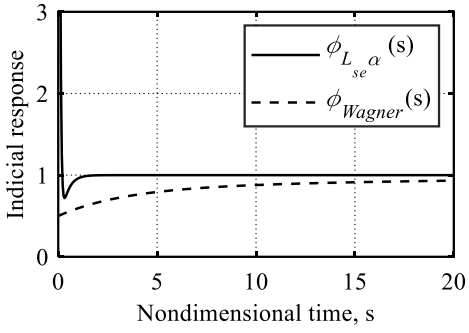
Indicial response
Nondimensional time, s
$\phi_{L_{se}\alpha}(s)$
$\phi_{Wagner}(s)$

(d)

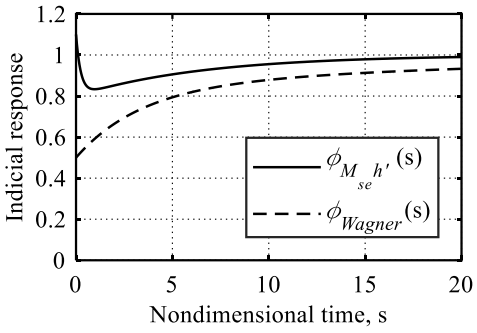
Indicial response
Nondimensional time, s
$\phi_{M_{se}h'}(s)$
$\phi_{Wagner}(s)$

(e)

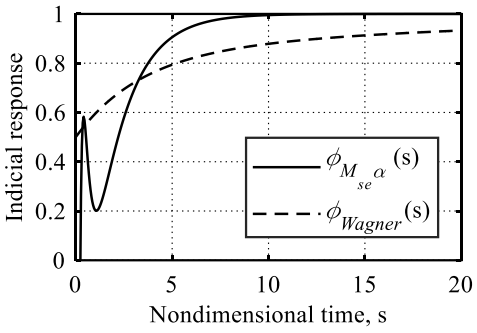
Indicial response
Nondimensional time, s
$\phi_{M_{se}\alpha}(s)$
$\phi_{Wagner}(s)$

(f)

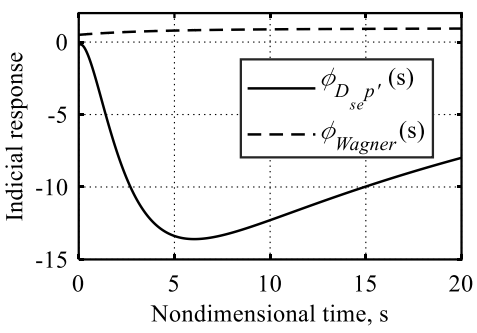
Indicial response
Nondimensional time, s
$\phi_{D_{se}p'}(s)$
$\phi_{Wagner}(s)$

(g)

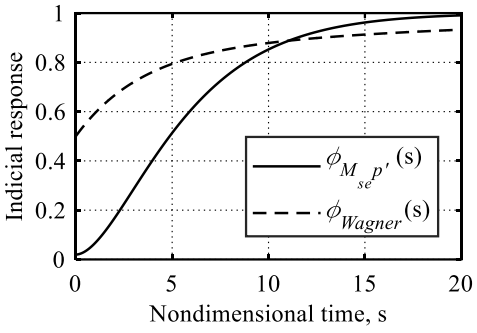
Indicial response
Nondimensional time, s
$\phi_{M_{se}p'}(s)$
$\phi_{Wagner}(s)$

(h)

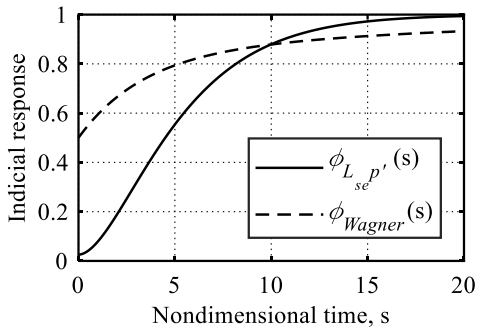

(e)

Figure 4-10 Comparison of first-order aeroelastic IFs of the Akashi-Kaikyo bridge deck and Wagner function of the airfoil at zero angle of attack

Kaikyo bridge deck behaves like a strongly bluff body in the case of buffeting force produced by the vertical fluctuation wind speed. On the other hand, the aerodynamic IFs (ψ_{Du}, ψ_{Lu} and ψ_{Mu}) exhibit the same behavior and/or evolving trend as of Kussner function, which indicates that the effect of longitudinal fluctuating wind speed component (u) in producing the overshooting phenomenon is relatively low as compared to the w in the case of example bridge. The comparison shown in Figure (4-11) also indicates that Kussner function starts from zero and approaches unity as s tends to be infinity, whereas aerodynamic IFs start from different unique values; however, each of them approaches unity asymptotically showing the stationary and steady-state behavior of a linear time-variant (LTI) system. Since the FDs are functions of the varying angles of attack, IFs might be different for a different set of FDs at different angles of attack. For instance, A_2^* is very sensitive to the variation in the angle of attack, thereby the IFs related to A_2^* derivative i.e., $\phi_{M\alpha}$ shows different behavior at a different angle of incidence as shown in Figure (4-12).

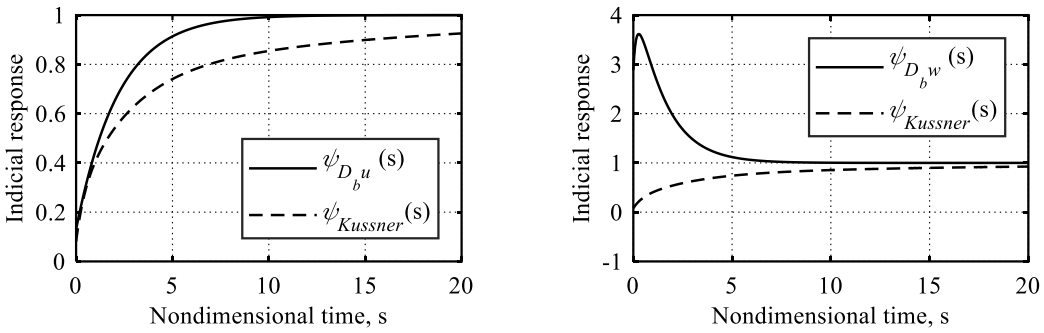

(a) (b)

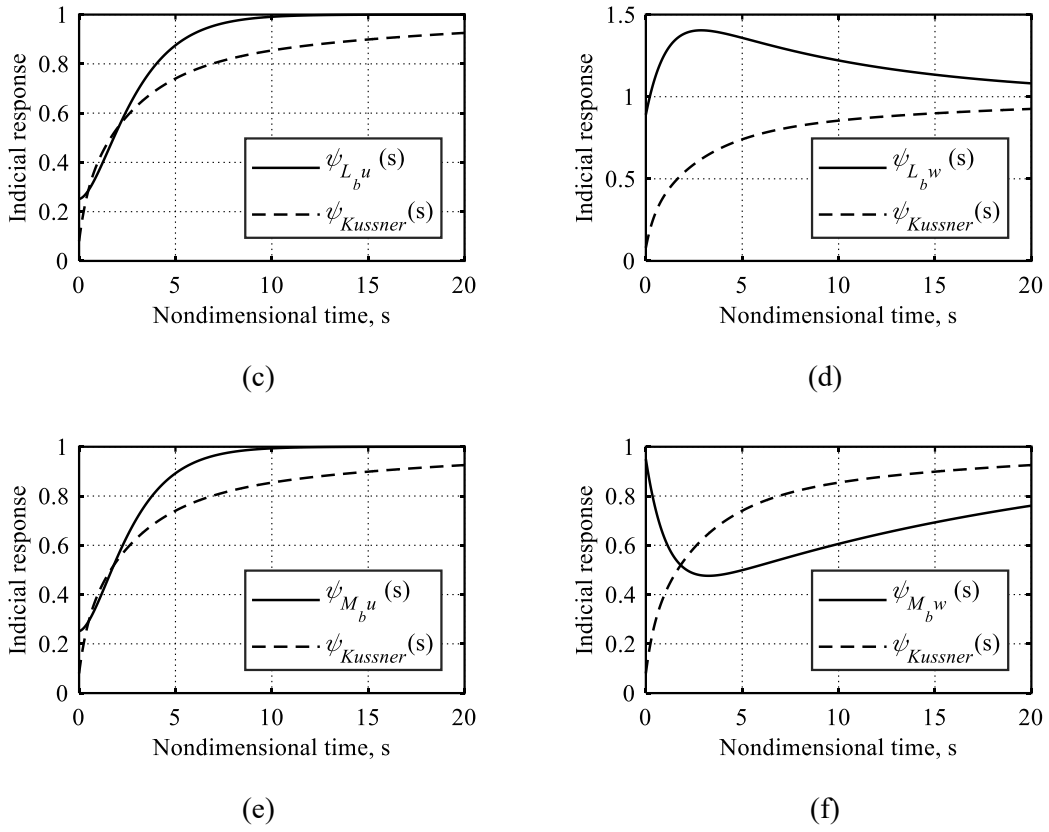

Figure 4-11 Comparison of first-order aerodynamic IFs of the Akashi-Kaikyo bridge deck and Kussner function of airfoil at zero angle of attack

Based on Eq. (3.28), the total response of the NLTI-MIMO system to multidimensional inputs can be obtained if the Volterra kernels up to second-order are known. However, it is not easy to identify the second-order Volterra kernels directly. These second-order kernels can be estimated by idealizing the NLTI-MIMO system as an equivalent block-oriented Wiener model as shown in Figure (4-13) in which $h(\cdot)$ denotes a stable linear dynamical block; $g(\cdot)$ denotes a static nonlinear block (memoryless function), and $z(t)$ is the intermediate state of the system. Then, the second-order kernels can be identified from the parameter estimation of each block using a suitable output static nonlinearity estimator i.e., polynomial function. Following it, a nonlinear system identification technique is employed based on the Wiener model to investigate the relationship between wind speed and bridge response. A second-order polynomial is used since it represents the nonlinear input-output relationship with high accuracy. Thus, the second-order Volterra kernels are computed based on the premise that the order p Volterra kernel of a Wiener system is proportional to the product of p copies of the first-order kernel of its linear element multiplied by the coefficient of a polynomial function raised to power p such as:

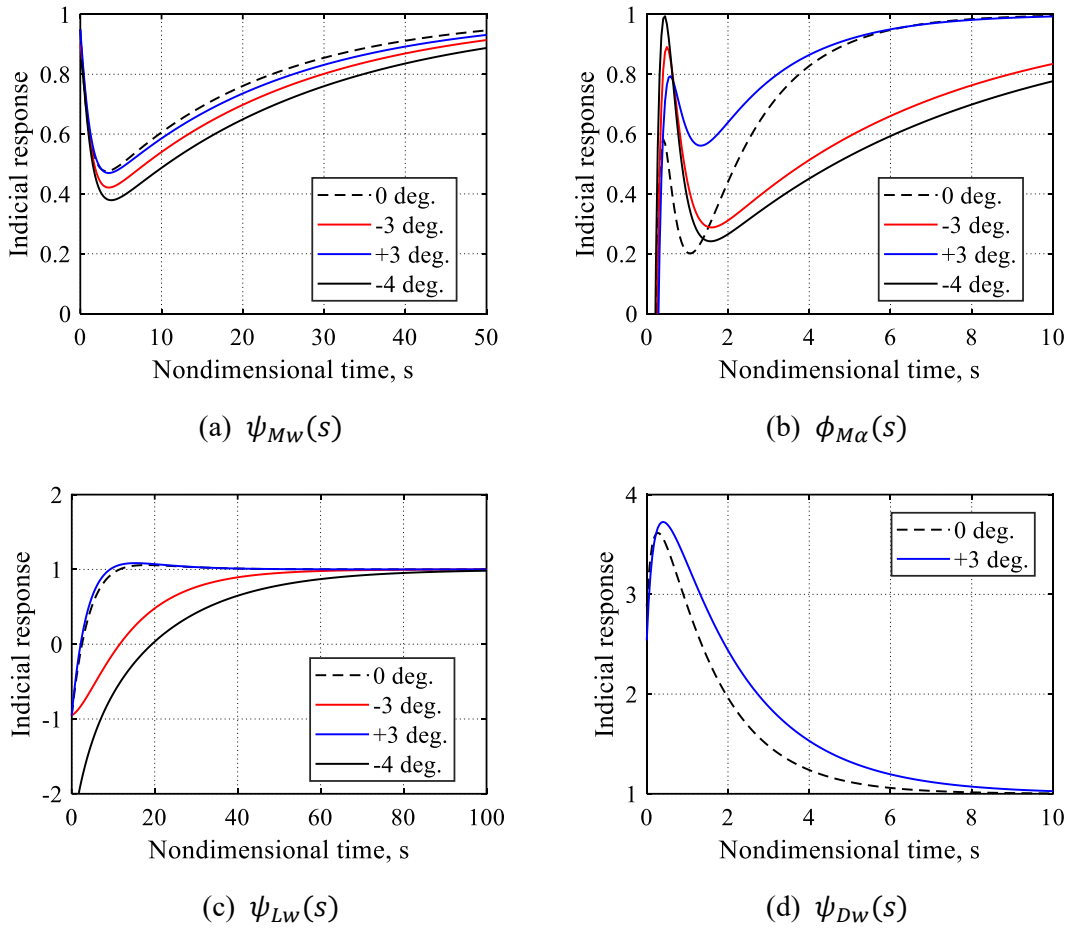

Figure 4-12 The effect of amplitude-dependency of FDs on the indicial response of first-order IFs of the Akashi-Kaikyo bridge deck at varying angles of attack

$$IF_{Qx_1x_2}(\tau_1,\tau_2) = c_2\left(IF_{Qx_1}(\tau_1) \times IF_{Qx_2}(\tau_2)\right) \tag{4.66}$$

where c_2 denotes the coefficient of polynomial term raised to power 2; x_1 and x_2 represent the two copies of inputs (fluctuating component of wind speed and/or bridge deck motion), and Q denotes the output (drag, lift, and pitching moment). The diagonals of each of the second-order kernels ($IF_{Qx_1x_2}$) will be proportional to the first-order IF of the linear subsystem. In addition to that, the effect of $\overline{U_{tv}}$ in the oncoming wind flow on first-and second-order kernels is also taken into account by extending $IF(t)$ to $IF\left(t,\overline{U_{tv}}(\tau)\right)$, where τ is a time scale representing the change in wind-bridge interaction system under non-stationary winds, whereas t shows a time scale in the convection of flow wake describing the fading effects of fluid memory (Hao and Wu 2011). The examples of two second-order kernels (ψ_{Mww} and $\phi_{M\alpha\alpha}$) are shown in Figure (4-14). These bi-dimensional kernels simulate the effects of aerodynamic and aeroelastic nonlinearities on the buffeting response of the bridge.

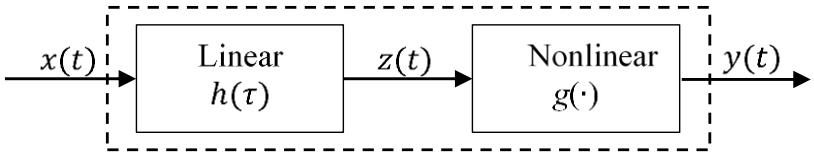

Figure 4-13 Block-structured Wiener model of an NLTI-SISO system

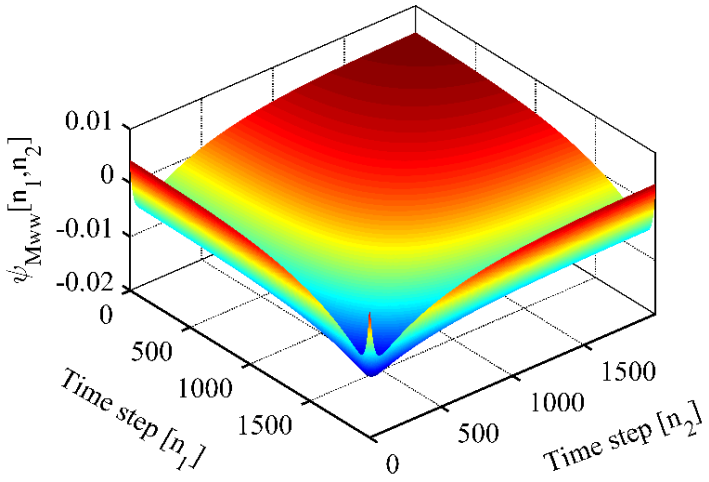

(a) Aerodynamic

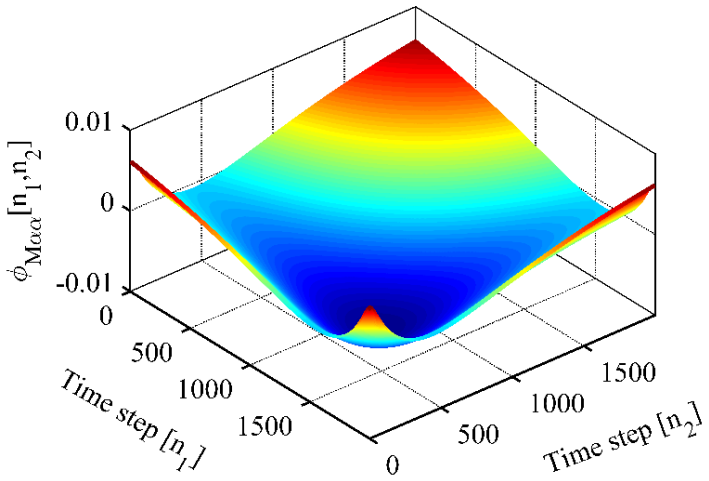

(b) Aeroelastic

Figure 4-14 Second-order kernels of the Akashi-Kaikyo bridge from experimental data

4.3 Artificial Neural Network technique

Artificial Neural Network (ANN) is a nonlinear function approximation tool that can be used to model complex relationships between the input and output of a system. ANNs can be classified based on the type of network architecture, type of connectivity between neurons and the number of layers in the network. The relationship between Volterra models and feedforward multilayer neural networks has been previously studied in a rudimentary manner, and various methods have been proposed for the estimation of Volterra kernels. Wray and Green (1994) introduced a method to calculate Volterra kernels through ANN by training a time-delay feedforward network. This method proposes a generalized expression in terms of the internal parameters of the network equivalent to a Volterra series to identify the higher-order Volterra kernels. Recently, Paula et al. (2019) applied the ANN technique to aerodynamic systems and identified the direct and cross Volterra kernels up to third-order. In this research, a feedforward type Time-delay Neural Network (TDNN) is adopted to derive the equations for the nonlinear dynamic system of wind-bridge interaction by treating it as a MIMO system. The architecture of the network is shown in Figure (4-15). The network consists of an input layer comprising $q + \sum_{i=1}^{q} M_i$ units of input (where q is the number of inputs and M is time-delay per input), a hidden layer with N neurons, and an output layer containing f output units. The input units are assembled into groups corresponding to each input, r_i (for $i = 1,2,...,q$). Each group contains M_i+1 time-delayed samples of ith-input. The lines connecting the ith-input unit and jth-neuron carries a synaptic weight denoted by $w_{ij}(k)$ where the index k represents the incremental time-delay of inputs. The value of k starts from zero in each group and goes up to M_i. The connecting links between jth-neuron and fth-output are weighted by amounts c_{jf}. Such a TDNN applies to a system with q inputs and f outputs. The weighted sum over time-delayed input units is expressed as:

$$x_j[n] = \sum_{i=1}^{q} \sum_{j=1}^{N} \sum_{k=0}^{M_i} w_{ij}[k] r_i[n-k] \tag{4.67}$$

where x_j is the weighted sum in all degrees of freedom representing the convolution of the input signal (r_i) with a finite impulse response (w_{ij}) for a tapped-delay network, and M_i is the measure of memory length of inputs. The basic function of a neuron is to process the weighted sum with a nonlinear activation function ($\varphi(\cdot)$). A bias (b_j) is also attached with each neuron to calibrate synaptic weights associated with each neuron. A typical sigmoidal activation function given by a hyperbolic tangent function is used. The Taylor series expansion of the activation function around the bias yields an equivalent polynomial expression such as:

$$\varphi_j(x_j + b_{1j}) = \sum_{j=1}^{N} \sum_{d=0}^{\infty} \frac{\tanh^{(d)}(b_{1j})}{d!} x_j^d \tag{4.68}$$

where $\tanh^{(d)}$ shows the dth derivative of tanh and b_{1j} is the bias on each neuron in the hidden layer. Expansion of Eq. (4.68) yields Eq. (4.69) such as:

$$\varphi_j(x_j + b_{1j}) = \sum_{j=1}^{N} \left(\frac{\tanh^{(0)}(b_{1j})}{0!} x_j^0 + \frac{\tanh^{(1)}(b_{1j})}{1!} x_j^1 + \frac{\tanh^{(2)}(b_{1j})}{2!} x_j^2 + \frac{\tanh^{(3)}(b_{1j})}{3!} x_j^3 + \cdots \right) \tag{4.69}$$

where $\tanh^{(0)}, \tanh^{(1)}, \tanh^{(2)}$ and $\tanh^{(3)}$ are the zeroth, first, second and third derivative of the tangent hyperbolic function. Eq. (4.69) can be re-written as:

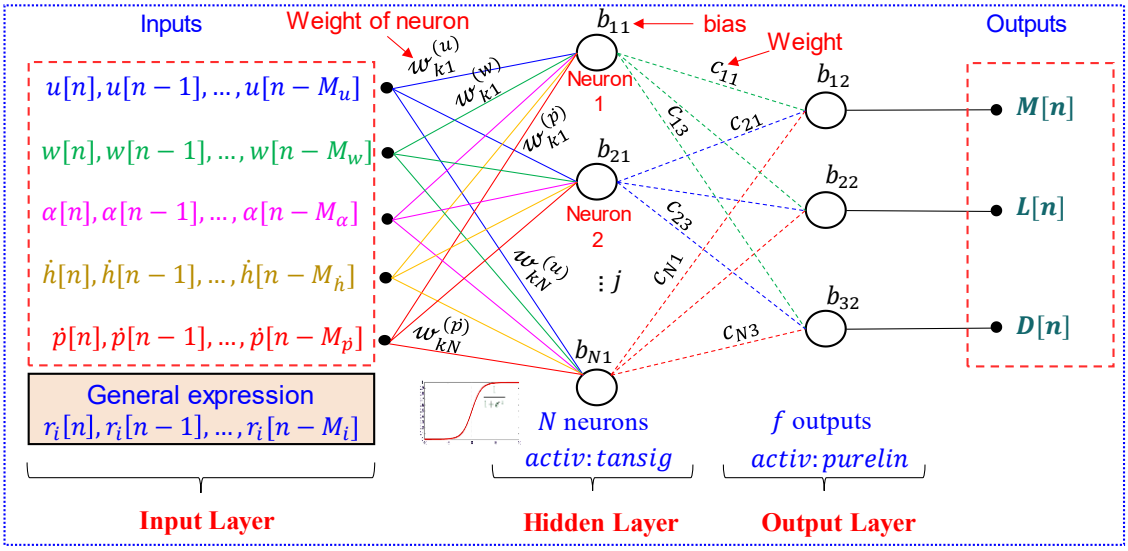

Figure 4-15 The architecture of TDNN with multiple inputs and multiple outputs

$$\varphi_j(x_j + b_{1j}) = \sum_{j=1}^{N} (a_{0j} x_j^0 + a_{1j} x_j^1 + a_{2j} x_j^2 + a_{3j} x_j^3 + \cdots) \tag{4.70}$$

where a_{0j}, a_{1j}, a_{2j} and a_{3j} are the coefficients of polynomial expansion. The calculation of these coefficients requires the determination of the derivatives of tangent hyperbolic functions which can be obtained analytically. By putting the values of x_j and a_{pj} in Eq. (4.70), the activation function can be determined analytically. As wind-bridge interaction is considered to be a weakly nonlinear dynamic system, an equation of activation function can be truncated up to second-order without any issue of convergency (Wu et al. 2013) such as shown in Eq. (4.71). In addition to that, output neurons have linear activation functions, as it is usual for function fitting problems (Paula et al. 2019). A bias of b_{2f} is also attached to each output unit in the output layer accounting for the adjustment of output along with the weighted sum of the inputs to the neuron. Thus, the expression for outputs, denoted by Q_f, can be formulated by linear combination of nonlinear activation function and synaptic weights (c_{jf}) linking the jth-neuron with fth-output

along with the biases associated with each output as written in Eq. (4.72). Insertion of Eq. (4.71) into Eq. (4.72) yields the generalized formulation of non-stationary buffeting forces considering the aerodynamic and aeroelastic nonlinearities up to second-order as shown in Eq. (4.73).

$$\varphi_j(x_j + b_{1j}) = \sum_{j=1}^{N} a_{0j} + \sum_{j=1}^{N} a_{1j}\left(\sum_{i=1}^{q}\sum_{k=0}^{M_i} w_{ij}[k] r_i[n-k]\right) + \sum_{j=1}^{N} a_{2j}\left(\sum_{i=1}^{q}\sum_{k=0}^{M_i} w_{ij}[k] r_i[n-k]\right)^2 \tag{4.71}$$

$$Q_f[n] = \frac{1}{2}\rho\overline{U_{tv}}[n]^2 B\left[\sum_{j=1}^{N} c_{jf}\,.\,\varphi_j(x_j + b_{1j}) + b_{2f}\right] \tag{4.72}$$

$$Q_f[n] = \frac{1}{2}\rho\overline{U_{tv}}[n]^2 B\left[b_{2f} + \sum_{j=1}^{N} c_{jf} a_{0j} + \sum_{i=1}^{q}\left(\sum_{k=0}^{M_i}\left(\sum_{j=1}^{N} c_{jf} a_{1j}\, w_{ij}[k]\right) r_i[n-k]\right) + \sum_{i_1=1}^{q}\sum_{i_2=1}^{q}\left(\sum_{k_1=0}^{M_{i_1}}\sum_{k_2=0}^{M_{i_2}}\left(\sum_{j=1}^{N} c_{jf} a_{2j}\, w_{i_1 j}[k_1] w_{i_2 j}[k_2]\right) r_{i_1}[n-k_1] r_{i_2}[n-k_2]\right)\right] \tag{4.73}$$

In this research, a second-order coupled nonlinear system with five inputs $[u,\ w,\ \alpha,\ \dot{h},\ \dot{p}]$ and three outputs [*M, L, D*] is idealized to elucidate the salient features of kernel identification through TDNN. Following it, Eq. (4.73) can be extended to a nonlinear and non-stationary aerodynamic wind load model by incorporating the five inputs and three outputs as shown in Eq. (4.74), where the terms in parenthesis denote the first-and second-order Volterra kernels (direct and cross). This formulation also considers the aeroelastic effects and the effects of coupling of deck motions and turbulent wind components. Figure (4-16) shows the block diagram of Eq. (4.74), which is named as the Volterra ANN model in this dissertation. It is important to note here that Eq. (4.74) is reminiscent and equivalent to Eq. (3.28); therefore, the corresponding terms shown by the curly brackets in both equations are equated, and first- and second-order IFs are expressed in terms of neural network parameters as shown in Eqs. (4.75a)−(4.75u) . Note that,

- Eq. (4.75a) shows the zeroth-order kernel of Volterra model;
- Eqs. (4.75b)−(4.75f) represent the first-order kernels of Volterra model;
- Eqs. (4.75g)−(4.75k) represent the direct second-order kernels of Volterra model;
- Eqs. (4.75l)−(4.75u) represent the cross second-order kernels of Volterra model;

To estimate these parameters, a feedforward TDNN with $M = 100$ time-delays per input and $N = 10$ neurons is trained with the Bayesian regularization algorithm, and the regularization scheme is performed within the Levenberg Marquardt optimization algorithm. It constrains the

magnitudes of network parameters to yield a smoother response, to prevent the overfitting, and to enhance the generalization properties. The stopping criterion considers the convergence of mean-squared error (MSE) between the predicted and numerically simulated outputs.

$$
\begin{aligned}
Q_f[n] = \frac{1}{2}\rho\overline{U_{tv}}[n]^2 B \Bigg[& b_{2f} + \sum_{j=1}^{N} c_{jf} a_{0j} + \Bigg\{ \sum_{k=0}^{M} \Bigg(\Bigg(\sum_{j=1}^{N} c_{jf} a_{1j}\, w_{uj}[k] \Bigg) u[n-k] + \Bigg(\sum_{j=1}^{N} c_{jf} a_{1j}\, w_{wj}[k] \Bigg) w[n-k] \\
& + \Bigg(\sum_{j=1}^{N} c_{jf} a_{1j}\, w_{\alpha j}[k] \Bigg) \alpha[n-k] + \Bigg(\sum_{j=1}^{N} c_{jf} a_{1j}\, w_{\dot{h}j}[k] \Bigg) \dot{h}[n-k] + \Bigg(\sum_{j=1}^{N} c_{jf} a_{1j}\, w_{\dot{p}j}[k] \Bigg) \dot{p}[n-k] \Bigg) \Bigg\} \\
& + \Bigg\{ \sum_{k_1=0}^{M} \sum_{k_2=0}^{M} \Bigg(\Bigg(\sum_{j=1}^{N} c_{jf} a_{2j}\, w_{uj}[k_1] w_{uj}[k_2] \Bigg) u[n-k_1] u[n-k_2] + \Bigg(\sum_{j=1}^{N} c_{jf} a_{2j}\, w_{wj}[k_1] w_{\mathrm{w}j}[k_2] \Bigg) w[n-k_1] \\
& \times w[n-k_2] + \Bigg(\sum_{j=1}^{N} c_{jf} a_{2j}\, w_{\alpha j}[k_1] w_{\alpha j}[k_2] \Bigg) \alpha[n-k_1]\, \alpha[n-k_2] + \Bigg(\sum_{j=1}^{N} c_{jf} a_{2j}\, w_{\dot{h}j}[k_1] w_{\dot{h}j}[k_2] \Bigg) \dot{h}[n-k_1] \\
& \times \dot{h}[n-k_2] + \Bigg(\sum_{j=1}^{N} c_{jf} a_{2j}\, w_{\dot{p}j}[k_1] w_{\dot{p}j}[k_2] \Bigg) \dot{p}[n-k_1] \dot{p}[n-k_2] + 2 \Bigg(\sum_{j=1}^{N} c_{jf} a_{2j}\, w_{uj}[k_1] w_{wj}[k_2] \Bigg) u[n-k_1] \\
& \times w[n-k_2] + 2 \Bigg(\sum_{j=1}^{N} c_{jf} a_{2j}\, w_{uj}[k_1] w_{\alpha j}[k_2] \Bigg) u[n-k_1] \alpha[n-k_2] + 2 \Bigg(\sum_{j=1}^{N} c_{jf} a_{2j}\, w_{uj}[k_1] w_{\dot{h}j}[k_2] \Bigg) u[n-k_1] \\
& \times \dot{h}[n-k_2] + 2 \Bigg(\sum_{j=1}^{N} c_{jf} a_{2j}\, w_{uj}[k_1] w_{\dot{p}j}[k_2] \Bigg) u[n-k_1] \dot{p}[n-k_2] + 2 \Bigg(\sum_{j=1}^{N} c_{jf} a_{2j}\, w_{wj}[k_1] w_{\alpha j}[k_2] \Bigg) w[n-k_1] \\
& \times \alpha[n-k_2] + 2 \Bigg(\sum_{j=1}^{N} c_{jf} a_{2j}\, w_{wj}[k_1] w_{\dot{h}j}[k_2] \Bigg) w[n-k_1] \dot{h}[n-k_2] + 2 \Bigg(\sum_{j=1}^{N} c_{jf} a_{2j}\, w_{wj}[k_1] w_{\dot{p}j}[k_2] \Bigg) w[n-k_1] \\
& \times \dot{p}[n-k_2] + 2 \Bigg(\sum_{j=1}^{N} c_{jf} a_{2j}\, w_{\alpha j}[k_1] w_{\dot{h}j}[k_2] \Bigg) \alpha[n-k_1] \dot{h}[n-k_2] + 2 \Bigg(\sum_{j=1}^{N} c_{jf} a_{2j}\, w_{\alpha j}[k_1] w_{\dot{p}j}[k_2] \Bigg) \alpha[n-k_1] \\
& \times \dot{p}[n-k_2] + 2 \Bigg(\sum_{j=1}^{N} c_{jl} a_{1j}\, w_{\dot{h}j}[k_1] w_{\dot{p}j}[k_2] \Bigg) \dot{h}[n-k_1] \dot{p}[n-k_2] \Bigg) \Bigg\} \Bigg]
\end{aligned}
\tag{4.74}
$$

$$
\frac{2C_Q \psi_{Qu}[0]}{\overline{U_{tv}}[n]} + \frac{C_Q' \psi_{Qw}[0]}{\overline{U_{tv}}[n]} + C_Q' \phi_{Q\alpha}[0] + \frac{C_Q' \phi_{Q\dot{h}}[0]}{\overline{U_{tv}}[n]} + \frac{C_Q' \phi_{Q\dot{p}}[0]}{\overline{U_{tv}}[n]} = b_{2f} + \sum_{j=1}^{N} c_{jf} a_{0j} \tag{4.75a}
$$

$$
\frac{C_Q' \dot{\psi}_{Qu}[k]}{\overline{U_{tv}}[n]} = \sum_{j=1}^{N} c_{jf} a_{1j}\, w_{uj}[k] \tag{4.75b}
$$

$$
\frac{C_Q' \dot{\psi}_{Qw}[k]}{\overline{U_{tv}}[n]} = \sum_{j=1}^{N} c_{jf} a_{1j}\, w_{wj}[k] \tag{4.75c}
$$

$$
C_Q' \dot{\phi}_{Q\alpha}[k] = \sum_{j=1}^{N} c_{jf} a_{1j}\, w_{\alpha j}[k] \tag{4.75d}
$$

$$
\frac{C_Q' \dot{\phi}_{Q\dot{h}}[k]}{\overline{U_{tv}}[n]} = \sum_{j=1}^{N} c_{jf} a_{1j}\, w_{\dot{h}j}[k] \tag{4.75e}
$$

$$
\frac{C_Q' \dot{\phi}_{Q\dot{p}}[k]}{\overline{U_{tv}}[n]} = \sum_{j=1}^{N} c_{jf} a_{1j}\, w_{\dot{p}j}[k] \tag{4.75f}
$$

$$\frac{2C_Q\dot{\psi}_{Quu}[k_1,k_2]}{\overline{U_{tv}}[n]^2}=\sum_{j=1}^{N}c_{jf}a_{2j}\,w_{uj}[k_1]w_{uj}[k_2] \tag{4.75g}$$

$$\frac{C_Q'\dot{\psi}_{Qww}[k_1,k_2]}{\overline{U_{tv}}[n]^2}=\sum_{j=1}^{N}c_{jf}a_{2j}\,w_{wj}[k_1]w_{wj}[k_2] \tag{4.75h}$$

$$C_Q'\dot{\phi}_{Q\alpha\alpha}[k_1,k_2]=\sum_{j=1}^{N}c_{jf}a_{2j}\,w_{\alpha j}[k_1]w_{\alpha j}[k_2] \tag{4.75i}$$

$$\frac{C_Q'\dot{\phi}_{Q\dot{h}\dot{h}}[k_1,k_2]}{\overline{U_{tv}}[n]^2}=\sum_{j=1}^{N}c_{jf}a_{2j}\,w_{\dot{h}j}[k_1]w_{\dot{h}j}[k_2] \tag{4.75j}$$

$$\frac{C_Q'\dot{\phi}_{Q\dot{p}\dot{p}}[k_1,k_2]}{\overline{U_{tv}}[n]^2}=\sum_{j=1}^{N}c_{jf}a_{2j}\,w_{\dot{p}j}[k_1]w_{\dot{p}j}[k_2] \tag{4.75k}$$

$$\frac{C_Q'\dot{\psi}_{Quw}[k_1,k_2]}{\overline{U_{tv}}[n]^2}=\sum_{j=1}^{N}c_{jf}a_{2j}\,w_{uj}[k_1]w_{wj}[k_2] \tag{4.75l}$$

$$\frac{C_Q'\dot{\phi}_{Qu\alpha}[k_1,k_2]}{\overline{U_{tv}}[n]}=\sum_{j=1}^{N}c_{jf}a_{2j}\,w_{uj}[k_1]w_{\alpha j}[k_2] \tag{4.75m}$$

$$\frac{C_Q'\dot{\phi}_{Qu\dot{h}}[k_1,k_2]}{\overline{U_{tv}}[n]^2}=\sum_{j=1}^{N}c_{jf}a_{2j}\,w_{uj}[k_1]w_{\dot{h}j}[k_2] \tag{4.75n}$$

$$\frac{C_Q'\dot{\phi}_{Qu\dot{p}}[k_1,k_2]}{\overline{U_{tv}}[n]^2}=\sum_{j=1}^{N}c_{jf}a_{2j}\,w_{uj}[k_1]w_{\dot{p}j}[k_2] \tag{4.75o}$$

$$\frac{C_Q'\dot{\phi}_{Qw\alpha}[k_1,k_2]}{\overline{U_{tv}}[n]}=\sum_{j=1}^{N}c_{jf}a_{2j}\,w_{wj}[k_1]w_{\alpha j}[k_2] \tag{4.75p}$$

$$\frac{C_Q'\dot{\phi}_{Qw\dot{h}}[k_1,k_2]}{\overline{U_{tv}}[n]^2}=\sum_{j=1}^{N}c_{jf}a_{2j}\,w_{wj}[k_1]w_{\dot{h}j}[k_2] \tag{4.75q}$$

$$\frac{C_Q'\dot{\phi}_{Qw\dot{p}}[k_1,k_2]}{\overline{U_{tv}}[n]^2}=\sum_{j=1}^{N}c_{jf}a_{2j}\,w_{wj}[k_1]w_{\dot{p}j}[k_2] \tag{4.75r}$$

$$\frac{C_Q'\dot{\phi}_{Q\alpha\dot{h}}[k_1,k_2]}{\overline{U_{tv}}[n]}=\sum_{j=1}^{N}c_{jf}a_{2j}\,w_{\alpha j}[k_1]w_{\dot{h}j}[k_2] \tag{4.75s}$$

$$\frac{C_Q'\dot{\phi}_{Q\alpha\dot{p}}[k_1,k_2]}{\overline{U_{tv}}[n]}=\sum_{j=1}^{N}c_{jf}a_{2j}\,w_{\alpha j}[k_1]w_{\dot{p}j}[k_2] \tag{4.75t}$$

$$\frac{C_Q'\dot{\phi}_{Q\dot{h}\dot{p}}[k_1,k_2]}{\overline{U_{tv}}[n]^2}=\sum_{j=1}^{N}c_{jl}a_{1j}\,w_{\dot{h}j}[k_1]w_{\dot{p}j}[k_2] \tag{4.75u}$$

Figure (4-17) depicts the comparison between the real bridge vibration and predicted signals after completion of the TDNN training, generalization testing, and validation. The training and testing results demonstrate that the neural network provides a good match to the real vibration of the bridge deck under typhoon-induced non-stationary winds. The validation results highlight the network performance in predicting the signals different from those used for training. Such results ensure that the TDNN satisfactorily represents the MIMO system.

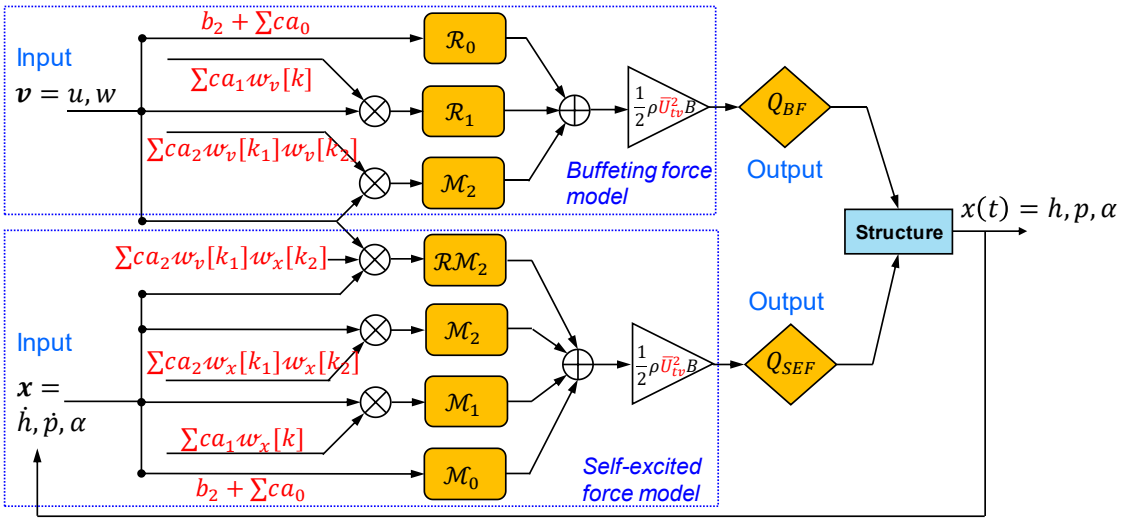

Figure 4-16 Block diagram of the Volterra ANN model

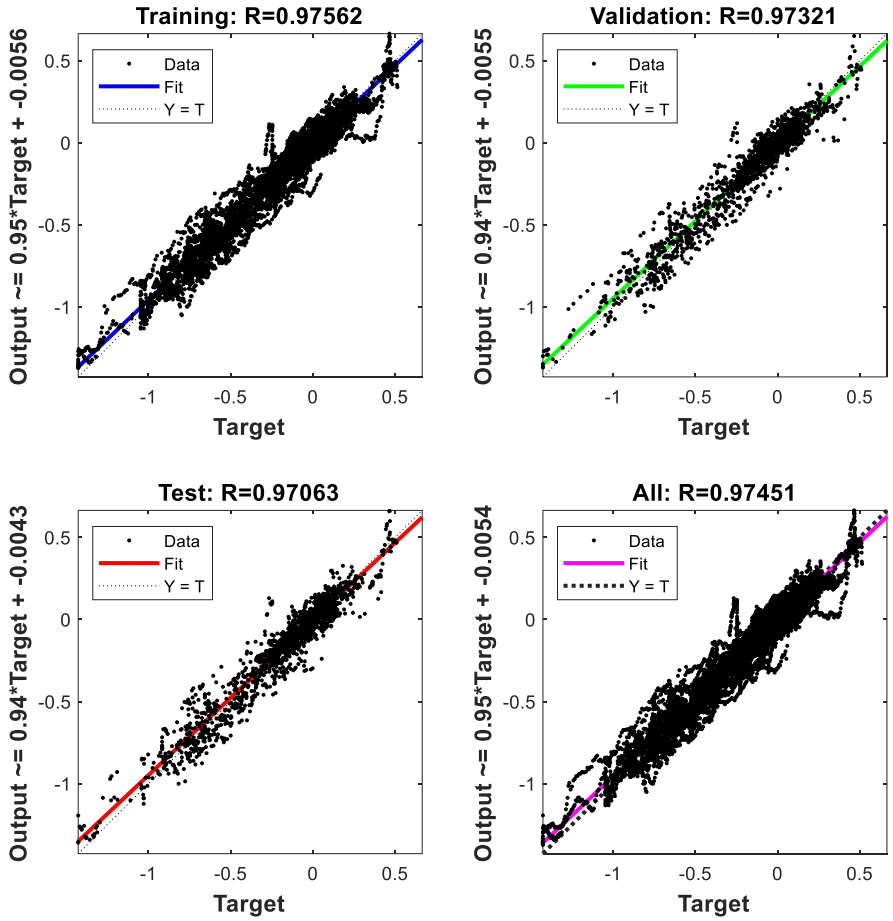

Figure 4-17 Training, validation, and testing results of TDNN compared with bridge vibration

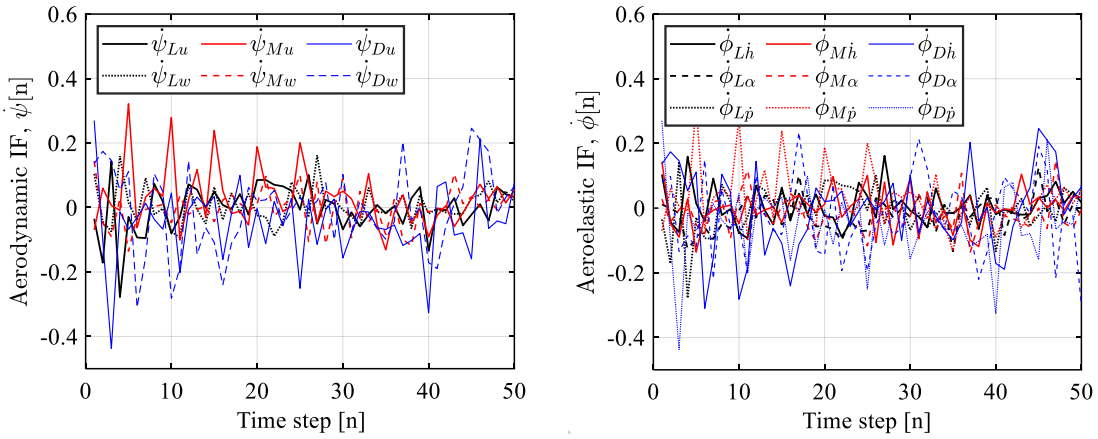

(a) Aerodynamic (b) Aeroelastic

Figure 4-18 First-order kernels of Akashi-Kaikyo bridge via ANN

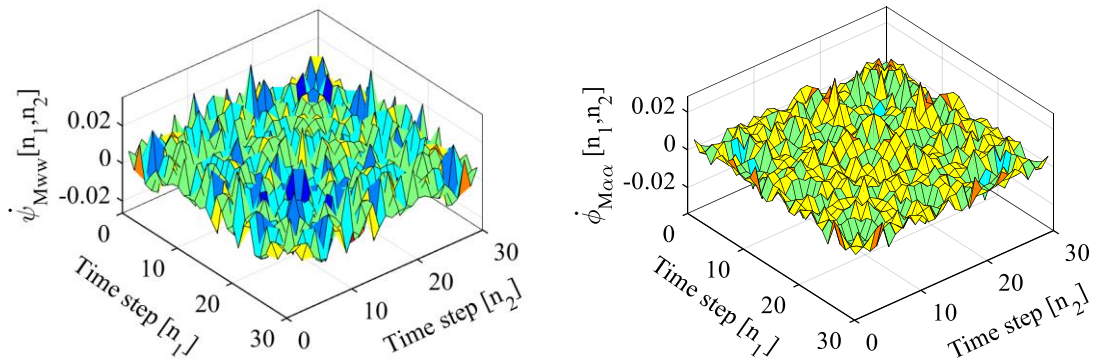

(a) Aerodynamic (b) Aeroelastic

Figure 4-19 Second-order kernels of Akashi-Kaikyo bridge via ANN

The next step is to extract the Volterra kernels from the TDNN internal parameters. Eqs. (4.75a)−(4.75u) are utilized to determine aerodynamic and aeroelastic IFs up to second-order through the neural network approach. Figure (4-18) shows the first-order direct kernels related to each input signal in which the asymmetry of the system can be observed from the differences between kernels. Figure (4-19) presents two second-order Volterra kernels ($\dot{\phi}_{Mww}$ and $\dot{\phi}_{M\alpha\alpha}$) as an example. The identified second-order direct and cross kernels also indicate the asymmetry of the system. Once the Volterra kernels are identified, they can be used as a reduced order model (ROM) to predict the system dynamics.

CHAPTER 5: SIMULATION OF NON-STATIONARY WIND FIELDS

This chapter focuses on the simulation of artificial non-stationary wind fields around the bridge site. The conventional buffeting analysis is performed based on the assumption of stationary and gaussian winds. However, typhoon-induced winds are highly non-synoptic and need to be modelled and analysed as a non-stationary process. In this chapter, the non-stationary wind field is simulated based on the typhoon data of wind speed time history by extending the conventional power spectral density (PSD) method to the evolutionary power spectral density (EPSD) approach. Two typhoon events herein are considered in order to study the transient effects of non-synoptic winds on the buffeting response of the bridge. First, the measured data of typhoon-induced wind speed time-history is divided into wind records of each 10 min time-history. Then, the stationarity test is performed by using the mean of wind records based on the reverse arrangement (RA) test to separate the non-stationary and stationary wind records. The time-varying mean wind speed is extracted from each wind record based on the empirical mode decomposition (EMD) method. Subsequently, the EPSD is evaluated for a 10 min wind record involving the maximum wind speed at the center of the main span of the bridge. Owing to the lack of measured data of wind speed time-history at each node of the bridge deck, the measured EPSD at the center node of the main span is assumed to be uniform along the bridge length. At last, based on this assumption, the non-stationary longitudinal fluctuating wind speed is simulated by using an unconditional simulation technique which utilizes the EPSD instead of conventional PSD in the simulation algorithm. The effect of coherence between wind fluctuations along the bridge length is also taken into account in the wind simulation. The results of this simulation can be used to compute the non-stationary wind loads on the bridge deck, which can produce the time-varying buffeting response. Simulation results also showed that the conventional PSD theory cannot deal with the non-stationary features existing in the real typhoon-induced non-synoptic winds; therefore, an extension of the spectral theory to the evolutionary power spectral theory is indispensable to predict the buffeting response of long-span bridges accurately.

5.1 Introduction

Air movement generated by the atmospheric pressure difference at various areas of the earth produces the global wind circulations. Air movement usually includes different temporal and spatial scales which may enlarge tremendously and form the cyclones. Tropical cyclones are intense cyclonic storms, usually occur over the tropical oceans, especially in late summer and

early autumn. These cyclones are named differently in different parts of the world i.e., hurricane in the Caribbean, cyclones in off the northwest coast of Australia, and typhoons in the South China Sea. In general, a fully mature typhoon has a three-dimensional vortex structure, with a horizontal dimension for several hundred kilometers and a vertical dimension of the order of ten kilometers. The central part of a typhoon is known as the eye which comprises relatively cloudless and quiescent air and the extreme winds occur just outside the eye wall, showing different wind characteristics as compared to monsoons and gales.

It is widely recognized that the long-span bridges built in the typhoon prone regions are inevitably vulnerable to typhoon-induced non-synoptic winds. These structures must be designed to resist such typhoon winds during their service lives. In the current design practice, the assumption of stationary wind flow is often made in the wind simulation for performing the buffeting analysis of bridges. The assumption of stationary processes may not be valid for extreme wind events such as typhoons, downbursts, and tornados because of their vortex or convective origins. Therefore, the response analysis of bridges under such extreme winds is a challenging issue and needs advanced research, which requires the accurate measurement of typhoon-induced winds in ABL. However, in many cases, there are only limited field measurement data available at a bridge site and the precise estimation of typhoon wind characteristics at the bridge site cannot be performed. To circumvent this limitation, many researchers (Chow 1970; Vickery and Twisdale 1995; Meng et al. 1995) investigated the modelling of typhoon wind fields based on different simulation techniques i.e., the Monte Carlo simulation method, along with the typhoon wind field model and statistical distributions of wind data to predict the design wind speeds for bridges.

Generally, the non-stationary winds are characterized by time-varying spectra instead of constant mean spectra. Numerous methods have been developed to explain time-varying spectra, such as evolutionary spectra (Priestley 1965), short-time Fourier transform (Zhan et al. 2006), and empirical mode decomposition-based spectra (Haung et al. 2016). Among all these approaches, the evolutionary power spectral density (EPSD) function explicates the evolution of the frequency content in the frequency- and time-domain and known as an extension of the power spectra density to the non-stationary process. Specifically, it facilitates the simulation of non-stationary processes by the spectral representation method (SRM) and the analysis of structural response under the non-stationary wind. In that context, Xu and Chen (2004) characterized typhoon wind as a time-varying mean wind speed plus stationary fluctuating component. Hu et al. (2011) further characterized typhoon wind as the time-varying mean wind speed plus non-stationary fluctuating component featured by EPSD. Peng et al. (2018) examined the effect of time-varying coherence on the alongwind tall building response by EPSD-based time-varying coherence function. The research presented that time-varying coherence function may cause a larger response as compared to the corresponding time-invariant coherence function.

5.2 Description of typhoon events

In this research, two typhoons are considered including (1) TY9807 and (2) 2018TY20. The data of these typhoons were measured by the anemometers installed at the main span of the Akashi-Kaikyo bridge. The descriptions of both typhoons are given in the subsequent subsections.

5.2.1 Typhoon TY9807

On September 24, 1998, a typhoon, known as TY9807, hit Akashi-Kaikyo bridge, west-central Japan between 11:53~16:31. The wind speed time history data of typhoon is recorded continuously for more than 4 hours by a set of few anemometers positioned along the bridge length just above the deck level as a part of the investigation done by Honshu-Shikoku Bridge Authority (2001). The mean and maximum wind speeds recorded by anemometers at the center of the main span were 32 m/s and 40 m/s for a 10 min duration, respectively, both of which were recorded at a height of 108 m above sea level. All anemometers were attached to the light poles of the bridge at a height of 8 m from bridge girder to avoid the disturbance of the incoming wind flow due to the bridge deck. Figure (5-1) shows the configuration of sensors on the Akashi-Kaikyo bridge. The sampling frequency was 20 Hz. As wind data was recorded only at a few locations, it is not enough to simulate the buffeting response of the bridge accurately. Therefore, wind speed time-history recorded at the center of the main span of the bridge is used in this research for the simulation of artificial non-stationary wind fields of TY9807 for the entire bridge.

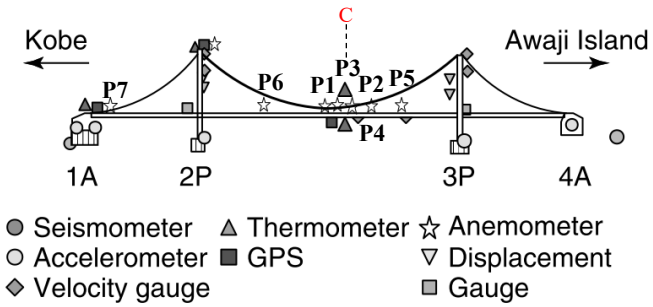

Figure 5-1 Akashi-Kaikyo bridge monitoring system and locations of 7-anemometers on deck

5.2.2 Typhoon 2018TY20

In 2018, another big typhoon, known as 2018TY20, hit Akashi-Kaikyo bridge that started at 2:21 p.m. on August 23rd and ended at 7:33 a.m. on August 24th. The maximum wind speed recorded by anemometer at the center of the main span was 51 m/s for a 10 min duration with a sampling frequency of 20 Hz. Owing to the limited number of anemometers installed along the

bridge deck, the wind speed time history data recorded at the center of main is used to simulate the non-stationary wind speed time history of 2018TY20 for the entire bridge.

5.3 Reverse arrangement test to check the stationarity of wind field

To bifurcate the wind records into stationary and non-stationary categories, the stationarity test is conducted on each 10 min wind record by employing a reverse arrangement (RA) test as proposed by Bendat and Piersol (2010). The RA test involves calculating the number of times, beginning with the first data point x_1 in the digitized input signal x_i, that each subsequent point (x_2, x_3, …,x_N) is less than x_1. Each such inequality count is called as a reverse arrangement. In other words, this test provides an evaluation of randomness and is useful to elucidate the underlying trends in wind data. The wind record is considered as stationary in the desired level of significance if the number of runs falls within the acceptance range, otherwise, it is treated as non-stationary. A general definition of reversals is as follows:

$$h_{ij} = \begin{cases} 1, & \text{if } x_i > x_j \\ 0, & \text{otherwise} \end{cases} \tag{5.1a}$$

Then,

$$\text{Reversal} = \sum_{i=1}^{N-1} A_i \tag{5.1b}$$

where

$$A_i = \sum_{j=i+1}^{N} h_{ij} \tag{5.1c}$$

If the sequence of N observations is independent observations of the same random variable, then the number of reversals is also a random variable, with mean $\mu_{reversal}$ and variance $\sigma_{reversal}$ values as follows:

$$\mu_{reversal} = \frac{N(N-1)}{4} \tag{5.2a}$$

$$\sigma_{reversal} = \frac{N(2N+5)(N-1)}{72} \tag{5.2b}$$

The RA test results of 5 anemometers installed at the main span of the bridge are presented in Figure (5-2) for typhoon TY9807, which shows that the wind records between 12:43~15:41 failed to be within the 5% of bound limits, whereas the wind records in the beginning and at the end show a stationary behavior. The stationarity test results of anemometer P3 is also shown in Figure (5-3), which indicates that the reversals for the measurement data of 10 min wind records in the time range of 11:53~12:43 are equal to lower bound value i.e., zero explicating that the wind records are strongly stationary in this time range, whereas the wind records between

12:43~15:41 failed to be within the 5% of bound limits elucidating that the wind records are strongly non-stationary in this time range after which the wind records again exhibit the stationary behavior. Similarly, the stationarity test is performed on typhoon 2018TY20 by dividing the full data of wind speed time history into 10 min wind records. The mean of each 10 min wind record is calculated, and the RA test is performed accordingly. Figure (5-4) shows the RA test results of anemometer P3 for typhoon 2018TY20, which indicates that the wind exhibits non-stationary behavior between 17:07~5:07, whereas it shows the stationary nature in the beginning and at the end of typhoon 2018TY20.

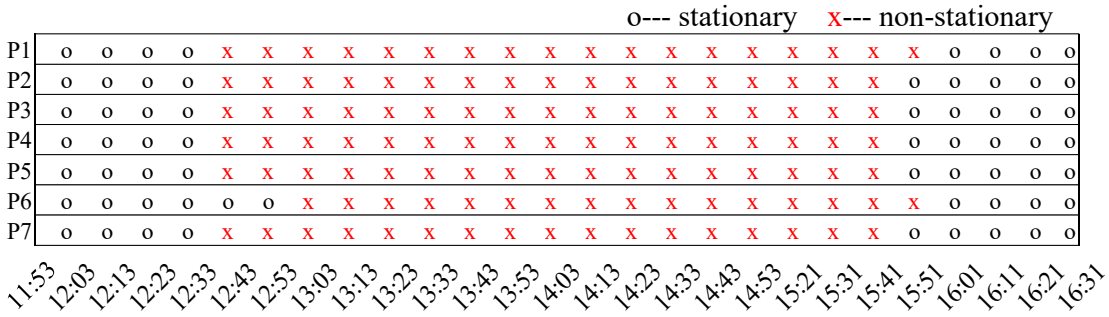

Figure 5-2 Stationarity test on 10 min recordings of TY9807

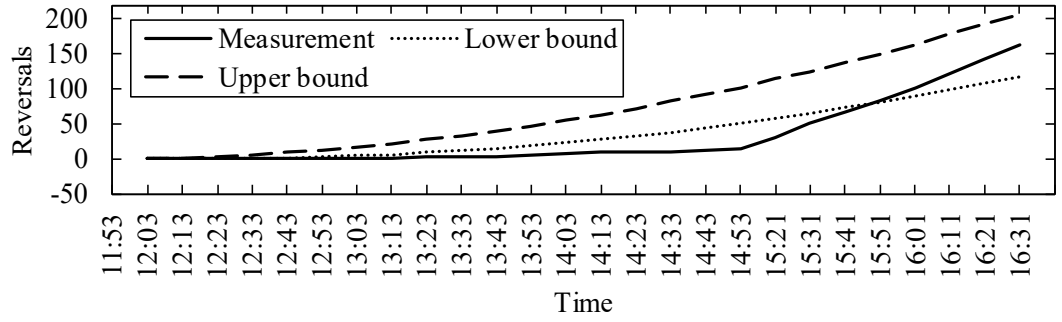

Figure 5-3 Stationarity test of anemometer P3 on 10 min wind records of TY9807

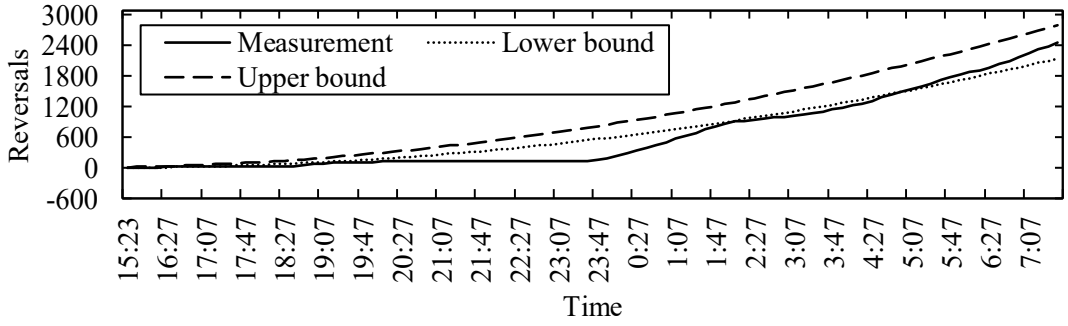

Figure 5-4 Stationarity test of anemometer P3 on 10 min wind records of 2018TY20

5.4 Empirical mode decomposition

It is a normal practice to decompose the wind speed time history into its mean and fluctuating components by considering a certain averaging time interval for performing the buffeting analysis. The constant mean wind speed is simply calculated through the arithmetic to mean for a 10 min duration, whereas the time-varying mean wind speed is evaluated by applying an empirical mode decomposition (EMD) method developed by Huang et al. (1998). The EMD mainly extracts the time-varying mean wind speed from the recorded wind speed data. According to the EMD method, the filtered lowest-frequency wind component signifies the time-varying mean, and the summation of the remaining filtered wind components denotes the fluctuating component (Haung et al. 2016; Xu and Chen 2004). Alternatively, using the EMD, any complicated time history can be decomposed into a finite number of intrinsic mode functions (IMF) using the sifting process. This decomposition is valid to the nonlinear and non-stationary processes. To perform the sifting process, the following steps are usually utilized (Huang et al. 1998; Rilling et al. 2003):

1. Find local maxima and minima for a non-stationary wind speed time history $U(t)$ to construct the upper and lower envelopes denoted by $s_+(t)$ and $s_-(t)$, respectively by using a cubic spline line.
2. The mean of the two envelopes is then calculated for ith iteration denoted by $m_{k,i}(t)$,
   $m_{k,i}(t) = \frac{1}{2}[s_+(t) + s_-(t)]$ (5.3)
3. The difference between the original time history and the mean value is called the first IMF, denoted by $c_1(t)$, if it satisfies the two conditions: (i) within the data range, the number of extrema and the number of zero-crossings are equal or differ by one only; (ii) at any point, the mean value of the envelope represented by the local maxima and the envelope represented by the local minima is zero.
4. The resulting IMF denotes a simple oscillatory mode as a counterpart to the simple harmonic function, but it is quite general and adopts a Hilbert transform. The difference between $U(t)$ and $c_1(t)$ is treated as a new time history and subjected to the same sifting process, giving the second IMF, $c_2(t)$. The EMD procedure continues until the residual becomes less than a predetermined value of consequence, or the residual becomes a monotonic function. In general, the time-varying mean can be expressed as the sum of the last a few IMFs plus the final residual. The original time history $U(t)$, containing the sinusoidal waves with different amplitudes and frequency values, is finally expressed as the sum of the IMFs plus the final residual:
   $$U(t) = \sum_{j=1}^{N} c_j(t) + r(t)_N \quad (5.4)$$

where N is the number of IMF components and $r(t)_N$ is the final residual which is defined as the time-varying mean wind speed $\overline{U_{tv}}(t)$ with frequency contents less than 1/600 Hz. The flowchart of EMD is shown in Figure (5-5).

Based on that, the wind speed time history of typhoon TY9807 is divided into 10 min wind records between 11:53~16:31. The maximum wind speed was observed during 14:13~14:23 at the center of main span of the bridge. Figure (5-6) shows the full wind speed time history of typhoon TY9807 along with the constant and time-varying means based on the averaging time of 10 min. Typhoon TY9807 reached its peak wind speed at 14:23 after which it dropped transiently. Figure (5-7) also highlights missing data around 14:53 due to the malfunction of the structural health monitoring (SHM) system. The wind record between 14:13~14:23 is also shown in Figure (5-7), indicating the constant mean of 32 m/s and time-varying mean in the range of 30.5 m/s to 36 m/s. Congruently, the time-varying mean wind speed is extracted from the original non-stationary wind speed time-history of typhoon 2018TY20 by using the EMD method. Figure (5-8) shows the wind speed time history of 2018TY20 as well as the constant and time-varying means measured based on the averaging time of 10 min, which elucidates that the constant mean remains the same, whereas time-varying mean changes continuously during an interval of 10 min wind. The maximum wind speed of typhoon 2018TY20 was recorded to be 51 m/s between 23:17~23:27 on August 23rd as shown in Figure (5-9).

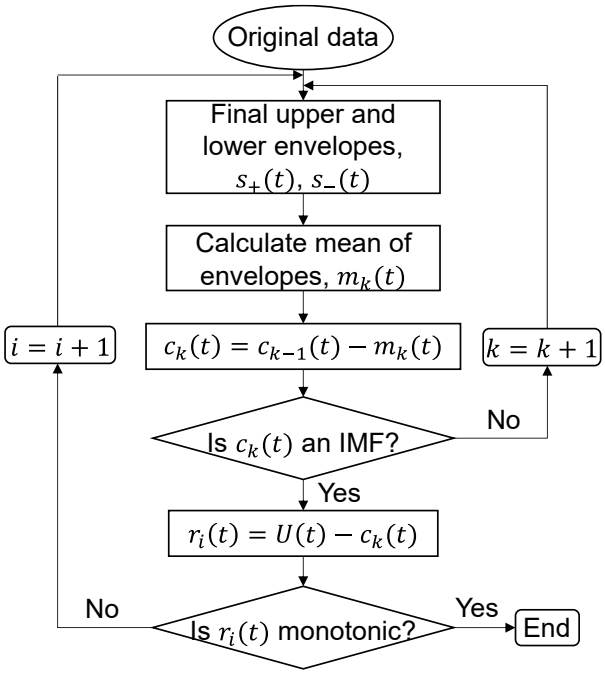

Figure 5-5 Flowchart of empirical mode decomposition estimation process

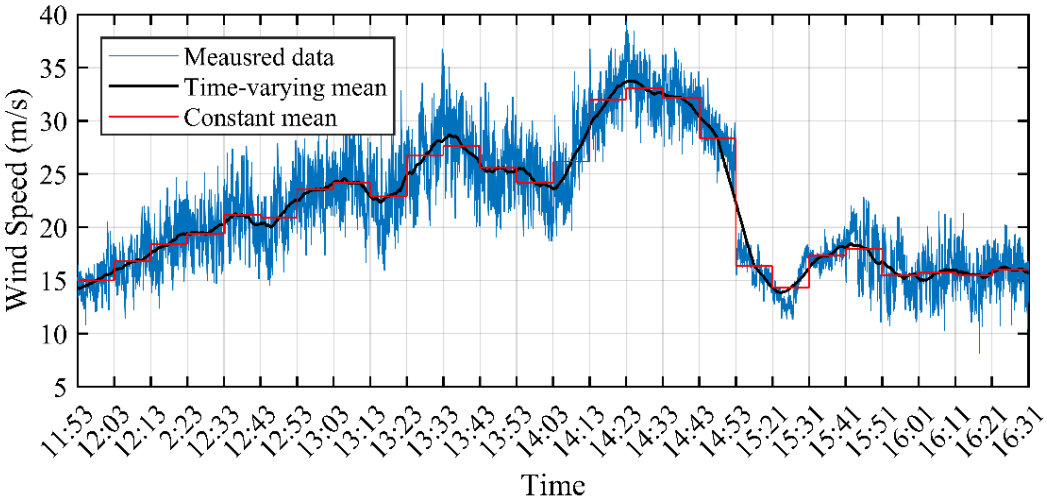

Figure 5-6 Wind speed time-history of typhoon TY9807 at the center of main span of bridge

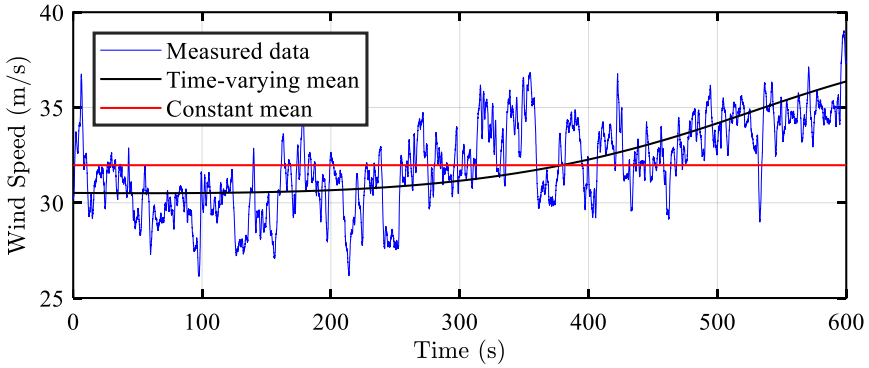

Figure 5-7 10 min wind record of typhoon TY9807 between 14:13~14:23

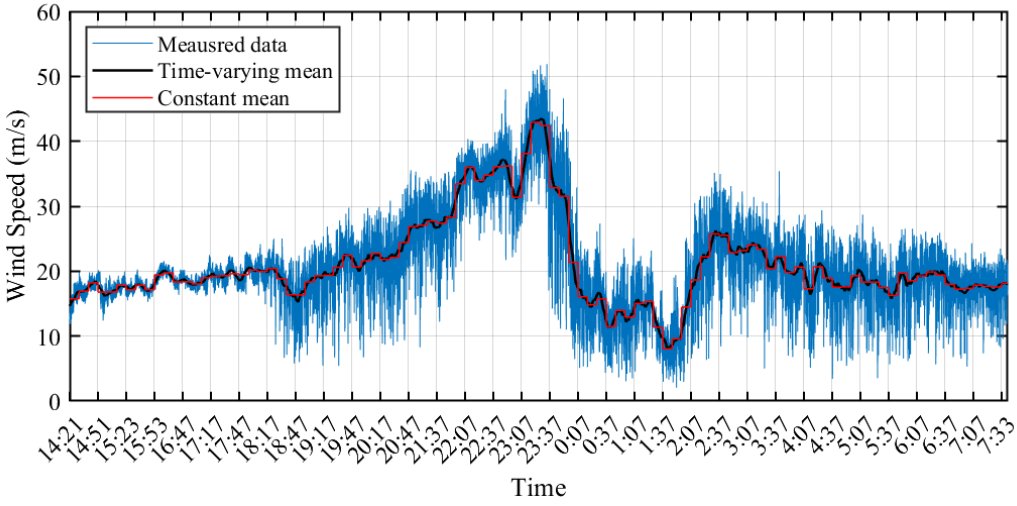

Figure 5-8 Wind speed time-history of typhoon 2018TY20 at the center of main span of bridge

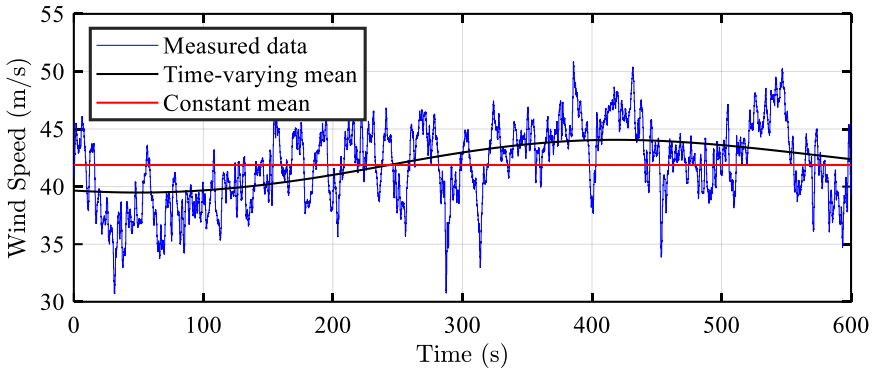

Figure 5-9 10 min wind record of typhoon 2018TY20 between 23:17~23:27

5.5 Evolutionary power spectral density analysis

After the decomposition and characterization of the wind records, the remaining fluctuating wind speed may still have time-varying characteristics of wind turbulence. Therefore, $u(t)$ is represented by a zero-mean oscillatory process that admits the representation (Priestly 1965; Priestly and Tong 1973).

$$u(t) = \int_0^{+\infty} A(\omega, t) e^{i\omega t} dZ(\omega) \tag{5.5}$$

where $Z(\omega)$ is a zero-mean gaussian orthogonal increment process having the properties as:

$$E[dZ(\omega)dZ(\omega')^*] = \begin{cases} 0 & \text{for } \omega \neq \omega' \\ S_0(\omega)d\omega & \text{for } \omega = \omega' \end{cases} \tag{5.6}$$

where the superscript "*" denotes the complex conjugate and $S_0(\omega)d\omega$ is the variance of the increment process. The auto evolutionary power spectral density (EPSD) of fluctuating wind component $u(t)$ is computed in time-frequency-domain at the time instant t by following the procedure presented in (Hu et al. 2013; Priestley 1965) such as:

$$S_{uu}(\omega, t) = |A(\omega, t)|^2 S_0(\omega) \tag{5.7}$$

where $A(\omega, t)$ is a slowly varying function with time; $S_0(\omega)$ is the one-sided auto power spectrum, and $S_{uu}(\omega, t)$ is the one-sided auto evolutionary power spectrum. First, the essence of Priestley's EPSD method is to perform a generalized linear transformation on the interesting data at a specific frequency by means of a filter function $g_h(\tau)$. Then, the other weight-function $W_{T'}(t)$ is used to smooth the estimated values for neighboring values of t in order to decrease the estimation error. Clearly, this method is restricted to the uncertainty principle and the selection of filter and weighting functions will have an influence on the estimated results. To compute the auto EPSD from the measurement data of typhoon-induced wind speed, the filter and weight functions are calculated by using the following expressions:

$$g_h(\tau) = \begin{cases} 1/(2\sqrt{h\pi}) & |\tau| \le h \\ 0 & |\tau| > h \end{cases} \tag{5.8}$$

$$W_{T'}(t) = \begin{cases} 1/T', & |t| \le \dfrac{T'}{2} \\ 0, & \text{otherwise} \end{cases} \tag{5.9}$$

where the window lengths are chosen as h = 2.3s and T' = 46s. The step-by-step procedure of the algorithm used for the computation of auto measured EPSD is shown in Figure (5-10).

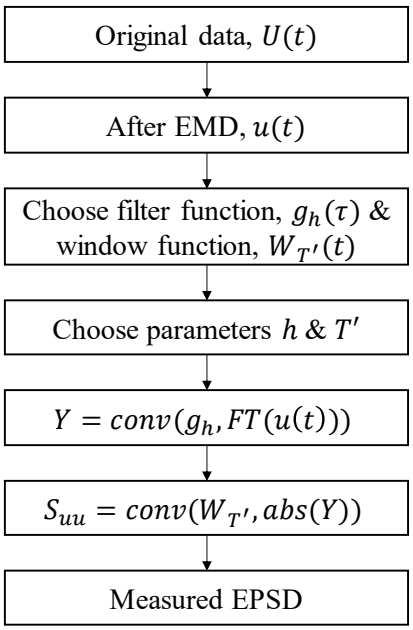

Figure 5-10 Flowchart of evolutionary power spectrum density computational process

After computation of the measured auto EPSD, the non-stationary wind characteristics such as time-varying variance $\sigma_u^2(t)$ and time-varying turbulence intensity $I_u(t)$ are evaluated using the following expressions:

$$\sigma_u^2(t) = \int_0^{+\infty} S_{uu}(\omega, t) d\omega \tag{5.10}$$

$$I_u(t) = \frac{\sqrt{\sigma_u^2(t)}}{\overline{U_{tv}}(t)} \tag{5.11}$$

In order to simulate the non-stationary longitudinal fluctuating wind speed, the time-varying integral length scale $L_u(t)$ is required, which is computed by using the measured auto EPSD. For that, the von-Karman longitudinal spectrum is extended to the evolutionary von-Karman longitudinal spectrum involving $\overline{U_{tv}}(t)$, $\sigma_u^2(t)$ and $L_u(t)$. By inserting the measured auto EPSD, $\overline{U_{tv}}(t)$ and $\sigma_u^2(t)$ into the evolutionary von-Karman spectrum formula for longitudinal direction, $L_u(t)$ can be obtained by solving an implicit equation as shown in Eq. (5.12).

$$\frac{S_{uu}(\omega,t)}{\sigma_u^2(t)} = \frac{1}{2\pi}\frac{\frac{4L_u(t)}{\overline{U_{tv}}(t)}}{\left[1+70.8\left(\frac{\omega L_u(t)}{2\pi\overline{U_{tv}}(t)}\right)^2\right]^{\frac{5}{6}}} \tag{5.12}$$

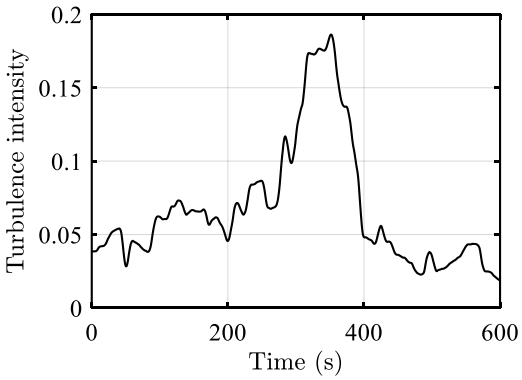

Figure 5-11 Time-varying turbulence intensity of non-stationary wind speed under typhoon TY9807 between 14:13~14:23

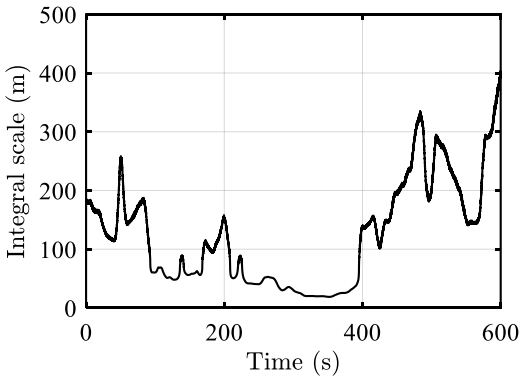

Figure 5-12 Time-varying integral length scale of non-stationary wind speed under typhoon TY9807 between 14:13~14:23

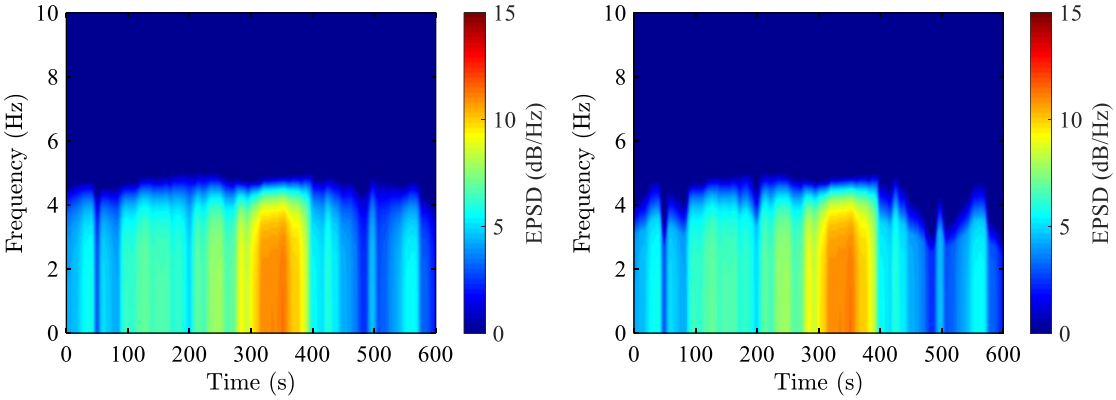

(a) Measured (b) Estimated

Figure 5-13 EPSD of longitudinal fluctuating wind speed of typhoon TY9807 between 14:13~14:23 at the center of the main span of the Akashi-Kaikyo bridge

Figures (5-11) and (5-12) show the time-varying turbulence intensity and time-varying longitudinal integral length scale, respectively for typhoon TY9807 between 14:13~14:23. The maximum turbulence intensity and longitudinal integral length scale are found to be around 0.18 and 400 m, respectively for 10 min time interval. Subsequently, the time-varying turbulence intensity, time-varying mean wind speed, and time-varying integral length scale are used to find the estimated EPSD by using von-Karman expression shown in Eq. (5.12). This estimated EPSD

is compared with the measured EPSD and good correspondence between both EPSDs is observed as shown in Figure (5-13(a) and (b)), where only spectral contents between 0 to 10 Hz are shown. It is observed that the maximum spectral values appear in between 300 to 400 seconds and the overall variation trends are consistent. This variation can also be observed in between 300 to 400 seconds in Figures (5-11) and (5-12), where turbulence intensity and integral length scale are maximum and minimum, respectively.

Similarly, the time-varying turbulence intensity and time-varying longitudinal integral length scales are computed for typhoon 2018TY20 by using time-varying mean wind speed and results are plotted in Figures (5-14) and (5-15). The estimated EPSD of 2018TY20 is also compared with the measured EPSD as shown in Figure (5-16), highlighting the regeneration of spectral density features of wind fluctuation in frequency- and time-domain.

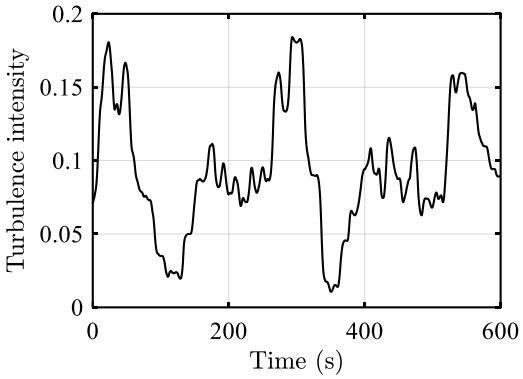

Figure 5-14 Time-varying turbulence intensity of non-stationary wind speed under typhoon 2018TY20 between 23:17~23:27

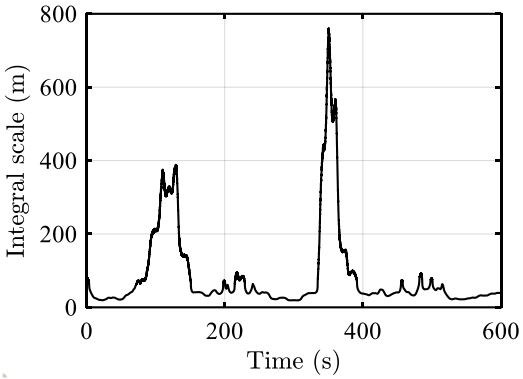

Figure 5-15 Time-varying integral length scale of non-stationary wind speed under typhoon 2018TY20 between 23:17~23:27

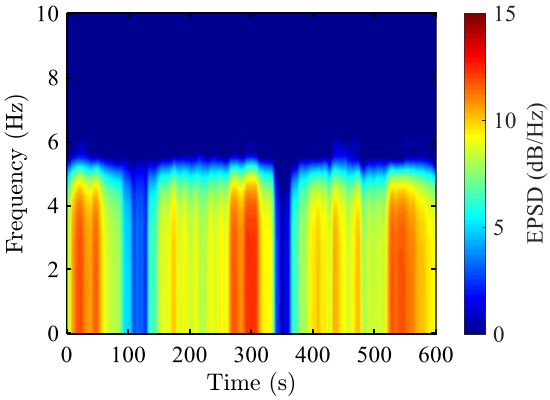

(a) Measured

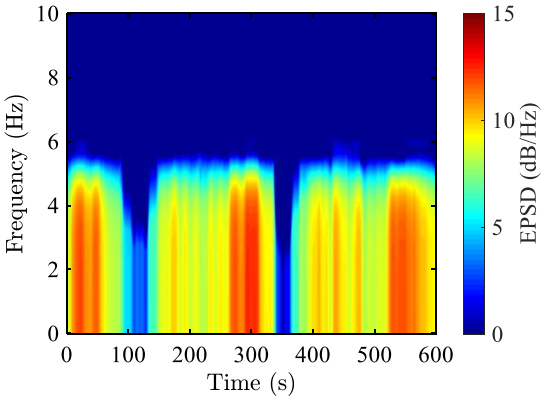

(b) Estimated

Figure 5-16 EPSD of longitudinal fluctuating wind speed of typhoon 2018TY20 between 23:17~23:27 at the center of main span of Akashi-Kaikyo bridge

5.6 Generation of artificial longitudinal and vertical wind fluctuations

The artificial non-stationary wind field is simulated based on the assumption that the estimated EPSD remains uniform along the length of the bridge deck. The wind history is generated through an unconditional simulation technique by extending the SRM to accommodate the EPSD matrix of non-stationary processes. For that, the main and side spans of the Akashi-Kaikyo bridge are divided into segments of equal lengths at the deck level such that the center of each segment receives a 10 min record of typhoon-induced wind speed time history as shown in Figure (5-17). Likewise, the towers and cables are also divided into segments for the generation of a wind field using wind speed profile constructed by the Power law.

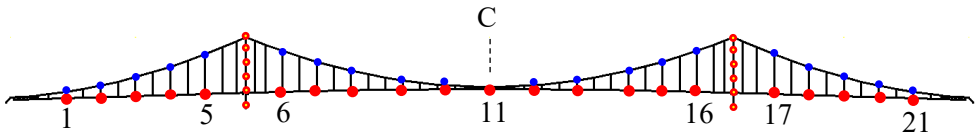

Figure 5-17 Distribution of nodes on which wind forces are acting

The vertical fluctuating wind speed on the bridge deck is simulated as an ergodic, Gaussian, and stationary process by using the vertical power spectrum proposed by von-Karman as shown in Eq. (5.9). In the case of tower and cables, both longitudinal and vertical wind components are generated as stationary processes as it is assumed that towers and cables only receive drag forces of stationary nature.

$$\frac{S_{ww}(\omega)}{\sigma_w^2} = \frac{1}{2\pi}\frac{\frac{4L_w}{\bar{U}}\left[1+755\left(\frac{\omega L_w}{2\pi\bar{U}}\right)^2\right]}{\left[1+283\left(\frac{\omega L_w}{2\pi\bar{U}}\right)^2\right]^{\frac{11}{6}}} \tag{5.13}$$

where $S_{ww}(\omega)$ is the power spectrum density of vertical fluctuating wind component and L_w is the vertical integral length scale. Generally, the coherence function of multivariate non-stationary process shows time-varying characteristics. Nevertheless, due to the lack of measurement data of multivariate non-stationary excitations and suitable time-varying coherence models, the time-invariant coherence model, which is suitable for the stationary process, has been widely adopted to model the multivariate non-stationary wind generation and compute the attendant structural response (Davenport 1961; Peng et al. 2017). For instance, Chen and Letchford (2004) used the time-invariant Davenport coherence function to model non-stationary downbursts and computed the non-stationary response of a cantilevered structure. Chen (2008) developed an analytical framework for estimating the alongwind response of a tall building to

non-stationary winds based on Davenport coherence model. Similarly, Kwon and Kareem (2009) proposed a concept of the gust-front factor based on the Davenport coherence function to estimate the equivalent static wind loads on the structures to gust-front winds. Also, Solari (2016) utilized the Davenport time-invariant coherence model to develop the thunderstorm-based response spectrum method. Following it, the coherence function used in the stationary wind model is herein adopted for the non-stationary wind model with the assumption that coherence is the only function of frequency and does not vary with time according to the Priestley's EPSD theory (Priestley 1965). Based on the coherence function, cross EPSD is determined as:

$$S_{pp,x_1x_2}(\omega,t) = \sqrt{S_{pp,x_1}(\omega,t)S_{pp,x_2}(\omega,t)}\,\gamma_{pp,x_1x_2}(\omega) \tag{5.14}$$

where symbol p denotes either u or w; $S_{pp,x_1}(\omega,t)$ and $S_{pp,x_2}(\omega,t)$ are the auto EPSDs of wind speed fluctuations at two discrete nodes x_1 and x_2, respectively; $S_{pp,x_1x_2}(\omega,t)$ is the cross EPSD of wind speed fluctuations between x_1 and x_2, and $\gamma_{pp,x_1x_2}(\omega)$ denotes the coherence function between x_1 and x_2, which is determined by using Devenport's exponential formulation such as:

$$\gamma_{pp,x_1x_2}(\omega) = \exp\left(-k\frac{\omega\Delta x}{2\pi\overline{U}}\right) \tag{5.15}$$

where Δx denotes the distance between two nodes under consideration; k is the decay coefficient (taken as 8) and $\overline{U}$ is the constant mean wind speed for 10 min time interval. Moreover, the cross-spectrum of u and w (S_{uw,x_1x_2}) is ignored in this study due to its minor effects on bridge response. Figure (5-18) shows the coherence function of wind speed time history data of five different anemometers, installed on the main span of the bridge, analysed under typhoon TY9807. It is observed that coherence of fluctuating wind speed between two points decreases as frequency increases. It is also noted that the coherence function starts from unity at zero frequency for all cases which shows that the wind speed time histories at all nodes correspond and correlate to one another completely. Finally, the artificial non-stationary fluctuating winds are generated by the following expression:

$$v_{sim}(t) = \sum_{i=1}^{M}\sum_{k=1}^{N}\sqrt{2\Delta\omega}R_i(\omega_k,t)cos(\omega_k t + \psi_{ki}) \tag{5.16}$$

where $v_{sim}(t)$ is the wind speed time history simulation containing M component processes whose ith component admits the spectral representation; ω_k is the uniformly spaced sequence of circular frequencies with the step $\Delta\omega$ which can be calculated as $\omega_k = k\Delta\omega$ for $k = 0,1,\dots,N$; $\Delta\omega$ is the ratio of the cut-off frequency to the prescribed number of segments N; ψ_{ki} is the random phase angle distributed uniformly over the range from 0 to 2π; $R_i(\omega_k,t)$ is the ith column of the matrix $R(\omega_k,t)$ obtained by the Cholesky decomposition of the EPSD matrix (consisting of auto and cross EPSD components) satisfying the Cholesky decomposition

transpose criteria. The flowchart of the simulation of non-stationary wind fields is presented in Figure (5-19). The artificial turbulent wind speed time histories of TY9807 and 2018TY20 at the center node of the main span of the Akashi-Kaikyo bridge are also shown in Figures (5-17) and (5-18), respectively.

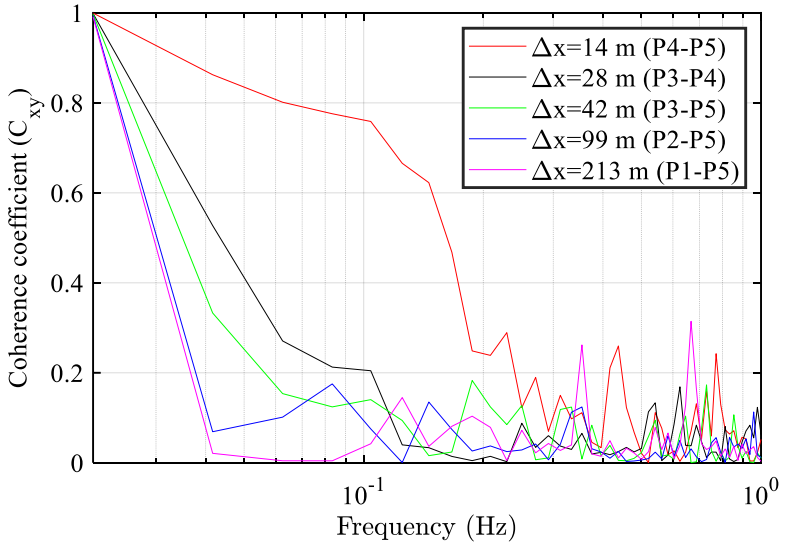

Figure 5-18 Spatial coherence of measurement data of wind speed time-history under typhoon TY9807 spanwise between 14:13~14:23

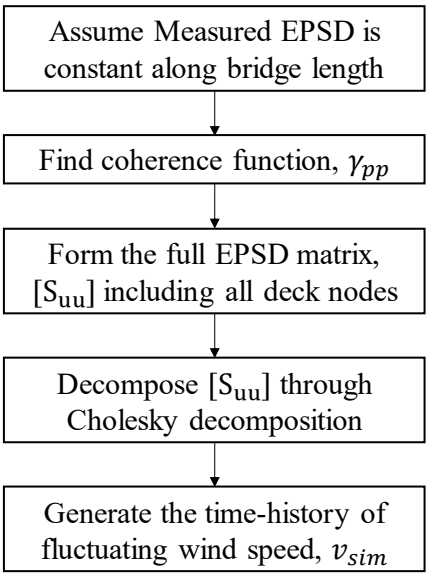

Figure 5-19 Flowchart of unconditional simulation technique for the generation of non-stationary wind field around the bridge site

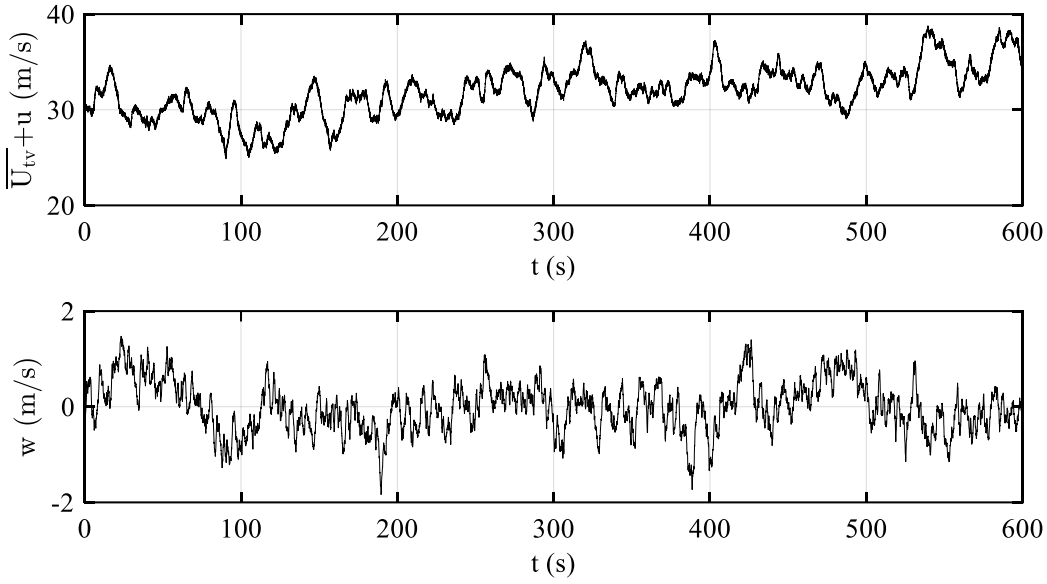

Figure 5-20 Simulated wind speed of typhoon TY9807 at 32 m/s with time-varying characteristics at the center of main span of the Akashi-Kaikyo bridge

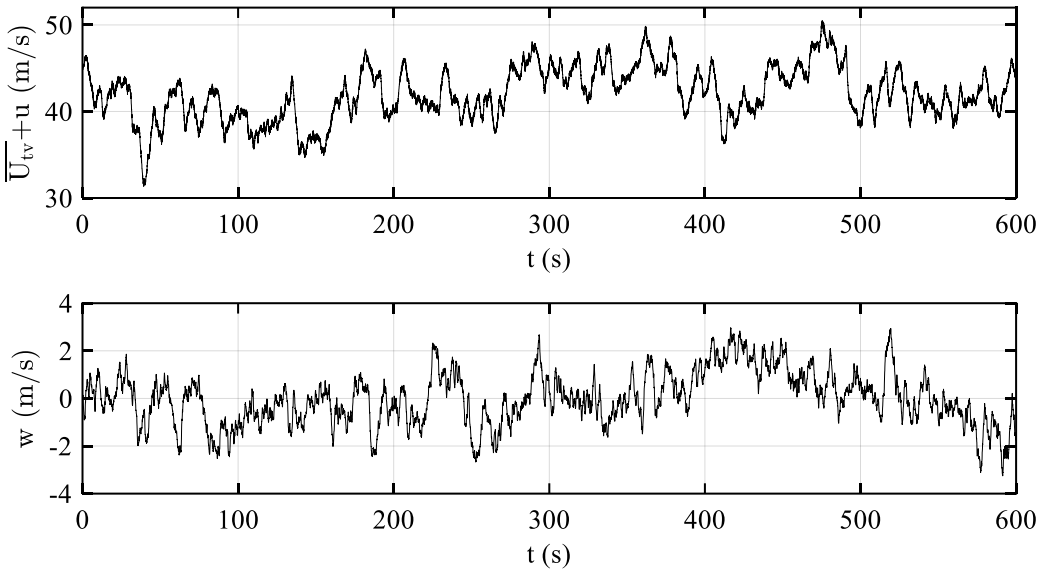

Figure 5-21 Simulated wind speed of typhoon 2018TY20 at 42 m/s with time-varying characteristics at the center of main span of Akashi-Kaikyo bridge

In order to check the accuracy of wind field simulation, the target power spectral densities of longitudinal and vertical fluctuating wind components given by von-Karman are compared with the simulation results, which indicates that the time-domain simulation corresponds very well with the target spectra as shown in Figure (5-22).

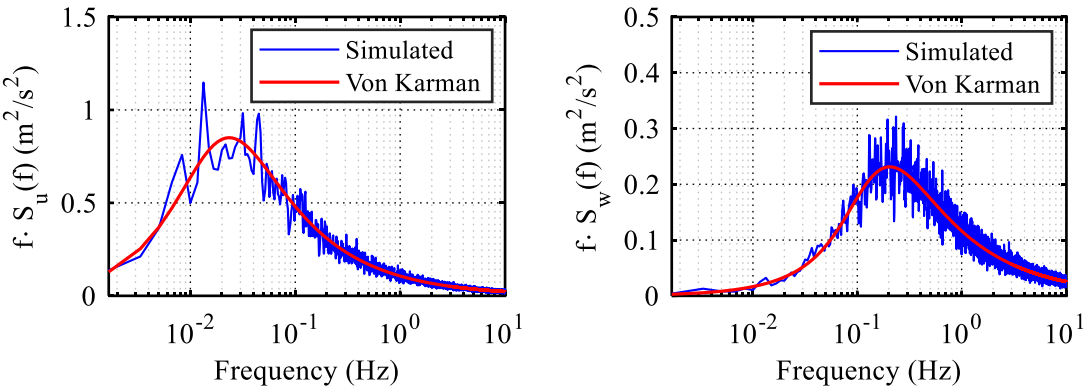

(a) Longitudinal fluctuating wind speed (b) Vertical fluctuating wind speed

Figure 5-22 Assigned and simulated wind spectra for typhoon TY9807 at 32 m/s

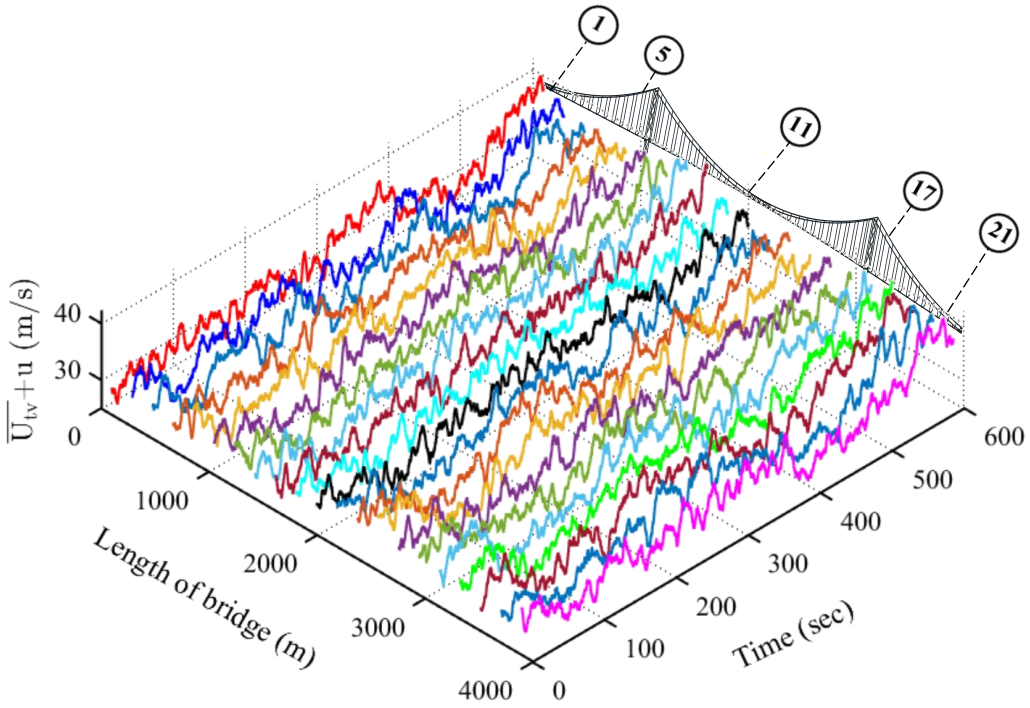

Figure 5-23 Wind inputs on the Akashi-Kaikyo bridge under typhoon TY9807 at spanwise locations

5.7 Wind-bridge interaction

After the simulation of non-stationary wind fields around the bridge site, the wind inputs are idealized to be applied on the span-wise locations of the bridge deck simultaneously such that each node receives a 10 min wind speed time history. The schematic diagram of the Akashi-

Kaikyo bridge and its corresponding wind speed time histories along the bridge deck during these two typhoon events are shown in Figures (5-23) and (5-24). It is shown that both events have time-varying characteristics, i.e., the wind speed increases and then decreases within a short time duration. As a result, the bridge starts vibrating about the time-varying mean while retaining its short-term fluid memory in the wake of flow separation owing to its bluff body.

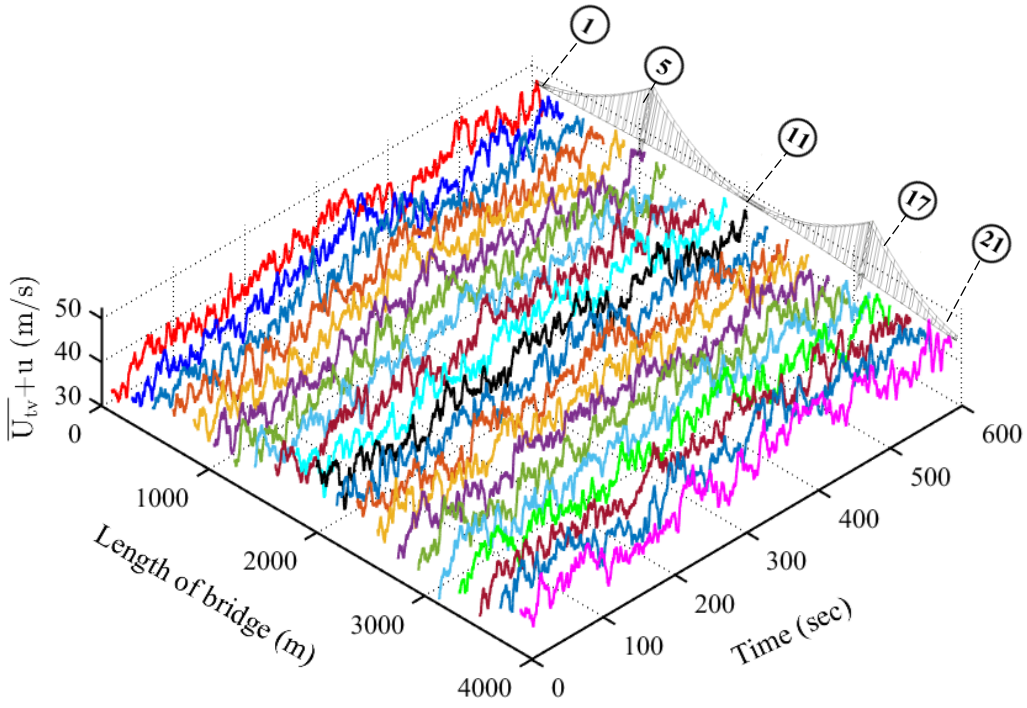

Figure 5-24 Wind inputs on the Akashi-Kaikyo bridge deck under typhoon 2018TY20 at spanwise locations

CHAPTER 6: NUMERICAL EXAMPLE

This chapter presents a numerical example of a real full-scale bridge on which the proposed framework is tested and validated. For that, the wind loads on the bridge deck are calculated in three-dimensional fashion using an FD-based Volterra model, named herein as *Volterra FD model*, a coalition of QS and Volterra FD models, named herein as *Hybrid Volterra FD* model, and an ANN-based Volterra model, named herein as *Volterra ANN* model, under typhoon events TY9807 and 2018TY20. The buffeting analyses are performed based on the Volterra FD, Hybrid Volterra FD, and Volterra ANN models as well as the existing aerodynamic models i.e., linear unsteady (LU) and hybrid nonlinear (HNL) models under typhoon wind speeds. For that, a finite element model (FEM) of the example bridge is first developed. Then, the aerostatic analysis is performed in order to examine the effects of the constant and time-varying mean wind speeds on the aerostatic response of the bridge. Subsequently, the eigenvalue analysis is performed to investigate the modal characteristics i.e., eigenmodes and natural frequencies of the bridge. At last, the time history dynamic analyses are performed based on the Volterra FD, Hybrid Volterra FD, and Volterra ANN models, and results are compared with the measurement data of the bridge displacement. Additionally, the buffeting analyses are also performed based on different existing aerodynamic load models, presented in Chapter 2, and comparison is made between the proposed and existing aerodynamic load models in terms of root-mean square (RMS) of fluctuating part of the buffeting response and relative errors in RMS.

The results of buffeting analyses are used to check the efficacy and applicability of the proposed framework to predict the buffeting response of long-span bridges subjected to non-synoptic winds accurately. It is also observed that all three non-stationary and nonlinear Volterra models produce the buffeting responses around the time-varying mean wind response, whereas the existing aerodynamic models estimate the buffeting response around the constant mean wind response. Simulation results also show that the conventional LU and HNL models, based on the assumptions of stationary and linear fluid memory effects, cannot regenerate the real phenomenon of buffeting response of the bridges under typhoon winds; therefore, in this dissertation, the Volterra series-based buffeting analysis framework is suggested because of its efficiency and ability to consider the effects of the nonlinear fluid memory and aerodynamic nonlinearity.

6.1 Introduction

The accurate estimation of the dynamic response of nonlinear structures is of paramount importance for the safe design of long-span bridges under typhoon winds. The wind-bridge

interaction under turbulent wind is a complex phenomenon and is demonstrated by several methods. In the past, traditional frequency-domain approaches were used to find the wind-induced response of bridges (Katsuchi et al. 1998; Katsuchi et al. 1999). These frequency-domain approaches are generally limited to the linear structures excited by stationary winds. To avoid this restriction, several researchers proposed the time-domain methods for the buffeting analysis of bridges (e.g., Chen and Kareem 2001; Chen and Kareem 2011; Ding and Lee 2000; Costa et al. 2007). For instance, Chen and Kareem (2001) presented the time-domain analysis framework for predicting the nonlinear response of long-span bridges under turbulent winds by separating the effective angle of attack into low- and high-frequency components. They modelled the low-frequency component of aerodynamic forces by the QS model, whereas the high-frequency component of aerodynamic forces is modeled by the LU model using impulse response functions. The time-domain methods not only provide the benefit of combining different types of loads and can consider the nonlinearities but also provide the only way to reproduce the transient nature of the bridge. That is the reason why the temporal simulations are increasingly performed. Besides this, in the last few decades, the numerical approaches based on computation fluid dynamics (CFD) have also received significant attention (Ge and Xiang 2008).

In the case of bridge decks, the wind-bridge interaction is usually simulated by wind tunnel tests or semi-analytical models based on the theory of aeroelasticity, accompanied by wind tunnel tests (Scanlan 1978(I); Scanlan 1978(II); Davenport 1962; Diana et al. 1993; Chen and Kareem 2002). The semi-analytical aerodynamic models are on the basis of the analytical solutions from the flat-plate aerodynamics. These analytical models simulate the complex unsteady behavior of bluff bodies subjected to high winds by modifying the aerodynamic coefficients obtained from the wind tunnel experiments. Two main assumptions, under which semi-analytical approaches are based, are the quasi-steady and linear unsteady. In the case of former assumption, the fluid memory is ignored, and aerodynamic nonlinearity is considered. In the latter assumption, the unsteady aerodynamic forces are separated into static, self-excited, and buffeting forces while considering the fluid memory effects to reveal the complex nature of bluff body aerodynamics in a linear manner. Wu and Kareem (2013) carried out a detailed analysis of the fundamental assumptions for the long-span bridge deck section. They determined that the fluid memory is one of the major factors affecting the aerodynamic response significantly.

Nevertheless, they did not stipulate whether it was the fluid memory effect of the buffeting or that of the self-excited forces that influenced the total response. Kavrakov et al. (2017) examined various formulations of buffeting and self-excited forces in time-domain by comparing the dynamic response of a multi-span cable-stayed bridge during the critical erection condition. They studied the aerodynamic models from a perspective of model complexity and compared the effect of the aerodynamic parameters utilized in the aerodynamic models, such as aerodynamic

damping and stiffness, aerodynamic nonlinearity, fluid memory, and aerodynamic coupling on the bridge response.

Besides the fluid memory effects, the aerodynamic nonlinearity has also a considerable impact on the buffeting response of the bridge, especially at high wind speed. Currently, only a few studies are available to model the aerodynamic and aeroelastic nonlinearities existing in wind-bridge interaction in addition to non-stationary effects. One of such studies includes a hybrid nonlinear model developed by Diana et al. (2008) which is based on the hysteretic nature of wind force on the bridge. Recently, Wu and Kareem (2013) also proposed a nonlinear scheme to model aerodynamic nonlinearity through the Volterra series of higher-order. However, this nonlinear model has not been verified on a real full-scale bridge model subjected to real typhoon winds, which calls into question its efficiency and applicability in the simulation of real bridge response.

In this research, the wind loads are modelled based on Volterra series under non-stationary winds by considering the higher-order fluid memory effects arising from wind-bridge interaction and aerodynamic nonlinearity effects due to the varying angle of incidence, amplitude-dependency of static wind force coefficients, flutter derivatives, and aerodynamic admittance functions, and non-proportional relationship between wind speed and bridge motion. The buffeting analysis results obtained from the proposed Volterra model are compared with the measurement response of the bridge. The eight different existing semi-analytical models in the time-domain, including steady (S), linear steady (LS), quasi-steady (QS), linearized quasi-steady (LQS), corrected quasi-steady (CQS), linear unsteady (LU) and hybrid nonlinear (HNL) models, are also compared with the measurement response in order to check the efficiency of existing aerodynamic models. The simulation results exhibit that the proposed Volterra FD, Hybrid Volterra FD, and Volterra ANN models can regenerate the real phenomenon of buffeting response of a long-span bridge around the time-varying response under non-stationary winds.

6.2 Description of bridge

The Akashi-Kaikyo bridge is one of the world's longest suspension bridges in west-central Japan having a main span of 1991 m and two side spans of 960 m each. The height and width of its stiffening truss girder are 14 m and 35.5 m, respectively, linking the city of Kobe with Iwaya on Awaji Island. It crosses the Akashi-Strait (Akashi-Kaikyo in Japanese) as a part of the Honshu-Shikoku Highway. It was completed in 1998. The height of the main towers is 282.8 m above the sea level and 297.3 m up to the top of the cables. The bridge can expand due to the thermal effects up to 2 m over a day. The bridge was designed to withstand extreme winds up to 80 m/s, earthquakes up to a magnitude of 8.5, and torrent sea currents. The mesmerizing view of the majesty Akashi-Kaikyo bridge is shown in Figure (6-1).

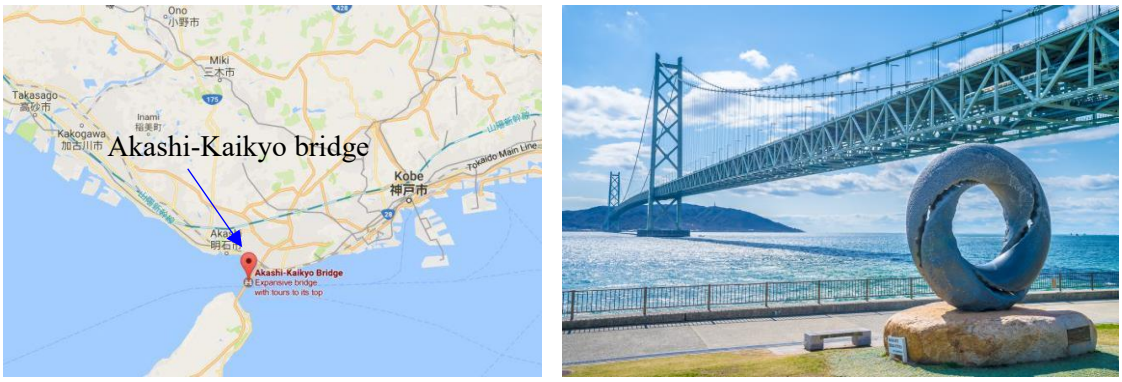

Figure 6-1 The location and mesmerizing view of the majesty Akashi-Kaikyo bridge in Japan

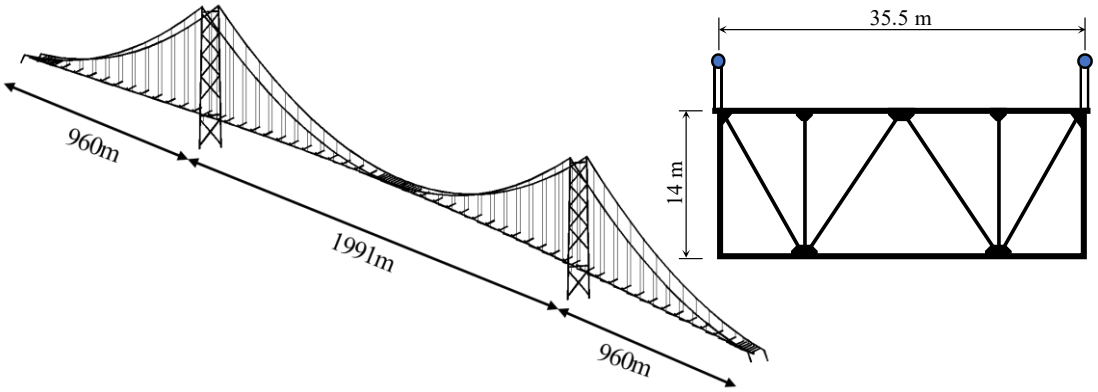

Figure 6-2 Finite element model of the Akashi-Kaikyo bridge and its deck cross-section

6.3 Finite element model

A 3D finite element model of Akashi-Kaikyo bridge is developed by using the commercial FE package ABAQUS (2014) in reference to the modelling technique used by Boonyapiyo et. al (1999). The FE model of the bridge along with its cross-section of truss deck is shown in Figure (6-2). The main stiffening girder and towers are simulated by spatial Timoshenko beam elements with six degrees of freedom (DOFs) at each node. The main cables, hangers and stay cables are simulated by 3D linear elastic truss elements with three DOF at each node. To ensure the 3D effect, the connection of shear center-to-hanger is assumed to be rigid link with very high stiffness. All masses are lumped to the gravity nodes of stiff deck including the polar moment of inertia and on main cable-hanger connection nodes. Since the mass center and the shear center of most girders do not coincide, they are also connected by a rigid link as shown in Figure (6-3). Both ends of the girder are coupled with the towers in a way that allows one end to move in the longitudinal direction. It is important to achieve the correct static state of a suspension bridge before modal and dynamic analysis for accurate results. The material properties and all characteristics of the

elements are determined according to the related design codes and the effect of geometric nonlinearity is also included in static analysis for the initial balanced state of the bridge by checking the NLGEOM option in ABAQUS. The deck and towers are coupled in 3DOF. The bottom of both towers and back cables are fixed at bases while ignoring the soil-structure interaction. The sectional and material properties of the Akashi-Kaikyo bridge are shown in Table 6-1 and Table 6-2, respectively.

6.4 Eigenvalue analysis of bridge

The eigenvalue analysis of the Akashi-Kaikyo bridge is performed to investigate its modal characteristics i.e., natural frequencies and mode shapes. First fifty eigenmodes are extracted in the frequency range from 0.040 Hz (1st mode) to 0.40 Hz (50th mode). According to this analysis, the first lateral symmetric mode occurs at 0.04 Hz, followed by a symmetric vertical mode at 0.0645 Hz. In addition to that, the first symmetric torsional mode occurs at 0.147 Hz. The fundamental eigenvalues and frequencies of the bridge are similar to those identified by the previous researchers (Boonyapiyo et. al 1999; Miyata et al. 2017). Figure (6-4) illustrates the significant eigenmodes of the bridge along with its natural frequencies, eigenvalues, and nature of the model. The eigenvalue analysis results elucidate that the first mode of Akashi-Kaikyo bridge is dominated in the lateral direction which contributes maximum in the lateral buffeting response, whereas the contribution of the second mode is maximum in the vertical buffeting response.

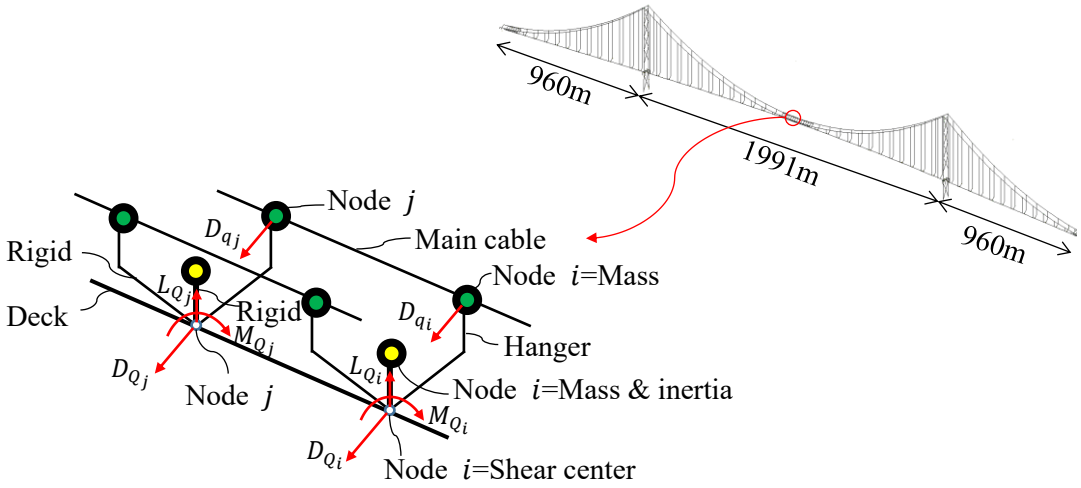

Figure 6-3 Finite element model of the Akashi-Kaikyo bridge deck along with the connected hangers and the main suspension cable

Table 6-1 Sectional properties of the Akashi-Kaikyo bridge

Item			Central and side spans
Stiffening truss	Cross-section (General)	Max. plate thick	38mm
		Class	HT780
	Cross-section of deck at the center of main span	Area	0.412m^2
		I11	20.188m^4
		I22	129.81m^4
		J	18.407m^4
Main cable	Composition		ϕ5.23mm×127wire×290strand 2 cables (36830 wires/cable)
	Sectional area		7882cm^2
	Diameter		1001.78mm
	Max. tension force		64961tf
	Allow. stress		82kgf/mm^2 (837MPa)
Hanger	Max. sectional area		0.0115m^2
	Max. diameter		121mm
	Max. tension force		1055.4tf
Tower	Height of tower (H)		T.P. + 297m (approx.)
	Sectional dimension (L×W)		14.8m – 10m×6.6m
	Thickness & class of plate		Base 50mm Top 40mm SM570
	Cross-section of tower at the height of H/2	Area	3.224m^2
		I11	17.04m^4
		I22	47.5m^4
		J	23.64m^4

Note: I11 and I22 are the moment of inertias about lateral and vertical directions of the bridge, whereas J is the polar moment of inertia of the bridge

Table 6-2 Material properties of the Akashi-Kaikyo bridge

Structural member	Modelled as	Elastic properties
Cable	Truss	E=203GPa
Hanger	Truss	E=140GPa
Deck (girder)	Beam	E=210GPa, G=807GPa, ν=0.3
Tower	Beam	E=210GPa, G=807GPa, ν=0.3
shear center -to-mass center	Rigid link	E, G=∞
shear center-to-hanger	Rigid link	E, G=∞

1st symmetric lateral

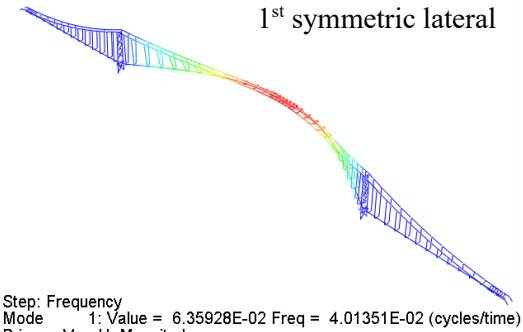

Step: Frequency
Mode 1: Value = 6.35928E-02 Freq = 4.01351E-02 (cycles/time)
Primary Var: U, Magnitude
Deformed Var: U Deformation Scale Factor: +2.604e+06

1st symmetric vertical

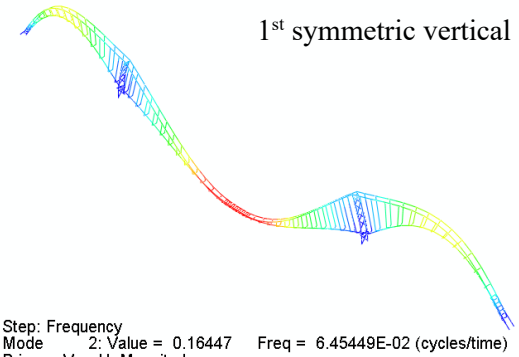

Step: Frequency
Mode 2: Value = 0.16447 Freq = 6.45449E-02 (cycles/time)
Primary Var: U, Magnitude
Deformed Var: U Deformation Scale Factor: +3.117e+06

1st asymmetric lateral

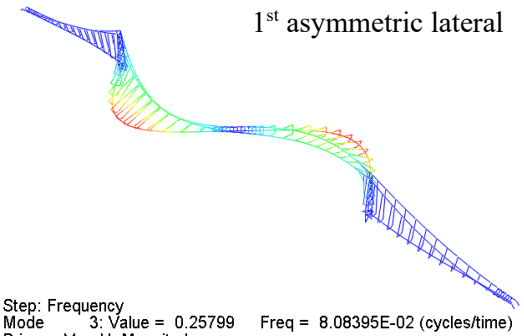

Step: Frequency
Mode 3: Value = 0.25799 Freq = 8.08395E-02 (cycles/time)
Primary Var: U, Magnitude
Deformed Var: U Deformation Scale Factor: +2.233e+06

1st asymmetric vertical

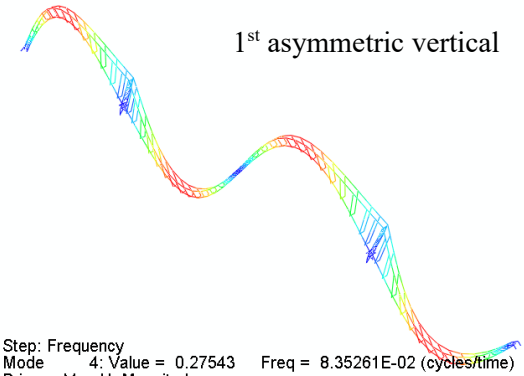

Step: Frequency
Mode 4: Value = 0.27543 Freq = 8.35261E-02 (cycles/time)
Primary Var: U, Magnitude
Deformed Var: U Deformation Scale Factor: +3.641e+06

2nd asymmetric vertical

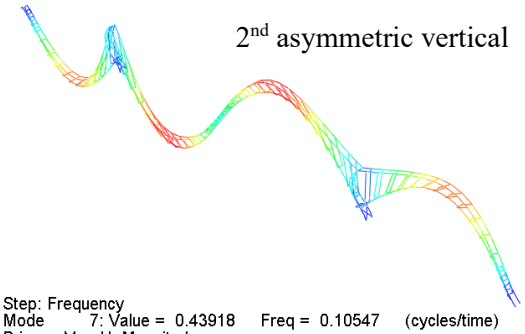

Step: Frequency
Mode 7: Value = 0.43918 Freq = 0.10547 (cycles/time)
Primary Var: U, Magnitude
Deformed Var: U Deformation Scale Factor: +3.798e+06

2nd symmetric vertical

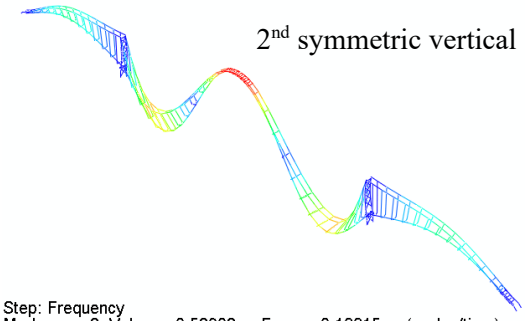

Step: Frequency
Mode 8: Value = 0.58908 Freq = 0.12215 (cycles/time)
Primary Var: U, Magnitude
Deformed Var: U Deformation Scale Factor: +2.414e+06

1st symmetric lateral-torsion

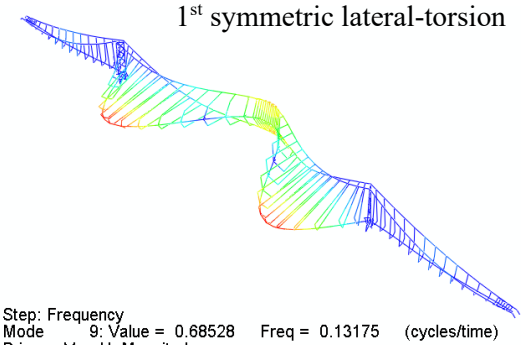

Step: Frequency
Mode 9: Value = 0.68528 Freq = 0.13175 (cycles/time)
Primary Var: U, Magnitude
Deformed Var: U Deformation Scale Factor: +2.146e+06

1st symmetric torsional

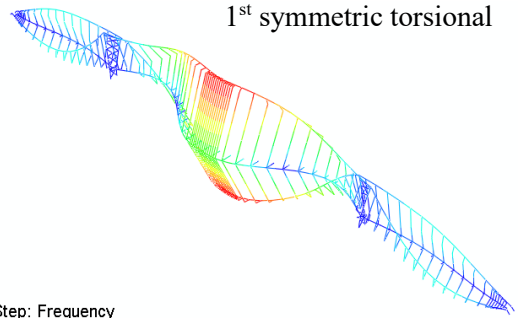

Step: Frequency
Mode 10: Value = 0.85554 Freq = 0.14721 (cycles/time)
Primary Var: U, Magnitude
Deformed Var: U Deformation Scale Factor: +2.410e+06

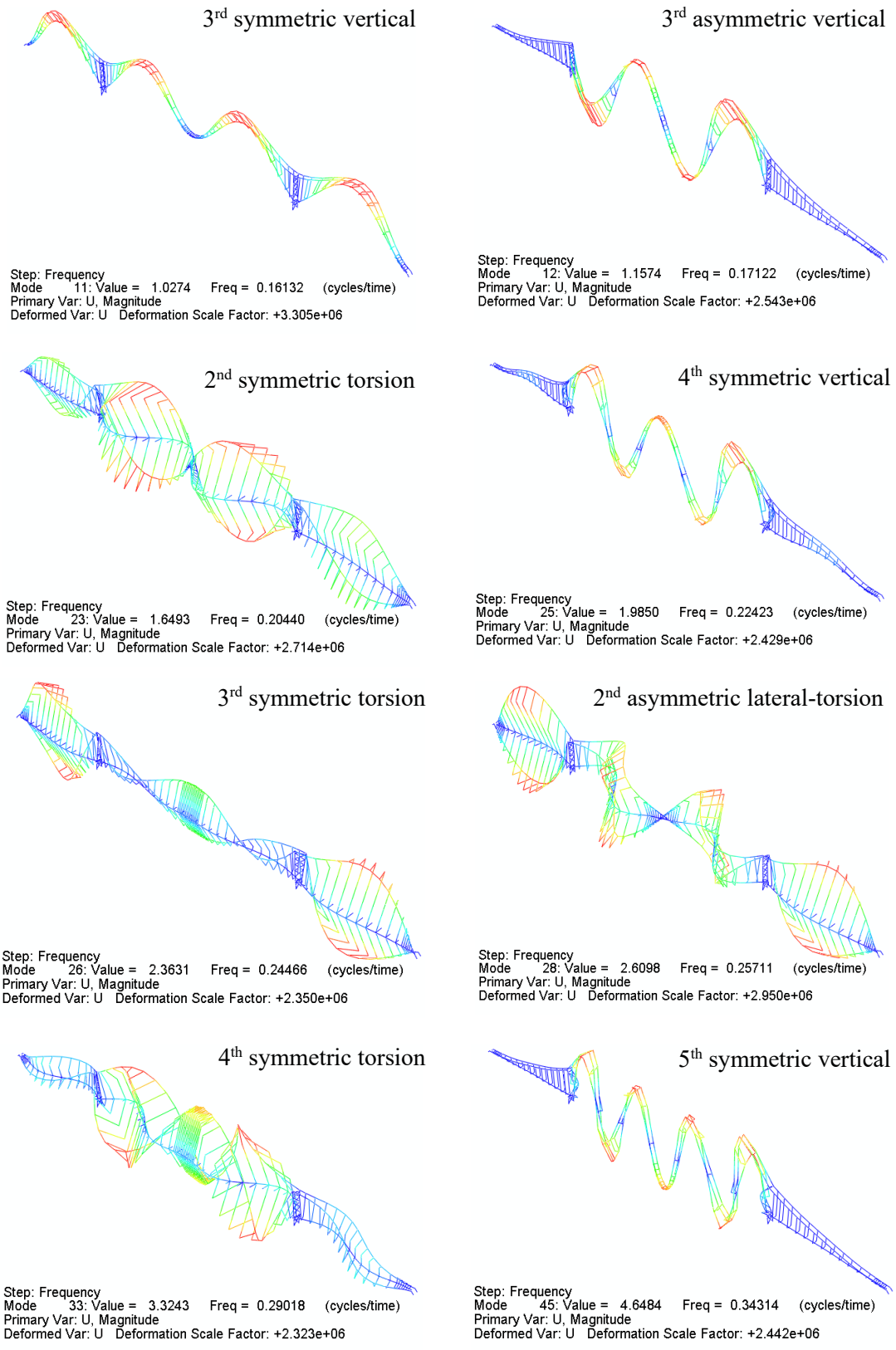

Figure 6-4 Mode shapes and natural frequencies of the Akashi-Kaikyo bridge

6.5 Computation of wind loads

Wind loads are computed in three parts i.e., time-varying static, buffeting, and self-excited forces. To compute the time-varying mean static forces, Eq. (3.6) is used considering the static wind force coefficients which depend on the effective angle of attack i.e., $C_Q(\alpha_{eff})$, where $Q: D, L, M$. The angle-varying static force coefficients utilized for the computation of time-varying static forces on the bridge deck are shown in Figure (4-2). The buffeting forces on the bridge deck are computed by employing various aerodynamic wind load models. Each model behaves differently based on the involved assumptions and limitations. For instance, the wind loads in the case of the Hybrid Volterra FD model are computed in the low- and high-frequency ranges separately. The demarcation between low- and high-frequency ranges is decided based on the cut-off frequency (which is the first mode natural frequency of the bridge for this case). For the low-frequency range, the QS model is adopted due to the high reduced velocity and its ability to take into account the static nonlinearity and self-excited force effects. The parameters used in the QS model for the low-frequency range are the low-frequency component of the effective angle of attack (α_{eff}^{low}), low-frequency components of wind speed fluctuations (both u^{low} and w^{low}), low-frequency components of the bridge vibration components ($\dot{p}^{low}$, $\dot{h}^{low}$ and $\dot{\alpha}^{low}$), and low-frequency components of effective angle-varying static forces coefficients (i.e., $C_Q(\alpha_{eff}^{low})$, where $Q: L, D, M$). Figure (6-5) illustrates the PSDs of low-frequency components of wind fluctuations demarcated at the cut-off frequency (0.04 Hz) in which the high-frequency components are removed by the Equiripple Lowpass filter.

Conversely, for the high-frequency range, a second-order Volterra FD model is employed to compute the buffeting and self-excited loads on the bridge deck numerically considering the high-frequency components of wind speed fluctuations (both u^{high} and w^{high}), high-frequency components of the bridge vibration components ($\dot{p}^{high}$, $\dot{h}^{high}$ and α^{high}), low-frequency components of effective angle-varying static forces coefficients, and amplitude-dependent IFs identified from FDs at varying angles of attack. Using these parameters, three-dimensional time-varying static forces and nonlinear buffering forces are first computed, acting on each node of the bridge deck by considering the 10 min records of wind speed time history. In the case of main cables and towers, only drag forces are calculated based on the quasi-steady model by using the static drag force coefficients of 0.7 and 1.8 for the main cables and towers, respectively. To compute the nonlinear self-excited forces on the bridge deck, three components of the bridge response ($\dot{p}$, $\dot{h}$ and α) are extracted from ABAQUS as a result of the preliminary modal analysis performed under time-varying static and nonlinear buffeting forces only. Like a feedback system, the effects of nonlinear self-excited forces on the bridge response are considered by applying them to the bridge deck directly. Thus, there is a total of nine force components at the high-frequency

range and three force components at low-frequency range acting upon each node of the bridge deck in the case of the proposed Hybrid Volterra FD model. The aerodynamic forces generated at low- and high-frequency ranges for the typhoon TY9807 by Hybrid Volterra FD model are shown in Figure (6-6) and Figure (6-7), respectively.

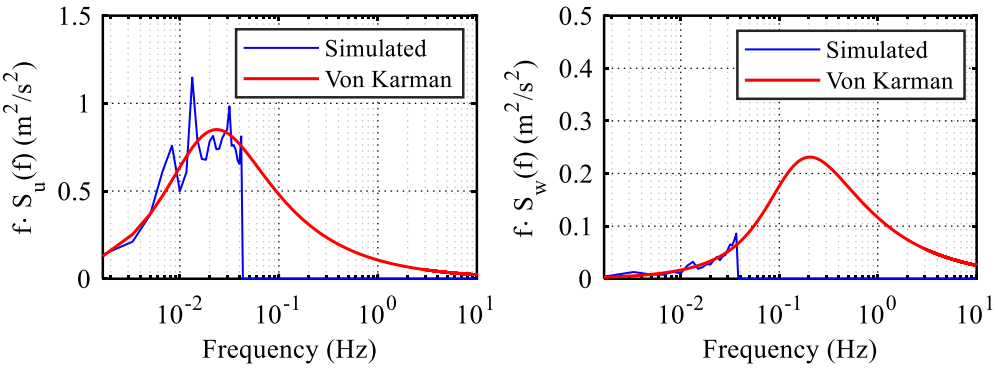

Figure 6-5 Power spectral density of low-frequency components of wind fluctuations at 32 m/s

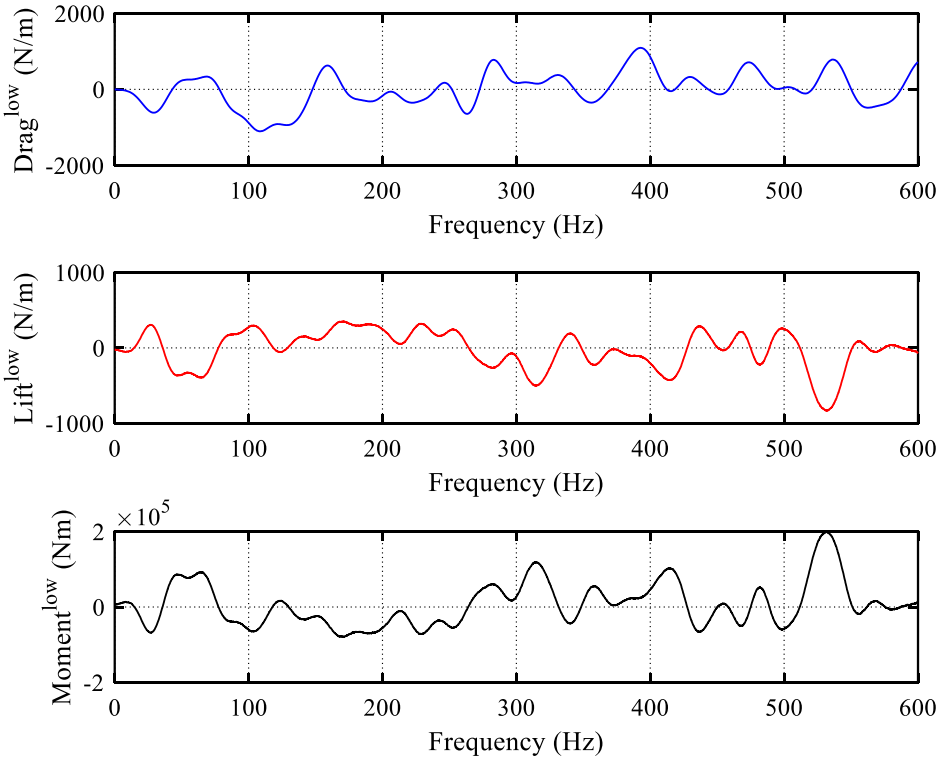

Figure 6-6 Low-frequency components of wind forces on the bridge deck computed by the Hybrid Volterra FD model under typhoon TY9807

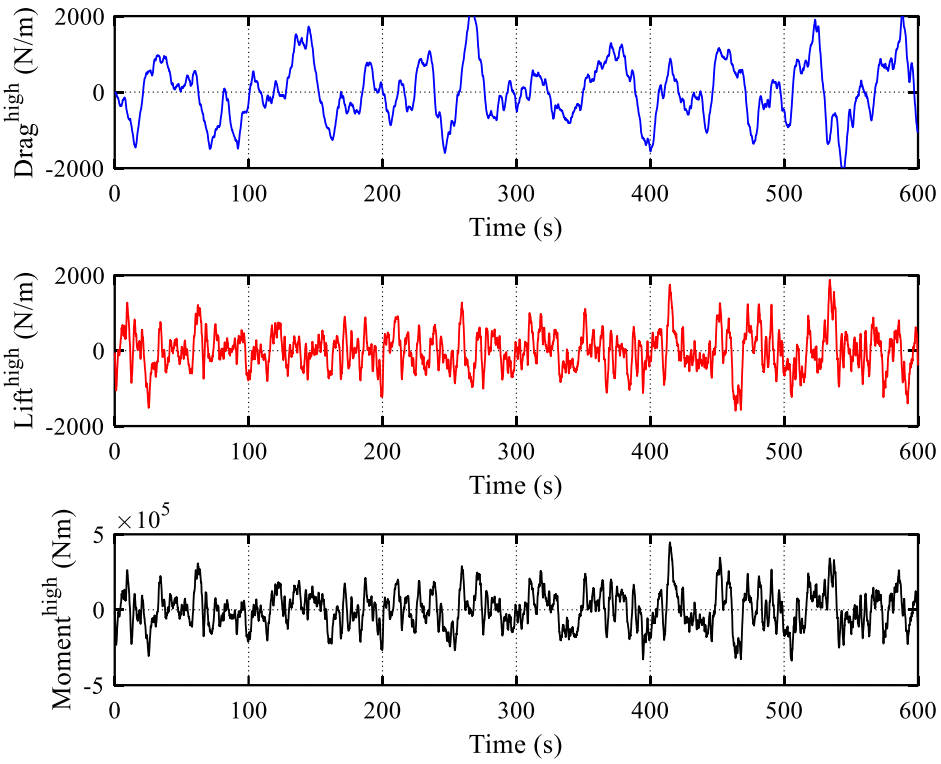

Figure 6-7 High-frequency components of buffeting forces on the bridge deck computed by the Hybrid Volterra FD model under typhoon TY9807

In the case of the Volterra FD model, the wind fluctuation and bridge motion components for the whole gamut of frequencies (from low to high) are considered to calculate the buffeting and self-excited forces on the bridge deck. The static force coefficients determined at a statically deformed position of the bridge deck (i.e., $C_Q(\alpha_s)$) and IFs identified at zero angle of attack are used in this model. On the other hand, the Volterra ANN model does not require static force coefficients or FDs to estimate IFs. In fact, the Volterra ANN model computes all components of wind loads based on the synaptic weights of activated neurons which captures the nonlinear aerodynamic features of the nonlinear input-output relationship existing in wind-bridge interaction. It is important to note here that the non-stationary wind effects are considered in the wind load calculations by all three proposed models using $\overline{U_{tv}}(t)$ and EPSD.

After the calculation of wind loads, each load component is applied to the bridge model as a nodal load as shown in Figure (6-3), and dynamic modal analysis is performed in time-domain. It is noted that the geometric nonlinearities in the structural characteristics are already incorporated in the modeling. For linear structures, modal analysis method can be utilized to take advantage from the reduction in computational cost afforded by limiting the number of

eigenmodes. The spatial correlation in buffeting forces at different nodes of the bridge is assumed to be the same as the corresponding wind fluctuations (Chen and Kareem 2001). To perform the buffeting analysis in time-domain, following parameters are used: (1) a critical damping fraction of 0.003 for all eigenmodes (2) the analysis is performed in two steps (i) transient step which is simulated for 60 sec time period considering the constant mean static wind forces on the bridge deck to simulate the initial condition of vibration for the bridge (ii) modal step which is simulated for 600 seconds time period considering the static and buffeting components of wind forces (including self-excited forces) having a time increment size of 0.05 sec (3) the attendant buffeting response of the bridge deck is obtained from 60th sec to 660th sec. This approach was also practiced by (Boonyapinyo et al. 1999).

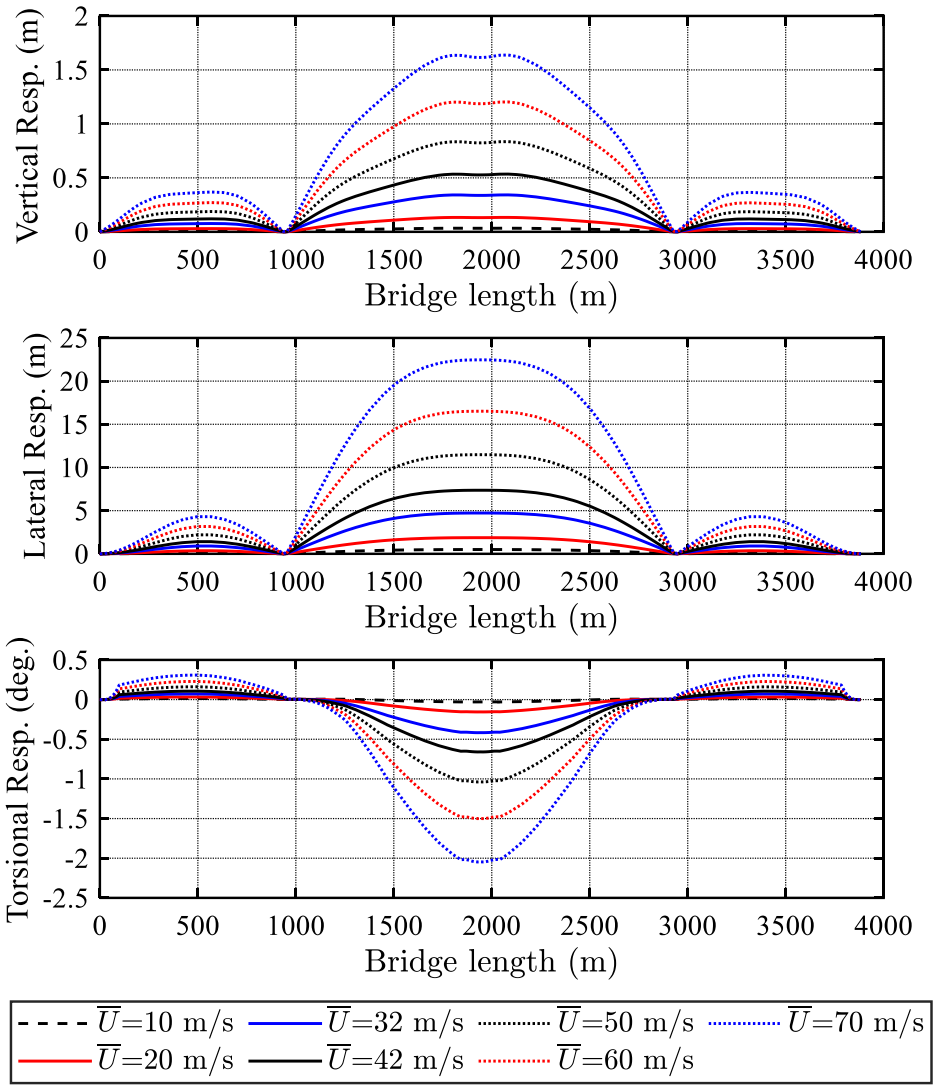

Figure 6-8 Aerostatic response of the deck of Akashi-Kaikyo bridge under different values of mean wind speeds including typhoon TY9807 (32 m/s) and 2018TY20 (42 m/s)

6.6 Aerostatic analysis

The nonlinear aerostatic analysis is performed based on the simple static wind model to investigate the effects due to the transient features of typhoon events on the aerostatic behavior of the bridge. The comparison of the mean values of bridge deck lateral, vertical, and torsional displacements at various mean wind speeds including the typhoon events TY9807 (32 m/s) and 2018TY20 (42 m/s) along the spanwise locations are plotted in Figure (6-8). The maximum displacement occurs at the center of the main span of the bridge deck. Moreover, the displacement increases proportionally with the square of wind velocity according to the Euler's beam theory.

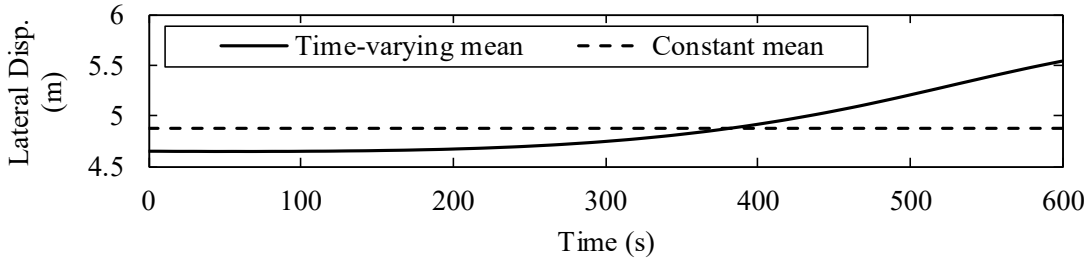

(a) Lateral displacement

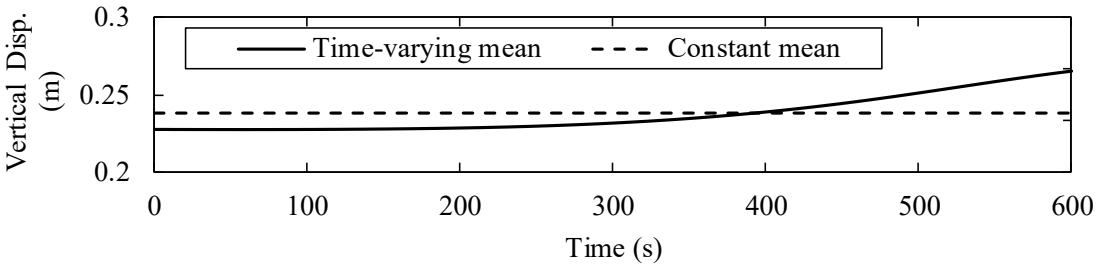

(b) Vertical displacement

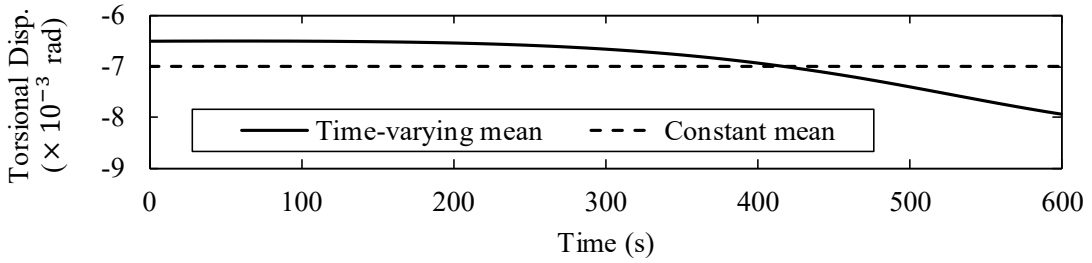

(c) Torsional displacement

Figure 6-9 The effects of constant and time-varying mean wind speeds on the static response of the Akashi-Kaikyo bridge under typhoon TY9807

Figure (6-9) shows a comparison between the effects of constant mean and time-varying mean wind speeds on the three-dimensional aerostatic response at the center node of main span of the bridge under typhoon TY9807. The time-varying mean wind speed causes the time-varying response of the bridge deck. The time-varying mean lateral displacement varies from 4.65 m to 5.54 m, whereas the constant mean lateral displacement is computed to be 4.88 m for 10 min time interval as shown in Figure (6.9a). The time-varying mean vertical displacement also shows similar behavior and varies about the corresponding time-invariant response obtained from the stationary constant mean wind speed as shown in Figure (6-9b). In the case of torsional displacement, both constant and time-varying mean responses show anti-clockwise angular motion, and it is interesting to note that the constant and time-varying means become equal at a time instant of 382 second as shown in Figure (6-5c). Similarly, the effects of constant and time-varying mean wind speeds on the three-dimensional aerostatic responses of the bridge deck are compared and investigated under typhoon 2018TY20, which elucidated that the time-varying mean wind speed can certainly cause a high aerostatic response of the bridge deck as compared to the constant mean wind speed. This highlights the paramount importance of adopting time-varying mean wind speed rather than the constant mean wind speed in the design of long-span bridges.

6.7 Buffeting analysis

The aerodynamic response of the Akashi-Kaikyo bridge deck under gusty wind conditions is interrogated using various aerodynamic wind load models. Since each wind load model has a unique way of formulating the aerodynamic forces; therefore, the time histories of responses computed by all models are to be compared with the measurement data of bridge displacement. Moreover, buffeting analysis results based on the proposed Volterra FD, Hybrid Volterra FD, and Volterra ANN models are also compared with the measurement response to check the efficacy of the proposed Volterra models. Figure (6-10) shows a comparison of time histories of the calculated aerodynamic response (vertical, lateral, and torsional displacements) based on each aerodynamic model including proposed Volterra models under typhoon TY9807 (mean wind speed of 32 m/s). The measurement data was recorded by GPS installed at the center of main span of the Akashi-Kaikyo bridge for the full duration of typhoon TY9807, in 1998, as a part of the investigation done by Honshu-Shikoku Bridge Authority (2001). Based on the aerodynamic response computed by each aerodynamic model, the following conclusions can be drawn:

1. the S model, being a 2D model, does not simulate the lateral response of the bridge. This shows the importance of accurate modeling the drag forces on the structure. Moreover, the S model yields a larger torsional displacement as compared to measurement data due to its

limitations for ignoring the effects of fluid memory and self-excited motion of the bridge deck as shown in Figure (6-10a),

2. the aerodynamic response based on LS model is higher than that based on S model, which indicates that the inclusion of static nonlinearity in terms of angle-varying static force coefficients (which are nonlinear functions of effective angle of attack) in S model reduces the aerodynamic response especially in the case of torsional degree of freedom (DOF) for the example bridge,
3. the three-dimensional aerodynamic response of the bridge based on the S model is close to the two-dimensional QS model. However, the QS model yields better simulation results than the S model, especially in the case of torsional displacement, which indicates that the efficiency of QS model to capture the effects of static nonlinearity is only improved in torsional DOF by including the self-excited motion of bridge deck. Conversely, no significant difference is observed between S and QS models in the case of lateral and vertical responses, which shows that the capability of 2D QS model is insufficient in vertical and lateral DOFs for the example bridge as shown in Fig (6-10a,c),
4. the aerodynamic response based on QS model is smaller than that based on the LQS model due to the linearization of QS model at the static angle of attack. This concludes that the linearization of static force coefficients at a statically deformed position of the bridge deck increases the aerodynamic response for this example bridge. In other words, the static nonlinearity included in the QS model decreases the aerodynamic response as compared to the LQS model in this case for the example bridge. Besides this, the comparison of the responses based on the QS and LQS models reveals that the static nonlinearity (without fluid memory effects) has significant effects on the torsional response, whereas its effect on the vertical response is minor. The differences between the QS and LQS models are due to the nonlinearity in the QS model arising from the dependency of static force coefficients on the effective angle of attack as shown in Figure (6-10c,d),
5. the aerodynamic response based on the CQS model is larger and smaller for the torsional and vertical responses, respectively as compared to that obtained from the QS model which indicates that the CQS model could not improve the torsional response even after considering the fluid memory effects at a fixed reduced frequency; however, it only improves the vertical response to some extent. The jaggedness in the CQS model results is due to relatively abrupt changes in the modified coefficient k_1 as shown in Figure (6-10e),
6. the torsional response based on the LU model is significantly lower than that based on 2D models i.e., QS model, and closer to the measured torsional response, which indicates that the inclusion of fluid memory effects arising from the history of motion due to wind flow substantially improves the prediction of torsional response of the bridge. As the LU model

is a 3D model, it also predicts the lateral response of the bridge utilizing the first-order IFs which exhibit transient characteristics of wind effects on the structure. Moreover, the efficiency of the LU model over 2D aerodynamic models is superior in the case of torsional response, which highlights that the effects of fluid memory are more significant on the torsional DOF than vertical DOF as shown in Figure (6-10f),

7. the vertical and torsional responses based on the LU model are larger than those based on the HNL model, which indicates that the inclusion of aerodynamic nonlinearity in the HNL model decreases the vertical and torsional displacements at 32 m/s for this example bridge. Moreover, introducing unsteady aerodynamic damping and stiffness in the QS model, which the HNL model uses to calculate wind forces for low-frequency range, reduces the response. This effect is more prominent in the torsional DOF. On the other hand, the lateral response obtained from the HNL model is larger than that obtained from the LU model. The increase in lateral response based on HNL may also be attributed due to the influence of choosing an appropriate cut-off frequency which is taken as the first fundamental frequency of the bridge model in this case. Although the HNL model yields better results than the LU model, yet it does not regenerate the time-varying behavior of the buffeting response owing to the assumptions of the stationary flow conditions as shown in Figure (6-10g),
8. the aerodynamic responses based on the Volterra FD, Hybrid Volterra FD and Volterra ANN models are close to the measurement response, which indicates that these models are suitable for capturing the higher-order aerodynamic nonlinearity and fluid memory effects arising from the amplitude-dependency of FDs, varying-angle static force coefficients, and history of bridge motion due to wind interaction on 2D time-scale in this case for the example bridge as shown in Figure (6-10h,i, j),
9. the aerodynamic response (both vertical and torsional) based on the Volterra FD model is closer to the measurement displacements as compared to the LU model; however, the results of the Volterra FD model are poorer than those of HNL model for all three-dimensional responses as shown in Figure (6-10h). This may be due to the fact that the Volterra FD model utilizes IFs identified at zero angle of attack while ignoring the amplitude-dependency of FDs and static force coefficients. However, the Volterra FD model incorporates the non-stationary wind effects on the buffeting response of the bridge, which are quite visible in the case of lateral response as shown in Figure (6-10h),
10. the simulation results of the buffeting response obtained from the Hybrid Volterra FD model are closer to the measurement data of bridge displacement as compared to the results obtained from the Volterra FD model. There are several reasons behind it, for instance, Hybrid Volterra FD model combines the QS model and the Volterra FD model while utilizing their best features. In other words, the Hybrid Volterra FD model segregates the effective

angle of attack into low- and high-frequency components. Correspondingly, aerodynamic forces are also separated based on the frequency components. For the low-frequency range, aerodynamic forces are modelled by the QS model just like HNL model, whereas the Volterra FD model is adopted for modeling the nonlinear aerodynamic forces for the high-frequency range while considering the amplitude-dependency of FDs, higher-order fluid memory effects and non-stationary wind effects simultaneously,

11. similar to the Hybrid Volterra FD model, the Volterra ANN also simulates the time-varying behavior of lateral response of the bridge under non-stationary winds. This model shows quite an improvement in the simulation of buffeting response, especially in the case of vertical and lateral responses. In other words, the Volterra ANN model yields the best simulation results of vertical and lateral responses among all aerodynamic models due to the capability of ANN to develop the nonlinear relationships between inputs and outputs through the associated synaptic weights carried by the activated neurons. However, a difference is observed between the measured and simulated torsional responses in the first 200 seconds where the amplitude of the simulated torsional response is smaller than the measured torsional response. Moreover, this model also considers the effects of nonlinear fluid memory and self-excited motion on the bridge deck accurately,
12. the aerodynamic response based on the Hybrid Volterra FD model is also close to that based on the Volterra ANN model, which highlights that both models consider the aerodynamic nonlinearity and nonlinear fluid memory effects accurately. Moreover, the inclusion of first- and second-order direct- and cross-terms of Volterra kernels at varying angles of attack in Hybrid Volterra FD and Volterra ANN models improves the simulation results,
13. the Hybrid Volterra FD and Volterra ANN models are capable to capture aerodynamic nonlinearities and fluid memory effects for all frequency ranges, whereas the HNL model captures nonlinearities for low-frequency range by using QS model and linear fluid memory effects for the high-frequency range by using LU model. Thereby, the torsional response based on the HNL model is higher than that based on Volterra models,
14. based on the comparative results, the contribution of the fluid memory effects to the aerodynamic response is significantly higher than that of aerodynamic nonlinearity effects for this example bridge. This comparison further indicates that the inclusion of fluid memory effects has a significant impact on the torsional response specifically since there are large differences between the torsional responses obtained from the 2D aerodynamic models i.e., S, QS, LQS models, and obtained from the Volterra FD, Hybrid Volterra FD, and Volterra ANN models. It can also be witnessed from the larger relative difference between torsional response calculated by 2D models and 3D proposed Volterra models as compared to the relative difference between the vertical response,

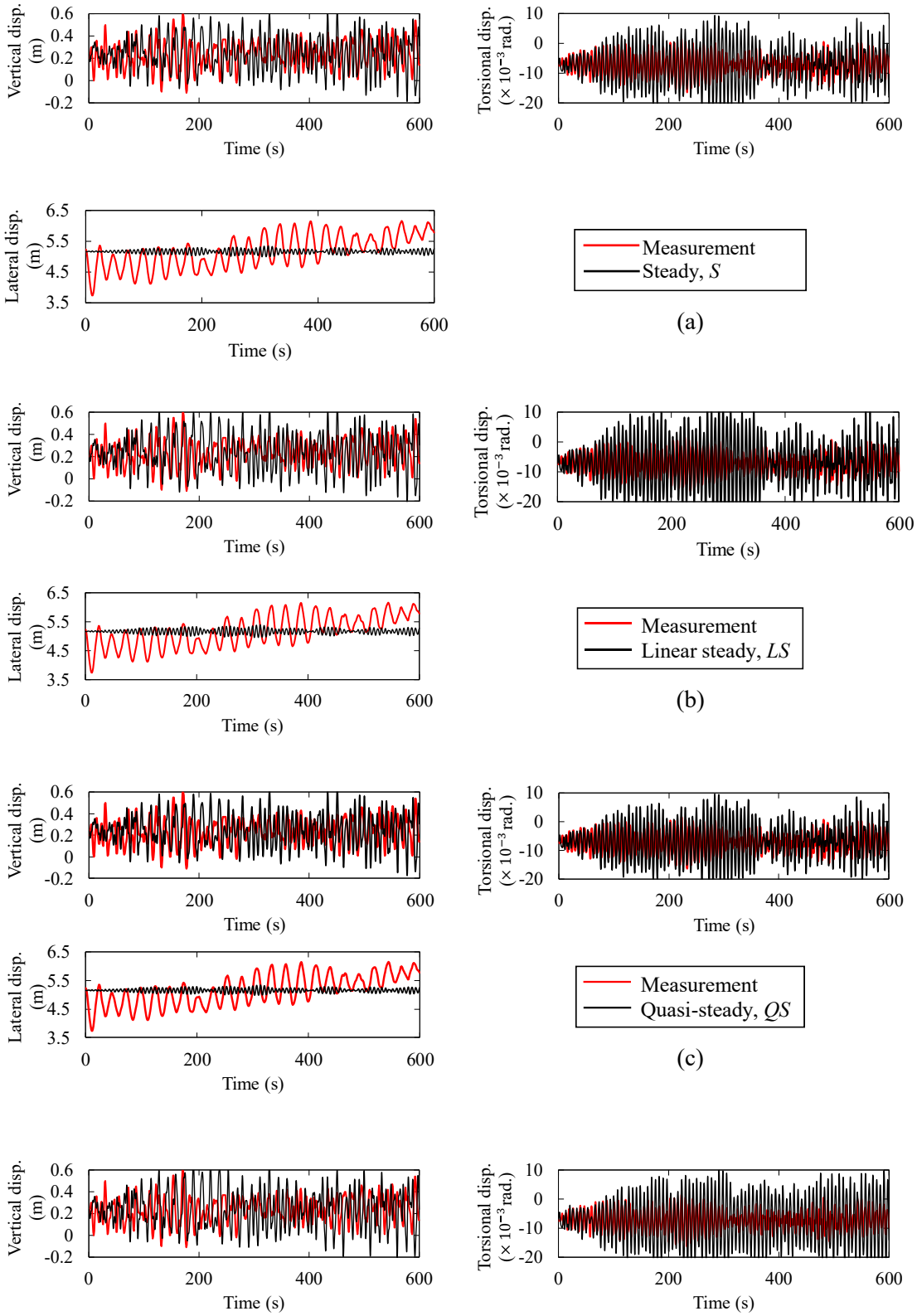
Vertical disp. (m)
Torsional disp. (× 10⁻³ rad.)
Lateral disp. (m)
Time (s)
Measurement
Steady, S
(a)
Measurement
Linear steady, LS
(b)
Measurement
Quasi-steady, QS
(c)

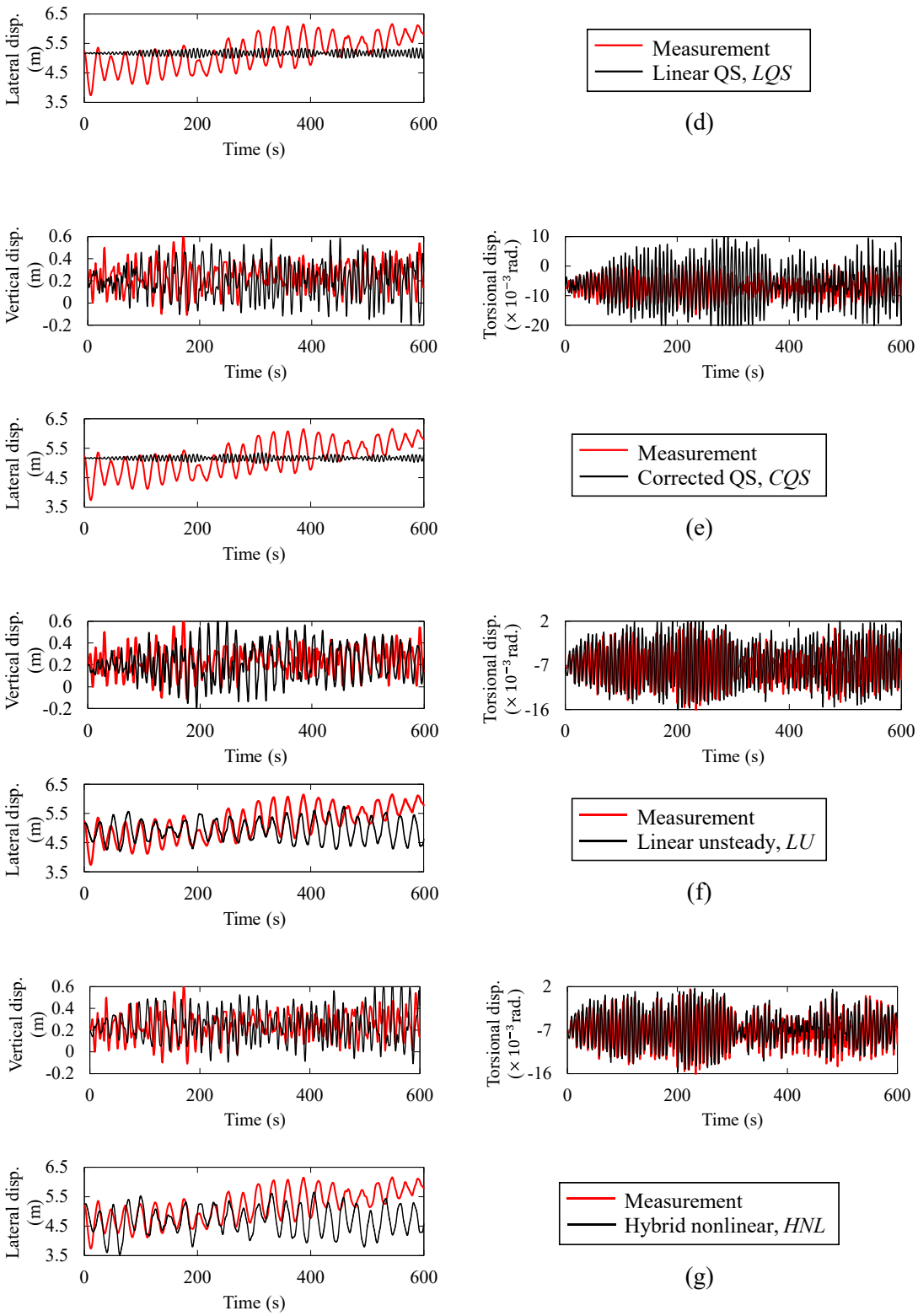
Lateral disp. (m)
Vertical disp. (m)
Torsional disp. (× 10⁻³ rad.)
Time (s)
Measurement
Linear QS, LQS
(d)
Measurement
Corrected QS, CQS
(e)
Measurement
Linear unsteady, LU
(f)
Measurement
Hybrid nonlinear, HNL
(g)

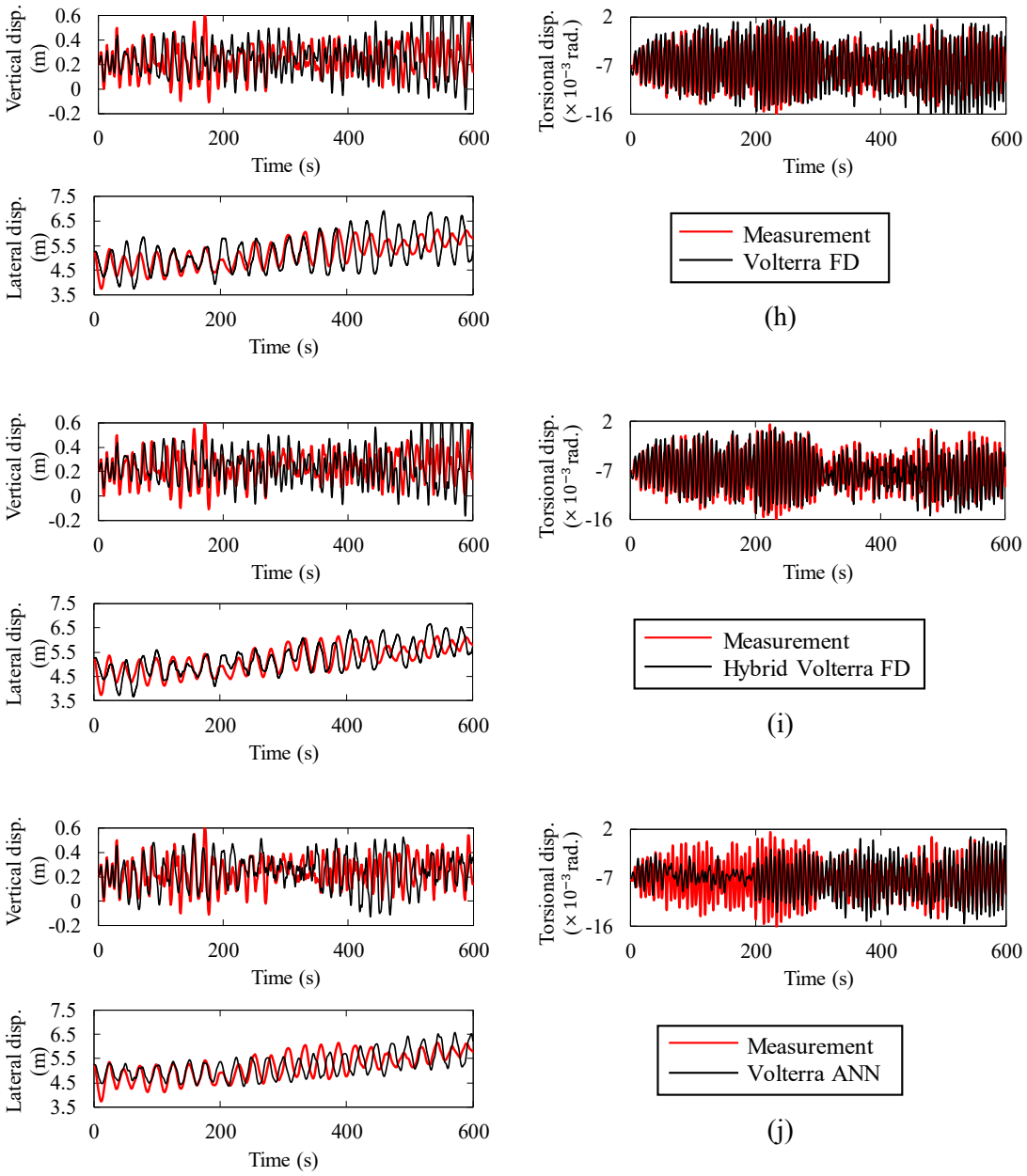

Figure 6-10 Time histories of the three-dimensional calculated responses based on each model: (a) comparison of results obtained from S model and measurement response, (b) comparison of results obtained from LS model and measurement response, (c) comparison of results obtained from QS model and measurement response, (d) comparison of results obtained from LQS model and measurement response, (e) comparison of results obtained from CQS model and measurement response, (f) comparison of results obtained from LU model and measurement response, (g) comparison of results obtained from HNL model and measurement response, (h) comparison of results obtained from Volterra FD model and measurement response, (i) comparison of results

obtained from Hybrid Volterra FD model and measurement response, and (j) comparison of results obtained from Volterra ANN model and measurement response

It is always lucrative to show the time history of random signals into frequency-domain in order to envisage the exciting frequency contents and associated amplitude of power spectral density (PSD) function. Following it, PSD of each component of buffeting response is plotted in the frequency-domain through Fourier transformation by using *fft* in-built function in MATLAB (2017) for 3D aerodynamic models including the LU, HNL, Volterra FD, Hybrid Volterra FD, and Volterra ANN models as shown in Figures (6-11)−(6-15). It is clear from the frequency-domain analysis results that the LU and HNL models do not fit the measured lateral response spectrum ($S_p(f)$) in the low-frequency range because of the assumption of stationary wind. Conversely, Volterra FD, Hybrid Volterra FD, and Volterra ANN models fit the measured lateral response in the low-frequency range. However, Volterra FD and Volterra ANN models show some deviations in the high-frequency range which is not so important for long-span bridges. Moreover, the Volterra FD, Hybrid Volterra FD, and Volterra ANN models are capable to capture the peaks of the measured response spectra. From this comparison, it can be concluded that Hybrid Volterra FD provides the best simulation results for lateral response spectra, whereas Volterra ANN yields the best results for torsional and vertical response spectra as shown in Figures (6-14) and (6-15).

Based on Figure (6-10), it is obvious that these models can be divided into two groups (1) the models which cannot take into account the fluid memory effects including the S, LS, QS and LQS models and (2) the models which account for the fluid memory effects including the LU, HNL, Volterra FD, Hybrid Volterra FD, and Volterra ANN models. The ability of the CQS to reasonably account for the fluid memory effects is not assured so far. It is observed that the models with the fluid memory yield the magnitude of buffeting response lesser than the models without fluid memory effects, which indicates that fluid memory effects reduce the response of the bridge deck. This is also consistent with the root-mean square (RMS) values of the simulation results for vertical and torsional responses as shown in Figure (6-16). Based on this comparison, it is observed that the LU model, among those models which include fluid memory effects, yields the largest RMSs of the vertical and torsional responses, whereas the models which do not include the fluid memory effects yield almost similar RMSs of the lateral and vertical responses of the bridge deck under typhoon TY9807 as shown in Figure (6-16). However, some variations in RMSs are also observed in the case of 2D models for the torsional response due to the effect of angle-varying static force coefficients i.e., S, QS, and CQS models. The effects of aerodynamic nonlinearity and fluid memory on the buffeting response are also investigated by comparing the responses obtained from the LU, HNL, and Volterra models. A hefty difference is observed in the vertical, lateral, and torsional responses obtained from all 3D wind load models.

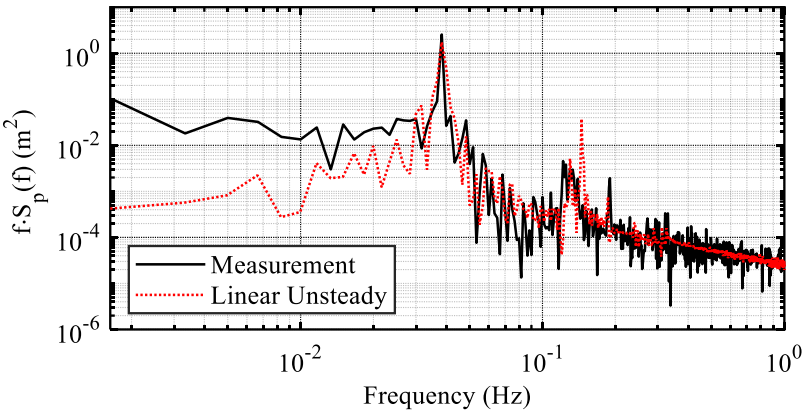

(a) PSD of lateral response

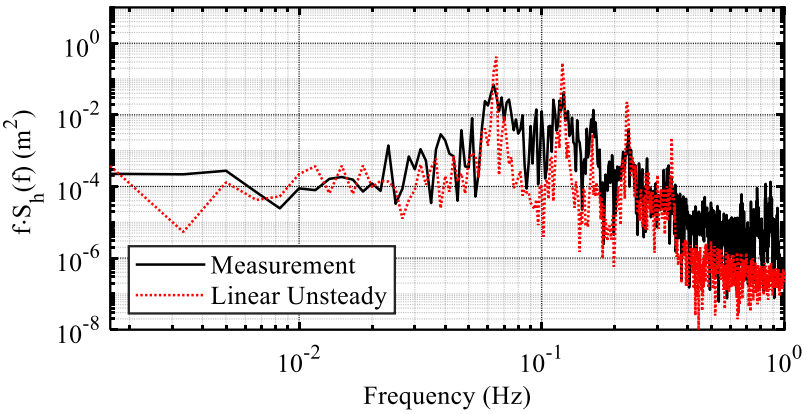

(b) PSD of vertical response

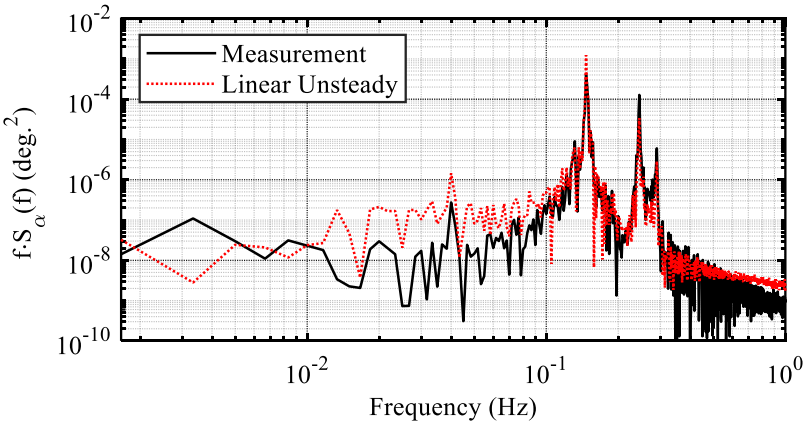

(c) PSD of torsional response

Figure 6-11 PSD comparison of measured response and simulated buffeting response using LU model in frequency-domain under typhoon TY9807

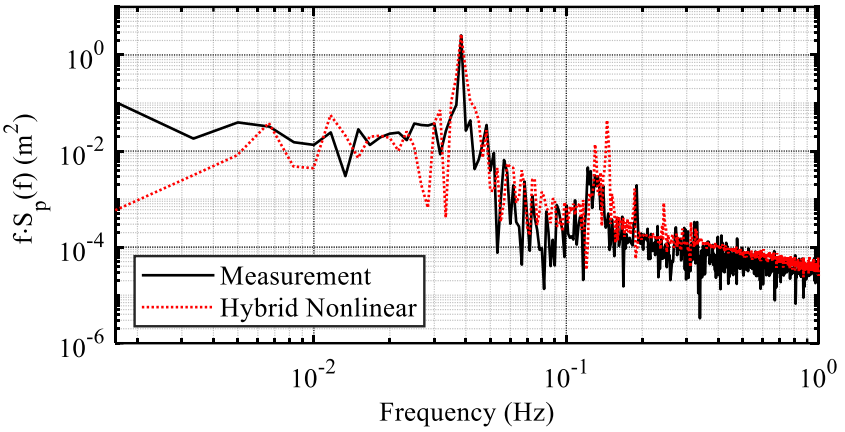

(a) PSD of lateral response

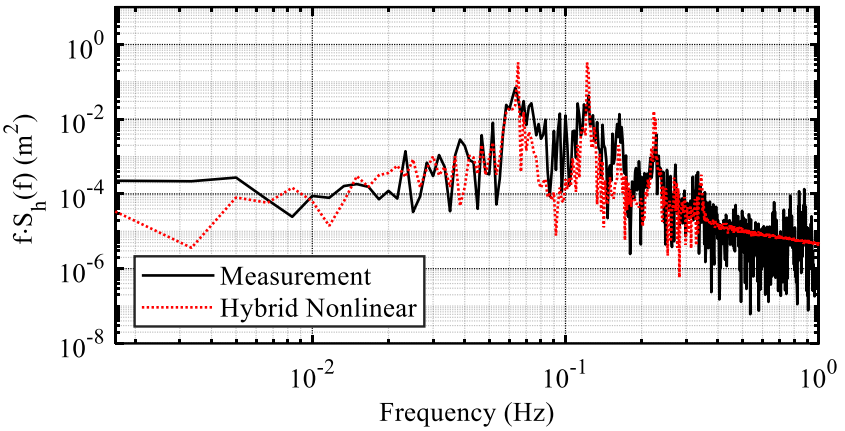

(b) PSD of vertical response

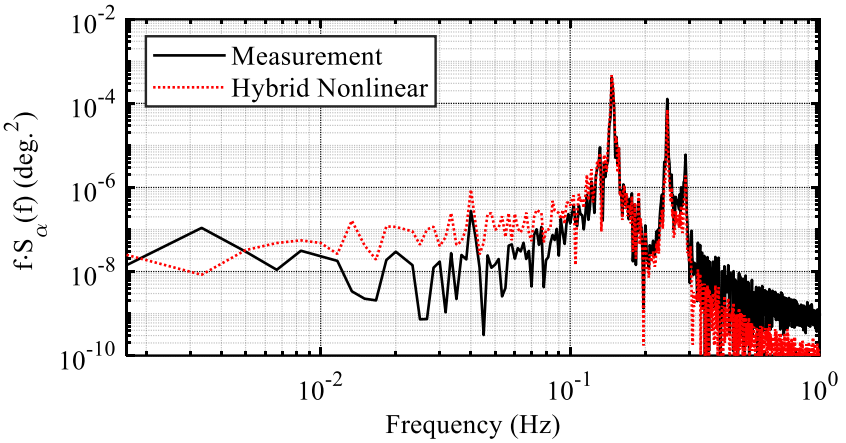

(c) PSD of torsional response

Figure 6-12 PSD comparison of measured response and simulated buffeting response using hybrid nonlinear (HNL) model in frequency-domain under typhoon TY9807

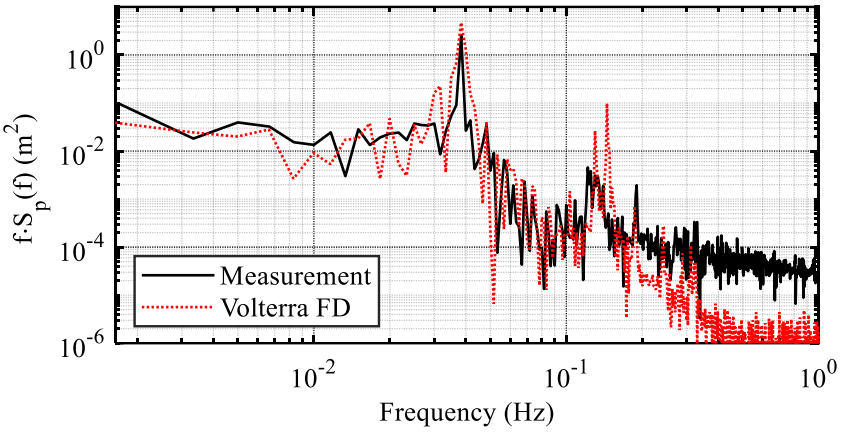

(a) PSD of lateral response

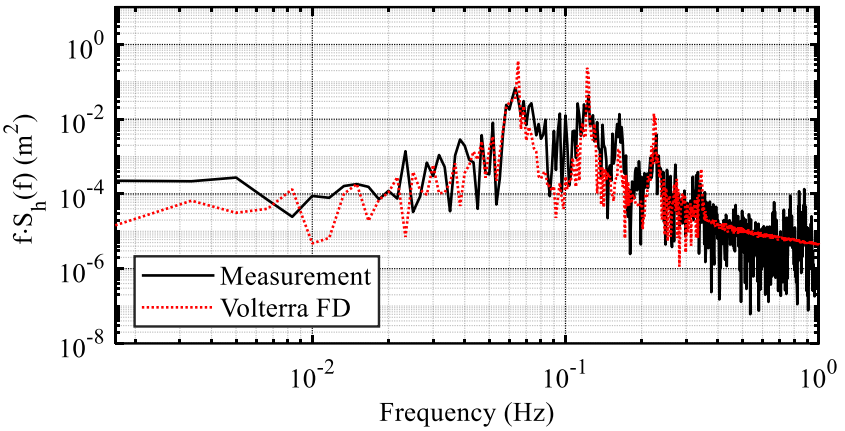

(b) PSD of vertical response

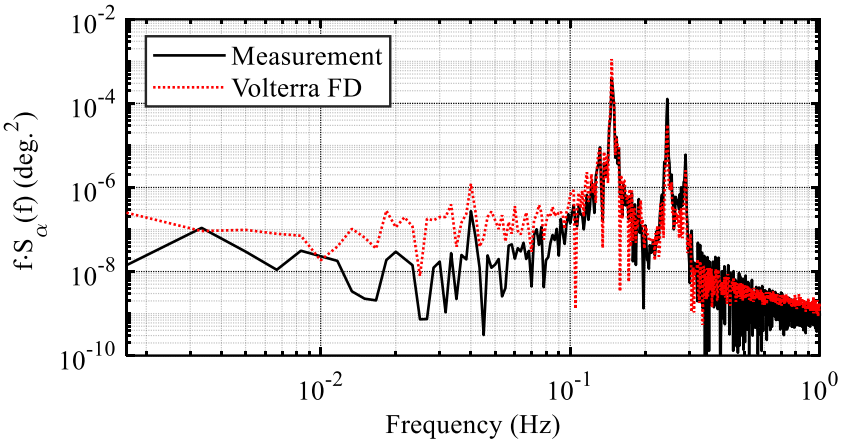

(c) PSD of torsional response

Figure 6-13 PSD comparison of measured response and simulated buffeting response using Volterra FD model in frequency-domain under typhoon TY9807

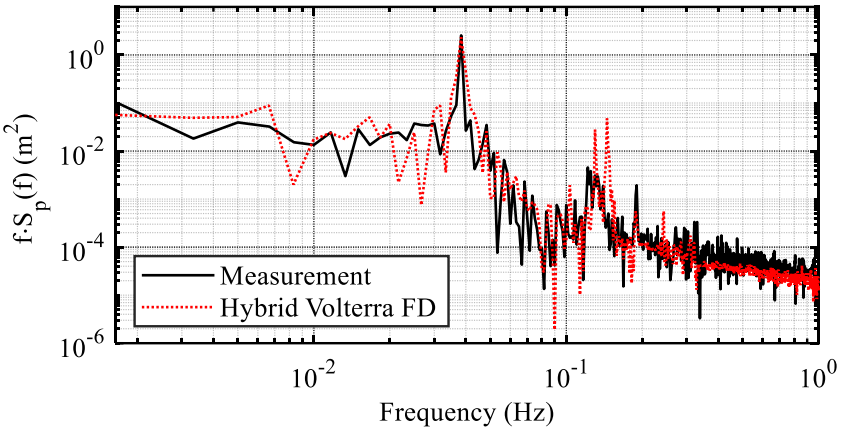

(a) PSD of lateral response

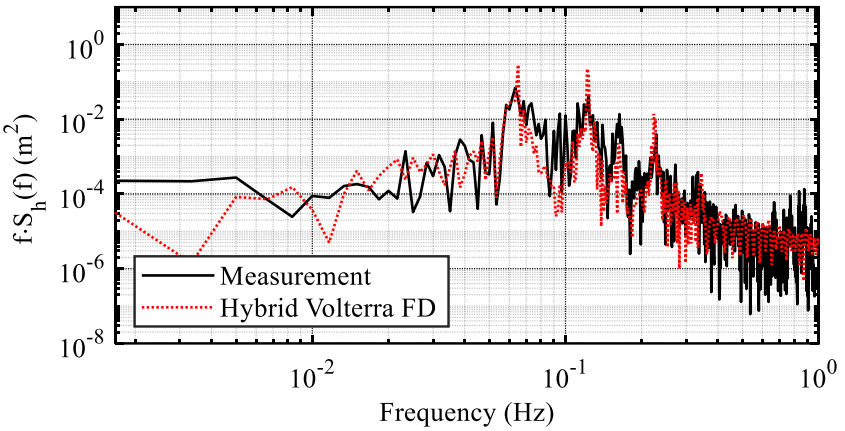

(b) PSD of vertical response

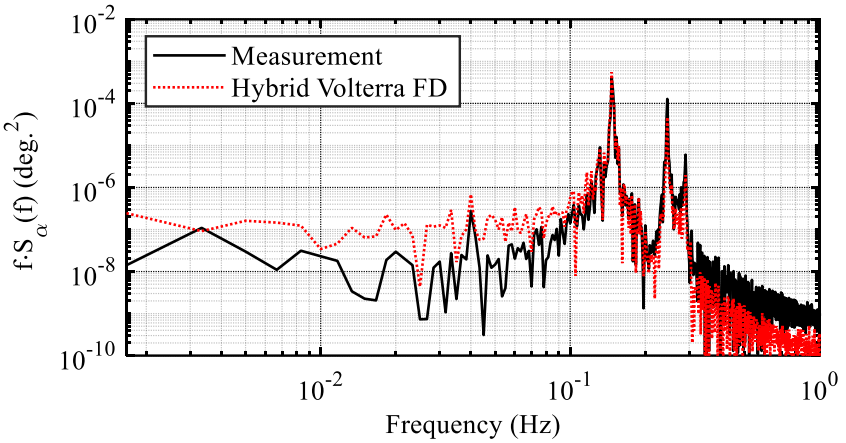

(c) PSD of torsional response

Figure 6-14 PSD comparison of measured response and simulated buffeting response using Hybrid Volterra FD model in frequency-domain under typhoon TY9807

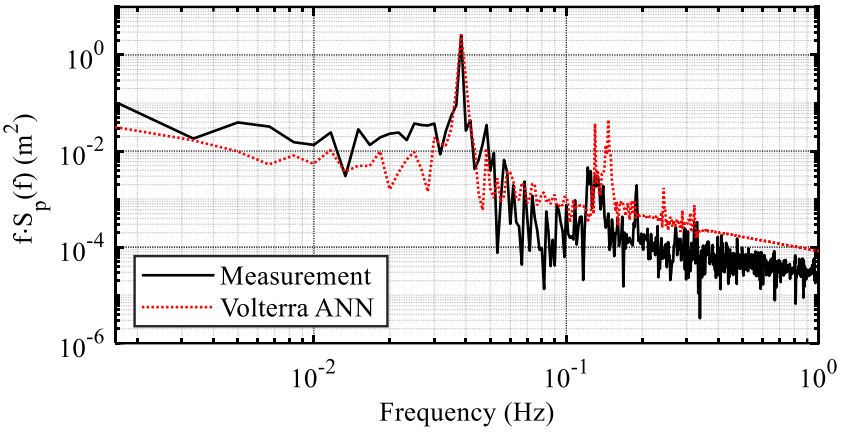

(a) PSD of lateral response

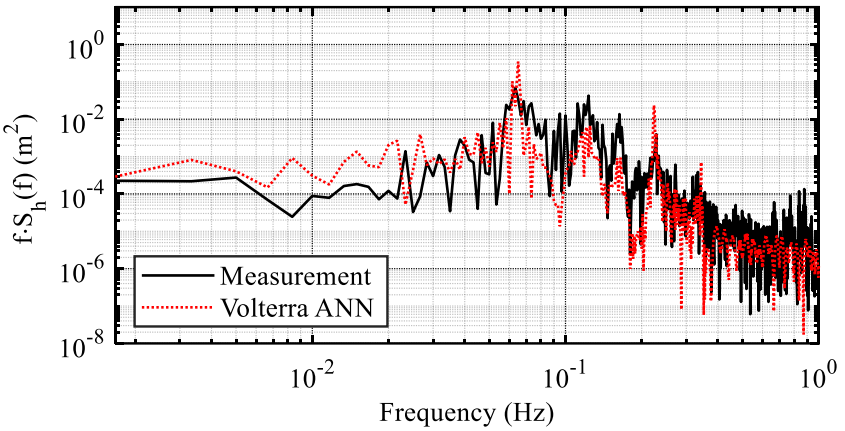

(b) PSD of vertical response

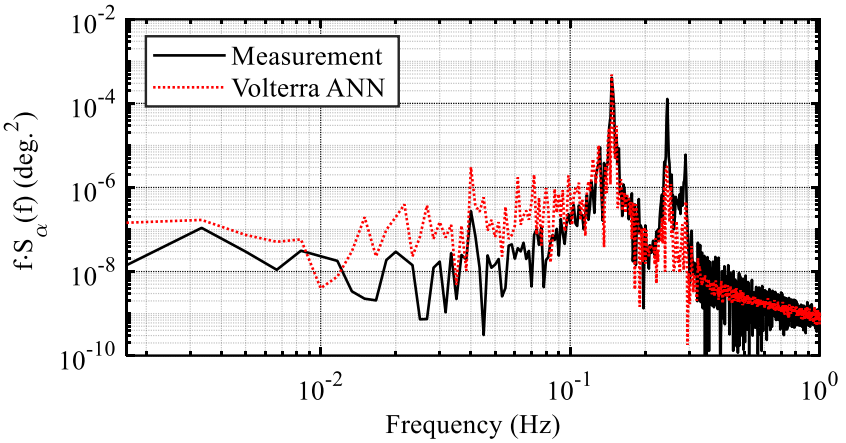

(c) PSD of torsional response

Figure 6-15 PSD comparison of measured response and simulated buffeting response using Volterra ANN model in frequency-domain under typhoon TY9807

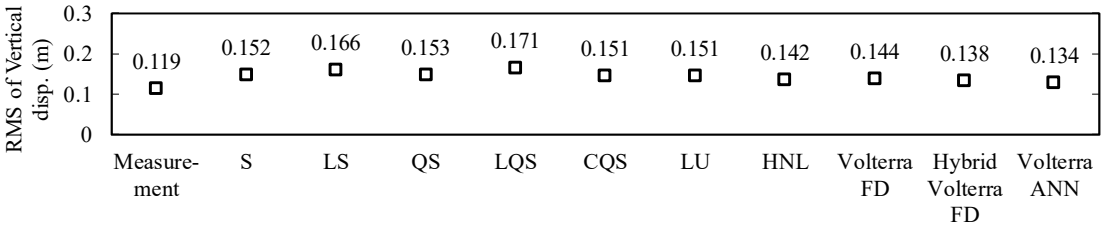

(a) RMS of vertical response

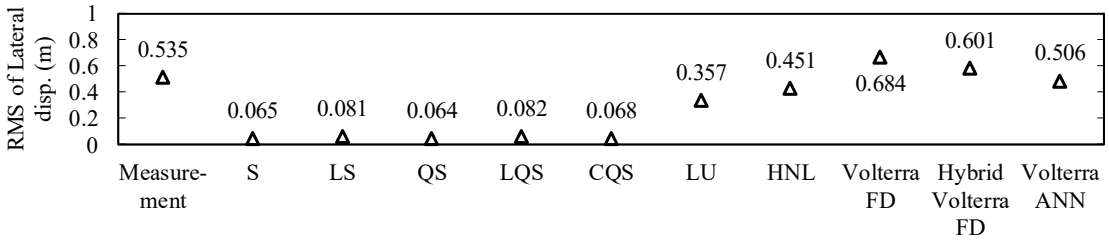

(b) RMS of lateral response

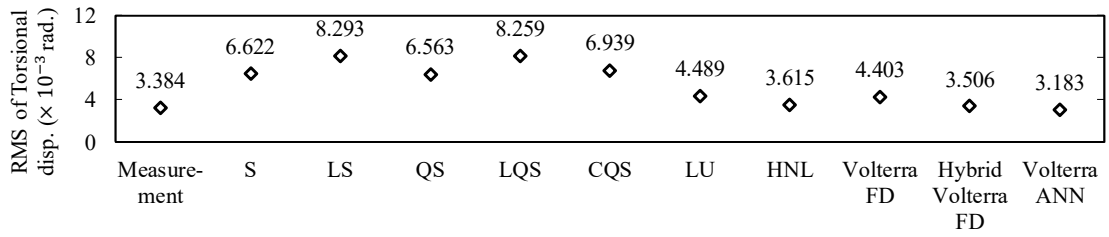

(c) RMS of torsional response

Figure 6-16 RMS comparison of fluctuating part of buffeting responses based on various aerodynamic models under typhoon TY9807

Comparing the LU and HNL models in the context of nonlinearity arising from the dependency of aerodynamic forces on the effective angle of attack, it is clear from Figure (6-16) that the RMSs of vertical and torsional responses obtained from the HNL model are lower than those obtained from the LU model. This indicates that the inclusion of nonlinearity reduces the RMS of vertical and torsional responses. However, different behavior is observed in the case of lateral response in which the HNL model shows a higher RMS than the LU model.

On the other hand, the Volterra FD model results are in between LU and HNL models because of the reason that Volterra FD model does not divide the wind speed fluctuations and bridge motions into low- and high-frequency ranges, instead, this model utilizes the wind speed fluctuations and bridge motion for the entire range of frequency while considering the static force coefficients identified at a statically deformed position of the deck as shown in Figure (6-16). The

improvement of the Volterra FD model is mainly due to the incorporation of nonlinear fluid memory effects in terms of second-order Volterra kernels in the LU model while keeping all other parameters same as in LU model.

With the further modification of the Volterra FD model to Hybrid Volterra FD model by incorporation of aerodynamic nonlinearity partly due to the nonlinear function of aerodynamic forces with varying angles of attack, the simulation results of buffeting response are significantly improved. This explicates that the inclusion of aerodynamic and aeroelastic nonlinearities in low-frequency range by the QS model, the nonlinear fluid memory effects in terms of second-order Volterra kernels identified at varying angles of attack in high-frequency range by the Volterra FD model and non-stationary wind effects improves the numerical simulation of buffeting response of long-span bridges under typhoon winds. This is also clear from the RMS comparison of fluctuating part of the buffeting response in all three-dimensions for the example bridge as shown in Figure (6-16). In short, it is reasonable to state herein that the Hybrid Volterra FD model considers the aerodynamic nonlinearity and nonlinear fluid memory effects precisely for super long-span cable-supported bridges subjected to the non-stationary winds.

The RMSs of the vertical and torsional displacements from LU and HNL models are higher as compared to the Volterra ANN model for the example bridge as shown in Figure (6-16). Comparing Volterra ANN model with Volterra FD and Hybrid Volterra FD models, it is obvious from the RMS comparison that Volterra ANN model yields RMSs of lateral and torsional responses closest to RMSs of measured lateral and torsional responses, which shows the superiority of Volterra ANN model over Volterra FD and Hybrid Volterra FD models because Volterra ANN intuitively captures the aerodynamic nonlinearity in terms of higher-order neural memory from the non-proportional relationship of wind speed (input) and bridge deck motion (output) while considering the effects of non-stationary winds on the bridge response.

In order to check the efficiency of the proposed Volterra models with respect to the measurement response and existing aerodynamic models, the relative error in root-mean square (RMS) with respect to measurement response is evaluated such as:

$$\text{Error} = \frac{\text{RMS}_{\text{exact}} - \text{RMS}_{\text{sim}}}{\text{RMS}_{\text{exact}}} \times 100 \tag{6.1}$$

where $\text{RMS}_{\text{exact}}$ is the RMS of the measured response and RMS_{sim} is the RMs of the simulated response obtained from each aerodynamic model. Figure (6-17) shows the comparison of relative error in RMSs in simulated buffeting response based on each aerodynamic model including the proposed Volterra FD, Hybrid Volterra FD, and Volterra ANN models with respect to the measurement response of the Akashi-Kaikyo bridge under typhoon TY9807. The maximum relative errors are observed in the simulation results obtained from LS and LQS models in the case of torsional and vertical responses, respectively, whereas the S, QS, and CQS models show

almost the same but the maximum relative errors in RMS of the torsional response of the bridge. On the other hand, Hybrid Volterra FD and Volterra ANN models show the least relative errors in RMSs of aerodynamic responses and exhibit the best simulation results for prediction of buffeting response of the bridge subjected to typhoon-induced non-stationary winds. In fact, Volterra ANN shows even better simulation results than Hybrid Volterra FD in the case of lateral and vertical responses. This is because the ANN approach builds up the mapping of nonlinear relationships between the incoming wind flow and bridge displacement through the synaptic weights of the activated neurons in a nonlinear fashion. However, in the case of torsional response, the Hybrid Volterra FD model shows better simulation results than Volterra ANN model due to fact that Hybrid Volterra FD model considers the Volterra kernels identified from experimental data of FDs measured at varying angles of attack, which has more impact on the torsional DOF than vertical DOF. These results confirm the suitability and superiority of the proposed Volterra FD model to the LU model, and proposed Hybrid Volterra FD model to the HNL model. Moreover, these results also show a very preponderant role of first- and second-order IFs at varying angles of attack in the nonlinear buffeting analysis of long-span bridges.

Apart from Volterra models, the HNL model is the second most suitable method to predict the buffeting response accurately for the example bridge as shown in Figure (6-17). For the sake of further investigation on the efficacy of the proposed Volterra models, the LU and HNL models are treated herein as representative/reference aerodynamic models because LU and HNL models are widely used in the field of bridge aerodynamic/aeroelasticity. A comparison is drawn for a 10 min time period of vibration history between the simulation results obtained from the LU and HNL models and the simulation results obtained from the Volterra FD, Hybrid Volterra FD, and Volterra ANN models under typhoon 2018TY20. The bridge exhibits a coupled 3D random vibration phenomenon about a time-varying mean displacement of the bridge deck based on Volterra models as shown in Figure (6-18). The bridge also shows a larger aerodynamic response under typhoon 2018TY20 ($\overline{U}$=42 m/s) as compared to typhoon TY9807 ($\overline{U}$=32 m/s), which is as expected. Owing to the lack of measurement data of bridge response under typhoon 2018TY20, the comparison of the time history of buffeting responses obtained from Volterra FD, Hybrid Volterra FD, and Volterra ANN models is investigated with respect to HNL and LU models in order to envisage their practicality and suitability. In the case of lateral displacement, the LU model produces the linear and stationary wind-induced buffeting response about a constant mean response, whereas Volterra FD, Hybrid Volterra FD, and Volterra ANN models exhibit buffeting response about the time-varying mean response of the bridge under non-stationary winds as shown in Figure (6-18). In the case of vertical response, the LU, HNL, and Volterra FD models simulate the almost same vertical response, whereas the Hybrid Volterra FD and Volterra ANN models show different vertical responses. In the case of lateral response, all models except the

Volterra ANN model generate in-phase buffeting responses having different magnitudes. More specifically, the LU, HNL, and Volterra FD models generate nearly the same in-phase buffeting response (all three-dimensional components) of the bridge except the fact that the Volterra FD model gives rise to a slightly higher response than that based on LU and HNL models as shown in Figure (6-18). Regarding the torsional response, the Volterra ANN model yields a higher torsional buffeting response as compared to other aerodynamic models at 42 m/s for this example bridge. However, this trend may vary depending on the turbulence intensity and mean wind speed.

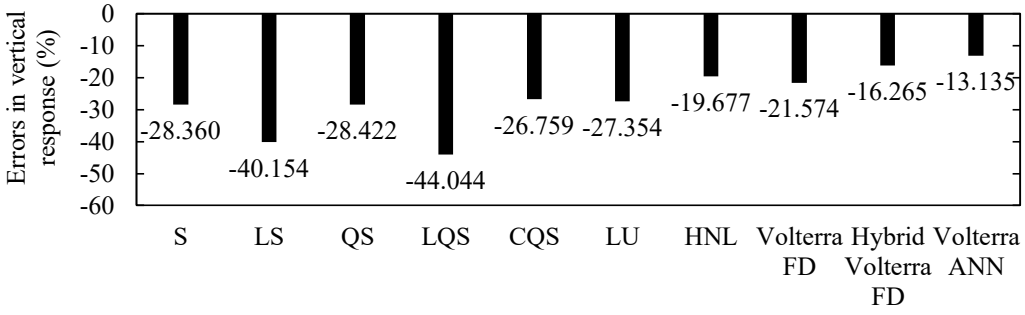

(a) Error in RMS of vertical response

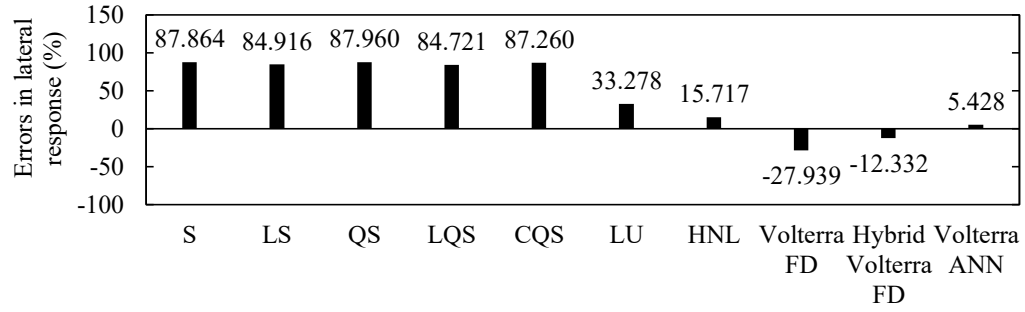

(b) Error in RMS of lateral response

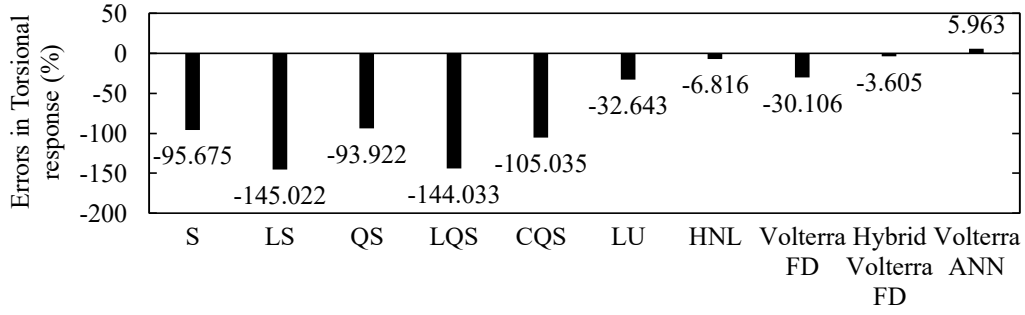

(c) Error in RMS of torsional response

Figure 6-17 Error in RMS of buffeting response of the Akashi-Kaikyo bridge based on various aerodynamic models under typhoon TY9807

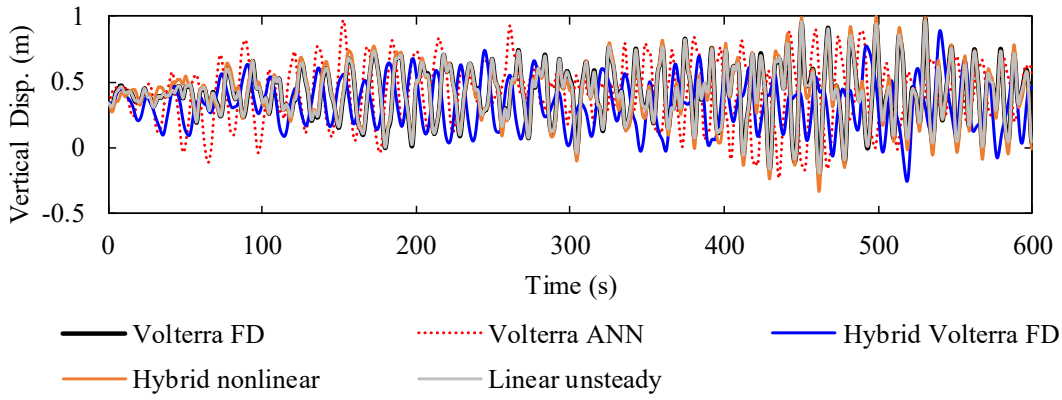

(a) Vertical response

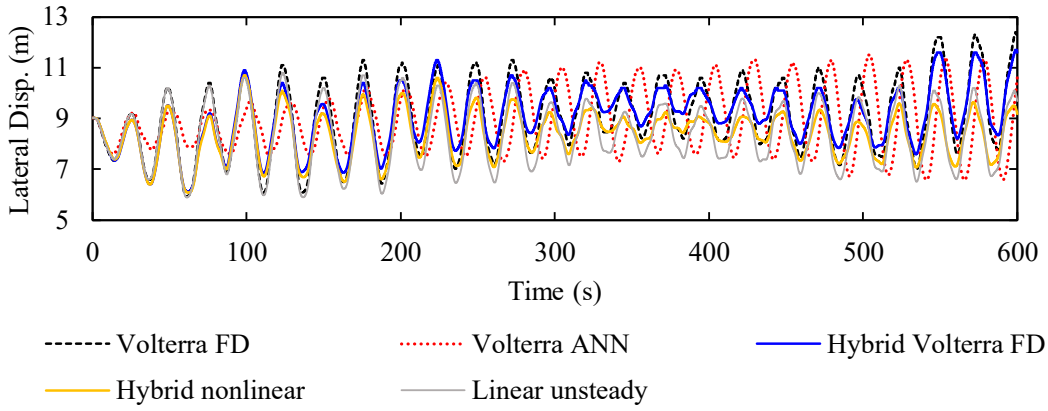

(b) Lateral response

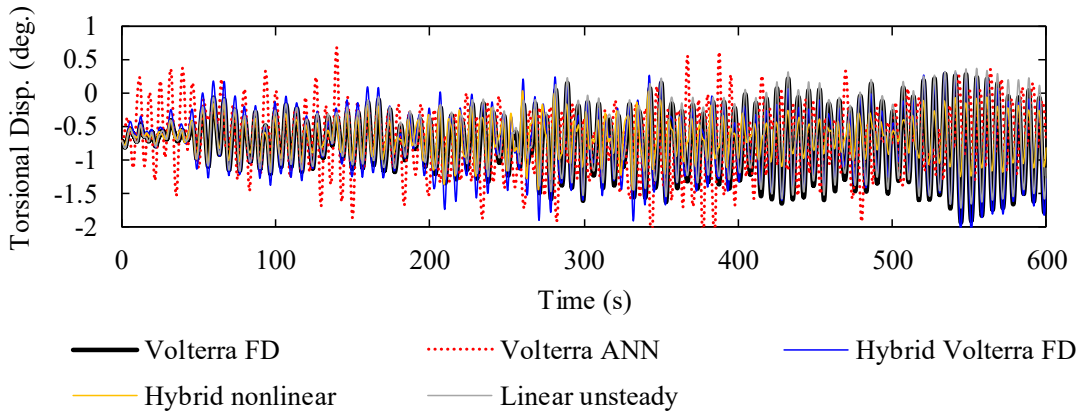

(c) Torsional response

Figure 6-18 Comparison between buffeting responses of the Akashi-Kaikyo bridge subjected to typhoon 2018TY20 obtained from LU, HNL, Volterra FD, and Volterra ANN models

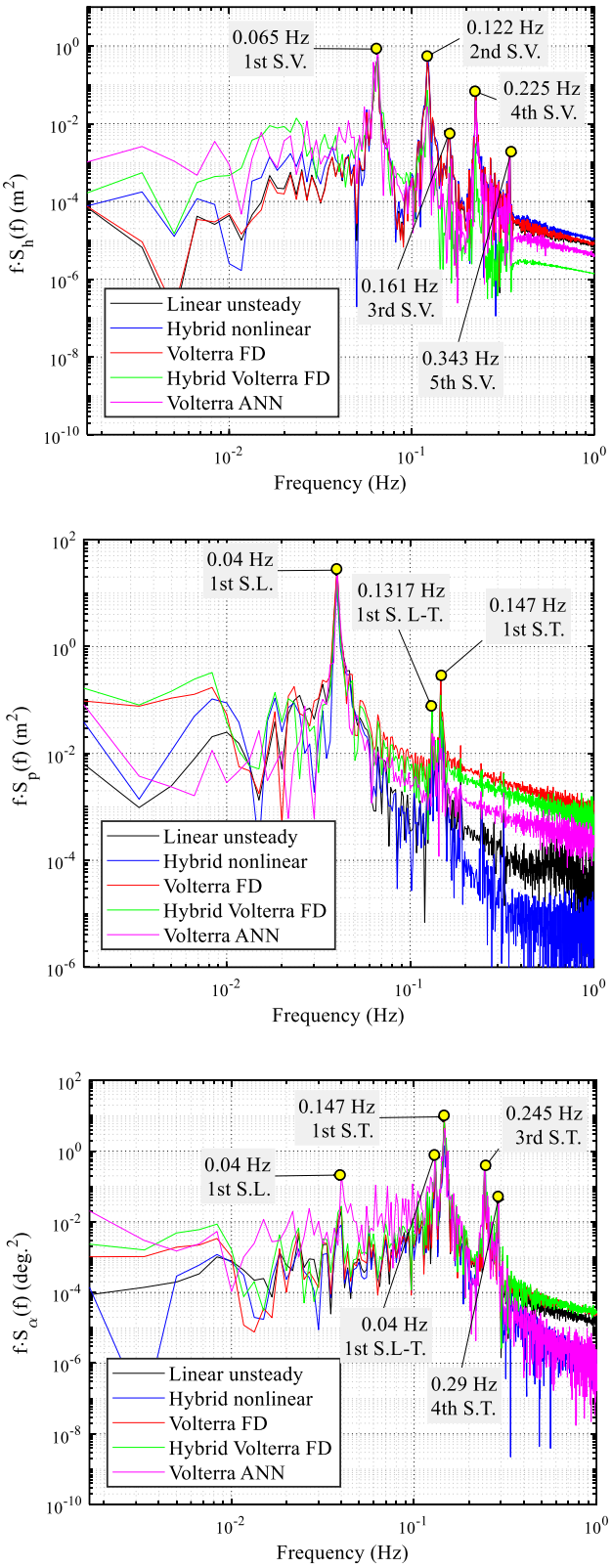

Figure 6-19 PSD Comparison of buffeting responses of obtained from different models under 2018TY20 (where S: symmetric, L: lateral, V: vertical, T: torsional, L-T: lateral-torsional)

To further investigate the simulation results obtained from different aerodynamic models under typhoon 2018TY20, PSDs of the fluctuating components of simulated lateral, vertical, and torsional displacements of the bridge are investigated in the frequency-domain as shown in Figure (6-19). The peaks of PSDs of lateral responses obtained from the Volterra models match well with PSD of LU and HNL models as shown in Figure (6-19); however, a difference is observed between simulated PSDs obtained from the Hybrid Volterra model and the LU model in the low-frequency range due to the impact of time-varying characteristics of wind speed on the simulated response. Similarly, the PSDs of the vertical and torsional responses obtained from the Hybrid Volterra model show large magnitude in the low-frequency range, explicating the effects of non-stationary winds on the buffeting response of the bridge. Besides this, the frequency contents of the eigenmodes of the Akashi-Kaikyo bridge are also captured from the PSD plots of the simulated buffeting responses in all three-dimensions as shown in Figure (6-19) in which S denotes symmetric; L denotes lateral; T represents torsion, and V is vertical.

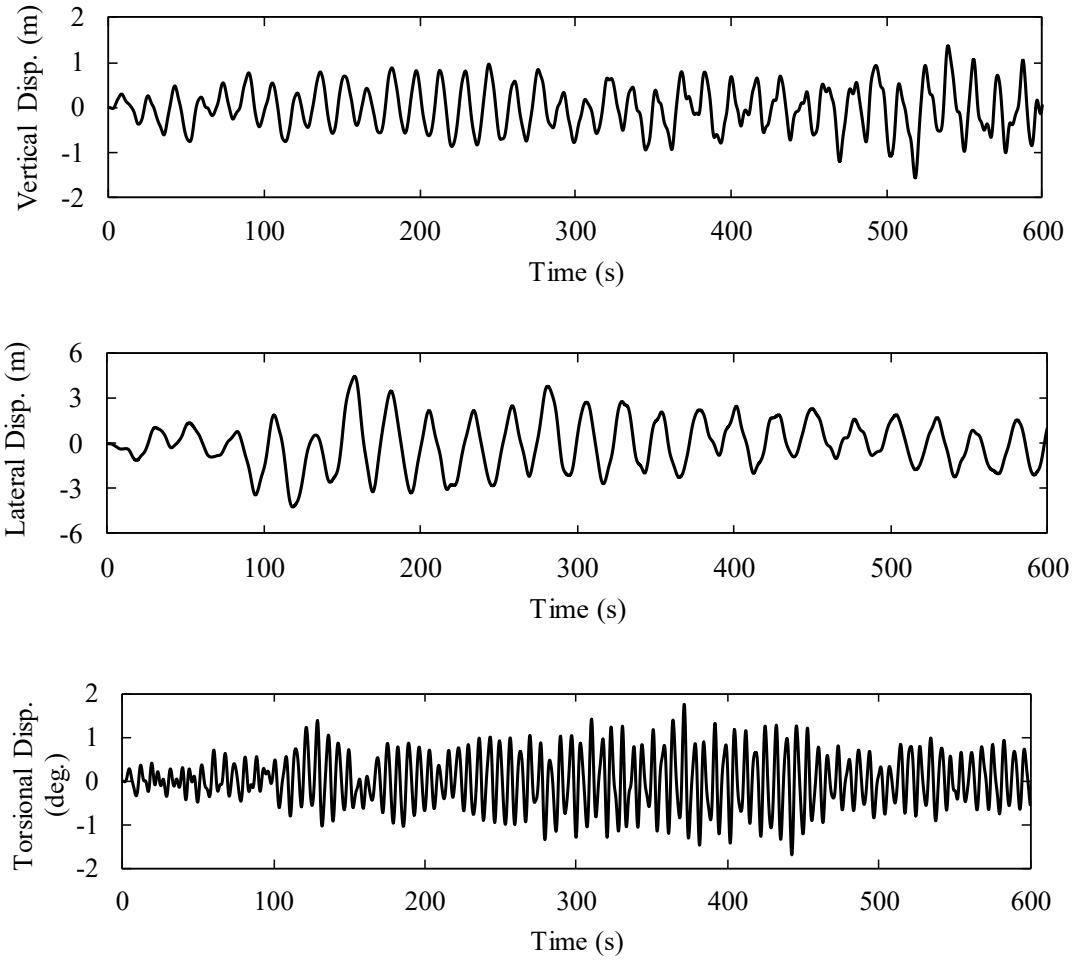

Figure 6-20 Buffeting response of the Akashi-Kaikyo bridge by nonlinear analysis based on the Hybrid Volterra FD model at 60 m/s

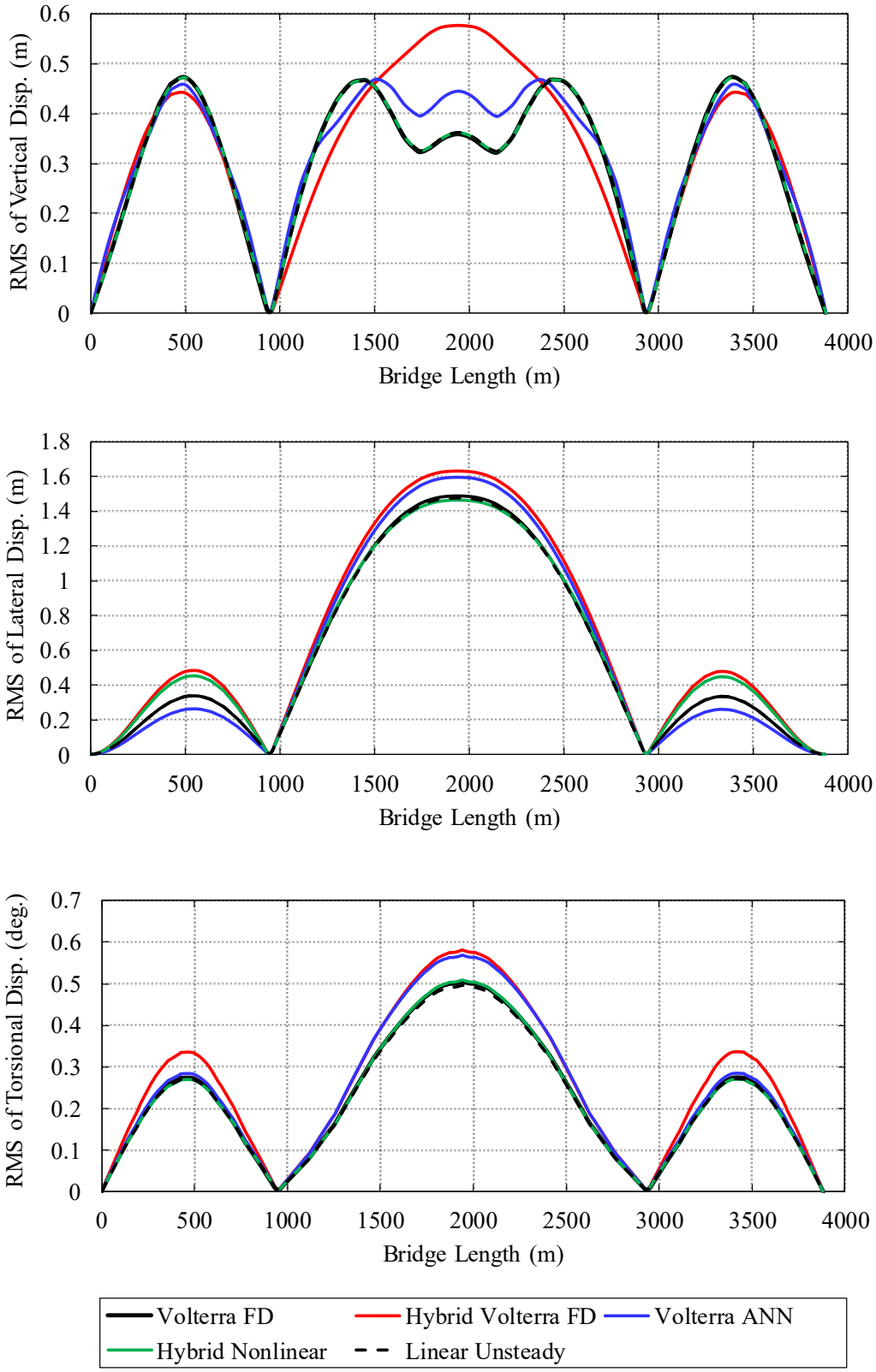

Figure 6-21 Comparison between RMS buffeting responses of the Akashi-Kaikyo bridge obtained from LU, HNL, Volterra FD, Hybrid Volterra FD and Volterra ANN models at 60 m/s

To examine the appropriateness of the proposed Volterra models at high wind speed, say 60 m/s, the nonlinear buffeting analyses are performed based on each aerodynamic model including LU, HNL, Volterra FD, Hybrid Volterra FD, and Volterra ANN models. Figure (6-20) shows the three-dimensional time-histories of buffeting response at the center node of the Akashi-Kaikyo bridge obtained from the Hybrid Volterra FD model at 60 m/s. The transient effects of nonlinear IFs identified at varying angles of attack can be visualized in the case of lateral response in between 100 to 200 seconds where the response experiences an abrupt step-change. This is possibly due to the flow separation in lateral DOF at high wind speed, which exerts significant pressure on the bridge bluff deck. Figure (6-21) compares the RMS of buffeting response of the bridge deck along the bridge length at 60 m/s calculated by LU, HNL, Volterra FD, Hybrid Volterra FD, and Volterra ANN models. It is noted that for this specific example the analysis based on the Hybrid Volterra FD model yields higher response as compared to other models, which shows that buffeting response is very sensitive to the changes in the wind angle of attack. However, the results of this example bridge regarding the effects of nonlinear aerodynamics may not simply be extended to other bridge structures that may require preliminary examination based on their aerodynamic and structural characteristics.

CHAPTER 7: CONCLUSIONS AND FUTURE DIRECTIONS

The safety of the long-span bridges against wind loads is of primary concern during the design process. Long-span bridges must be designed against non-stationary winds while considering all kinds of structural and aerodynamic nonlinearities existing in the wind-bridge interaction. This interaction can result in the wind loads that cause violent motion of the girder such as flutter and buffeting. Currently, the wind tunnel test is considered to be the most effective means of determining the aerodynamic characteristics of the newly proposed bridge sections during the design process. However, the extent of data available from these tests is insufficient for real typhoon-induced non-stationary winds to comprehensibly explicate the complex flow mechanisms involved and these tests prove to be very expensive and time-consuming, in addition the controlling of structural properties like damping, etc. is not easy. Apart from this, the nonlinear bridge aerodynamics may become increasingly crucial issue when the aerodynamic characteristics of a modern bridge deck exhibit significant vulnerability with respect to the effective angle of attack and with the increase in the bridge main span length. These issues may not be addressed by utilizing the existing aerodynamic load models due to so many assumptions involved. This dissertation presents the development of an efficient framework for performing the nonlinear buffeting analysis in time-domain based on the Volterra series to investigate the non-stationary wind effects on long-span bridges. The conclusions from this thesis and possible further directions for future work are presented in the following sections.

Concluding remarks

- It has been shown that an additional time scale in the formulation of indicial response function is introduced to simulate the changes in bridge aerodynamics resulting from the fluid memory effects as well as the non-stationary wind effects. The present research explicates the physical meaning on the underlying mechanism of the changing bridge aerodynamics owing to transient effects of typhoon-induced non-stationary winds.
- The buffeting analyses of an example bridge subjected to the typhoon winds are presented based on the proposed Volterra FD, Hybrid Volterra FD, and Volterra ANN models as well as based on the existing aerodynamic wind load models. The proposed nonlinear Volterra FD, Hybrid Volterra FD and Volterra ANN models can simulate the real phenomenon of typhoon-induced buffeting response of long-span bridges around the time-varying mean wind response, whereas the existing aerodynamic wind load models show the significant errors in the simulation of buffeting response of the bridge around the constant mean wind

response.

- The time-history analysis results show that the non-stationary wind forces modify the aerodynamics of wind-bridge interaction system and increase the mean wind response of long-span bridges; therefore, it is important to consider the time-varying mean wind speed induced by typhoon winds instead of straight-line constant mean wind speed in the simulation of wind-induced buffeting response; otherwise, the wind design of the long-span bridges may be on the unsafe side.
- The traditional approach of spectral representation is not capable to explicate the time-varying characteristics of real typhoon-induced non-stationary winds owing to its limitation of being a frequency-domain approach, rather an evolutionary power spectral density (EPSD) method, being a frequency- and time-domain approach, is utilized herein to generate the artificial non-stationary wind fluctuations along the bridge deck, which also conforms the measurement data of wind speed.
- The inclusion of drag forces in the LU, HNL, Volterra FD, Hybrid Volterra FD, and Volterra ANN models modifies the lateral buffeting response of the bridge deck significantly, whereas the 2D aerodynamic models do not incorporate the drag forces and show almost similar but very minute lateral buffeting response of the bridge.
- The QS model considers the static nonlinear effects but fails to include nonlinear fluid memory effects; the corrected QS model takes into account the nonlinearity effects with linear fluid memory effects at a fixed reduced frequency; the linearized QS model considers the linear aerodynamic effects without the fluid memory effects; the LU model considers linear aerodynamic effects with linear fluid memory effects; hybrid model includes the nonlinearity effects only at low-frequency range with linear fluid memory effects at high-frequency range; the Volterra FD model considers aerodynamic nonlinearity effects in terms of higher-order Volterra kernels with nonlinear fluid memory effects; the Hybrid Volterra FD model takes into account the nonlinearity arising from the instantaneous angle of attack at low-frequency range as well as the nonlinear fluid memory and aerodynamic nonlinearity effects at the high-frequency range, and the Volterra ANN also considers the aerodynamic nonlinearity and nonlinear fluid memory effects for a whole range of frequencies in terms of higher-order Volterra kernels whose values are obtained based on the synaptic weights of the activated neurons.
- Although the HNL model is partly able to reproduce the nonlinear behavior of bridge response while considering the effect of linear fluid memory in the high-frequency range, this model cannot be considered as fully nonlinear nor fully unsteady. On the contrary, the Volterra FD, Hybrid Volterra FD and Volterra ANN models fully characterize the bridge aerodynamic and aeroelastic behaviors under non-stationary winds while considering

aerodynamic and aeroelastic nonlinearities as well as the nonlinear fluid memory or unsteady effects on the buffeting response of the bridge.

- As compared to the Volterra FD model, the Hybrid Volterra FD and Volterra ANN models yield more accurate buffeting analysis results of the example bridge because the Hybrid Volterra FD model considers the aerodynamic nonlinearity effects both in low- and high-frequency ranges mainly arising from the instantaneous angle of attack of wind and amplitude-dependency of FDs, respectively. In the case of the Volterra ANN model, the ANN technique builds the mapping of the nonlinear relationship between incoming flow as inputs and bridge response as outputs through the associated synaptic weights carried by activated neurons, which simulate the buffeting response with relatively high accuracy.
- The effects of non-stationary winds on the buffeting response of the bridge are more pronounced than the aerodynamic nonlinearities.
- At high wind speed, i.e., 60 m/s, the Hybrid Volterra FD model produces the slightly larger RMS of the buffeting response as compared to the LU, HNL, Volterra FD and Volterra ANN models due to the influence of the changes in the mean angles of attack at high wind speed. This characteristic is successfully be modelled by using the Hybrid Volterra FD model. However, the difference in RMS results obtained from the Hybrid Volterra FD and Volterra ANN models is not so large because these both models consider the effects of aerodynamic nonlinearity, nonlinear fluid memory, and non-stationary winds on the buffeting response of the bridge accurately for this example bridge. However, the results of this example bridge may not simply be extended to other bridge structures which may require preliminary interrogation based on their aerodynamic and structural characteristics thoroughly.

Future directions

Through the present study, the current status of the analytical methods in the field of bridge aerodynamics was grasped. Extensions of the present study can be made in many ways. In this research work, the effects of non-stationary winds and aerodynamic nonlinearity along with the self-excited force effects on the buffeting response of the bridge have been clarified in the case of a three-dimensional FE model. Based on these observations and experience in implementing the developed aerodynamic wind load model in this dissertation, the following directions of future research are suggested:

- To perform the flutter analysis for each aerodynamic wind load model including Volterra FD, Hybrid Volterra FD, and Volterra ANN models in order to elucidate the suitability of each aerodynamic model for checking the flutter critical wind speeds of the long-span bridges.
- To pursue the analysis of full span bridge under buffeting loads with due attention to fluid-

structure interaction using CFD applications.

- To investigate the effects of time-varying coherence function on the buffeting response of the long-span bridges.
- To try some other techniques for the identification of Volterra kernels and compare them with the present techniques used in this dissertation for accurate outcomes.
- To conduct the buffeting analysis of bridge in time-domain in the wake of a hill considering the non-uniformity and non-stationarity of wind characteristics, i.e., time-varying mean wind speed, evolutionary power spectral density and time-varying coherence of wake flow at the bridge location.
- To extend the proposed Volterra FD, Hybrid Volterra FD, and Volterra ANN models in order to simulate the effects of some other extreme wind events such as tornadoes, microbursts, and downbursts. In this case, a new framework is required to generate the tornado-induced wind speed while considering the time-varying coherence functions and EPSD to explicate the mechanism of tornado-structure interaction.
- Current wind design guidelines in Japan suggest the 10 min averaging time to find the mean wind speed for the calculation of bridge response based on linear, stationary, and steady-state model. However, the real phenomenon of typhoon-induced buffeting response may entail a different averaging time. Therefore, there is a need to optimize the best combination of averaging time and aerodynamic parameters for long-span bridges under real typhoon winds.

REFERENCES

Aas-Jakobsen, K., & Strømmen, E. (2001). Time domain buffeting response calculations of slender structures. Journal of Wind Engineering and Industrial Aerodynamics, 89(5), 341–364. doi:10.1016/s0167-6105(00)00070-2

Bendat, J.S., Piersol, A.G. (2010). Random Data: Analysis and Measurement Procedures, 4th ed. Wiley, Hoboken, NJ.

Bisplinghoff, R. L., & Ashley, H. (1962). Principles of aeroelasticity. John Wiley and Sons, New York, N. Y.

Boonyapinyo, V., Miyata, T., & Yamada, H. (1999). Advanced Aerodynamic Analysis of Suspension Bridges by State-Space Approach. Journal of Structural Engineering, 125(12), 1357–1366. doi:10.1061/(asce)0733-9445(1999)125:12(1357)

Boyd, S., & Chua, L. (1985). Fading memory and the problem of approximating nonlinear operators with Volterra series. IEEE Transactions on Circuits and Systems, 32(11), 1150–1161. doi:10.1109/tcs.1985.1085649

Cao, B., & Sarkar, P. P. (2015). Numerical simulation of dynamic response of a long-span bridge to assess its vulnerability to non-synoptic wind. Engineering Structures, 84, 67–75. doi:10.1016/j.engstruct.2014.11.009

Caracoglia, L., & Jones, N. P. (2003a). A methodology for the experimental extraction of indicial functions for streamlined and bluff deck sections. Journal of Wind Engineering and Industrial Aerodynamics, 91(5), 609–636. https://doi.org/10.1016/S0167-6105(02)00473-7

Caracoglia, L., & Jones, N. P. (2003b). Time domain vs. frequency domain characterization of aeroelastic forces for bridge deck sections. Journal of Wind Engineering and Industrial Aerodynamics, 91(3), 371–402. https://doi.org/10.1016/S0167-6105(02)00399-9

Chay, M. & C. Letchford (2002). Pressure distributions on a cube in a simulated thunderstorm downburst—Part A: stationary downburst observations. Journal of Wind Engineering and Industrial Aerodynamics. 90(7), 711-732

Chen, L., & Letchford, C. W. (2004). A deterministic–stochastic hybrid model of downbursts and its impact on a cantilevered structure. Engineering Structures, 26(5), 619–629. doi:10.1016/j.engstruct.2003.12.009

Chen, X. (2008). Analysis of Alongwind Tall Building Response to Transient Nonstationary Winds. Journal of Structural Engineering, 134(5), 782–791. doi:10.1061/(asce)0733-9445(2008)134:5(782)

Chen, X. (2015). Analysis of Multimode Coupled Buffeting Response of Long-Span Bridges to Nonstationary Winds with Force Parameters from Stationary Wind. Journal of Structural Engineering, 141(4), 04014131. doi:10.1061/(asce)st.1943-541x.0001078

Chen, X., & Kareem, A. (2001). Nonlinear response analysis of long-span bridges under turbulent winds. Journal of Wind Engineering and Industrial Aerodynamics, 89(14-15), 1335–1350. doi:10.1016/s0167-6105(01)00147-7

Chen, X., & Kareem, A. (2002). Advances in Modeling of Aerodynamic Forces on Bridge Decks. Journal of Engineering Mechanics, 128(11), 1193–1205. doi:10.1061/(asce)0733-9399(2002)128:11(1193)

Chen, X., & Kareem, A. (2003). Aeroelastic Analysis of Bridges: Effects of Turbulence and Aerodynamic Nonlinearities. Journal of Engineering Mechanics, 129(8), 885–895. doi:10.1061/(asce)0733-9399(2003)129:8(885)

Chow S. H. (1970). A study of the wind field in the planetary boundary layer of a moving tropical cyclone, master thesis, New York university, New York.

Costa, C., & Borri, C. (2006). Application of indicial functions in bridge deck aeroelasticity. Journal of Wind Engineering and Industrial Aerodynamics, 94(11), 859–881. doi:10.1016/j.jweia.2006.06.007

Costa, C., Borri, C., Flamand, O., & Grillaud, G. (2007). Time-domain buffeting simulations for wind–bridge interaction. Journal of Wind Engineering and Industrial Aerodynamics, 95(9-11), 991–1006. doi:10.1016/j.jweia.2007.01.026

Davenport, A. G. (1961). The application of statistical concepts to the wind loading of structures. Proceedings of the Institution of Civil Engineers, 19, 449–472.

Davenport, A. G. (1961). The spectrum of horizontal gustiness near the ground in high winds. Quarterly Journal of the Royal Meteorological Society, 87(372), 194–211. doi:10.1002/qj.49708737208

Davenport, A. G. (1962a). Buffeting of a suspension bridge by storm winds. Journal of Structural Division ASCE. 88(3), 233–268.

Davenport, A. G. (1962b). The response of slender, line-like structures to a gusty wind. Proceedings of the Institution of Civil Engineers, 23(3), 389–408. doi:10.1680/iicep.1962.10876

Davenport, A. G. (1966). The action of wind on suspension bridges. Proceedings of the International Symposium on Suspension Bridges. Laboratorio Nacional De Engenharia Civil, Lisbon, Portugal, 79–100.

De Paula, N. C. G., & Marques, F. D. (2019). Multi-variable Volterra kernels identification using time-delay neural networks: application to unsteady aerodynamic loading. Nonlinear Dynamics, 97(1), 767–780. doi:10.1007/s11071-019-05011-8

Diana, G., Bruni, S., Cigada, A., & Collina, A. (1993). Turbulence effect on flutter velocity in long span suspended bridges. Journal of Wind Engineering and Industrial Aerodynamics, 48(2-3), 329–342. doi:10.1016/0167-6105(93)90144-d

Diana, G., Resta, F., & Rocchi, D. (2008). A new numerical approach to reproduce bridge aerodynamic non-linearities in time domain. Journal of Wind Engineering and Industrial Aerodynamics, 96(10-11), 1871–1884. doi:10.1016/j.jweia.2008.02.052

Diana, G., Rocchi, D., & Argentini, T. (2013). An experimental validation of a band superposition model of the aerodynamic forces acting on multi-box deck sections. Journal of Wind Engineering and Industrial Aerodynamics, 113, 40–58. doi:10.1016/j.jweia.2012.12.005

Diana, G., Rocchi, D., Argentini, T., & Muggiasca, S. (2010). Aerodynamic instability of a bridge deck section model: Linear and nonlinear approach to force modeling. Journal of Wind Engineering and Industrial Aerodynamics, 98(6-7), 363–374. doi:10.1016/j.jweia.2010.01.003

Ding, Q., & Lee, P. K. K. (2000). Computer simulation of buffeting actions of suspension bridges under turbulent wind. Computers & Structures, 76(6), 787–797. doi:10.1016/s0045-7949(99)00197-2

Farsani, H. Y., Valentine, D. T., Arena, A., Lacarbonara, W., & Marzocca, P. (2014). Indicial functions in the aeroelasticity of bridge decks. Journal of Fluids and Structures, 48, 203–215. doi.org/10.1016/j.jfluidstructs.2014.02.015

Garrick, I. E. (1938). NACA Report No. 629: On some reciprocal relations in the theory of nonstationary flows. Washington, DC: National Advisory Committee for Aeronautics.

Ge, Y. J., & Xiang, H. F. (2008). Computational models and methods for aerodynamic flutter of long-span bridges. Journal of Wind Engineering and Industrial Aerodynamics, 96(10-11), 1912–1924. doi:10.1016/j.jweia.2008.02.017

Hao J., & Wu T. (2011). Nonsynoptic wind-induced transient effects on linear bridge aerodynamics via cellular automata nested neural network. Journal of Wind Engineering and Industrial Aerodynamics, 99(4), 378–388.

Honshu-Shikoku Bridge Authority. (2001). Wind Resistant Design Codes for the Honshu Shikoku Project in Japan (in Japanese)

Hu, L., Xu, Y. L., & Huang, W. F. (2013). Typhoon-induced non-stationary buffeting response of long-span bridges in complex terrain. Engineering Structures, 57, 406–415. doi.org/10.1016/j.engstruct.2013.09.044

Hu, L., Xu, Y. L., Huang, W.F. and Liu, H. J. (2011). Typhoon-induced nonstationary buffeting response of long-span bridges. Proceedings of 14th Asia Pacific Vibration Conference, Hong Kong, December 5–8, 173–182.

Huang N. E, Shen, Z. & Long. S. R. et al (1998) The empirical mode decomposition and the Hilbert spectrum for nonlinear and non-stationary time series analysis. Proceedings of the Royal Society of London series A-mathematical Physical and Engineering Sciences, 454(1971), 903 – 995.

Huang, G., Su, Y., Kareem, A., & Liao, H. (2016). Time-Frequency Analysis of Nonstationary Process Based on Multivariate Empirical Mode Decomposition. Journal of Engineering Mechanics, 142(1), 04015065. doi:10.1061/(asce)em.1943-7889.0000975

Jones, R. T. (1939). NACA Report No. 682: The unsteady lift of a finite wing. Washington, DC: National Advisory Committee for Aeronautics

Jones, R. T. (1940). NACA Report No. 681: The unsteady lift on a wing of finite aspect ratio. Washington, DC: National Advisory Committee for Aeronautics

Katsuchi, H., Jones, N. P., & Scanlan, R. H. (1999). Multimode Coupled Flutter and Buffeting Analysis of the Akashi-Kaikyo Bridge. Journal of Structural Engineering, 125(1), 60–70. doi:10.1061/(asce)0733-9445(1999)125:1(60)

Katsuchi, H., Jones, N. P., Scanlan, R. H., & Akiyama, H. (1998). Multi-mode flutter and buffeting analysis of the Akashi-Kaikyo bridge. Journal of Wind Engineering and Industrial Aerodynamics, 77-78, 431–441. doi:10.1016/s0167-6105(98)00162-7

Kavrakov, I., & Morgenthal, G. (2017). A Comparative Assessment of Aerodynamic Models for Buffeting and Flutter of Long-Span Bridges. Engineering, 3(6), 823–838. doi:10.1016/j.eng.2017.11.008

Kavrakov, I., Legatiuk, D., Gürlebeck, K., & Morgenthal, G. (2019). A categorical perspective towards aerodynamic models for aeroelastic analyses of bridge decks. Royal Society Open Science, 6(3), 181848. doi:10.1098/rsos.181848

Kovacs, I., Svensson, H. S., & Jordet, E. (1992). Analytical Aerodynamic Investigation of Cable-Stayed Helgeland Bridge. Journal of Structural Engineering, 118(1), 147–168. doi:10.1061/(asce)0733-9445(1992)118:1(147)

Kwon, D.-K., & Kareem, A. (2009). Gust-Front Factor: New Framework for Wind Load Effects on Structures. Journal of Structural Engineering, 135(6), 717–732. doi:10.1061/(asce)0733-9445(2009)135:6(717)

Lazzari, M. (2005). Time domain modelling of aeroelastic bridge decks: a comparative study and an application. International Journal for Numerical Methods in Engineering, 62(8), 1064–1104. doi:10.1002/nme.1238

Letchford, C. and M. Chay (2002). Pressure distributions on a cube in a simulated thunderstorm downburst. Part B: moving downburst observations. Journal of Wind Engineering and Industrial Aerodynamics. 90(7), 733-753

Lin, R. M., & Ng, T.-Y. (2018). Identification of Volterra kernels for improved predictions of nonlinear aeroelastic vibration responses and flutter. Engineering Structures, 171, 15–28. doi:10.1016/j.engstruct.2018.05.073

MATLAB. (2017). version 9.3.0.713579 (R2017b). Natick, Massachusetts: The MathWorks Inc.

Meng, Y., Matsui, M., & Hibi, K. (1995). An analytical model for simulation of the wind field in a typhoon boundary layer. Journal of Wind Engineering and industrial aerodynamics, 56 (2–3), 291 – 310.

Miyata, T., Yamada, H., Boonyapinyo, V., Santos, J.S. (1995). Analytical investigation on the response of a very long suspension bridge under gusty wind. IN: Proceedings of Ninth ICWE, New Delhi, Vol 2., 1006 – 1017.

Miyata, T., Yokoyama, K., Yasuda, M., & Hikami, Y. (2017). Akashi Kaikyo Bridge: Wind effects and full model wind tunnel tests. Aerodynamics of Large Bridges, 217–236. doi:10.1201/9781315136950-16

Øiseth, O., Rönnquist, A., & Sigbjörnsson, R. (2011). Time domain modeling of self-excited aerodynamic forces for cable-supported bridges: A comparative study. Computers and Structures, 89(13–14), 1306–1322. https://doi.org/10.1016/j.compstruc.2011.03.017

Parkinson, G. V., & Brooks, N. P. H. (1961). On the Aeroelastic Instability of Bluff Cylinders. Journal of Applied Mechanics, 28(2), 252–258. doi:10.1115/1.3641663

Paula, N. C., Marques, F. D., & Silva, W. A. (2018). Volterra Kernels Assessment via Time-Delay Neural Networks for Nonlinear Unsteady Aerodynamic Loading Identification. AIAA/ASCE/AHS/ASC Structures, Structural Dynamics, and Materials Conference. doi:10.2514/6.2018-1209

Peng, L., Huang, G., Chen, X., & Kareem, A. (2017). Simulation of Multivariate Nonstationary Random Processes: Hybrid Stochastic Wave and Proper Orthogonal Decomposition Approach. Journal of Engineering Mechanics, 143(9), 04017064. doi:10.1061/(asce)em.1943-7889.0001273

Peng, L., Huang, G., Chen, X., & Yang, Q. (2018). Evolutionary Spectra-Based Time-Varying Coherence Function and Application in Structural Response Analysis to Downburst Winds. Journal of Structural Engineering, 144(7), 04018078. doi:10.1061/(asce)st.1943-541x.0002066

Petrini, F., Giuliano, F., & Bontempi, F. (2007). Comparison of time domain techniques for the evaluation of the response and the stability in long span suspension bridges. Computers & Structures, 85(11-14), 1032–1048. doi:10.1016/j.compstruc.2006.11.015

Priestley, M. B. (1965). Evolutionary Spectra and Non-Stationary Processes. Journal of the Royal Statistical Society: Series B (Methodological), 27(2), 204–229. doi:10.1111/j.2517-6161.1965.tb01488.x

Priestley, M. B., & Tong. H. (1973). On the analysis of bivariate nonstationary processes. Journal of Royal Statistical Society Series. B, 35(2), 153–166.

Raveh, D. (2000). Reduced order models for nonlinear unsteady aerodynamics. 8th Symposium on Multidisciplinary Analysis and Optimization. doi:10.2514/6.2000-4785

Raveh, D. E. (2001). Reduced-order models for nonlinear unsteady aerodynamics. AIAA Journal, 39, 1417–1429. doi:10.2514/3.14885

Rilling, G., Patrick F., & Paulo G. (2003). On empirical mode decomposition and its algorithms. IEEE-EURASIP Workshop on Nonlinear Signal and Image Processing. NSIP-03. Grado, Italy. 8–11.

Salvatori, L., & Borri, C. (2007). Frequency- and time-domain methods for the numerical modeling of full-bridge aeroelasticity. Computers & Structures, 85(11-14), 675–687. doi:10.1016/j.compstruc.2007.01.023

Scanlan, R. H. & Rosenbaum, R. (1951). Aircraft vibration and flutter, Macmillan, Inc., New York, N. Y.

Scanlan, R. H., Beliveau, J.-G., & Budlong, K. S. (1974). Indicial aerodynamic functions for bridge decks. Journal of the Engineering Mechanics, 100(4)(4), 657–672

Scanlan, R. H. (1978). The action of flexible bridges under wind, I: Flutter theory. Journal of Sound and Vibration, 60(2), 187–199. doi:10.1016/s0022-460x(78)80028-5

Scanlan, R. H. (1978). The action of flexible bridges under wind, II: Buffeting theory. Journal of Sound and Vibration, 60(2), 201–211. doi:10.1016/s0022-460x(78)80029-7

Scanlan, R. H. (1984). Role of indicial functions in buffeting analysis of bridges. Journal of Structural Engineering, 110(7), 1433–1446.

Scanlan, R. H. (1987). Interpreting Aeroelastic Models of Cable-Stayed Bridges. Journal of Engineering Mechanics, 113(4), 555–575. doi:10.1061/(asce)0733-9399(1987)113:4(555)

Scanlan, R. H. (1993). Problematics in Formulation of Wind-Force Models for Bridge Decks. Journal of Engineering Mechanics, 119(7), 1353–1375. doi:10.1061/(asce)0733-9399(1993)119:7(1353)

Scanlan, R. H., & Jones, N. P. (1990). Aeroelastic analysis of cable-stayed bridges. Journal of Structural Engineering, 116(2), 279-297.

Silva, W. (1997). Discrete-time linear and nonlinear aerodynamic impulse responses for efficient CFD analyses. Ph.D. thesis, College of William & Mary, Williamsburg, Virgina.

Silva, W. (2005). Identification of Nonlinear Aeroelastic Systems Based on the Volterra Theory: Progress and Opportunities. Nonlinear Dynamics, 39(1-2), 25–62. doi:10.1007/s11071-005-1907-z

Simiu, E. & Scanlan R. (1996). Wind effects on structures 3rd edn. New York, NY: John Wiley & Sons.

Smith, M. (2014). ABAQUS/Standard User's Manual, Version 6.14-5, Providence, RI: Dassault Simulia

Solari, G. (2016). Thunderstorm response spectrum technique: Theory and applications. Engineering Structures, 108, 28–46. doi:10.1016/j.engstruct.2015.11.012

Theodorsen, T. (1935). NACA Report 496: General theory of aerodynamic instability and the mechanism of flutter. Washington, DC: National Advisory Committee for Aeronautics.

Tubino, F. (2005). Relationships among aerodynamic admittance functions, flutter derivatives and static coefficients for long-span bridges. Journal of Wind Engineering and Industrial Aerodynamics, 93(12), 929–950. https://doi.org/10.1016/j.jweia.2005.09.002

Vickery, P.J & Twisdale, L.A. (1995). Wind-field and filling models for hurricane wind-speed predictions. Journal of Structural Engineering, 121 (11), 1700 – 1709.

Volterra, V. (1959). Theory of functionals and of integral and integro-differential equations. London, Dove Press.

Wagner, H. (1925). Über die Entstehung des dynamischen Auftriebes von Tragflügeln. ZAMM - Zeitschrift Für Angewandte Mathematik Und Mechanik, 5(1), 17–35. doi:10.1002/zamm.19250050103 (in German)

Wray, J., & Green, G. G. R. (1994). Calculation of the Volterra kernels of non-linear dynamic systems using an artificial neural network. Biological Cybernetics, 71(3), 187–195. doi:10.1007/s004220050081

Wu, T. & Kareem, A. (2015). A low-dimensional model for nonlinear bluff-body aerodynamics: A peeling-an-onion analogy. Journal of Wind Engineering and Industrial Aerodynamics, 146(2015), 128–138.

Wu, T., & Kareem, A. (2011). Modeling hysteretic nonlinear behavior of bridge aerodynamics via cellular automata nested neural network. Journal of Wind Engineering and Industrial Aerodynamics, 99(4), 378–388. doi:10.1016/j.jweia.2010.12.011

Wu, T., & Kareem, A. (2013). A nonlinear convolution scheme to simulate bridge aerodynamics. Computers & Structures, 128, 259–271. doi:10.1016/j.compstruc.2013.06.004

Wu, T., & Kareem, A. (2013). Bridge aerodynamics and aeroelasticity: A comparison of modeling schemes. Journal of Fluids and Structures, 43, 347–370. doi:10.1016/j.jfluidstructs.2013.09.015

Wu, T., Kareem, A., & Ge, Y. (2013). Linear and nonlinear aeroelastic analysis frameworks for cable-supported bridges. Nonlinear Dynamics, 74(3), 487–516. doi:10.1007/s11071-013-0984-7

Xu, F. Y. (2015). System Decoupling Approach for 3-DOF Bridge Flutter Analysis. Journal of Structural Engineering, 141(7), 04014168. doi:10.1061/(asce)st.1943-685 541x.0001129

Xu, Y. L., & Chen, J. (2004). Characterizing Nonstationary Wind Speed Using Empirical Mode Decomposition. Journal of Structural Engineering, 130(6), 912–920. doi:10.1061/(asce)0733-9445(2004)130:6(912)

Zhan, Y., Halliday, D., Jiang, P., Liu, X., & Feng, J. (2006). Detecting time-dependent coherence between non-stationary electrophysiological signals—A combined statistical and time–frequency approach. Journal of Neuroscience Methods, 156(1-2), 322–332. doi:10.1016/j.jneumeth.2006.02.013